Rational Design of Novel Halide Perovskites Combining Computations and Experiments

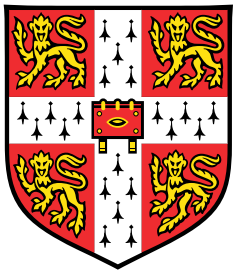

Zeyu Deng

Department of Materials Science and Metallurgy
University of Cambridge

This dissertation is submitted for the degree of
Doctor of Philosophy

Clare College November 2018

For my beloved parents: Zhiping Deng and Licheng Deng.

Declaration

I hereby declare that except where specific reference is made to the work of others, the contents of this dissertation are original and have not been submitted in whole or in part for consideration for any other degree or qualification in this, or any other university. This dissertation is my own work and contains nothing which is the outcome of work done in collaboration with others, except as specified in the text and Acknowledgements. This dissertation contains fewer than 60,000 words in length, exclusive of tables, footnotes, bibliography, and appendices.

Zeyu Deng
November 2018

Acknowledgements

I would like to acknowledge my supervisors Dr. Paul D. Bristowe and Prof. Anthony K. Cheetham for their continuous support, scientific discussions and provision of computational and experimental facilities. All of my calculations were performed at the UK National Supercomputing Service, ARCHER. Access was obtained via the UKCP consortium and funded by EPSRC under Grant No.EP/K014560/1 and No.EP/P022596/1. Also I am grateful to my sponsors: Cambridge Commonwealth and International Trust and China Scholarship Council for giving me the opportunity to undertake this project. Besides my supervisors and sponsors, I would like to express my gratitude to all of my colleagues: Dr. Jung-Hoon Lee, Dr. Federico Brivio, Dr. Yue Wu, Dr. Gregore Kieslich, Dr. Jingwei Hou, Dr. Thomas Bennett, Dr. Shafqat Shah, Dr. Eric Schmidt, Sammy Shaker and Tianwei Wang. In particular I am hugely indebted to Dr. Fengxia Wei and Dr. Shijing Sun for their help in discussions, sharing the experimental results and guidance with experimental synthesis and characterisation. Also I am grateful to all the collaborators and co-authors listed in my publication author lists. Finally, I want to thank to my family and friends for their support and encouragement during my project and thesis writing.

Abstract

The perovskite family of materials is extremely large and provides a template for designing materials for different purposes. Among them, hybrid organic-inorganic perovskites (HOIPs) are very interesting and have been recently identified as possible next generation light harvesting materials because they combine low manufacturing cost and relatively high power conversion efficiencies (PCEs). In addition, some other applications like light emitting devices are also highly studied. This thesis starts with an introduction to the solar cell technologies that could use HOIPs. In Chapter 2, previously published results on the structural, electronic, optical and mechanical properties of HOIPs are reviewed in order to understand the background and latest developments in this field. Chapter 3 discusses the computational and experimental methods used in the following chapters. Then Chapter 4 describes the discovery of several *hybrid double perovskites*, with the formula $(MA)_2M^{I}M^{III}X_6$ (MA = methylammonium, CH_3NH_3, M^{I} = K, Ag and Tl, M^{III} = Bi, Y and Gd, X = Cl and Br). Chapter 5 presents studies on the variable presure and temperature response of formamidinium lead halides $FAPbBr_3$ (FA = formamidinium, $CH(NH_2)_2$) as well as the mechanical properties of $FAPbBr_3$ and $FAPbI_3$, followed by a computational study connecting the mechanical properties of halide perovskites ABX_3 (A = K, Rb, Cs, Fr and MA, X = Cl, Br and I) to their electronic transport properties. Chapter 6 describes a study on the phase stability, transformation and electronic properties of low-dimensional hybrid perovskites containing the guanidinium cation Gua_xPbI_{x+2} (x = 1, 2 and 3, Gua = guanidinium, $C(NH_2)_3$). The conclusions and possible future work are summarized in Chapter 7. These results provide theoreticians and experimentalists with insight into the design and synthesis of novel, highly efficient, stable and environmentally friendly materials for solar cell applications as well as for other purposes in the future.

Publication

Below are the papers that I published during my 3 years PhD study:

- Jung-Hoon Lee*, **Zeyu Deng***, Nicholas C. Bristowe, Paul D. Bristowe, Anthony K. Cheetham, "Understanding the Conflict Between Mechanical Stability and Charge Carrier Mobility in Organic-Inorganic Perovskites: Insight from DFT ", *J. Mater. Chem. C* 2018, Accepted (*co-first author)

- **Zeyu Deng**, Gregor Kieslich, Paul D. Bristowe, Anthony K. Cheetham and Shijing Sun, "Octahedral Connectivity and its Role in Determining the Phase Stabilities and Electronic Structures of Low-Dimensional, Perovskite-Related Iodoplumbates", *APL Mater.* 2018, 6, 114202

- Liyuan Dong, Shijing Sun, **Zeyu Deng**, Wei Li, Fengxia Wei, Yajun Qi, Yanchun Li, Xiaodong Li, Peixiang Lu and U. Ramamurty, "Elastic properties and thermal expansion of lead-free halide double perovskite $Cs_2AgBiBr_6$", *Comput. Mater. Sci.*, 2018, 141 49–58

- **Zeyu Deng**, Fengxia Wei, Federico Brivio, Yue Wu, Shijing Sun, Paul D. Bristowe, and Anthony K. Cheetham, "Synthesis and Characterization of the Rare-Earth Hybrid Double Perovskites: $(CH_3NH_3)_2KGdCl_6$ and $(CH_3NH_3)_2KYCl_6$", *J. Phys. Chem. Lett.* 2017, 8(20) 5015–5020

- Shijing Sun, Furkan H Isikgor, **Zeyu Deng**, Fengxia Wei, Gregor Kieslich, Paul D. Bristowe, Jianyong Ouyang, Anthony K. Cheetham, "Factors influencing the mechanical properties of formamidinium lead halides and related hybrid perovskites", *ChemSusChem*, 2017, 10(19) 3740–3745

- Shijing Sun, **Zeyu Deng**, Yue Wu, Fengxia Wei, Furkan H Isikgor, Federico Brivio, Michael Gaultois, Jianyong Ouyang, Paul D. Bristowe, Anthony K. Cheetham, Gregor Kieslich, "Variable temperature and high-pressure crystal chemistry of perovskite

formamidinium lead iodide: a single crystal X-ray diffraction and computational study", *Chem. Commun.*, 2017, 54(53) 7537–7540

- Fengxia Wei, **Zeyu Deng**, Shijing Sun, Fenghua Zhang, Donald M Evans, Gregor Kieslich, Satoshi Tominaka, Michael A. Carpenter, Jie Zhang, Paul D. Bristowe, Anthony K. Cheetham, "Synthesis and Properties of a Lead-Free Hybrid Double Perovskite: $(CH_3NH_3)_2AgBiBr_6$", *Chem. Mater.*, 2017, 29(3) 1089–1094

- **Zeyu Deng**, Fengxia Wei, Shijing Sun, Gregor Kieslich, Anthony K. Cheetham, Paul D. Bristowe, "Exploring the properties of lead-free hybrid double perovskites using a combined computational-experimental approach", *J. Mater. Chem. A*, 2016, 4(31), 12025–12029

- Fengxia Wei, **Zeyu Deng**, Shijing Sun, Fei Xie, Gregor Kieslich, Donald M. Evans, Michael A. Carpenter, Paul D Bristowe, Anthony K Cheetham, "The synthesis, structure and electronic properties of a lead-free hybrid inorganic–organic double perovskite $(MA)_2KBiCl_6$ (MA= methylammonium)", *Mater. Horiz.*, 2016, 3(4) 328–332

Table of contents

List of figures

List of tables

Chapter 1

Introduction

1.1 The Emergence of Hybrid Perovskite Solar Cells

Solar energy is one of the cleanest, almost unlimited and easily accessible renewable energy resources, and the *solar cell* (also called *photovoltaic (PV) cell*) was invented to harvest this ideal energy resource into electricity using the photoelectric effect. However, its relatively low power-conversion efficiency (PCE) limits its applications as shown theoretically by Shockley and Queisser[1] (Fig. 1.1a). Therefore, over the past 40 years, researchers around the world have performed extensive studies to improve the PCE of solar cells, and have pushed its value from 4.5% in 1954 to 26.1% in 2017 (see Fig. 1.1b[2]). The first generation PV technology has used wafers of crystalline silicon[40] as the light harvesting material. As shown in Fig. 1.1a, although crystalline silicon (with a band gap of 1.1 eV) is not the best light harvesting material optoelectronically, its abundance on earth and the high PCEs of devices using it, makes it dominant in today's PV field. However, highly efficient Si solar cells need a thick wafer ($\sim$ 200 nm) in order to absorb enough light, and the fabrication process needs high temperatures and a clean room environment. Therefore, 2nd generation solar cells have emerged which use thin-film technologies ($\sim$ few μm to few nm thick), e.g. amorphous silicon[41], CdTe[42] or copper indium gallium diselenide (CIGS)[43] instead of thick crystalline Si wafers to reduce fabrication costs. However, they are not able to challenge the widespread use of crystalline Si due to their relatively lower PCEs. In order to discover more highly efficient and lower-cost PV technologies, 3rd generation technologies have emerged, e.g. dye-sensitized solar cells (DSSCs)[44], organic solar cells[45] and quantum dot solar cells[46]. Among them, DSSCs developed by Grätzel et al.[44] have received much attention because the materials are solution processable so the fabrication cost is much lower than traditional Si solar cells and they can achieve satisfactory efficiencies (>

10%, see Fig. 1.1b). Recently, based on the device architectures of DSSCs, hybrid organic-inorganic perovskite solar cells (HOIPSCs)[47, 48, 3] have been fabricated using the hybrid organic-inorganic perovskites (HOIPs) e.g. $MAPbBr_3$ and $MAPbI_3$ (MA=methylammonium $[CH_3NH_3]^+$) as the light absorber, and their PCEs soared from 3.8%[49] to 22.7% (Fig. 1.1). One of the great advantages of HOIPs is that they are solution processable, therefore they are lower-cost compared with Si-based devices, and can be easily fabricated in a normal chemistry laboratory by spin coating. Because of their high efficiency and relatively low cost, they are likely to become the next generation photovoltaic technology. Although there are some problems and challenges as described later in this chapter, HOIPs are still promising and worth studying. Within the whole HOIPSC device, the most crucial part is the light harvesting material – HOIP. Therefore, the rational design of highly efficient, low-cost, stable and nontoxic HOIPs combining computations and experiments is chosen as the research topic for this thesis. Before giving more details about HOIPs, in the following sections, some background to the development, working mechanism, current advances and challenges of HOIPSCs is described. A more detailed description of HOIP material will then be given in Chapter 2.

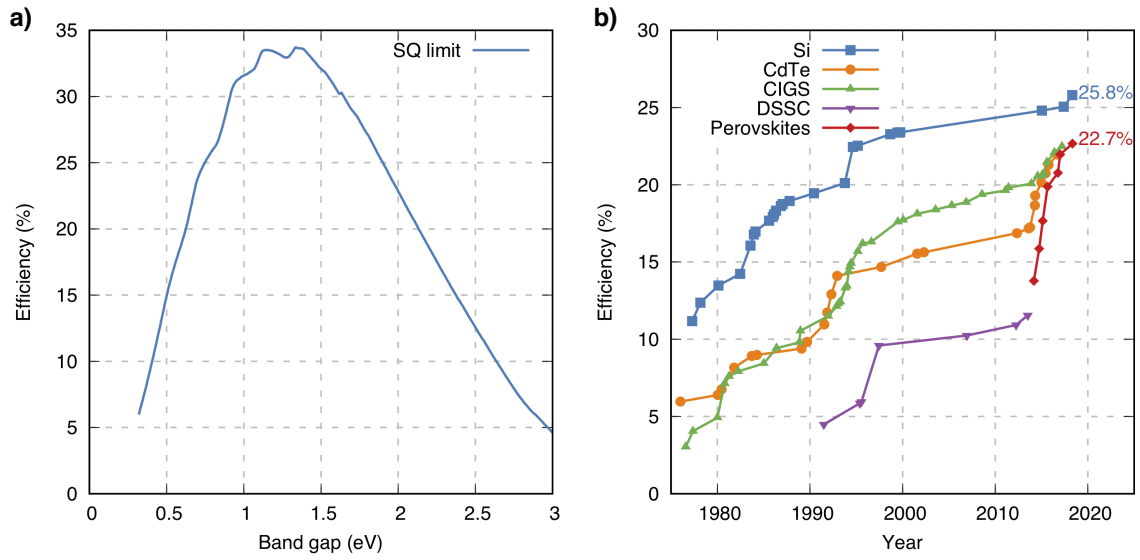

Fig. 1.1 a) The Shockley Queisser (SQ) theoretical PCE limit[1]. b) The efficiency of research solar cells, data is from the National Renewable Energy Laboratory (NREL)[2].

1.2 HOIP Solar Cells

1.2.1 Working Mechanism and Device Structure

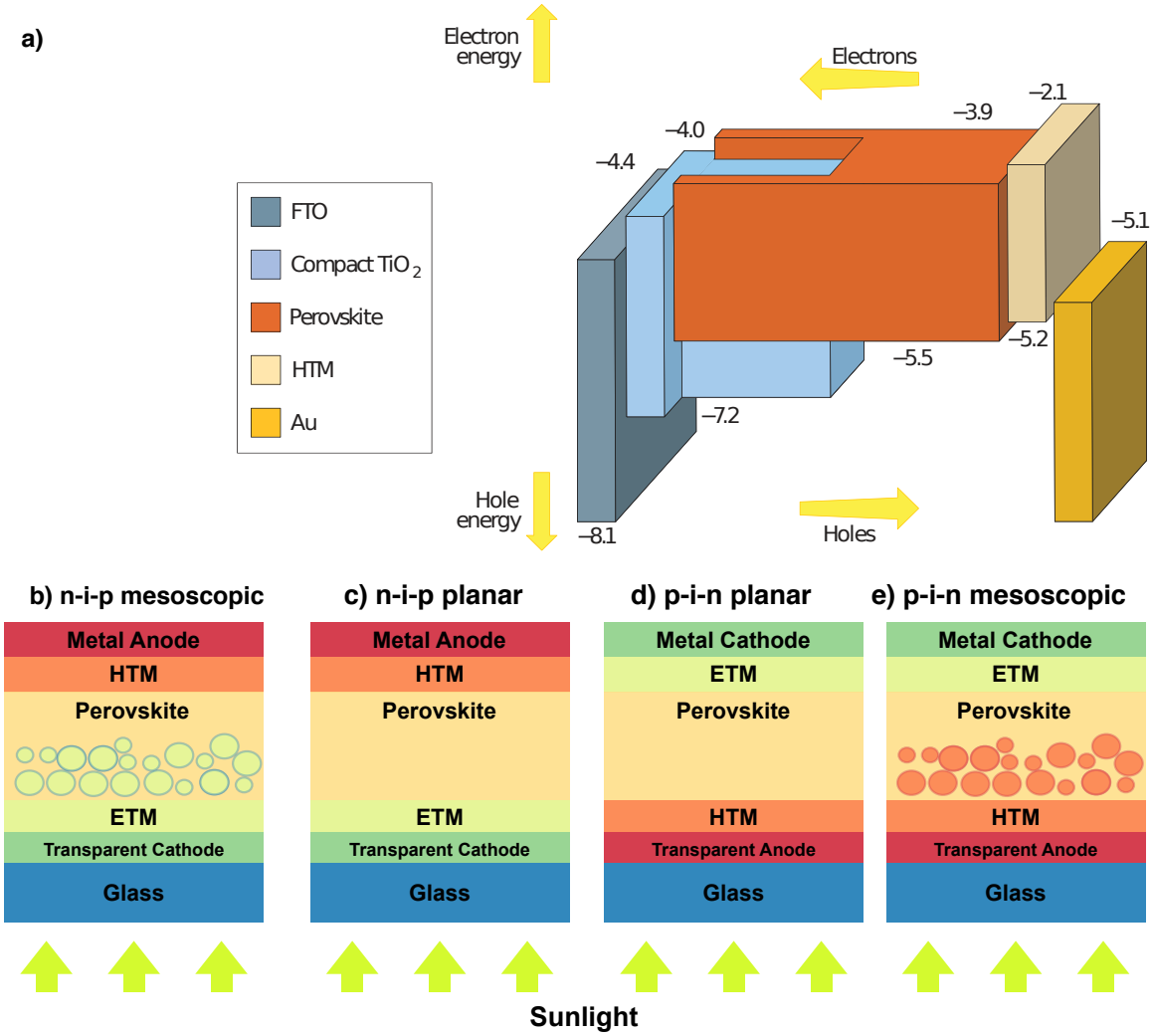

Fig. 1.2 a) Working mechanism of HOIPSCs (n-i-p structure) with electron/hole energies shown in eV (adapted from Green et al.[3] with permission from Springer Nature.); Typical HOIPSC device structures: b) n-i-p mesoscopic, c) n-i-p planar, d) p-i-n planar and e) p-i-n mesoscopic structures.

The working mechanism of the HOIPSC is quite simple as shown in Fig. 1.2a[3]. When electron-hole pairs are generated by the absorbed incident light, the energy potential (band alignment) in the device causes electrons to flow to the *electron transporting medium* (ETM) while holes go to the *hole transporting medium* (HTM), resulting in electron-hole separation.

Electrons in the ETM and holes in the HTM will go to the anode and cathode, respectively, driven by the internal energy potential and contributing to the current in the external circuit.

There are four types of HOIPSC architecture as shown in Fig. 1.2: n-i-p structures (n, p and i refer to n-type, p-type and intrinsic semiconductor, respectively) with (Fig. 1.2b) and without (Fig. 1.2c) a mesoscopic ETM, and inverted p-i-n structures with (Fig. 1.2d) and without (Fig. 1.2c) a mesoscopic HTM.

n-i-p structures are most widely studied and date back to the DSSC and organic solar cells. The mesoporous ETM was considered to be crucial for achieving high efficiency because the effective diffusion length L_D of the hole is much larger than that of the electron in $MAPbI_3$[50]. However, by controlling the interfacial contact, an efficient device without a mesoporous ETM can also be fabricated[51]. In addition, the process for fabricating mesoporous TiO_2 needs a high temperature which would increase cost and time for production[52]. Therefore, the non-mesoporous planar structure is considered to be the natural evolution of the mesoporous structure. However, a planar structure suffers greater J-V hysterisis[53, 54, 51, 55, 36], which leads to severely inaccurate results for measured device performance. Therefore, a novel planar device usually has a mixed mesoporous TiO_2/perovskite layer to combine the advantages of these two structures[56]. Nevertheless, for devices using small L_D absorbers such as Sn-based HOIPSCs[57], the mesoporous structure is still necessary.

Changing the deposition order can form a p-i-n structure. Different HTM - PEDOT:PSS (poly(3,4-ethylenedioxythiophene):poly(styrenesulfonic acid)) and ETM - PCBM ([6,6]-phenyl-C_{61}-butyric acid methyl ester) layers are used for p-i-n structure. A p-i-n structure suffers less J-V hysteresis, but the band alignment between the perovskite and PEDOT:PSS is not perfect, leading to a loss in the open-circuit voltage V_{oc}[52]. Both n-i-p and p-i-n structures can achieve high PCEs.

1.2.2 Advances

High Power Conversion Efficiency

As described in the previous sections, HOIPSCs are an emerging low cost and highly efficient PV technology. They originated from DSSCs which have mesoporous TiO_2 as the ETM covered by a light absorbing material – *the sensitizing dye*, contained in an HTM - redox electrolyte. Due to the dye that is used, it needs a thickness of ~10 μm to absorb sunlight optimally, but this is impractical in solid-state DSSCs, which are usually only able to have a thickness of 2 μm. Because of that, a more advanced dye is needed to absorb sunlight

within a much thinner layer, and thus led to Miyasaka et al.'s pioneering work using the HOIP $MAPbI_3$ as the absorber and this subsequently achieved a PCE of 3.8%[49]. In 2011, Park et al.[58] obtained an efficiency of 6.5% by improving the TiO_2 surface and fabrication process. However, due to the liquid electrolyte, the poor stability and relatively low PCE of the device, HOIPSCs did not receive much attention.

The huge rise in the PCEs of HOIPSCs and the subsequent interest from the whole research community, dubbed *perovskite fever*[59], began in 2012 when Park and Grätzel et al.[60] used solid state spiro-MeOTAD (2,2'7,7'-tetrakis. (N,N-di-p-methoxyphenylamine)-9,9'- spirobifluorene) to replace the previously used liquid electrolyte to increase the PCE to 9.7%. The stability of the device was also improved significantly. At the same time, Snaith et al.[61] replaced TiO_2 with Al_2O_3 and used the mixed halide $MAPbI_2Cl$, forming a "meso-superstructured" device, and achieving a PCE of 10.9%. Then in 2013, Seok and Grätzel et al.[62] improved the PCE to 12% by introducing a sandwich type (planar) structure including mesoporous TiO_2, with $CH_3NH_3PbI_3$ as the absorber, and polymeric HTM. Snaith et al.[63] obtained a PCE of 12.3% using $MAPbI_{3-x}Cl_x$ and a planar structure by low-temperature processing below 150°C. Seok et al. also reported a cell with the same PCE by using mixed halide perovskites $MAPb(I_{1-x}Br_x)_3$ which have a tunable band gap with respect to their composition[20]. In the meantime, by introducing sequential deposition methods, Grätzel et al.[64] enhanced the performance of HOIPSCs and achieved a PCE of 15%. Then Snaith et al.[65] obtained a PCE of 15.4% just by using a simple planar heterojunction device architecture and a vapour deposition method instead of using previous solution methods. In 2014, Seok et al.[55] combined mesoscopic and planar structures by performing solvent engineering, which resulted in uniform and dense perovskite layers, and significantly improved the PCE to 16.2% without any hysteresis. A few months later, Seok et al[66] mixed $MAPbBr_3$ with the narrower band gap, but less stable $FAPbI_3$ (FA = formamidinium $[CH(NH_2)_2]^+$) achieving a PCE of 17.9%. Yang et al. [51] reached a 19.3% PCE by carefully choosing and controlling the perovskite layer and other materials. In 2015, Seok et al.[56] reported an HOIPSC based on a $FAPbI_3$ absorber, crystallized by the intramolecular exchange process, attaining a PCE of 20.1%. At the present time, the PCE of HOIPSCs has reached around 22.7% (Fig. 1.1b), which is really high compared with other technologies.

High Quantum Efficiency

Quantum efficiency (QE), defined as the number of converted electrons divided by the number of incident photons, is another indicator of solar cell performance. Because the

Table 1.1 Charge carrier lifetimes (µs) of various photovoltaic materials, adapted from Stranks et al.[36] with permission from Springer Nature.

Technology	Charge carrier lifetime (µs)
GaAs	1
CdTe	0.07
Crystalline Si	500
$MAPbI_3$ or $MAPbI_{3-x}Cl_x$	2
CIGS	0.25
Organics	0.001

recombination process is mostly radiative, the photoluminescence (PL) quantum efficiency of a solar cell can be up to 70%[67] and even 100%[68] at low temperature, which is really high. This enables researchers to push the PCEs of these devices towards the theoretical limit.

Long Charge Carrier Diffusion Length, Lifetime, and Mobilities

As described in the previous section, electrons and holes generated by incident light will diffuse out of the perovskite layer of a HOIPSC into the ETM and HTM. Therefore a long diffusion length L_D is desirable for the thin-film device architectures that are currently used, especially for planar structures, and should be larger than the film thickness. L_D measured by electron-beam induced current (EBIC) and terahertz (THz) spectroscopy, strongly depends on charge carrier lifetime τ and diffusivity D:

$$L_D = \sqrt{D\tau} \tag{1.1}$$

D depends on charge carrier mobility: a higher mobility results in a larger D. Therefore, any condition that favours long charge carrier lifetimes and high mobilities can increase L_D. The large L_D of $MAPbI_3$ (~100 nm)[69] and $MAPbI_xCl_{1-x}$ (~1 µm)[70] and a report on single crystal $MAPbI_3$ (175 µm)[71] (>10 µm Shi et al.[72]) enables the possibility of using a sandwich type planar structure (Fig. 1.2 b)).

Charge carrier lifetimes from PL measurements of HOIPs vary from 300 ns to a few µs. Usually, charge carrier lifetime depends on the defect or electron trap densities of the film. Low trap densities are reported for $MAPbX_3$[72] and a comparison of the lifetimes of HOIPSCs using $MAPbI_3$ or $MAPbI_{3-x}Cl_x$ with other PV techniques is shown in Table 1.1.

It can be seen that HOIPSCs have the highest charge carrier lifetime (~2 µs) if crystalline Si, which is an indirect band gap material, is disregarded. As for single crystal HOIPs, a few hundred µs has been reported. This makes HOIPs the promising materials for PV applications. The dominant radiative recombination process, low intergrain potential barrier ($\sim$ 45 meV[50]) and benign grain boundaries[73] might also contribute to this.

High mobility which depends on carrier effective mass, can also contribute to a long L_D. Miyata et al.[74] have reported an exceptionally low measured value of the effective mass, $0.104m_e$ (where m_e is the electron rest mass) for HOIPs, which indicates a high charge carrier mobility.

1.2.3 Problems and Challenges

Despite the successes described above, HOIP is not perfect and there are still many problems and challenges that have hindered its wide application. Among them, current research is mostly focused on long term stability, toxicity and the issue of J-V hysteresis.

Long Term Stability

One of the greatest issues for HOIPSC applications is the stability of the device. Modern commercial solar cells should usually remain working for around 30 years. Previous studies reported the long time stability of HOIPSCs without encapsulation but they were stored in dark places[60]. However, when it is exposed to sunlight without encapsulation, the device degrades rapidly. In addition to sunlight, moisture and temperature can also affect device stability significantly. Moisture can react with the perovskite and make it decompose[75]. Furthermore, even encapsulated in an inert atmosphere, when exposed to the full spectrum of light, the excitation of mesoporous TiO_2 with ultraviolet radiation results in a huge drop in photocurrent. HOIPs can also degrade at high temperatures. Methods such as incorporating more thermally stable FA inside the perovskite to form mixed HOIPSCs $(FA_{1-y}MA_y)Pb(I_{3-x}Br_x)$ can improve the thermal stability of the device[76]. Recently, there are some reports on using low dimensional perovksites to achieve better device stabilities and high performance[77–80] but they are not as good as the devices using 3D HOIPs. More details on low dimensional perovskites are given in Chapter 2.

Toxicity of Pb

Another issue is that most HOIPs are Pb-based materials, which is an environmental problem for global applications[81]. Much effort has been made searching for lead-free substitutions

like Sn-based HOIPs[57, 82]. But Sn-based HOIPs are very unstable in air due to the oxidation of Sn^{2+} to Sn^{4+}[83]. Very recently, Babayigit et al.[84] have shown that even Sn-based devices can be toxic in the form of acidification. Other studies include the partial substitution of Pb with Sn forming $MASn_{1-x}Pb_xI_3$[85] and the substitution of Pb with other divalent metals including Ge[9]. However their efficiency and stability are not comparable with Pb-based materials. Chapter 4 describes some progress in this area.

J-V Hysteresis

As mentioned previously, J-V hysteresis[53] undermines the accuracy of the PCE measurements, which is not ideal for progress in the field. The origin of J-V hysteresis is still controversial. Hypotheses including ferroelectricity of the perovskite[86], charge traps in the active layer's surface[53] and ion drift[87] have been proposed to explain this anomalous phenomenon. It is most likely that ion migration is the origin for hysteresis as shown by Xiao et al.[87]. The inverted p-i-n structure suffers much less hysteresis, which is considered due to surface passivation by the fullerene derivative[88].

1.3 Methods

1.3.1 Density Functional Theory

It is now clear that, HOIPs are really promising materials for solar cell applications and finding a highly efficient, low-cost, stable and nontoxic absorbing material for the purpose is urgent in this rapidly growing field. However, because of the structural diversity of HOIPs (See Chapter 2), exploring new materials by trial synthesis and then characterization is not efficient. *Density Functional Theory* (DFT)[89–91] is an affordable, powerful tool for solving the atomic and electronic structure of candidate materials and to obtain their various properties without much information from experiments. Furthermore with the growth in computational power and the development of large database and analysis tools, DFT can be extensively used for new materials discovery and design. Recently, for example, it has been applied to solve very complex problems such as crystal structure prediction[92–94]. Therefore it is an ideal tool for exploring new materials in this case. Hence, most of the theoretical work in this thesis will use DFT to study and predict the various properties of hybrid perovskite materials. In addition to using DFT to guide experimental synthesis and new materials discovery, it can also be employed to interpret and understand experimental data in more detail, e.g. Raman and solid-state NMR spectra. DFT can also be used to

probe properties which we are interested in but cannot measure easily experimentally such as the electronic band structure. This can be easily calculated using DFT but is much harder, expensive and time-consuming using, for example, angle-resolved photoemission spectroscopy (ARPES).

1.3.2 Experimental

The experimental part of this thesis includes materials synthesis and characterisation. Materials are mostly grown as single crystals from solution and their crystal structures characterised by *single crystal and powder X-ray diffraction (SCXRD and PXRD)*. X-ray patterns are solved and refined in order to obtain various structural properties such as lattice parameters, atomic coordinates etc., which can also be used as input for DFT calculations. Optical band gaps are measured from *UV-vis spectroscopy* using the Tauc plot[95]. Phase transitions are detected from thermoanalytical techniques including *differential scanning calorimetry (DSC)*, *thermogravimetric analysis (TGA)* and *variable temperature/pressure X-ray diffraction (VT-/VP-XRD)*. More details of the experimental methods used in the present work can be found in Chapter 3.

1.4 Outline

This thesis is mostly focused on halide perovskites (HPs), both hybrid organic-inorganic and inorganic phases. In Chapter 2, a literature review of the major developments and advances related to HPs is presented. Chapter 3 gives a more detailed description of the computational methods and experimental methods employed. Chapter 4 describes materials discoveries in lead-free HPs starting with bismuth-based perovskites and ending with rare-earth hybrid double perovskites. This work addresses the important issue of the toxicity of Pb. Chapter 5 mainly concerns the high pressure and mechanical properties of HPs. Chapter 6 presents studies on low-dimensional HPs. After these results and analysis, this thesis ends with a Chapter of summary and conclusions.

Chapter 2

Literature Review

2.1 Chemistry of Perovskites

2.1.1 Perovskites

Perovskites, named after Russian mineralogist Lev Perovski, are a family of materials whose crystal structure is close to the mineral $CaTiO_3$. Over the past 100 years, this family has been studied extensively and many properties including colossal magnetoresistance[96], ferroelectricity[97] and, most famously, superconductivity[98] have been revealed. The perovskite structure has the chemical formula ABX_3, where A and B are cations of different size and charge and X is the anion. Ideal perovskite has the cubic structure, as shown in 2.1, with B and X forming a 3D corner-sharing octahedral framework which is covalently bonded, and A occupying the centre of the B-X cavity. The interactions between A and the B-X cavity are mostly electrostatic. Traditionally, perovskites are oxides, where A and B have 2+ and 4+ valencies and X is the divalent oxygen ion, although B-site can be replaced by a trivalent and pentavalent ions forming $A_2B^{III}B^{V}O_6$ (Sr_2FeMoO_6), which is called *double perovskite*. X can also be a monovalent halogen (e.g. Cl^-) or even an organic group such as cyanide (CN^-)[99], thiocyanate (SCN^-)[100] or formate ($HCOO^-$)[101, 102]. For the purpose of the PV applications discussed here, most perovskites are halides, where X is a halogen and A and B have 1+ and 2+ valencies. Because of the great number of A, B and X combinations, one of the interesting characteristics of halide perovskites is their structural diversity providing us with a huge area for the exploration and design of materials with specific properties[17, 8, 103].

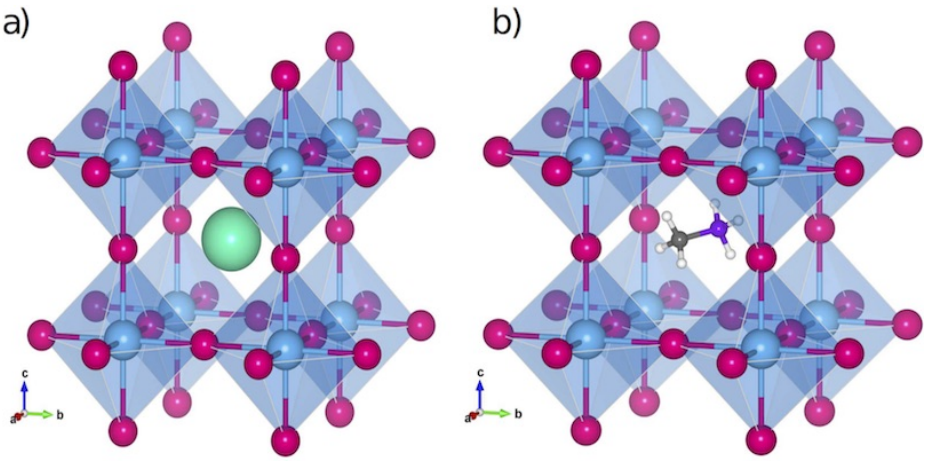

Fig. 2.1 Structures of ideal a) inorganic ($CsPbI_3$) and b) hybrid halide perovskite ($MAPbI_3$).

2.1.2 From Inorganic Perovskites to HOIPs

By changing the A-site cation from an inorganic cation to a charged organic molecule, a hybrid organic-inorganic perovskite (HOIP) can be obtained (Fig. 2.1). As discussed in Chapter 1, $MAPbX_3$ (MA = methylammonium) and $FAPbX_3$ (FA = formamidinium) are the most studied HOIPs used for PV applications. Although these applications arose only recently, the first synthesis of $MAPbI_3$ dates back to 1978[104]. Furthermore the first report on a halide perovskite, $CsPbI_3$, is even earlier, in 1958 [105]. The main feature of hybrid perovskites is the diversity of organic cation A compared with inorganic, which is usually chosen from the alkaline elements. There are far fewer inorganic halide perovskites compared with their oxide counterparts because i) the halogen ion has less negative charge and this can only compensate a B site cation in a lower oxidation state, and ii) the halogen ion except F^- is much larger than oxygen, which eliminates most small size metal elements[106]. Also choosing the appropriate organic cation A, e.g. MA ($[CH_3NH_3]^+$) and FA ($[CH(NH_2)_2]^+$), enables us to design the materials for different applications because of their structural tunability as discussed below.

Despite the advantages of HOIPs, incorporating the organic cation brings some problems for both experiments and DFT calculations. The main experimental characterization technique, X-ray diffraction (XRD), fails to accurately determine the position of the light elements (H, C and N, especially H) in the organic cation, especially in the presence of heavy elements like Pb and I within the octahedral framework. One problem this causes is an ambiguity in the symmetry of the low temperature structure of $MAPbI_3$. $MAPbI_3$ was initially refined as $Pna2_1$. However in 2013, Baikie et al.[107] corrected the space group

to *Pnma* using single crystal XRD and in 2015 Weller et al.[108] completely solved the structure (also *Pnma*) using Neutron Diffraction (ND) including the positions of the hydrogen atoms. Another issue is the lowering of the crystal symmetry by the introduction of the organic cation, e.g. the symmetry of MA^+ (C_{3v}) is not compatible with the Pb-I framework (O_h). However, due to the dynamic rotations of the MA ions, partial site occupancies were assigned to maintain the higher symmetry. In addition, due to the soft nature of these materials, these materials are not well ordered in local structure, including anharmonic lattice and local structure disorder, which bring lots of challange for structure characterisation using the traditional Bragg diffraction techniques such as XRD and ND.

As for the calculations, incorporating an organic cation means that non-local, long range van der Waals forces become more important compared with inorganic perovskites, which brings an issue since these forces are not well described using DFT. Some semi-empirical corrections such as Grimme's scheme e.g. DFT-D[109], DFT-D2[110] and DFT-D3[111], as well as quantum mechanical methods due to Tkatchenko-Scheffler[112], and non-local van der Waals functionals (vdw-DF)[113] have been used to describe the perovskite structures with sufficient accuracy. Another issue is the relative flat energy surface, which results in many local minima. This, together with experimental uncertainty in the positions of the light elements, has made it difficult to find the global minimum structure. Also, because the whole structure is dynamic and strongly dependent on temperature, traditional static DFT calculations may fail to predict some structural properties. Using *ab intio molecular dynamics* (AIMD) is possible but is very resource consuming because a long simulation time is needed to reach equilibrium and a large supercell should be used. However, calculations still can be performed with some constraints, such as fixing the experimental lattice constants, and the positions of some of the ions, e.g. Pb. Similar as discussed before, these materials are highly anharmonic[114]. Therefore their thermal expansion coefficients are high, i.e. there are significant structural changes at different temperatures. The widely used DFT employs the Born-Oppenheimer approximation where all the nuclei are treated classically and does not include the effect of temperature. Therefore, phonon calculations should be performed and the quasi-harmonic approximation (QHA) should be used for thermodynamic properties and thermal expansion calculations[115]. As for thermal conductivity and phonon lifetime, they should be calculated with higher order pertubation techniques. However, these calculations are extremely expensive and there are limited data available in the literature[116].

2.1.3 Distortions and Phase Transformations

Although the perovskite family is large and contains many well-known examples, not all compounds with the formula ABX_3 have the perovskite structure. Except for a few materials like $SrTiO_3$ which have the ideal "perfect" perovskite structure, most of them are more or less distorted including the rotations and tilting of the BX_6 octahedra and off-center displacement of the A-site cations. Environmental conditions such as pressure and temperature can affect the structure significantly, especially for HOIPs. Since the electronic, optical and mechanical properties of a material are strongly related to its structure, these conditions can be used to tune the properties of perovskites.

As for pressure, a well known example in the field of oxide perovksites is the transformation between the perovskite and post-perovskite (2D) form of $MgSiO_3$ under high hydrostatic pressure[117, 118]. For HOIPs (mostly $MAPbX_3$, where X= I[119–121] and Br[122, 123]), pressure usually lowers the crystal symmetry mainly by octahedral tilting and disordering of the MA^+ cation accompanied by a small volume reduction. Furthermore this pressure-induced phase transition is highly reversible. Jaffe et al.[119] found that even after partial amorphization, structures can still transform back. Octahedral tilting, which is correlated with electronic properties, can be characterized using high pressure *in situ* single crystal XRD[119], synchrotron powder XRD[121] and powder ND[123].

Temperature can also affect the perovskite structure. Perovskites usually have high symmetry at high temperature possibly due to the effect of entropy[124] and their symmetry lowers when they cool down. Some perovskites can even transform into lower dimensional structures at low temperature. In oxide perovskites, the most famous example of a symmetry change is the ferroelectric phase transition of $BaTiO_3$[97], which transforms from a cubic $Pm\bar{3}m$ structure to a tetragonal $P4mm$ structure at 130 °C. In halide perovskites, $CsSnI_3$, shown in Fig. 2.2, exhibits phase transitions between 4 polymorphs when it cools down[4]: cubic (α-phase), tetragonal (β-phase), orthorhombic (γ-phase) and a low dimensional structure (δ-phase). $MAPbI_3$[10] and $CsPbI_3$[125], exhibit similar transformations from α-phase to β-phase and γ-phase although $MAPbI_3$, does not usually transform to the δ-phase. However, by using a solvent with strong hydrogen bonding such as H_2O, DMF or DMSO, $MAPbI_3$ can show a reconstructive transition to a low dimensional form ($MAPbI_3 \cdot X$), and this might be the origin of its instability under humid conditions[126, 127].

Besides external environmental effects, the perovskite structure itself can distort due to the relative size of the A, B, and X ions, which is called the *steric effect*. DFT phonon calculations on $CsSnI_3$ have shown that α and β-$CsSnI_3$ have soft phonon modes (imaginary frequencies), which indicates a structural instability, while γ and δ-$CsSnI_3$ are stable[115, 128]. The

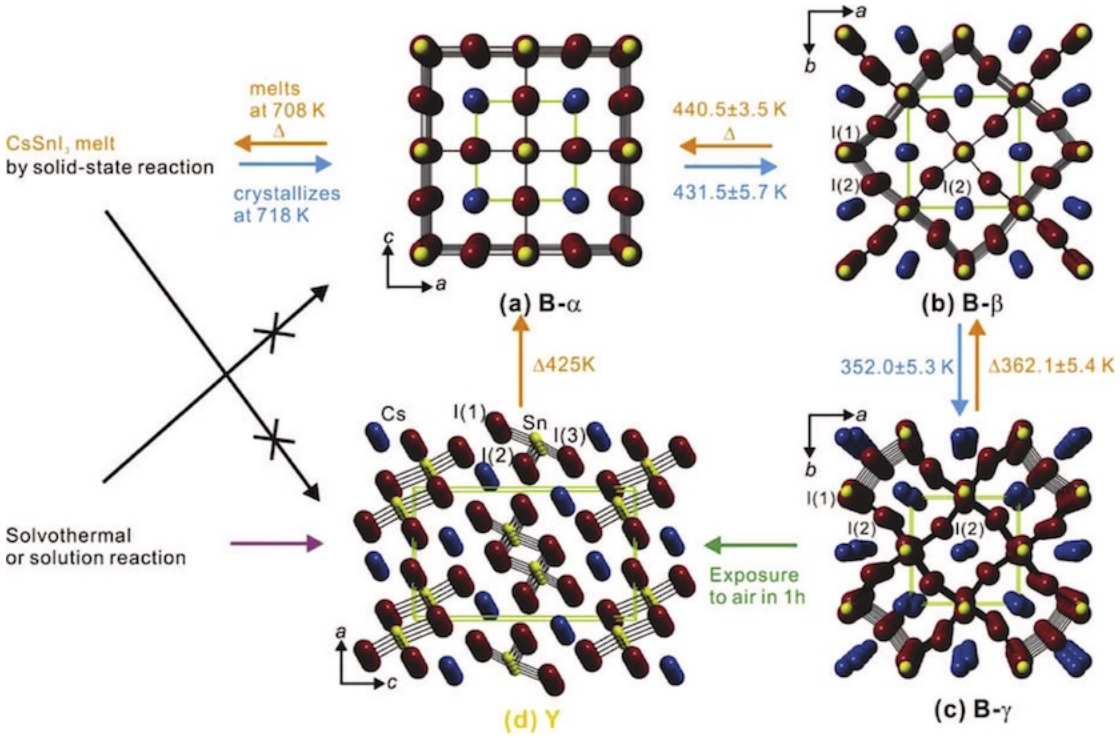

Fig. 2.2 Phase transitions in $CsSnI_3$ between a) cubic, b) tetragonal, c) orthorhombic and d) low-dimensional (1D) structures. Reprinted with permission from Chung et al.[4]. Copyright (2012) American Chemical Society.

phonon calculations, which use the quasi-harmonic approximation, showed that even at room temperature, the cubic α structure is still not stable, so the experimentally observed cubic structure might be a crystallographic average, but this needs further investigation[115]. In addition to the steric effect, hydrogen bonding[129] and van der Waals interactions[130] can also distort the structure.

Tolerance Factor

In order to geometrically quantify the steric effect, Goldschmidt in 1926 introduced an empirical parameter to describe the stability of a 3D perovskite structure, known as the *tolerance factor*[131]:

$$t = \frac{r_A + r_X}{\sqrt{2}(r_B + r_X)} \tag{2.1}$$

where r is the effective ionic radius[38]. For a perovskite containing an organic cation like MA^+, a revised method such as that of Kieslich et al.[132, 133] can be used. Usually, when $t = 0.8 \sim 1.0$, the sizes of A, B and X are ideal and close-packed, and a cubic perovskite

structure can be obtained. When $0.8 < t < 1.0$, the A-site cation is too small while for $t > 1$, the A-site cation is too large for the B-X cage. When the A-site cation is too small for the B-X cage, the BX_6 octahedra will tilt and the structure will lower its symmetry to become tetragonal or orthorhombic.

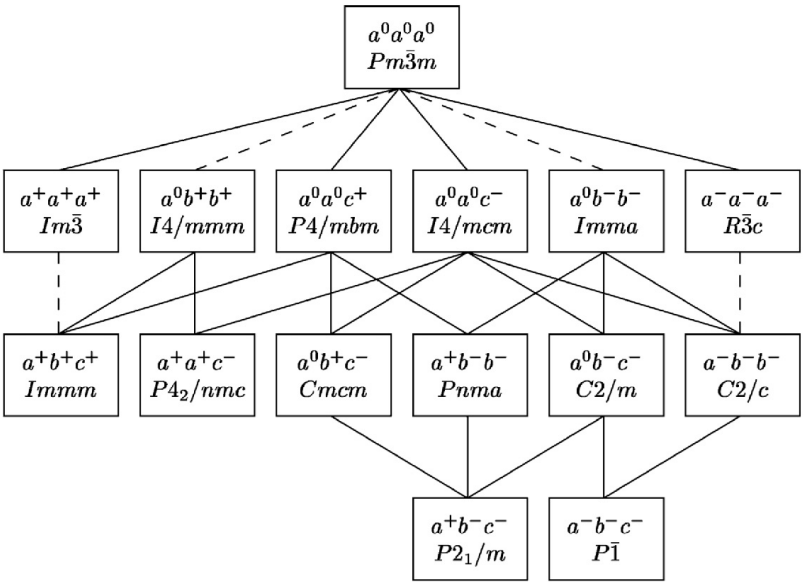

Fig. 2.3 The group-subgroup relationship of 15 possible tilting space group for perovskites. Dashed line indicates the phase transition between two joint space group is first order as required by the Landau theory. Reproduced from Stokes et al.[5, 6] with permission from John Wiley & Sons.

Glazer Notation

Octahedral tilting can be classified using the *Glazer Notation*[134]. The magnitude of the tilting around [100], [010] and [001] is described by three letters. Unequal tilts about all three axes is denoted *abc*, while *aac*, for example, indicates equal tilts about [100] and [010], with a different tilt about [001]. Superscripts "+, -, 0" show that the octahedra in successive layers have the same tilt, opposite tilt or no tilt respectively. There are in total 23 different tilting systems in the perovskite family found by implementing the Glazer notation. Stokes et al.[5, 6] further reduce this number to 15 by performing group theory analysis and their group-subgroup relationship is shown in Fig. 2.3.

2.1.4 Low dimensional HOIPs

An A-site cation that is either too small or too large can result in a new low-dimensional structure. However, in the literature researchers still called it a low-dimensional perovskite[135, 136] because of its similarity to the traditional $CaTiO_3$ type structure, although strictly speaking, perovskite should have a 3D framework formed by corner-sharing octahedra. Low-dimensional perovskite can be 0, 1 or 2-D materials formed by controlling the ionic sizes, the functional groups of the precursors and the synthesis conditions[135]. Because of the quantum confinement effect, when the dimensionality of the structure lowers, the band gap increases significantly, making the structure unsuitable for PV applications[137]. However, Cs_2SnI_6 (Fig. 2.5 b)[138, 10] which has isolated octahedra (0D structure) can still be a low band gap semiconductor with a value of 1.3 eV.

Recently, the Ruddlesden-Popper type HOIPs, e.g. $(BA)_2(MA)_{n-1}Pb_nI_{3n+1}$ (n = 1, 2, 3, 4, ..., $BA^+ = [CH_3(CH_2)_3NH_3]^+$) (Fig. 2.4) are claimed to be more stable to moisture and light soaking than 3D HOIPs[137, 139]. Their band gap can be tuned by changing *n*, which is the number of the metal-halide sheet separated by the large organic ligands: when n is smaller, the material is becoming more stable against moisture whereas when n becomes larger, a better performance device can be achieved. Therefore optimisation can be done to get a optimum balance between material stability and device performance. In 2016, Mohite et al.[79] reported a 12.52% PCE device with $(BA)_2(MA)_{n-1}Pb_nI_{3n+1}$ for n = 3 and 4. At the same time, Sargent et al.[78] also reported this type of optimisation for $(C_8H_9NH_3)_2(MA)_{n\text{-}1}Pb_nI_{3n+1}$ and achieved a 15.3% PCE. Recently, Snaith et al.[80] combined 3D mixed cation ligand perovskite $FA_{0.83}Cs_{0.17}Pb(I_yBr_{1-y})$ with BA ligand and showed a 2D-3D heterostructured device with a 17.5% PCE and long term stability.

2.1.5 Lead-free HOIPs

Some examples of lead-free HOIPs are shown in Fig. 2.5. Except for the Sn and Ge-based (Fig. 2.5 a-b) HOIPs mentioned before, Bi^{3+} based compounds have gained recent attention. This includes the preparation of low-dimensional compounds such as $A_3Bi_2I_9$ (Fig. 2.5 d-e) (A = K^+, Cs^+,Rb^+, NH_4^+ and MA^+)[11, 12, 140], as well as the investigation of (hybrid) double perovskites. Halide double perovskites (HDPs), in which the 3D perovskite-motif is maintained, seems to be a particularly promising avenue. In these materials, the perovskite formula is essentially doubled and the two divalent metal cations, e.g. Pb^{2+}, are replaced by

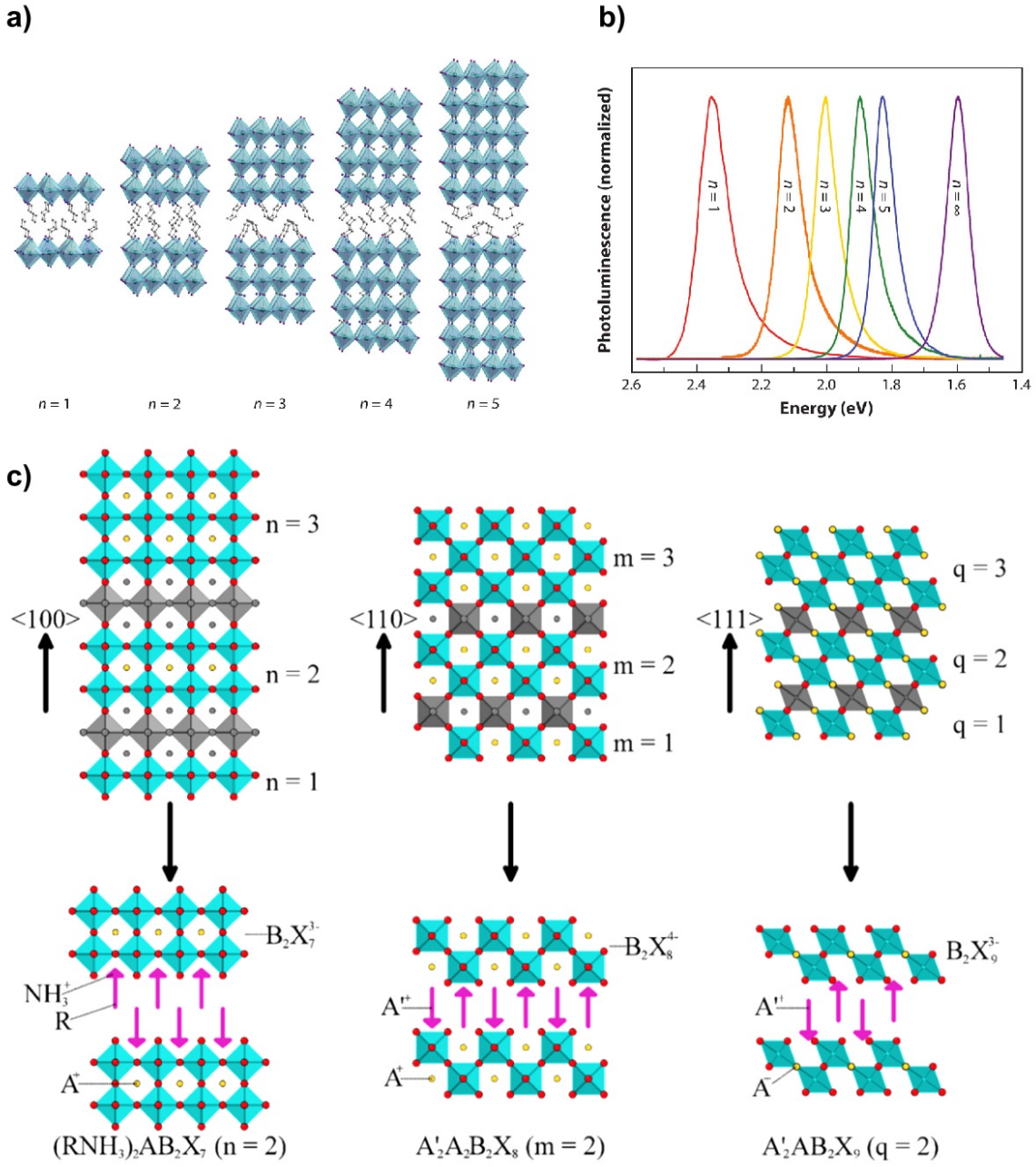

Fig. 2.4 a) The crystal structure of Ruddlesden-Popper type 2D perovskite: $(BA)_2(MA)_{n-1}Pb_nI_{3n+1}$ and b) their photoluminescence (adapted from Smith et al.[7] with permission from Annual Reviews). c) The relationship between 3D and 2D perovskites. (Reprinted with permission from Saparov et al.[8]. Copyright (2016) American Chemical Society.)

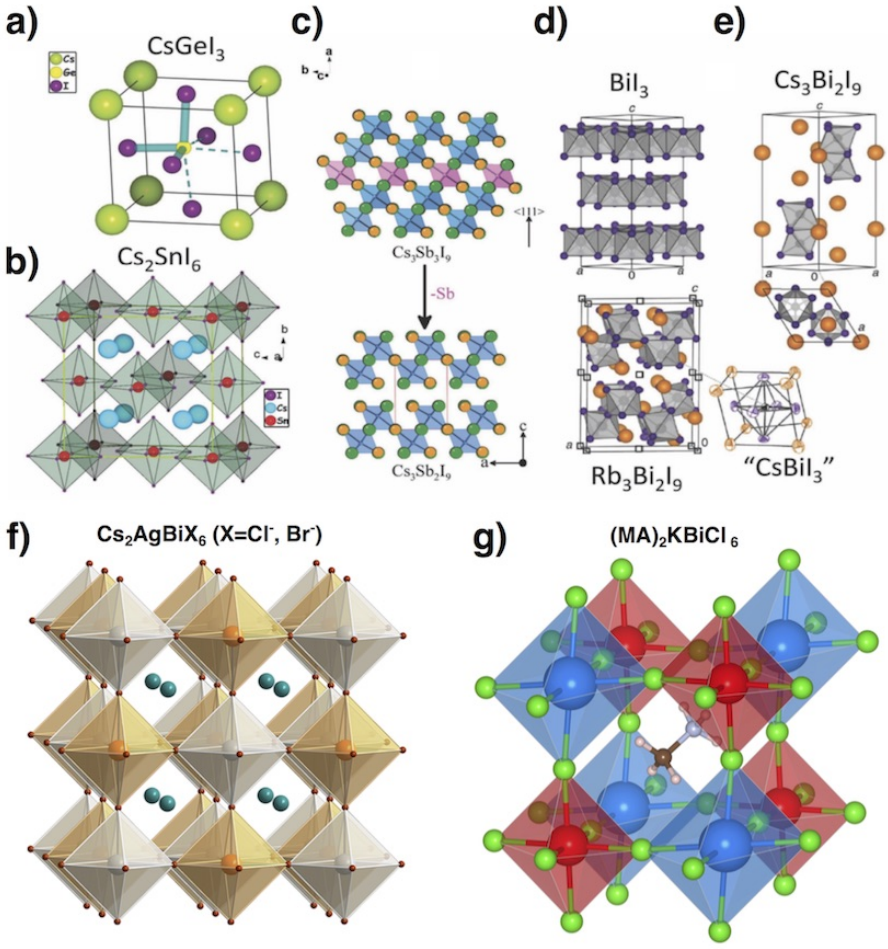

Fig. 2.5 Various lead-free HOIPs including: a) $CsGeI_3$[9], b) Cs_2SnI_6[10], c) $Cs_3Sb_2I_9$[11], d) $Rb_3Bi_2I_9$[12], e) $Cs_3Bi_2I_9$[11, 12], f) Cs_2AgBiX_6 (X = Cl and Br)[13–15] and g) $(MA)_2KBiCl_6$[16]. (a)–e) Reproduced from Stoumpos et al.[17] with permission from John Wiley & Sons. f) Reprinted with permission from Slavney[13]. Copyright (2016) American Chemical Society. g) Reproduced from Wei et al.[16] with permission from The Royal Society of Chemistry.)

one monovalent and one trivalent cation, e.g. Na^+ and Bi^{3+}:

$$2\,AB^{II}X_3 \longrightarrow A_2B^{I}B^{III}X_6 \tag{2.2}$$

where A = Cs^+, B^I = Na^+, Ag^+, B^{II} = Pb^{2+}, Sn^{2+}, B^{III} = Bi^{3+} and X = Cl^-, Br^- and I^- (Fig. 2.5 f)). The emergence of HDPs began at the end of 1960s with the synthesis of $Cs_2NaAmCl_6$ and $Cs_2NaBkCl_6$.[141, 142] This was closely followed by the preparation and characterisation of over twenty similar Cs-Na-based HDPs: $Cs_2NaB^{III}Cl_6$ (B = lanthanides, Bi, Fe,

etc)[143]. Motivated by these studies, a significant number of new double perovskites were subsequently explored,[144] with interest mostly focusing on understanding the optical absorption, emission and magnetism in structures containing B^{III} rare-earth elements[145, 146]. Compared with single perovskites, double perovskites have a broader chemical diversity since both the B^{I} and B^{III} site can be modified. Recently, there are great amount of interest on inorganic HDPs: $Cs_2AgBiBr_6$, $Cs_2AgBiCl_6$ and $Cs_2AgInBr_6$[13–15, 147, 147]. Very recently, the synthesis and properties of the first organic-inorganic hybrid double perovskite $(MA)_2KBiCl_6$[16] as well as $(MA)_2TlBiBr_6$[26] and $(MA)_2AgBiBr_6$[27] (Fig. 2.5 g) have been reported. The chemistry of HDPs was further expanded into the rare-earth regime by discovering the first two rare earth hybrid double perovskites: $(MA)_2KGdCl_6$ and $(MA)_2KYCl_6$[29]. More details these studies are given in Chapter 4. However, at the present time, the application of (hybrid) double perovskites as photovoltaic absorbers is hindered due to their unfavourable electronic properties (large, indirect band gap) originating from the ionic character of the Cl^- and Br^- bonds, the lack of lone pair electrons for B^{I} = Ag[148, 149] and parity-forbidden optical transitions[150].

2.1.6 Dynamical Structure and Disorder in HPs

If cubic $MAPbI_3$ is undistorted, the B-X framework has O_h symmetry while the MA^+ cation in the Pb-I cage has C_{3v} symmetry. They are therefore not symmetry compatible with each other and experimentally the MA^+ cations are refined as disordered[104]. In fact by measuring the dielectric response of $MAPbI_3$, Poglitsch and Weber[151]reported that the MA^+ cations are disordered with a picosecond relaxation time, similar to a molecular crystal. Pair distribution functions (PDF) obtained from X-ray scattering measurements by Choi et al.[152] revealed that 70% of MA^+ cations are disordered. Further studies using quasi-elastic neutron scattering by Leguy et al.[153]showed that realignment of the MA^+ cations takes place in the interval 3-14 ps and the dynamical response of the $CH_3{}^-$ and $NH_3{}^-$ groups is in sub-ps range. A drop in the mean squared displacement of the H atom in $MAPbBr_3$ when it cools down indicates that the associated rotational displacment is strongly related to temperature[154]. The rotation of the MA^+ cation is coupled with the distortion of the inorganic framework and is key to understanding temperature dependent phase transitions in HOIPs[155]. As for the calculations, AIMD clearly reveals the rotations of the organic cations as well as the dynamics of B-X framework[156, 157], Time scales of 3 ps (MA^+)[153]and 2 ps (FA^+)[157] for molecular rotation were reported. The inorganic framework contains ionic transport as shown from spectroscopic impedance experiments[158]. Islam et al.[159]

identified the activation energy of the iodine ion in $MAPbI_3$ as 0.6 eV. These are crucial for understanding hysteresis in HOIP devices.

2.2 Electronic Properties

The electronic properties of HPs are strongly correlated with their structure and composition. This section mainly reviews the electronic properties of the most studied HOIP: $MAPbI_3$.

2.2.1 Electronic Structure and its Interplay with Structural Properties

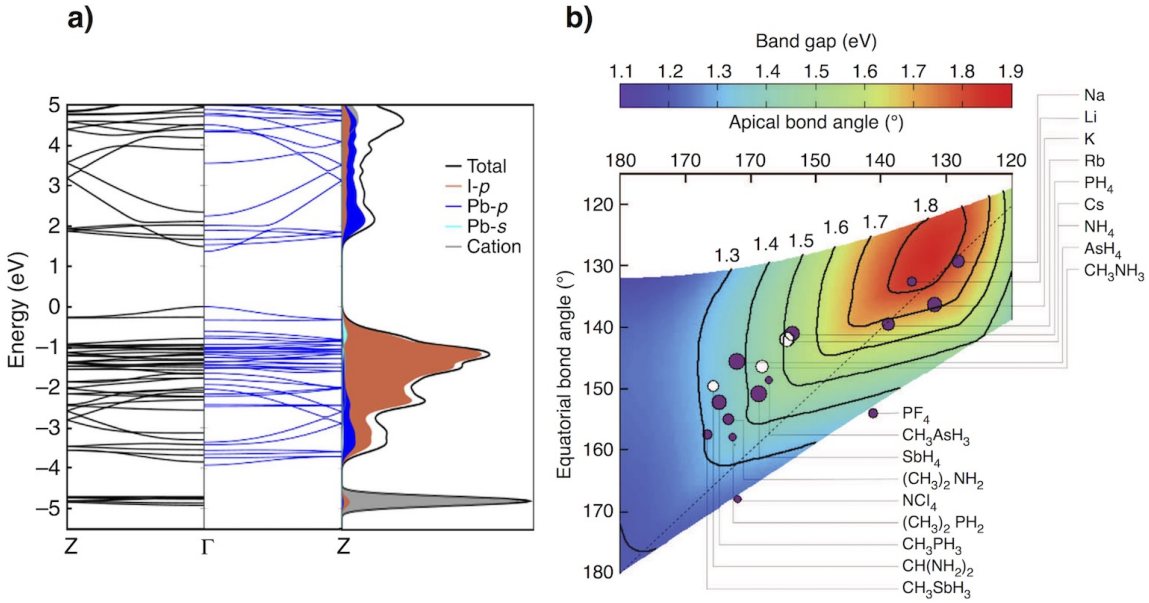

Fig. 2.6 a) DFT calculated band structure of orthorhombic $MAPbI_3$ with (left) and without the cation (left and centre) and DOS (right); b) Map of the band gap as a function of equatorial and apical Pb-I-Pb bond angle for various perovskites; Adapted from Filip et al.[18] with permission from Springer Nature.

$MAPbI_3$ has a direct band gap of around 1.5 eV[10]. For the α phase (cubic), the band edges are at the R point of the Brillouin Zone while for β (tetragonal) and γ (orthorhombic) phases, the band edges are located at the Γ point[160, 161, 107, 162]. The calculated band structure and density of states (DOS) of orthorhombic $MAPbI_3$ is shown in Fig. 2.6 a. One of the significant features seen from the DOS is that the band edges, which are of most interest for the optoelectronic properties, originate mainly from Pb-I states, while the eigenstates of organic cation are located deep in the band structure.. For $MAPbI_3$, the

valence band maximum (VBM) contains mostly Pb-6s and I-5p antibonding states while the conduction band minimum (CBM) has mostly Pb-6p and I-5p antibonding states. Hence, the optoelectronic properties of $MAPbI_3$, depend mainly on the structure of its inorganic framework. Filip et al.[18] showed that even removing the MA^+ cation and holding the Pb-I framework fixed, does not change the band structure near the band edges very much (Fig. 2.6 a). Therefore, as pointed out by Filippetti et al.[160], Giorgi et al.[163] and Motta et al.[164], the role of the organic cation is to simply support the whole perovskite structure, and does not directly affect the electronic properties. However, they also argued that the organic cation can be used to tune the electronic properties by inducing octahedral tilting of the inorganic framework through the hydrogen bonding or van der Waals forces. Filip et al.[18] and Amat et al.[165] performed DFT calculations in which the MA^+ cation in $MAPbI_3$ is substituted with various other cations and obtained a relationship between the band gap and the degree of octahedra tilting in the form of the apical and equitorial Pb-I-Pb bond angles, as shown in Fig. 2.6 b. Both studies found that a smaller band gap, which is suitable for PV applications, can be obtained from a less tilted structure, by incorporating a larger A-site cation. On the other hand, a more tilted structure will result in a larger band gap by incorporating a small A-site cation such as Cs^+, Na^+ or $NH_4{}^+$, and this could be useful for other optoelectronic applications such as LEDs.

2.2.2 The effect of Spin-Orbit Coupling (SOC)

Since most HPs contain heavy elements such as Pb, relativistic effects are significant. Because, as shown before, the band edge states originate mostly from Pb and I, the band gap and the shape of the bands near the band gap are dominated by a strong *spin-orbit coupling* (SOC) effects and normal DFT techniques such as scalar relativistic DFT (SR-DFT) are not sufficient to describe the electronic structure accurately. This was initially pointed out by Even et al.[166] as shown in Fig. 2.7 a. There are two effects of SOC. First, SOC can significantly affect the calculated value of the band gap. However, previous calculations showed that even without SOC, good agreement with the experimental band gap could be achieved. This is due to a cancellation of errors caused by ignoring SOC (overestimation) and using standard single particle DFT (underestimation) [166, 167]. The latter originates from the physical meaning of the Kohn-Sham energy band gap E_g^{KS} which is different from the experimentally measured (e.g. ARPES *Angle-Resolved Photoemission Spectroscopy*) quasi-particle band gap E_g^{qp}[168]. Therefore in most cases DFT will underestimate band gaps. Based on SOC, much more computationally expensive beyond-DFT methods should be used

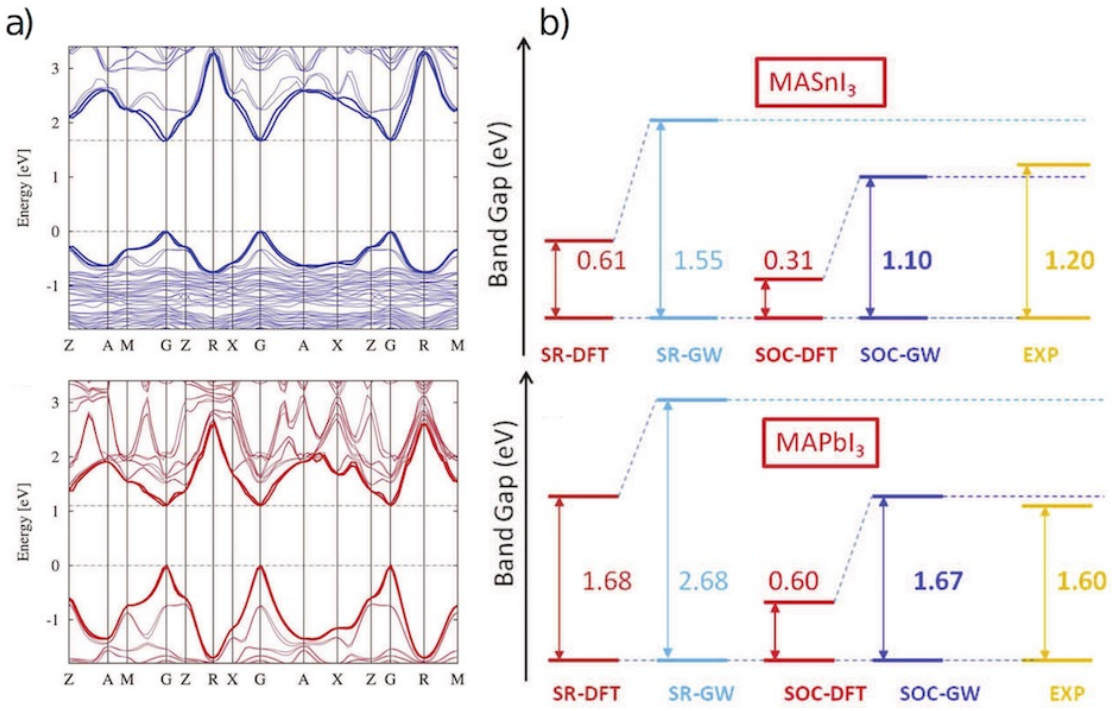

Fig. 2.7 a) Band structure of cubic $MAPbI_3$ with (bottom) and without (top) considering SOC effects; b) Band gap of $MAPbI_3$ and $MASnI_3$ using different methodologies, adapted from Umari et al.[19] with permission from Springer Nature.

in order to obtain an accurate band gap value. Calculations using hybrid functionals such as HSE06 are still able to open up the band gap[169] but many-body GW methods[19] can achieve a satisfactory result. However, the shape of the bands does not change too much even using the self-consistent GW (sc-GW) method[170] and only a rigid shift of the conduction band is observed. Therefore, an approximation is to use the so-called scissor operator to shift the whole conduction band relative to the valence band obtained from normal DFT calculations[171]. Another effect of SOC is to cause band splitting at symmetric points in the band structure, which is called the *Rashba-Dresselhaus effect*. Studies have shown that the effect is more significant in the conduction band because of the larger contribution from heavy Pb in this band compared to the valence band. In addition, the band splitting makes the "strict" direct band gap become slightly indirect, possibly reducing recombination rates and causing a longer charge carrier lifetime for HOIPs[165]. The effect of SOC on structure is marginal as shown by Egger et al.[130]. Hence, for geometry optimization, there is no need to switch on SOC since it is really expensive.

2.3 Optical Properties

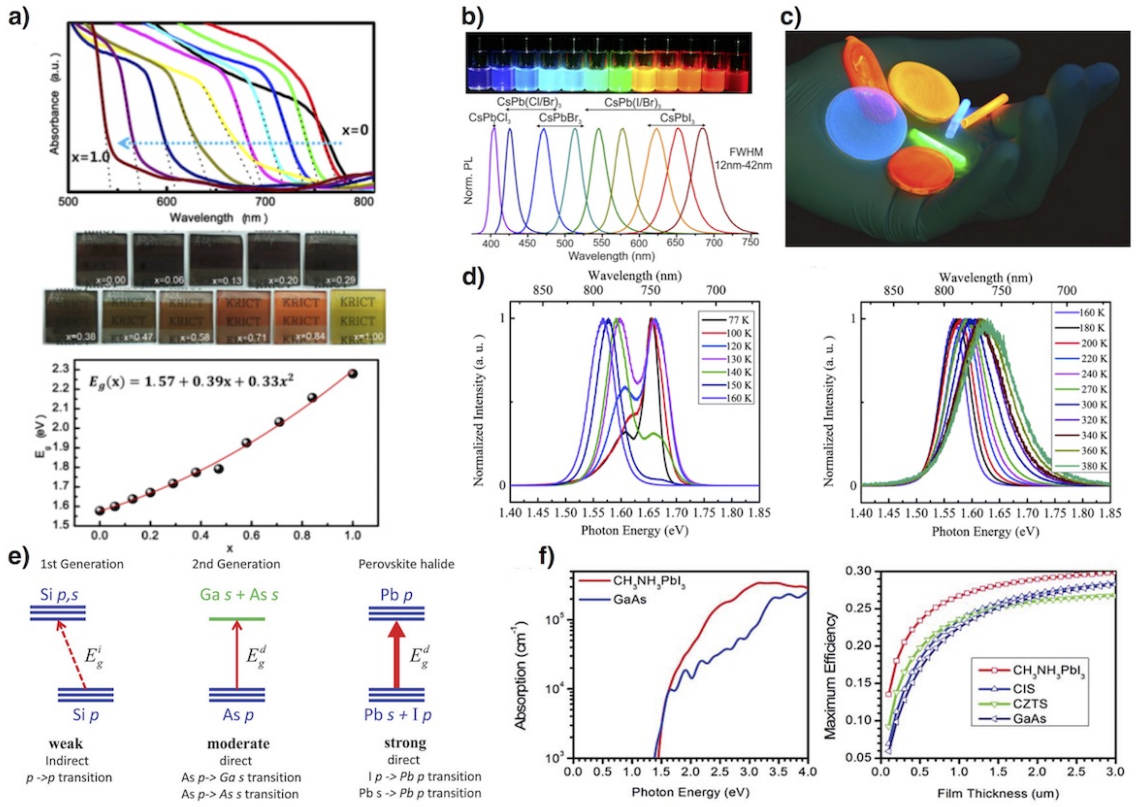

Fig. 2.8 a) Change in optical absorption (top) and colour (centre) and electronic band gap (bottom) by modifying the compositions (x) of $MAPb(I_{1-x}Br_x)_3$[20] (Reprinted with permission from [20]. Copyright (2013) American Chemical Society.); b-c) PL tuning by modifying the compositions of $CsPbX_3$ (X = Cl, Br and I)[21] (Reprinted with permission from [21]. Copyright (2015) American Chemical Society.); d) Temperature dependence of the PL properties of $MAPbI_{3-x}Cl_x$[22] (Reproduced from [22] with permission from The Royal Society of Chemistry.); e) Schematic of optical absorption in Si, GaAs and HOIPs solar cells[23] (Reproduced from [23] with permission from The Royal Society of Chemistry.); f) DFT calculated optical absorption curves (left) and absorption efficiency curves (right)[23]. (Reproduced from Yin et al.[23] with permission from The Royal Society of Chemistry.)

Optical absorption and photoluminescence (PL) are the most studied optical properties of HOIPs[172]. Since optical properties depend strongly on electronic structure, they can be tuned by managing the composition of the material, as shown in Fig. 2.8 a-d. Strong optical absorption (Fig. 2.8 a) indicates that HOIPs are characterized by a direct band gap. The PL effect is intense in halide perovskites and can be used for light emission as shown in Fig. 2.8 b-c[21]. However, temperature dependent wavelength shifts have been reported

(Fig. 2.8 d), which strongly depends on the methods used for synthesis and fabrication[22]. To calculate the effects of optical absorption, the absorption coefficient (α)[173], can be determined, which is defined as:

$$\alpha = \frac{2\pi}{\hbar} \int |\langle v|\hat{H}|c\rangle|^2 \frac{2}{8\pi^3} \delta(E_c(\mathbf{k}) - E_v(\mathbf{k}) - \hbar\omega) d^3\mathbf{k} \tag{2.3}$$

An approximation is usually made in which the transition matrix $\langle v|\hat{H}|c\rangle$ is taken as independent of $\mathbf{k}$[161, 23], therefore:

$$\alpha = \frac{2\pi}{\hbar} |\langle v|\hat{H}|c\rangle|^2 \cdot \int \frac{2}{8\pi^3} \delta(E_c(\mathbf{k}) - E_v(\mathbf{k}) - \hbar\omega) d^3\mathbf{k} \tag{2.4}$$

where the integral in Eq.2.4 is called the joint density of states (JDOS). Therefore α is mainly dependent on the elements of the transition matrix between VB and CB states and the joint density of states (JDOS). The transition matrix gives the probability of transitions between the VB and CB while the JDOS refers to the number of such transitions. Compared to Si and GaAs, $MAPbI_3$ has a more "direct" band gap (strictly indirect due to SOC) than Si and a higher JDOS than GaAs, which leads to larger transition matrix elements and higher JDOS than Si and GaAs, respectively as shown in Fig. 2.8 e. In real devices, optical absorption is related to the thickness of the absorption layer. Yu et al.[174, 175] reported a method for calculating the maximum efficiency considering the thickness and absorption coefficients, as shown in Fig. 2.8 f from Yin et al.[23]. The result shows that $MAPbI_3$ can be made into a thinner film while maintaining a relatively high PCE compared with other PV techniques.

2.4 Mechanical Properties

Understanding the mechanical properties of a material such as the Young's modulus (E), shear modulus (G), bulk modulus (B) and Poisson's ratio (ν) is essential for device applications since they are closely related to phase stability and device performance. Experimentally Sun et al.[176] recently reported the Young's modulus of $MAPbX_3$ (X=Cl, Br and I) using nanoindentation, showing the following trend: $E_{Cl} > E_{Br} > E_I$. Computationally, $MAPbX_3$ and $MASnX_3$ (X= Br, I) have been studied by Feng[177] using DFT who showed that the mechanical properties are mainly determined by the strength of the B-X bonds. From the Poisson ratio and the ratio of bulk modulus to shear modulus (B/G), it was shown that $MAPbX_3$ and $MASnX_3$ are ductile and flexible, making them candidates for strain engineering applications. However, Feng[177] obtained highly anisotropic elastic properties,

which contradicts the nanoindentation measurements by Sun et al.[176] and Rakita et al.[178]. The reason for this discrepancy is unknown, but possibly due to the dynamical rotation of the MA^+ cations. Other papers[163, 130, 179] have reported the bulk modulus without further detailed analysis. Reyes-Martinez et al.[180] showed that HOIPs have large creep deformation, stress relaxation and significant rate-dependent mechanical behavior which behaves like a ionic crystal like KBr. Recently, we summarised previous results and found $FAPbBr_3$ is significantly softer than $MAPbBr_3$[31]. More details of this study will be given in Chapter 5.

Chapter 3

Methodology

3.1 Theory

As described in Chapter 1, density functional theory (DFT) was extensively used in this thesis, and DFT is a better tool for simulations of new materials than empirical force field simulation or data driven method. Starting with the fundamental many-body Schrödinger equation, this section introduces the modern DFT along with its applications.

3.1.1 Many-Body Schrödinger Equation

In quantum mechanics, a complete system of interacting nuclei and electrons is described by the time dependent *Many-Body Schrödinger Equation (MBSE)* (Eq. 3.1),

$$\begin{aligned} i\hbar\frac{\partial\Psi}{\partial t} = [&\underbrace{-\sum_i \frac{\hbar^2}{2m_i}\nabla_i^2}_{\hat{T}_e} \underbrace{-\sum_I \frac{\hbar^2}{2M_I}\nabla_I^2}_{\hat{T}_N} + \underbrace{\frac{1}{2}\sum_{i\neq j}\frac{e^2}{4\pi\varepsilon_0}\frac{1}{|\mathbf{r}_i-\mathbf{r}_j|}}_{V_{ee}} \\ &+ \underbrace{\frac{1}{2}\sum_{I\neq J}\frac{e^2}{4\pi\varepsilon_0}\frac{Z_I Z_J}{|\mathbf{R}_I-\mathbf{R}_J|}}_{V_{NN}} \underbrace{-\sum_{i,I}\frac{e^2}{4\pi\varepsilon_0}\frac{Z_I}{|\mathbf{r}_i-\mathbf{R}_I|}}_{V_{Ne}}]\Psi \end{aligned} \tag{3.1}$$

where "i, j" represent electrons, "I, J" represent nuclei, M_I and m_i are the masses of the nuclei and electrons and Z_I are the atomic number of each nuclei. It should be noticed that relativistic effect is not included in Eq. 3.1. $\Psi = \Psi(\mathbf{r}_i, \mathbf{R}_j, t)$ is called the total many-body wavefunction. The MBSE can also be written as:

$$[\hat{T}_e + \hat{T}_N + V_{ee} + V_{NN} + V_{Ne}]\Psi = i\hbar\frac{\partial\Psi}{\partial t} \tag{3.2}$$

Interactions within the MBSE are mainly Coulombic between the electrons and nuclei. This introduces the kinetic energy terms ($\hat{T}_e$ and $\hat{T}_N$) for the electrons (i) and nuclei (I), a potential energy term (V_{ee}) between electrons, a potential energy term between nuclei (V_{NN}) and a potential energy term between electrons and nuclei (V_{Ne}). Sometimes for the convenience, V_{Ne} can be written as:

$$V_{Ne}(\mathbf{r},\mathbf{R}) = -\sum_i \sum_I \frac{e^2}{4\pi\varepsilon_0}\frac{Z_I}{|\mathbf{r}_i - \mathbf{R}_I|} = \sum_i \frac{e^2}{4\pi\varepsilon_0} V_N(\mathbf{r}_i) \tag{3.3}$$

where $V_N(\mathbf{r}_i) = -\sum_I \frac{Z_I}{|\mathbf{r}_i - \mathbf{R}|}$ is the Coulombic potential of the nuclei for each electron. Often for convenience, *Hartree Atomic Units* ($\hbar = m_e = e = 4\pi/\varepsilon_0 = 1$) are used to obtain:

$$[-\sum_i \frac{\nabla_i^2}{2} - \sum_I \frac{\nabla_I^2}{2M_I} + \frac{1}{2}\sum_{i\neq j}\frac{1}{|\mathbf{r}_i - \mathbf{r}_j|} + \frac{1}{2}\sum_{I\neq J}\frac{Z_I Z_J}{|\mathbf{R}_I - \mathbf{R}_J|} - \sum_{i,I}\frac{Z_I}{|\mathbf{r}_i - \mathbf{R}_I|}]\Psi = i\frac{\partial\Psi}{\partial t} \tag{3.4}$$

Since the many body wave-function,$\Psi(\mathbf{r}_i, \mathbf{R}_J, t)$ contains all the information we want for the whole system, the main task is to solve Eq. 3.2. However, Eq. 3.2 is impossible to solve analytically except for the simplest case of H atom. Even using a modern supercomputer which can perform substantial numerical computations, it is still very hard or impossible to solve because the complexity of this problem grows exponentially with the size of the whole system. Therefore some approximations need to be applied to make Eq. 3.2 solvable.

3.1.2 Born-Oppenheimer Approximation

Because the electrons are much lighter than the nuclei, we can assume that they will respond instantaneously to any change in the nuclear configuration. Therefore, the many body wavefunction Ψ can be separated into a electronic wavefunction $\psi(\mathbf{r}_i, \mathbf{R}_J)$ and a nuclear wavefunction $\chi(\mathbf{R}_J, t)$:

$$\Psi(\mathbf{r}_i, \mathbf{R}_J, t) = \psi(\mathbf{r}_i, \mathbf{R}_J)\chi(\mathbf{R}_J, t) \tag{3.5}$$

This decoupling is called the *Born-Oppenheimer Approximation*[181] or sometimes called the *Adiabatic Approximation*. Eq. 3.2 becomes:

$$[\hat{T}_e + \hat{T}_N + V_{ee} + V_{NN} + V_{Ne}]\psi\chi = i\psi\frac{\partial\chi}{\partial t} \tag{3.6}$$

where the energies of the electrons ε are defined by the time-independent Schrödinger equation:

$$[\hat{T}_e + V_{ee} + V_{Ne}]\psi(\mathbf{r}_i, \mathbf{R}_J) = \varepsilon\psi(\mathbf{r}_i, \mathbf{R}_J) \tag{3.7}$$

The nuclear wave-function χ can then be described by:

$$[\hat{T}_N + V_{NN}]\chi(\mathbf{R}_J, t) = i\frac{\partial}{\partial t}\chi(\mathbf{R}_J, t) \tag{3.8}$$

Because we know that the nuclear masses are large we can assume that their motion is classical and ignore their wavefunctions. The wavefunctions collapse into a single state and the nuclei can be treated as point particles obeying Newtonian dynamics:

$$M_J\frac{\partial^2\mathbf{R}_J}{\partial t^2} = -\nabla U(\mathbf{R}_J) \tag{3.9}$$

where $U(\mathbf{R}_J)$ is the potential for the nuclei. Eq. 3.9 describes the nuclei moving on the ground state potential surface of the electronic structure. Following the Born-Oppenheimer Approximation, the initial problem is simplified to one of solving the ground state electronic structure to obtain $\psi(\mathbf{r}_i, \mathbf{R}_J)$. However, this problem is still difficult to solve.

3.1.3 Hartree-Fock Method

The *Hartree-Fock Method* (HF method)[182] is an approximation to deal with this problem, starting from the assumption that the many body electronic wave-function can be approximated by a Slater determinant for a given nuclear configuration:

$$\psi(\mathbf{r}_1 \cdots \mathbf{r}_N) = \frac{1}{\sqrt{N!}}\begin{vmatrix} \phi_1(\mathbf{r}_1) & \cdots & \phi_N(\mathbf{r}_1) \\ \vdots & \ddots & \vdots \\ \phi_1(\mathbf{r}_N) & \cdots & \phi_N(\mathbf{r}_N) \end{vmatrix} \tag{3.10}$$

where ϕ_i is the single electron wave-function or *orbital*. Therefore $\psi(\mathbf{r}_i)$ is decomposed into $\phi_i(\mathbf{r}_i)$, which is much easier to determine. This results in the well-known *Hartree-Fock Equation*[182] for calculating the electron eigenvalues ε_i:

$$[\hat{T}_e + V_n(\mathbf{r}) + V_H(\mathbf{r})]\phi_i(\mathbf{r}) + \int d\mathbf{r}' V_X(\mathbf{r}, \mathbf{r}')\phi_i(\mathbf{r}') = \varepsilon_i\phi_i(\mathbf{r}) \tag{3.11}$$

where $V_H(\mathbf{r}) = \int d\mathbf{r}' \frac{n(\mathbf{r}')}{|\mathbf{r}-\mathbf{r}'|}$ is the *Hartree potential* obtained using a mean-field approximation, describing the electrostatic potential for the electrons using the electron density $n(\mathbf{r})$, and $V_X(\mathbf{r},\mathbf{r}') = -\sum_j \frac{\phi_j^*(\mathbf{r}')\phi_j^*(\mathbf{r})}{|\mathbf{r}-\mathbf{r}'|}$ is the *Fock exchange potential* for electrons arising from the Pauli exclusion principle and the quantum nature of electrons. Eq. 3.11 can be solved using the variational principle by minimizing the total energy $E = \langle\psi|\hat{H}|\psi\rangle$ with respect to the variation of the electronic orbitals ϕ_i in the Slater determinant:

$$\frac{\delta E}{\delta \phi_i^*} = 0 \tag{3.12}$$

where $\hat{H}$ is the electronic Hamiltonian. However, the HF method neglects the *correlation* between electrons (V_C), which arises from Coulomb repulsion. Some methods such as the Configuration Interaction (CI)[183] method, the Coupled Cluster (CC)[184] method and Møller-Plesset perturbation theory(MP2[185], MP3[186], MP4[187]), use different techniques to include some part of the correlation and are called *Post-HF methods*. Discussion of these methods is important in the field of *Quantum Chemistry*.

3.1.4 Density Functional Theory

Kohn-Sham Equation

The starting point of *Density Functional Theory* (DFT) is the statement that the ground state energy of a system of interacting electrons in an external field ($V_n(\mathbf{r})$) is a unique functional $F[n(\mathbf{r})]$ of the single particle electron density $n(\mathbf{r})$:

$$E[n(\mathbf{r})] = F[n(\mathbf{r})] + \int V_n(\mathbf{r})n(\mathbf{r})d\mathbf{r} = T_{s,e}[n(\mathbf{r})] + E_H[n(\mathbf{r})] + E_{xc}[n(\mathbf{r})] + \int V_n(\mathbf{r})n(\mathbf{r})d\mathbf{r} \tag{3.13}$$

where $T_{s,e}$ is the kinetic energy of non-interacting electrons, and this functional is minimal at the equilibrium density $n_0(\mathbf{r})$ according to the variation $\delta n(\mathbf{r})$:

$$\left.\frac{\delta E[n(\mathbf{r})]}{\delta n(\mathbf{r})}\right|_{n=n_0} = 0 \tag{3.14}$$

This is called the *Hohenberg-Kohn Theorem*. One of the advances in Eq. 3.13 compared with the HF method is that it includes electron correlation in the *exchange and correlation energy* E_{xc}. The resulting wave equation for the single particle wavefunction ϕ_i which is called the

Kohn-Sham equation is then written:

$$[\hat{T}_{s,e} + V_n(\mathbf{r}) + V_H(\mathbf{r}) + V_{xc}(\mathbf{r})]\phi_i(\mathbf{r}) = \varepsilon_i \phi_i(\mathbf{r}) \tag{3.15}$$

where V_{xc} is called the *exchange and correlation potential* defined by:

$$V_{xc}(\mathbf{r}) = \frac{\delta E_{xc}[n]}{\delta n} \tag{3.16}$$

Exchange-Correlation Functional

The greatest problem for Eq. 3.15 is that V_{xc} (or E_{xc}) is not known precisely. Therefore, some approximations need to be used to construct E_{xc}. The accuracy of a DFT calculation depends mainly on the level of theory dealing with E_{xc}, as shown in Fig.3.1. The higher up the ladder

Fig. 3.1 Schematic of Perdew's classification of DFT functionals using a Jacob's ladder[24]

means the theory is more complicated and the computational resources are more consuming. The lowest level, the Local Density Approximation (LDA)[90, 188], approximates E_{xc} using the energy of a uniform electron gas with the same local density obtained from a quantum Monte Carlo calculation:

$$E_{xc}^{LDA}(\mathbf{r}) = E_{xc}^{electron\,gas}[n(\mathbf{r})] \tag{3.17}$$

The next level of theory, the *Generalized Gradient Approximation* (GGA), considers in addition to $n(\mathbf{r})$ the gradient of the electron gas based on the idea that the electron gas is not uniform in reality:

$$E_{xc}^{GGA}(\mathbf{r}) = E_{xc}[n(\mathbf{r}), \nabla n(\mathbf{r})] \tag{3.18}$$

GGA is commonly used in current calculations and in most cases it works quite well. Two examples of standard GGA are the Perdew-Wang 91 (PW91)[189] and Perdew-Burke-Ernzerhof (PBE)[190] functionals. Meta-GGA[191] includes $\nabla^2 n(\mathbf{r})$, which gives better

atomization energy. However, most meta-GGA functional does not improve geometries compared with PBE-GGA level[192]. Also, same as LDA/GGA the van der Waals effect is beyond the capabilities of meta-GGA. Therefore nowadays GGA level theory is still mostly used. However, rencently, the strongly constrained appropriately normed (SCAN) metta-GGA functional was proposed and showed improvements over GGA in several systems.

3.1.5 Beyond Density Functional Theory

DFT at LDA/GGA level is good at ground state properties such as atomic structures and lattice parameters. However, it has several problems which come from the incomplete description of exchange-correlation in the Kohn-Sham equation. For example, the band gaps of semiconductors and van der Waals interactions are poorly described. In addition, for materials containing transition and rare-earth elements with localised d and f orbitals, e.g. transition metal oxides, it is problematic as well. These materials are called *strongly correlated materials* and should be treated using the theory beyond DFT.

Hybrid Functional

The first step going beyond DFT is to include Hartree-Fock exchange in the LDA/GGA level of theory, forming so called *hybrid functionals*:

$$E_{xc}^{hyb} = \alpha E_{xc}^{HF} + (1-\alpha)E_{x}^{DFT} + E_{c}^{DFT} \tag{3.19}$$

Various hybrid functioanls e.g. PBE0[193], B3LYP[194] and HSE (Heyd-Scuseria-Ernzerhof) [195] can be obtained by choosing a different mixing parameter α. α can also be determined by fitting to experimental data. A detailed review of these functionals can be found in Burke et al[196].

GW Method

There is another method that comes from quantum field theory, which replaces the single particle wavefunction with a one particle Green's function[197–199]:

$$[\frac{\hbar^2}{2m}\nabla^2 + V_{ext}(\mathbf{r}) - E]G(\mathbf{r},\mathbf{r}',E) - \int \Sigma(\mathbf{r},\mathbf{r}'';E)G(\mathbf{r}''\mathbf{r}';E)d\mathbf{r}'' = -\delta(\mathbf{r}-\mathbf{r}') \tag{3.20}$$

where G is the one particle Green's function, representing the probability of finding an electron at $\mathbf{r}$ in presence of another electron at $\mathbf{r}'$ at energy E; Σ is the self energy, which

is non-local, non-Hermitian and energy dependent. Other local components such as the Hartree potential are included in Σ and the remaining non-local parts are included in Σ as well. Solving Eq. 3.20 is equivalent to solving the MBSE (Eq. 3.1). All the information can be obtained once G is known for the many body system. In Eq. 3.20, Σ can be calculated through many body perturbation theory by solving Dyson's equation:

$$G(\mathbf{r},\mathbf{r}';E) = G_0(\mathbf{r},\mathbf{r}';E) + \iint G_0(\mathbf{r},\mathbf{r}_1;E)\Delta\Sigma(\mathbf{r}_1,\mathbf{r}_2;E)G(\mathbf{r}_2,\mathbf{r}';E)d\mathbf{r}_1\mathbf{r}_2 \tag{3.21}$$

where $G_0(\mathbf{r},\mathbf{r}';E) = \sum_n \frac{\phi_0(\mathbf{r})\phi_0^*(\mathbf{r}')}{E-\varepsilon_n}$ is the Green's function for the reference system like LDA, GGA or hybrid functional and $\Delta\Sigma = \Sigma - V_H - \mu_{XC}$. μ_{XC} is the exchange-correlation potential from LDA, GGA or hybrid functional calculation. Σ can be computed using the *GW approximation*[197] by expanding Σ in terms of a dynamically screened Coulomb potential W:

$$\Sigma_{GW}(\mathbf{r},\mathbf{r}';E) = i\int G(\mathbf{r},\mathbf{r}';E+E')W(\mathbf{r},\mathbf{r}';E)dE' \tag{3.22}$$

and W can be evaluated through:

$$W(\mathbf{r},\mathbf{r}';E) = \iint \varepsilon^{-1}(\mathbf{r},\mathbf{r}_1;E)v_2(\mathbf{r}_1,\mathbf{r}')d\mathbf{r}_1 \tag{3.23}$$

where $\varepsilon(\mathbf{r},\mathbf{r}_1;E)$ is the dielectric function calculated within the *random phase approximation (RPA)* and $v_2(\mathbf{r}_1,\mathbf{r}')$ is the interaction potential for a referenced system ($v_2(\mathbf{r}_1,\mathbf{r}') = 0$ for a non-interacting electron system). Similar to DFT, the many body problem, Eq. 3.20 to Eq. 3.23[197], can be solved self-consistently. The full self-consistent GW calculation (scGW) is extremely expensive and can only be applied to a very small system. Therefore, practically, further simplifications are made: G_0W_0 with G evaluated non-self-consistently from the non-interacting system and W determined at the RPA level; GW_0 with G computed self-consistently and W worked out at the RPA level. The properties at G_0W_0 are already significantly improved, so G_0W_0 has been used quite often. The GW method also gives access to excitation. Other methods like the *time-dependent DFT (TDDFT)* and *Bethe–Salpeter equation (BSE)* methods can also achieve this level of theory but they are beyond the scope of the discussion in this thesis. More details can be found in Onida et al.[199]

Hubbard +U Method

The hybrid functional and GW methods can improve some materials properties like the electronic band gap. However, they are very computationally expensive and are usually applied based on the GGA optimised crystal structure. Another widely used method to cope

with a strongly correlated system is the *Hubbard+U method*[200–206] by adding a Hubbard type on-site Coulombic repulsion to the LDA/GGA energy:

$$E_{GGA/LDA+U} = E_{LDA/GGA} - \frac{1}{2}UN(N-1) + \frac{1}{2}U\sum_{i\neq j} f_i f_j \tag{3.24}$$

where f_i and f_j are the orbital occupancies for d/f orbitals and N is the total number of d/f electrons[206]. The U value can be determined by fitting to experimental data. The Hubbard+U method is much more computational efficient compared with the hybrid functional and is widely used in strongly correlated systems.

Dispersion Corrections

It is well known that non-local dispersion interactions such as van der Waals (vdW) forces are not well described in LDA/GGA level DFT. There are many ways of correcting for these interactions as mentioned in the literature review. The general idea is that:

$$E_{DFT-D} = E_{DFT} + E_{disp} \tag{3.25}$$

where E_{DFT-D}, E_{DFT} and E_{disp} are the dispersion corrected energy, the standard DFT energy and the dispersion energy correction, respectively. E_{disp} is defined as:

$$E_{disp} = -s_6 \sum_{i=1}^{N-1} \sum_{j=i+1}^{N} \frac{C_6^{ij}}{R_{ij}^6} f_{dmp}(R_{ij}) \tag{3.26}$$

where N, s_6, C_6^{ij} are the number of atoms, the global scaling factor and the dispersion coefficients, respectively. s_6 is only dependent on the functional used in the calculation and C_6^{ij} depends on the elements i and j. The f_{dmp} is a damping function, which is used to avoid near atom singularities, defined as:

$$f_{dmp}(R_{ij}) = \frac{1}{1+e^{-d(R_{ij}/R_0-1)}} \tag{3.27}$$

where d and R_0 are the damping steepness and vdW radius. d is fixed while R_0 depends on the elements considered. Usually, C_6 and R_0 need to be declared explicitly in the input file using Grimme's method (DFT-D[109] DFT-D2[110] and DFT-D3[111]). These data are pre-calculated theoretically therefore Grimme's method is called a semi-empirical correction.

For the method provided by Tkatchenko et al[112], C_6 is derived from the electron density and this method yields a much better description of vdW interactions.

Another method is the non-local van der Waals density functional (vdW-DF) developed by Dion et al.[113], which is a non-local correlation functional that includes dispersion interactions directly calculated from the electron density. The exchange-correlation energy E_{xc} is expressed as:

$$E_{xc} = E_x^{GGA} + E_c^{LDA} + E_c^{nl} \tag{3.28}$$

where the exchange energy E_x^{GGA} is taken from the GGA functional (revPBE) and the correlation energy from the LDA functional E_c^{LDA} plus the non-local correlation energy E_c^{nl} from double space integration[113]. However, although vdW-DF includes dispersion interactions, it produces results that are worse than normal GGA calculations, including hydrogen bonds. Therefore, the GGA part in Eq. 3.28 has been modified to produce new functionals such as optPBE-vdW, optB88-vdW and optB86b-vdW[207], which significantly improve the results of related calculations[208].

3.1.6 Spin-Orbit Coupling

Spin-orbit coupling (SOC) is the interaction between an electron's spin magnetic moment and its orbital angular momentum. Its effect is to lift the degeneracy of one-electron levels in solids. SOC is particularly large when heavy elements like Pb or I are present in the solid (e.g. $MAPbI_3$) since in these elements electrons reach relativistic speeds. Proper account of SOC therefore requires solving the relativistic *Dirac equation*. However, the non-relativistic Kohn-Sham equation can be used as a first approximation by substituting a spin dependent term in the Hamiltonian:

$$[-\frac{1}{2}\nabla^2 + V_n(\mathbf{r}) + V_H(\mathbf{r}) + V_{xc}(\mathbf{r}) + \mu_B \boldsymbol{\sigma} \cdot \mathbf{B}_{xc}(\mathbf{r})]\phi_i(\mathbf{r}) = \varepsilon_i \phi_i(\mathbf{r}) \tag{3.29}$$

where μ_B is the Bohr magneton, $\mathbf{B}_{xc}$ is the exchange and correlation magnetic field, and $\boldsymbol{\sigma}$ is the matrix vector defined by:

$$\boldsymbol{\sigma} = \sigma_x \mathbf{u}_x + \sigma_y \mathbf{u}_y + \sigma_z \mathbf{u}_z \tag{3.30}$$

where σ_x, σ_y and σ_z are the Pauli matrices and $\mathbf{u}_x$, $\mathbf{u}_x$ and $\mathbf{u}_x$ are the unit vectors along x, y and z direction. The derivation of Eq. 3.29 is beyond the scope of this thesis. The spin calculation includes a collinear and non-collinear part. The collinear calculation assumes that the spin densities are in the same direction. The SOC effect can be included by performing a

non-collinear spin calculation, which is supported by many DFT software packages such as VASP and Quantum Espresso.

3.2 Implementation of DFT

3.2.1 Total energy minimization

The main task for DFT is to solve the Kohn-Sham equation (Eq. 3.15). This equation can be solved self-consistently as shown in Fig.3.2. The calculation starts from the initial atomic

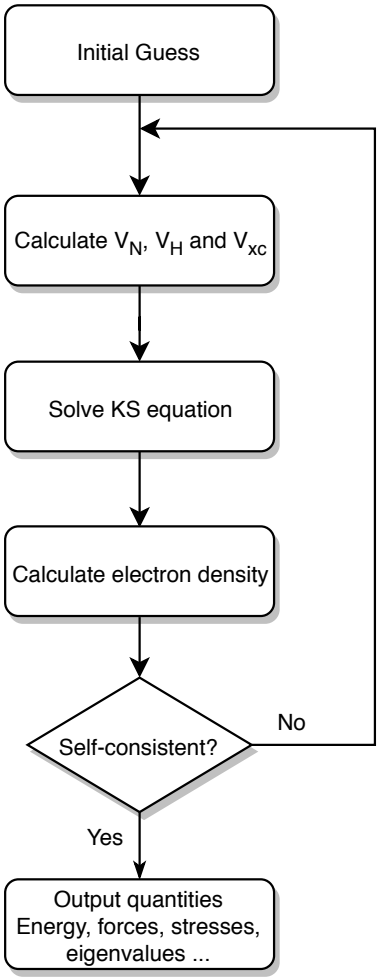

Fig. 3.2 Flow-chart of the self-consistent calculation of the Kohn-Sham equation.

.

coordinates and determines the nuclear potential V_N. Then an initial guess for the electron density is generated in order to calculate the Hartree potential V_H and exchange-correlation potential V_{xc}. In principle, this guess could be random but usually in practice, it is generated from the superposition of the atomic charge densities. After constructing the Hamiltonian, the single particle state ϕ_i can be determined. Then the new charge density can be obtained to construct the new Hamiltonian. These calculations are repeated until the difference between new density and old density is smaller than the tolerance set for the calculation to achieve *self-consistency*. Convergence can be improved by mixing the input and output densities. If the difference between the new electron density and old electron density is smaller than the tolerance set for the calculation, then the calculation is finished. A better way to solve the Kohn-Sham equation, which is implemented by the most DFT codes, is the iterative direct minimization of the total energy functional[209] using algorithms like direct inversion of the iterative subspace (DIIS), the Blocked Davison (DAV) method or conjugate gradient (CG) method. In practice, the self-consistent method and direct minimization method can be combined to achieve higher efficiency. Other methods like Car-Parrinello molecular dynamics (CPMD)[210] can also be used to complete this task.

3.2.2 Solving the Kohn-Sham Equation in Solids

Since most materials studied are crystalline solids, periodic boundary conditions can be used to significantly reduce the computational requirements, i.e.:

$$\phi_i(\mathbf{r}+\mathbf{R}) = \phi_i(\mathbf{r}) \tag{3.31}$$

where $\mathbf{R}$ is lattice vector. From Bloch's theorem, the periodic electronic wavefunction can be written as,

$$\phi_i(\mathbf{r}) \rightarrow \phi_{n\mathbf{k}}(\mathbf{r}) = u_{n\mathbf{k}}(\mathbf{r})e^{i\mathbf{k}\cdot\mathbf{r}} \tag{3.32}$$

where $u_{n\mathbf{k}}(\mathbf{r})$ are cell periodic functions called *crystal functions*, n is the band index for electronic states and $\mathbf{k}$ are wavevectors. Then the periodic Kohn-Sham equation can be expressed using the crystal function $u_{n\mathbf{k}}(\mathbf{r})$ as:

$$[-\frac{1}{2}(\nabla + i\mathbf{k})^2 + V_{tot}(\mathbf{r})]u_{n\mathbf{k}}(\mathbf{r}) = \varepsilon_{i\mathbf{k}}u_{n\mathbf{k}}(\mathbf{r}) \tag{3.33}$$

and the electron density can be calculated as:

$$n(\mathbf{r}) = \frac{1}{\Omega_{BZ}} \sum_n \int_{BZ} f_{n\mathbf{k}} |u_{n\mathbf{k}(\mathbf{r})}|^2 d\mathbf{k} \tag{3.34}$$

where $f_{n\mathbf{k}}$ are the occupation numbers equivalent to the number of electrons that occupy the state $n\mathbf{k}$ and Ω_{BZ} is the volume of the first Brillouin zone. For numerical calculation, the integral is substituted by a weighed summation:

$$n(\mathbf{r}) = \sum_n \sum_{\mathbf{k}} \omega_{\mathbf{k}} f_{n\mathbf{k}} |u_{n\mathbf{k}(\mathbf{r})}|^2 \tag{3.35}$$

where $\omega_{\mathbf{k}}$ are the weights for the discrete k-points. Solving Eq. 3.33 in planewave form is quite common because it can be easily translated between real space and reciprocal space using a *fast Fourier transform* (FFT) algorithm. The crystal function $u_{n\mathbf{k}}$ can be written as:

$$u_{n\mathbf{k}} = \sum_{\mathbf{G}} c_{n\mathbf{k}}(\mathbf{G}) e^{i\mathbf{G}\cdot\mathbf{r}} \tag{3.36}$$

where $\mathbf{G}$ are reciprocal lattice vectors, $c_{n\mathbf{k}}$ are coefficients of the Fourier series and $exp(i\mathbf{G}\cdot\mathbf{r})$ are the *planewaves*. This satisfies the periodic condition in Eq. 3.31. Then $\phi_{n\mathbf{k}}$ can be expressed as:

$$\phi_{n\mathbf{k}}(\mathbf{r}) = \sum_{\mathbf{G}} c_{n\mathbf{k}}(\mathbf{G}) e^{i(\mathbf{G}+\mathbf{k})\cdot\mathbf{r}} \tag{3.37}$$

The Fourier coefficients can be obtained by multiplying the two sides of Eq. 3.36 by $exp(-i\mathbf{G}'\cdot\mathbf{r})$ and taking the summation over the computational cell. In principle, wavefunction $\phi_{n\mathbf{k}}(\mathbf{r})$ in Eq. 3.37 is composed of an infinite set of planewaves, which is called the *planewave basis set*. However, in practice, only planewaves whose kinetic energy is smaller than a *planewave kinetic energy cutoff* (in Hartree a.u.) are included:

$$E_{cut} = \frac{|(\mathbf{G}+\mathbf{k})_{max}|^2}{2} \geq \frac{|\mathbf{G}+\mathbf{k}|^2}{2} \tag{3.38}$$

E_{cut} should be chosen carefully using a convergence test. Too large E_{cut} will increase the computational demand and too small E_{cut} will cause incompleteness in the description of the wavefunction, i.e. an error. Using the planewave representation, the electron density can be calculated as:

$$n(\mathbf{G}) = \frac{1}{\Omega} \int d\mathbf{r}\, e^{-i\mathbf{G}\cdot\mathbf{r}} n(\mathbf{r}) \tag{3.39}$$

The other cell periodic functions then can be expressed using planewaves:

$$V_{tot}(\mathbf{G}) = \frac{1}{\Omega}\int d\mathbf{r}\, e^{-i\mathbf{G}\cdot\mathbf{r}} V_{tot}(\mathbf{r}) \tag{3.40}$$

where V_{tot} is defined as:

$$V_{tot}(\mathbf{r}) = V_n(\mathbf{r}) + V_H(\mathbf{r}) + V_{xc}(\mathbf{r}) \tag{3.41}$$

By inserting Eq. 3.37, Eq. 3.40 and Eq. 3.41 into Eq. 3.33, the Kohn-Sham equation in planewave representation can be obtained, and this equation can be solved starting from $c_{n\mathbf{k}}(\mathbf{G})$ self-consistently. In the field of quantum chemistry, the focus is often on molecules, and therefore instead of using a planewave basis set, an atomic orbital basis set, e.g. Gaussian type orbital (GTO) and Slater type orbital (STO), is mostly used.

3.2.3 Brillouin Zone Sampling

Many key properties like electron density are evaluated by integration over the first Brillouin Zone. Therefore, the method for selecting the k-points over which the integration takes place is important, since the number of potential k-points is substantial. The *Monkhorst-Pack method*[211] is commonly used. In this method, the k-points are equally spaced in the Brillouin Zone. Firstly, the coordinates of the sampled k-points are defined as:

$$\mathbf{k}_{prs} = v_p\mathbf{b}_1 + v_r\mathbf{b}_2 + v_s\mathbf{b}_3 \tag{3.42}$$

where $\mathbf{b}_i$ are the three lattice basis vectors in reciprocal space and v_j ($j = p,r,s$) are the three groups of k-points in the p, r and s direction. v_j are defined as:

$$v_j = \frac{2j - q_j - 1}{2q_j}, \quad j = 1,2,\ldots,q_j \tag{3.43}$$

where q_j is the number of the k-points in the j direction. In practice, the symmetry of the reciprocal lattice is considered, reducing the number of k-points to a set called the *irreducible k-points*. The region constructed by the irreducible k-points is called the *irreducible Brillouin zone* (IBZ). The weights of the k-points can also be obtained from symmetry. Choosing the proper number of k-points is very important in DFT calculations. Similar to the number of planewaves, more k-points leads to a finer mesh, which makes the calculation more expensive. Therefore, before a calculation, a convergence test should be performed to obtain the optimal number of k-points. On the other hand, in order to be in consistent with the symmetry of the structure, the number of k-points should be proportional to the length of the lattice vectors of

reciprocal space, for example, if $\mathbf{b}_1 : \mathbf{b}_2 : \mathbf{b}_3 = 1 : 2 : 3$, $q_p : q_r : q_s$ should also be $1 : 2 : 3$. One point that should be noted is that for a hexagonal cell, many tests[212] have shown that using a Γ centered grid converges the energy much faster than using the standard Monkhorst-Pack mesh.

3.2.4 Pseudopotentials

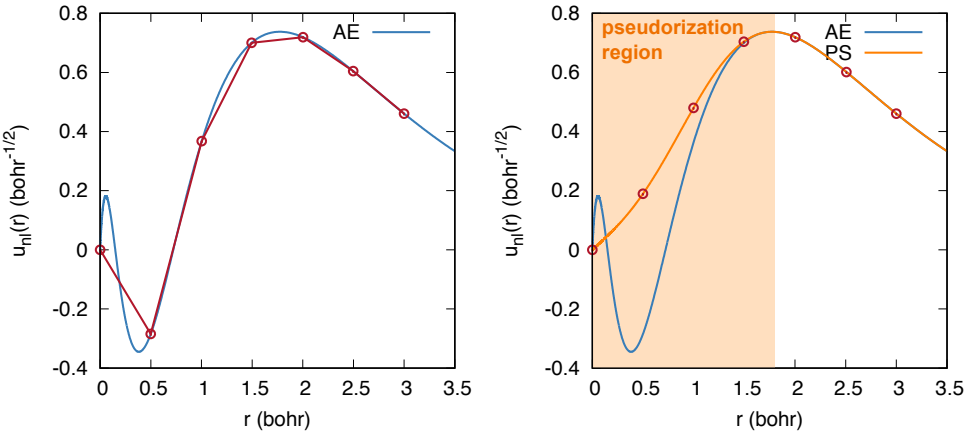

Fig. 3.3 Left panel shows the difficulties in expressing the all electron (AE) nodal structure (blue curve) using coarse mesh points (red points and lines) for a Si 3s orbital. Right panel shows the norm-conserving pseudopotential (PS, orange curve) and the AE potential (blue curve). Also in the right panel, the pseudorized region is shown. Data is generated using on-the-fly pseudopotential generation function as implemented in CASTEP[25] code.

It is known that only the valence electrons of an atom are sensitive to changes in local chemical environment (being responsible for bonding) while the core electrons of an atom remain inert. Therefore, the *pseudopotential*, an approximation method describing the valence electrons of an atom explicitly while freezing the core electrons can be applied to simplify DFT calculations. However, there are two points to be noted. Firstly, the valence states might oscillate near the core region (to make them orthogonal to the core states) to form a so called *nodal structure*. If we simply ignore the core states, the nodal structure would not be described correctly. Secondly, those oscillating nodal structures are very hard to express using planewaves, i.e. a very fine k-point mesh or a very high E_{cut} would have to be used. Therefore, substantial computational resources would be consumed. The modern pseudopotential method which avoids this problem is as follows: Firstly, calculate the all electron (AE) wavefunction from the Kohn-Sham equation at a reference energy. Then, select a cutoff radius r_c which corresponds to the core radius of the atom, and substitute the potential inside r_c with a nodeless smooth curve such as a polynomial or spherical Bessel

function so that the function is continuous and continuously differentiable at r_c. Therefore, the pseudo-wavefunction is identical to the AE-wavefunction when $r \geqslant r_c$ and is smooth and nodeless in the *pseudorized region* ($0 < r < r_c$). The method for obtaining such a smooth curve is rather complicated and the details can be found in Martin's book[213]. An example is given in Fig.3.3. Norm-conserving pseudopotentials (NCPP)[214] and ultrasoft pseudopotentials (USPP)[215] are the two popular pseudopotentials widely used today. NCPP keep the charge within r_c fixed (so called conserved) and a high E_{cut} should be used for the first row and transition metal elements because of their strongly localized orbitals. In USPP, the norm-conserving condition is relaxed and localized atom-centered augmentation charges are introduced to make up the charge deficits when $r < r_c$. One of the advantages of USPP over NCPP is that USPP need much lower E_{cut}. However, for USPP, the construction of pseudopotentials is complicated so many tests should be performed in order to obtain reliable results. A method was proposed by Blöchl called the *projector augmented wave method* (PAW)[216, 217] which can avoid these problems. The PAW method is closely related to USPP. In the PAW method, a linear transformation between the pseudopotential and the AE potential is introduced. Therefore, the PAW method works directly with the AE potential. The PAW method can handle most cases with exceptional precision and it is also highly efficient. In terms of doing calculations, a recent systematic benchmark study[218] showed that there is not much difference in using USPP and PAW, and both of them can produce satisfied results.

3.3 Applications for DFT

3.3.1 Equilibrium Structure

Atomic Forces

It was mentioned previously that the nuclei in standard DFT are treated as classical particles and therefore the Newtonian equation (Eq. 3.9) can be used for their dynamics. From classical mechanics, the total force on each atom can be calculated as:

$$\mathbf{F}_I = -\frac{\partial U}{\partial \mathbf{R}_I} \tag{3.44}$$

where $\mathbf{F}_I$ is the force on I-th nucleus and U is the total potential energy. However, $\partial U/\partial \mathbf{R}_I$ is not easy to calculate. The finite displacement method might work here but it is very time-consuming. However the *Hellmann-Feynman theorem*[219] can help deal with this

problem using first-order perturbation theory:

$$\mathbf{F}_I = -\langle\Psi|\frac{\partial H}{\partial \mathbf{R}_I}|\Psi\rangle - \frac{\partial V_{NN}}{\partial \mathbf{R}_I} \tag{3.45}$$

where V_{NN} is the classical potential energy of nuclei. The second term in Eq. 3.45 comes from the electrostatic field of the nuclei.

Ionic Optimization

After the atomic forces on each atom are determined, the structure can be optimized using various algorithms including conjugate gradient (CG), quasi-Newton and damped molecular dynamics[213]. The equilibrium structure can be obtained starting from an initial guess of the atomic positions, and then calculating the electron density and energy by performing Kohn-Sham self-consistent calculations. This is called the electronic step. Then the atomic force on each atom can be determined from Eq. 3.45. The new atomic positions are obtained from an algorithm like CG. These atomic positions can be used as a new start for the cycle, which is called the ionic step. The condition for ending the loop can be selected from either the atomic forces and stress, or the energy for the whole structure. A schematic of the ionic optimization procedure is shown in Fig.3.4.

3.3.2 Band Structures and Density of States (DOS)

After solving the periodic Kohn-Sham equation (Eq. 3.33), the energy states can be obtained, which are called the Kohn-Sham states. The total energy obtained from Eq. 3.33 is:

$$E = \frac{1}{\Omega_{BZ}}\sum_n \int_{BZ} d\mathbf{k}\, f_{n\mathbf{k}}\varepsilon_{n\mathbf{k}} - [E_H + \int d\mathbf{r}\, V_{xc}(\mathbf{r})n(\mathbf{r}) - E_{xc}] \tag{3.46}$$

where the first term is the *band structure energy* and the second term contains the double counting energies in the first term. The *electronic density of states* (DOS) can be calculated as:

$$\rho(E) = \frac{1}{\Omega_{BZ}}\sum_n \int_{BZ} d\mathbf{k}\, \delta(E - \varepsilon_{n\mathbf{k}}) \tag{3.47}$$

$\rho(E)dE$ expresses the number of the Kohn-Sham states between E and $E + dE$. The band structure and DOS are powerful tools for analyzing the electronic structure. In addition to the total DOS, partial density of states can be determined for each orbital.

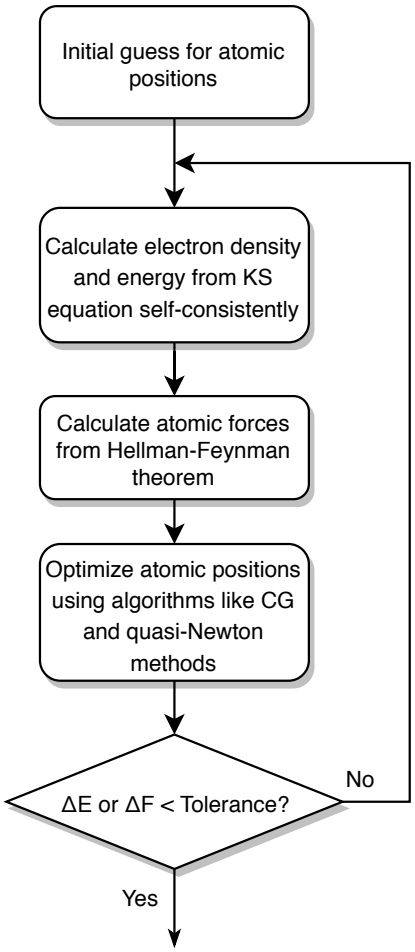

Fig. 3.4 Flow-chart of ionic optimization

3.3.3 Vibrational Properties

Discrete lattice vibrations or phonons, which are ignored in ground state DFT calculations, are crucial in condensed matter physics for understanding many material properties including thermodynamic quantities, electrical and thermal conductivity. A detailed introduction to lattice dynamics can be found in Dove's book[220]. Basically, the quantized lattice vibration can be evaluated by moving each ion along three Cartesian axes in very small steps and calculating the forces. The procedure is called the *finite displacement method (FDM)*. It is noticed that vibrational properties can also be calculated using *density functional perturbation theory (DFPT)*[221] which is not described here. In FDM, the force constants matrix Φ is

calculated from the Hellman-Feynmann force theorem using DFT[219] as discussed above:

$$\Phi_{\alpha,\alpha'}^{\kappa,\kappa'} = \frac{\partial^2 E}{\partial(u)_{\kappa,\alpha}(u)_{\kappa',\alpha'}} \tag{3.48}$$

where κ, α, u are indices for the nucleus, Cartesian axes and displacement with respect to equilibrium structure, respectively. In Eq. 3.48, only terms up to second order in the displacements are included, which is known as the *harmonic approximation*. In a periodic structure, the dynamical matrix D can be determined by performing a mass reduced Fourier transformation on Φ:

$$D_{\alpha,\alpha'}^{\kappa,\kappa'}(\mathbf{q}) = \frac{1}{\sqrt{M_\kappa M_{\kappa'}}} \sum_{\alpha} \Phi_{\alpha,\alpha'}^{\kappa,\kappa'} e^{-i\mathbf{q}\cdot\mathbf{r}_\alpha} \tag{3.49}$$

which can form an eigenvalue problem:

$$D_{\alpha,\alpha'}^{\kappa,\kappa'}(\mathbf{q})\varepsilon_{\nu\kappa,\alpha\mathbf{q}} = \omega_{\nu,\mathbf{q}}^2 \varepsilon_{\nu\kappa,\alpha\mathbf{q}} \tag{3.50}$$

Therefore by diagonalizing $D(\mathbf{q})$, normal mode wave vectors $\varepsilon_{\nu\kappa,\alpha\mathbf{q}}$ and corresponding normal mode frequencies $\omega_{\nu,\mathbf{q}}$ can be obtained. ν is the band number in the phonon dispersion. Similar as the electronic band structure, phonons also have a dispersion relationship ($\mathbf{q}$ vs. ω) and this reciprocal space is called q-space.

Once the phonon calculation is completed by sampling different q-points in q-space, various thermodynamic properties can be computed including the partition function Z:

$$Z = exp(-\phi/k_B T) \prod_{\mathbf{q}\nu} \frac{exp(-\hbar\omega(\mathbf{q}\nu)/2k_B T)}{1 - exp(-\hbar\omega(\mathbf{q}\nu)/k_B T)} \tag{3.51}$$

Using the partition function Z, the Helmholtz free energy F and vibrational entropy S can be calculated:

$$F = -k_B T lnZ \tag{3.52}$$

$$S = -\frac{\partial F}{\partial T} \tag{3.53}$$

The lattice thermal expansion and Gibbs free energy can be computed using the *quasi-harmonic approximation* (QHA) whereby harmonic phonon calculations are performed for the relaxed structures at different volumes. The Gibbs free energy can be obtained by finding the minimum of the energy-volume curves fitted to the equation of states at different

temperatures and pressures:

$$G(T,p) = \min_{V}[U(V) + F_{phonon}(T;V) + pV] \tag{3.54}$$

The thermal expansion coefficients can be easily derived from the minimum volume at each temperature.

3.3.4 Elastic Constants Calculation

The generalized form of Hooke's law states:

$$\sigma_i = C_{ij}\varepsilon_j \tag{3.55}$$

where σ_i, ε_j and C_{ij} are the stress, strain and elastic stiffness constants simplified using Voigt notation from the corresponding second ($\sigma_{\alpha\beta}$, $\varepsilon_{\gamma\delta}$) rank and fourth rank ($C_{\alpha\beta\gamma\delta}$) tensors. The elastic stiffness constants can be obtained using the so called the stress-strain method:

$$C_{ij} = \left.\frac{\partial\sigma_i}{\partial\varepsilon_j}\right|_{\varepsilon=0} \tag{3.56}$$

and the elastic compliance constants S_{ij}, can be evaluated by:

$$S_{ij} = C_{ij}^{-1} \tag{3.57}$$

The stress can be obtained by applying a strain to the unit cell in a DFT calculation and using the stress theorem[222]:

$$\sigma_i = \frac{1}{V_0}\frac{\partial E_{tot}}{\partial\varepsilon_i} \tag{3.58}$$

where E_{tot} is the DFT total energy and V_0 is the equilibrium unit cell volume.

Elastic Modulus Calculation

Once the stiffness constants matrix C_{ij} has been determined, the isotropic elastic moduli such as the bulk modulus (B), shear modulus (G), Young's modulus (E) and Poisson's ratio (ν) can be calculated by combining the C_{ij} components. First, for the bulk modulus,

$$B_V = \frac{1}{9}[(C_{11}+C_{22}+C_{33}) + 2(C_{12}+C_{13}+C_{23})] \tag{3.59}$$

and

$$B_R = \frac{1}{[(S_{11}+S_{22}+S_{33})+2(S_{12}+S_{13}+S_{23})]} \tag{3.60}$$

where "V" and "R" denote the *Voigt and Reuss* upper and lower bound respectively of the modulus for a polycrystalline material[223, 224]. The *Voigt-Reuss-Hill average* (VRH)[37], is the average of these two quantities:

$$B_{VRH} = \frac{B_R + B_V}{2} \tag{3.61}$$

For the shear modulus, the upper and lower bounds are:

$$G_V = \frac{1}{15}[(C_{11}+C_{22}+C_{33})-(C_{12}+C_{13}+C_{23})+3(C_{44}+C_{55}+C_{66})] \tag{3.62}$$

and

$$G_R = \frac{15}{4(S_{11}+S_{22}+S_{33})-4(S_{12}+S_{13}+S_{23})+3(S_{44}+S_{55}+S_{66})} \tag{3.63}$$

leading to the VRH average:

$$G_{VRH} = \frac{G_V + G_R}{2} \tag{3.64}$$

The VRH average of the Young's modulus can be determined from a combination of B_{VRH} and G_{VRH}:

$$E_{VRH} = \frac{9B_{VRH}G_{VRH}}{3B_{VRH}+G_{VRH}} \tag{3.65}$$

The anisotropic Young's modulus can be specifically calculated using:

$$E(\mathbf{u}) = \frac{1}{S'_{1111}} = \frac{1}{u_i u_j u_k u_l S_{ijkl}} \tag{3.66}$$

where S'_{1111} is S_{1111} transformed to an arbitrary direction and $\mathbf{u}$ is the related direction cosine, defined by:

$$\mathbf{u} = \mathbf{u}(\theta,\phi) = (sin(\theta)cos(\phi), sin(\theta)sin(\phi), cos(\theta)), \tag{3.67}$$

where θ and ϕ are the appropriate azimuthal angle and polar angle in a spherical coordinate system. Finally, the isotropic Poisson's ratio can be calculated as:

$$\nu_{VRH} = \frac{3B_{VRH}-2G_{VRH}}{3(2B_{VRH}+G_{VRH})} \tag{3.68}$$

3.4 Experimental Methods

This section briefly introduces the experimental techniques that were used in this thesis ranging from materials synthesis to characterisation. Different materials have different synthesis and characterisation parameters, and details will be given in the results chapters later. For this part a great amount of help was received from colleagues and mostly from: Dr. Fengxia Wei, Dr. Shijing Sun and Dr. Yue Wu.

3.4.1 Synthesis

One of the great advantages of HPs is their ease of synthesis, because these materials can be solution processed, and thin films can be fabricated by spin coating. However, in this thesis, only bulk phases have been synthesised, which are single crystals and powder HPs. There are various methods that can be used to make HPs and basically they follow the reaction route below:

$$AX + B^{II}X_2 \longrightarrow AB^{II}X_3 \tag{3.69}$$

and similarly, for double perovskites:

$$2\,AX + B^{I}X + B^{III}X_3 \longrightarrow A_2B^{I}B^{III}X_6 \tag{3.70}$$

The easiest way of making HPs is by mechanical synthesis[10, 225] such as direct grinding of AX and BX_2 in a grinding mortar in air or by ball milling. However, some amount of secondary phases will be obtained using this type of synthesis. HPs can also be made by mixing molten AX and BX_2 but this method needs high temperatures and can only be used for some inorganic HPs. In terms of structure solution for new phases using XRD, the single crystal material is much preferred to the powder form. Therefore the solution growth method was mostly used during my PhD for obtaining high quality single crystalline material with high purity and the lowest amount of defects.

AX and BX_2 were weighed in the stochiometry ratio of 1:1 and dissolved in solvent like dimethylforammide (DMF) or halide acid like HI[10]. The solution was stirred in a glass vial on a hot plate heated at around 80-120 °C for 1-2 hour until clear. The cap was then opened and some solvent was evaporated as it is allowed to cool down to room temperature. Some crystals precipitated at the bottom of glass vial. For some compounds studied in this thesis, such as $(MA)_2KYCl_6$ and $(MA)_2KGdCl_6$, which are extremely hygroscopic and deliquescent, the solution should be evaporated to dryness at a proper rate. More detailed

descriptions of synthesis conditions are given in the method section in following results chapters.

Another method used in this thesis is the *hydrothermal method*. In this method, reagents were put in a stainless steel autoclave with a small amount of solvent. Then the autoclave was sealed and put into an oven at 150 °C for few days and then cooled down to room temperature to precipitate the crystals.

3.4.2 Characterisation

X-ray Diffraction

After obtaining high quality single crystals, their crystal structures can be characterised using the traditional diffraction techniques like X-ray diffraction (XRD). The theory of XRD can be found in Cullity's book[226]. For new materials, single crystal X-ray diffraction (SCXRD) is favoured for structure solution and refinement, which was used mostly in my studies. Powder X-ray diffraction (PXRD)[227] is quicker and easier to perform than SCXRD for known crystal structures and is often used for a quick check.

For PXRD, a Bruker D8 DAVINCI diffractometer was employed. The sample holder was disk-shaped and spinning with a spinning angle Ω during data collection. For a qualitative study such as phase identification, direct comparison with a reference pattern from a database is enough. For a quantitative study, further refinement is needed. The most widely used method is *Rietveld refinement*[228, 229] in which the whole powder pattern is fitted using least-square fitting to obtain a theoretical powder profile that matches the experimental pattern. Therefore a reasonable model is needed for Rietveld refinement. Another much easier and widely used method is *Pawley refinement*[230] in which the experimental powder pattern is refined without a structural model but is constrained by the unit cell parameters, crystal size and symmetry. This is often used as a pre-processing step for Rietveld refinement. In terms of software, TOPAS[231] and HighScore Plus are commonly employed for phase identification and refinement.

For SCXRD, a 4 circle diffractometer Gemini from Oxford Diffraction was used. It has 2 X-ray tubes: Mo ($\lambda = 0.71073$ Å) and Cu ($\lambda = 1.54184$ Å). The Mo beam is recommended for inorganic and organometallic materials whereas Cu is preferred for organic molecules. Since Cu beam has lower energy and organic molecules does not absorb X-ray as much as metals, using Cu beam is appropriate for organic molecules. The crystal was mounted using Paratone-N on a goniometer which was used to adjust the orientation. Unlike PXRD, where there only one measured angle θ was varied (Fig.3.5 a, Ω is the rotation angle, same

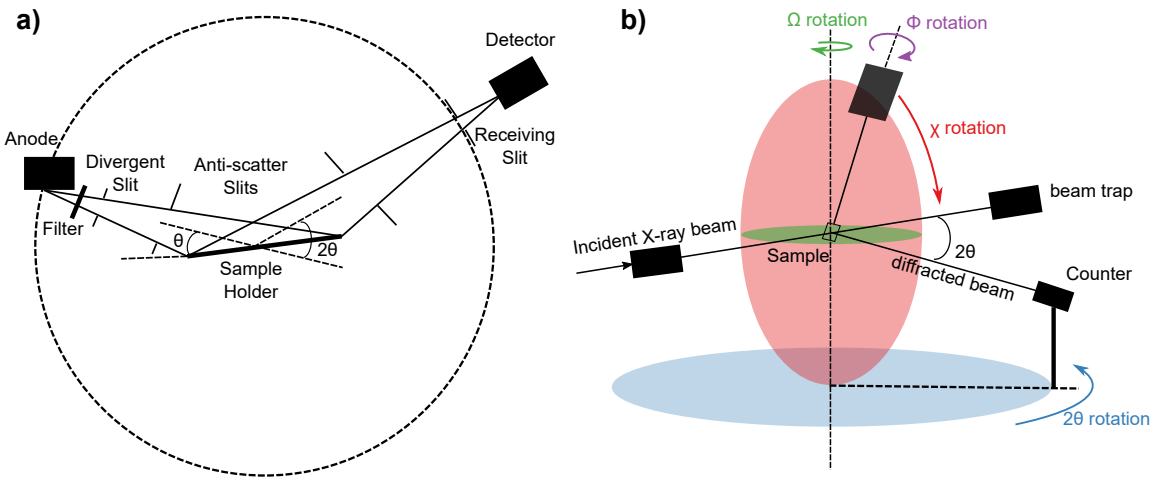

Fig. 3.5 Schematic for a) PXRD and b) SCXRD experiment.

as SCXRD but not essential), SCXRD has 4 angles: θ, χ, ϕ and Ω (Fig.3.5 b). After data collection and reduction, the structure was solved by the direct method using the ShelXS[232] program and refined using ShelXL[233] with the least-square method as implemented in the Olex2 software[234]. In addition, this diffractometer is equipped with a Cryojet device which enables structural characterisation at different temperatures ranging from 90K to 490K.

Thermal Analysis

Thermal analysis can be performed to detect phase transitions when changing temperature. In this thesis, *differential scanning calorimetry (DSC)* and *thermogravimetric analysis (TGA)* were mostly used, and were conducted using the SDT (simultaneous DSC-TGA) Q600 instrument. The sample was put in a ceramic sample holder and heated up starting from room temperature at a constant rate (usually $10\,\mathrm{K}\cdot\mathrm{min}^{-1}$) under nitrogen flow. DSC detects the heat flow whereas TGA measures the weight of the sample as the temperature increases.

UV-vis Spectroscopy

Optical properties were characterised using UV-vis spectroscopy with a PerkinElmer Lambda 750 UV-vis spectrometer. Bulk powder samples were used for measurements. Data was collected in the reflectance mode with a 2 nm slit width, a 1 nm interval and a range between 300 and 1200 nm, which is enough to cover the band gaps of most semiconductors. The band gap was estimated using a Tauc plot[95], which starts from the conversion of the reflectance

R into the Kubelka-Munk function $F(R)$:

$$F(R) = \frac{\alpha}{S} = \frac{(1-R)^2}{2R} \tag{3.71}$$

where α are S are absorption and scattering coefficients, respectively. S depends on sample condition such as thickness, particle size etc. and is treated as constant for all plots. Then $(h\nu F(R))^{\frac{1}{n}}$ was plotted against photon energy $h\nu$ and Eq. 3.72 was used to determine band gap using a spectral function:

$$(h\nu F(R))^{\frac{1}{n}} = A(h\nu - E_g) \tag{3.72}$$

$n = 0.5$ for a direct allowed transition, $n = 2$ for an indirect allowed transition and E_g is the optical band gap. Whether the band gap is direct or indirect can be determined from DFT band structure calculations. Practically, one can perform a linear least square fitting at the absorption edge region and get E_g from the interception with the $h\nu$ axis .

Chapter 4

Lead-free Hybrid Double Perovskites

This chapter summarizes recent work on lead-free hybrid double perovskites [16, 26, 27, 29] .

4.1 Introduction

As mentioned in Chapter 2, there has been significant recent progress in the incorporation of Bi into hybrid perovskite-related halides. For example, $(MA)_3Bi_2I_9$ can be readily obtained using a synthetic route analogous to that used for $MAPbI_3$[235], and an ammonium bismuth iodide phase, $(NH_4)_3Bi_2I_9$, was recently reported to show a bandgap of 2.04 eV[140]. A number of alkali metal systems of composition $M^I{}_3Bi_2I_9$ (M = K, Rb, Cs) have also been described[11, 236]. None of these systems is a perovskite, however, and their structures have lower dimensionalities and therefore wider band gaps than their 3D analogues. In order to maintain the 3D perovskite architecture, an alternative approach is to use a combination of a monovalent cation, such as an alkali metal or Ag, and a trivalent cation such as Bi, in an ordered B-site arrangement to form a double perovskite structure of general formula $A^I{}_2B^IB^{III}X_6$. During the 1970s, a number of double perovskites (which were described by their alternative name, elpasolites) of composition $Cs_2NaM^{III}Cl_6$ (M^{III} = lanthanide, actinide, bismuth, and so on) were reported in $Fm\bar{3}m$ symmetry, wherein the perovskite network contains alternating $NaCl_6$ and $M^{III}Cl_6$ octahedra on the B-sites[143]. At that time, particular interest focused on a ferroelectric phase transition that was observed on cooling $Cs_2NaBiCl_6$[237–240]. Very recently, and in the light of the intense interest in halide perovskites, McClure et al.[14] reported Cs_2AgBiX_6 (X = Cl, Br) with a bandgap of 2.77 eV for X = Cl and 2.19 eV for X = Br, while a separate paper by Slavney et al.[13] described the X = Br phase with a bandgap of 1.95 eV and a long photoluminescence lifetime of ca. 660 ns. The

observation that hybrid perovskites are more easily processed into devices and show different optical properties compared with their inorganic analogues[241] encouraged work to investigate the possibility of making hybrid double perovskites. Here we describe the discovery of lead-free hybrid double perovskites with the chemical formula: $(MA)_2M^IM^{III}X_6$. In particular the work produced the first hybrid double perovskite–$(MA)_2KBiCl_6$[16]. Then density functional theory was used to understand its structure-property relationships and subsequently the first direct band gap compound $(MA)_2TlBiBr_6$ was made[26]. The investigation further synthesised the first environmental friendly hybrid double perovskite–$(MA)_2AgBiBr_6$ using the seed crystal method[27], and, finally, to demonstrate the structural diversity of the hybrid double perovskite family, the first two rare-earth hybrid double perovskites–$(MA)_2KYCl_6$ and $(MA)_2KGdCl_6$ were produced[29].

4.2 Methodology

This work is accompanied by experimental synthesis and characterizations mostly performed by Dr. Fengxia Wei. I contributed DFT calculations to all the studies described here. However, I did carry out the experiments on the rare-earth hybrid double perovskites. Therefore, most of the experimental methodologies are not described here except concerning the rare-earth hybrid double perovskites. Later on in this chapter where the results are described, credit is given to Dr. Wei and co-workers when appropriate.

All of the DFT calculations were performed using the Vienna Ab Initio Simulation Package (VASP)[242, 243]. Projector-augmented wave (PAW)[216, 217] pseudopentials were used with the following valence electrons for each ion treated explicitly: H ($1s^1$), C ($2s^22p^2$), N ($2s^22p^3$), K ($3s^23p^64s^1$), Bi ($5d^{10}6s^26p^3$), Tl ($5d^{10}6s^26p^1$), Cu ($3p^63d^{10}4s^1$), Ag ($4p^64d^{10}5s^1$), Pb ($5d^{10}6s^26p^2$), Gd ($4f^75s^25p^65d^16s^2$), Y ($4s^24p^64d^15s^2$), Cl ($3s^23p^5$), Br ($4s^24p^5$) and I ($5s^25p^5$). The non-local van der Waals functional (vdW-DF) was used[113, 207, 208], with the exchange energy calculated using the optimised optB86b generalised gradient approximation (GGA) functional. The correlation energy was obtained from the local density approximation (LDA) and the nonlocal correlation energy calculated from double space integration. All structures were visualized using VESTA[244] program.

For the calculations on $(MA)_2KBiCl_6$ and DFT chemical screening of $(MA)_2B^IB^{III}X_6$, a 500 eV E_{cut} was used for all the calculations (B^I = K, Cu, Ag and Tl; B^{III} = Bi; X = Cl, Br and I; 12 compounds in total). For geometry optimisation a $4 \times 4 \times 2$ Monkhorst-Pack[211] k-point mesh was employed, while for the electronic density of states (DOS) calculations a finer $8 \times 8 \times 3$ mesh was used. The ions were relaxed until the forces on them were less

than 0.01 eV Å^{-1}. Relativistic spin-orbit coupling (SOC) was included in the DOS and band structure calculations. As for the computational screening, since $(MA)_2KBiCl_6$ is observed to crystallise in the $R\bar{3}m$ space group, the same symmetry was applied to all the calculated structures initially and during geometry optimization. This allows for direct comparison with the experiments and enables trends in behavior to be studied. In addition to the group of 12 double hybrid perovskites listed above, a further 3 structures of the form $MAPbX_3$ with $B^I = B^{III}$ = Pb were computed as a reference set. Following equilibration, the atomic and electronic structures of each perovskite were analysed with particular focus on the effect of ionic radius on the band gap and the mechanical stability of the structures.

For the study on $(MA)_2AgBiBr_6$, the calculations began by taking the primitive cell of the experimental structure and orienting the MA^+ ions so that pairs of symmetry equivalent C-N bonds pointed along opposing [111]-type directions. This orientation was chosen because it is analogous to that found in rhombohedral $(MA)_2KBiCl_6$ where the C-N bonds point along the c-direction[16]. However tests have shown that orientating the MA^+ ion along [100]-type directions does not have a significant effect on the resulting band structure near the band edges. Following this, the experimental lattice constants and inorganic framework were fixed so that no octahedral tilting was allowed and a standard geometry optimisation performed until the interatomic forces on the MA^+ ions were less than 0.01 eV/Å. This structure was then used to perform all the electronic structure calculations which included relativistic spin-orbit coupling (SOC). A 500 eV plane wave kinetic energy cutoff was used. For Brillouin zone sampling, $4 \times 4 \times 4$ and $6 \times 6 \times 6$ Γ-centered Monkhorst-Pack meshes[211] were used for geometry optimisation and the density of states calculations respectively.

For the study on $(MA)_2KYCl_6$ and $(MA)_2KGdCl_6$, a 500 eV plane-wave kinetic energy cutoff and a Monkhorst-Pack k-point mesh[211] were employed for all calculations. The ground state structures of $(MA)_2KYCl_6$ and $(MA)_2KGdCl_6$ were obtained starting from the primitive unit cell reported previously[16] for $(MA)_2KBiCl_6$ with Bi substituted by Y or Gd, and the structures relaxed until the interatomic forces were less than 0.001 eV/Å. The band structures and the densities of states (DOS) of the relaxed structures were obtained with the inclusion of relativistic spin-orbital coupling (SOC)[166] in the hexagonal structural setting, and for $(MA)_2KGdCl_6$, the Gd $4f$ electrons were treated with +U method,[245] taking U = 8 eV for the Hubbard term. The following high symmetry points in the first Brillouin zone were used for band structure calculation: (0, 0, 0), A (0, 0, 0.5), H (-0.333, 0.667, 0.5), K (-0.333, 0.667, 0), M (0, 0.5, 0) and L (0, 0.5, 0.5). The mechanical response of the two HHDPs was evaluated by calculating the single crystal stiffness constants and the corresponding polycrystalline values of the Young's, bulk and shear moduli together with

Poisson's ratio. The stiffness constants were calculated from the strain-stress relationship by applying two different types of strain, e_1 and $e_3 + e_4$, with magnitudes of 0%, $\pm$ 0.5% and $\pm$ 1%[26]. Energetic stabilities were probed by calculating the decomposition enthalpy, ΔH_d, and formation enthalpy, ΔH_f, defined by:

$$\Delta H_d = 2E[(MA)Cl] + E[KCl] + E[MCl_3] - E[(MA)_2KMCl_6]$$

and

$$\Delta H_f = E[(MA)_2KMCl_6] - 6E[H_2] - E[N_2] - 2E[C] - E[K] - E[M] - 3E[Cl_2]$$

where E represents the total energy per formula unit. For ΔH_f, the following standard phases were used: H (hydrogen gas), N (nitrogen gas), C (graphite), M (Gd, Y and Bi hcp or rhombohedral metals) and Cl (chlorine gas), and all gas phases are simulated by relaxing a dimer in a $15 \times 15 \times 15$ Å^3 computational cell.

For the experimental study on the rare-earth hybrid double perovskites, a solution evaporation method was used to prepare crystals of $(MA)_2KYCl_6$ and $(MA)_2KGdCl_6$, both of which were colourless and transparent. The materials were synthesized by dissolving Y_2O_3 / Gd_2O_3 (1 mmol), KCl (1 mmol) and (MA)Cl (2 mmol) in 2 mL HCl solution (32 wt%) and placing the solution in a capped glass vial on a hot plate at 80 °C. The solution was stirred for 1 hour at 80 °C until it became clear and colourless. The cap was then opened and the solution was evaporated until dry at 85 °C. Crystals suitable for single crystal X-ray diffraction (SCXRD) were chosen from the dried sample. Some secondary phases ($YCl_3 \cdot 6H_2O$, $GdCl_3 \cdot 6H_2O$ and KCl) were obtained using this method. Other synthesis methods were therefore tried, including vapor diffusion, slow cooling of the oversaturated solution, hydrothermal and solid-state reactions, but only the procedure described above was successful. Unfortunately, this prevented us from obtaining phase-pure bulk samples that could be used for magnetic and optical characterization. Variable temperature single crystal X-ray diffraction (VT-SCXRD) measurements were conducted on the two materials from 300 K in intervals of 30 K up to 450 K. Suitable crystals were selected and mounted using Paratone-N on an Xcalibur/Gemini Ultra diffractometer with an Eos CCD area detector. The structures were solved by direct methods using Olex2[234] with the ShelXS[232] structure solution program and refined with the ShelXL[233] refinement package using least squares minimization. For the high temperature cubic structures, the positions of the H, C and N atoms were not refined due to the limited ability of X-ray diffraction to detect light elements in the presence of heavy elements such as Gd and Y.

4.3 Discovery of $(MA)_2KBiCl_6$

4.3.1 Crystal Structure

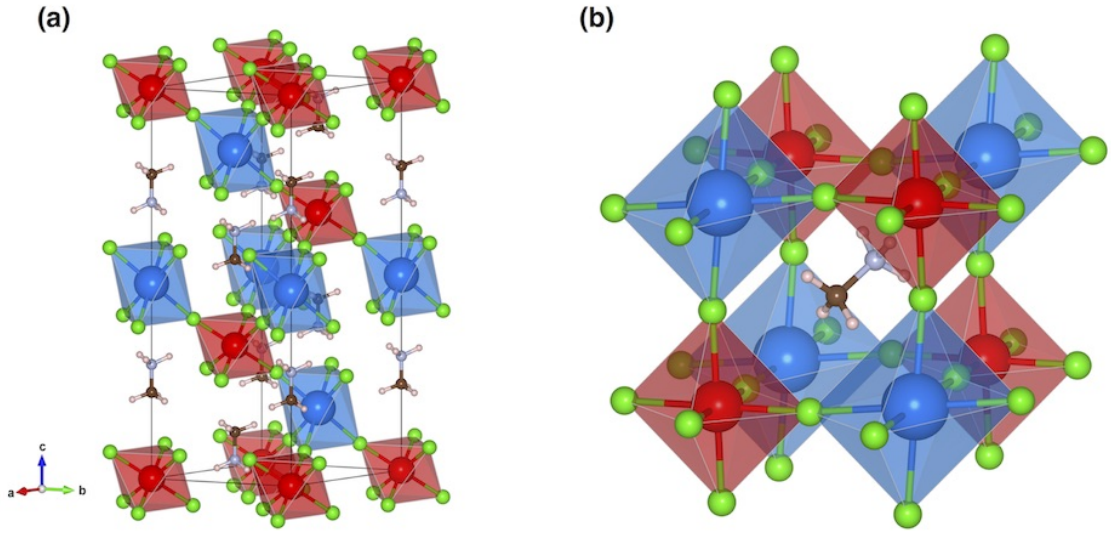

Fig. 4.1 Crystal structure of hybrid double perovskites $(MA)_2B^IB^{III}X_6$ using (a) hexagonal and (b) cubic setting. Following color scheme is used: B^I (blue), B^{III} (red), H (white), C (brown), N (purple) and X (green). Reproduced from Wei et al.[16] with permission from The Royal Society of Chemistry.

X-ray measurements by Wei and coworkers showed that $(MA)_2KBiCl_6$ crystallises in $R\bar{3}m$ symmetry, with lattice parameters a = 7.8372(2) Å and c = 20.9938(7) Å. Alternating KCl_6 and $BiCl_6$ octahedra share corners to form an ReO_3-like framework and the MA cations occupy the A-site cavities to complete the double perovskite structure. It is estimated that $(MA)_2KBiCl_6$ has a tolerance factor of 0.93, which is well within the range (0.80–1.0) where the perovskite structure can be expected to form[132]. Due to the obvious size difference between the radii of K^+ (1.38 Å) and Bi^{3+} (1.03 Å)[38], the 3D network is distorted from the cubic stacking that is seen in caesium-based Na/Bi and Ag/Bi double perovskites. The KCl_6 octahedra are slightly distorted with K–Cl bond lengths of 3.049(2) Å and two octahedral bond angles of 81.67(9)° and 98.33(9)°, while the $BiCl_6$ octahedra are more regular in shape with Bi-Cl distances of 2.681(2) Å and bond angles of 91.76(10)° and 88.24(10)° (Tables A.2 and A.3). The bridging angle between the KCl_6 and $BiCl_6$ octahedra is slightly bent with a K–Cl–Bi angle of 173.04(12)°. The structure is less tilted than the low-temperature

orthorhombic form of $MAPbCl_3$, where the Pb–Cl–Pb bond angles range from 154.88(11) to 169.46(4)°[246].

The MA cations in the perovskite A-site are aligned along the c direction (Fig. 4.1 a) and alternate; symmetry-equivalent MA cations adopt opposite orientations (C–N···N–C) and have C–N bond lengths of 1.35(3) Å. The X-ray measurements are unable to locate the hydrogen atoms, so we cannot be sure whether the MA cations are ordered (which is allowed in space group $R\bar{3}m$), or disordered. However, hydrogen bonding is implied between the amine and the chloride anion since the N···Cl distance (3.406(1) Å) is shorter than the C···Cl one (3.848(2) Å). The corresponding distances for N···Cl in orthorhombic $MAPbCl_3$ are 3.273(2) Å, 3.346(2) Å, 3.366(10) Å and 3.421(2) Å[246], suggesting that hydrogen bonding is important for both structures. Strong anisotropic atomic displacement parameters for the Cl anions indicate a possible rotational/tilting feature for the octahedra, which may be associated with MA cation disorder.

DFT geometry optimisation in $R\bar{3}m$ results in lattice parameters of a = 7.8165 Å and c = 20.9904 Å, which agree well with the single crystal XRD measurements. The DFT methods were used to predict the locations of the hydrogen atoms which could not be determined using X-rays (though they could in principle be obtained using neutron diffraction[108]). Note that since the space group could be consistent with both ordered or disordered hydrogen positions, the calculations do not establish whether the system is ordered at room temperature. Tables A.1, A.2 and A.3 compare the fractional atomic coordinates, bond lengths and bond angles obtained from the calculations with those from the X-ray measurements; again it is seen that the agreement is very good. The maximum deviation is in the C–N bond distance (1.492 Å vs. 1.35(3) Å), which is a possible indication of MA disorder in the experimental structure.

4.3.2 Electronic Structure

The optical bandgap was estimated by Wei and co-workers using UV-visible spectrometry. The reflectance spectrum shows two edges and values of 3.04 eV and 3.37 eV were obtained for the apparent optical bandgaps from the corresponding Tauc plot. Fig. 4.2 shows the DFT calculated band structure of $(MA)_2KBiCl_6$, which predicts an indirect band gap of 3.02 eV, in good agreement with our optical measurements (3.04 eV). It is postulated that such good agreement is probably due to the weaker spin–orbit coupling effect on K. Note that a direct transition would also be possible at 3.15 eV, which is consistent with the experimental feature at 3.37 eV (see above). The corresponding total and partial electronic density of states (Fig.

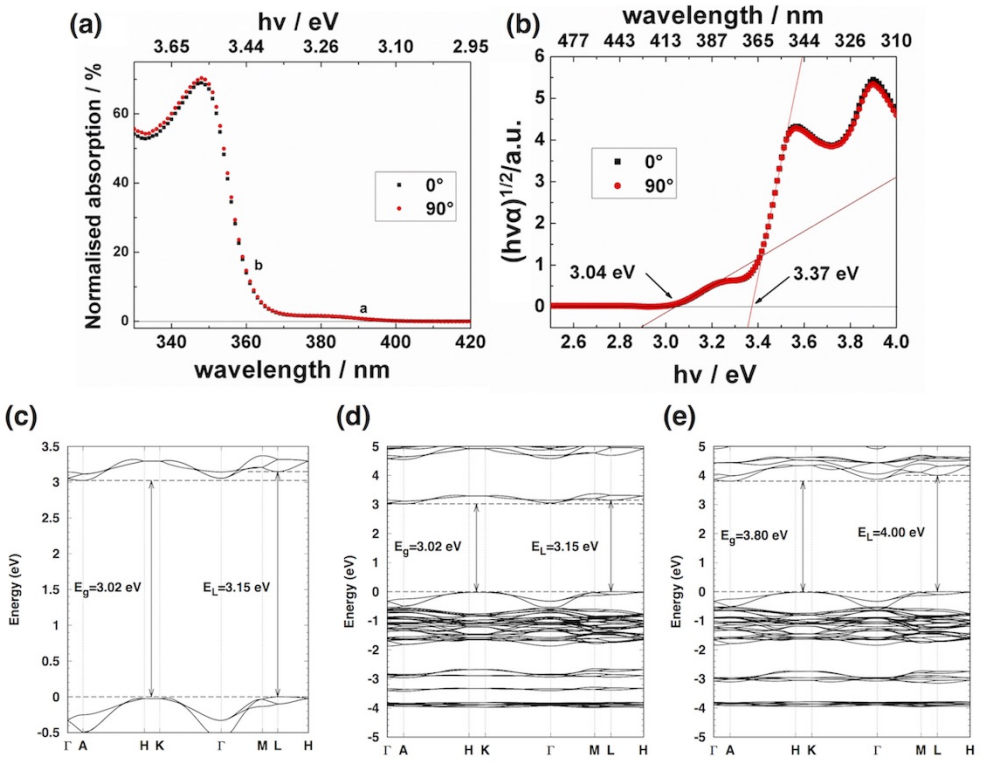

Fig. 4.2 (a) Normalised absorption spectra converted from reflectance data and (b) the Tauc plot (assumed indirect bandgap). (c) Enlarged view of the calculated band structure near the band gap. Comparison of the band structure of $(MA)_2KBiCl_6$ (d) with and (e) without considering spin-orbit coupling (SOC). Band gap drops around 0.78 eV compared with 1.08 eV for $MAPbI_3$ in previous study[19]. The following high symmetry points in the first Brillouin zone were used: Γ(0,0,0), A (0,0,0.5), H (-0.333,0.667,0.5), K (-0.333,0.667,0), M (0,0.5,0) and L (0,0.5,0.5). The band edges are found at L in the valence band and A in the conduction band. Reproduced from Wei et al.[16] with permission from The Royal Society of Chemistry.

4.3 a) reveal that MA does not contribute to states near the valence band maximum (VBM) or the conduction band minimum (CBM), which is similar to the case for $MAPbI_3$[160]. It is seen that Bi and Cl are the main contributors to states near the band gap. This can be further visualised in real space (Fig. 4.3 b) by calculating the band decomposed partial charge density (PCD). It is seen that the valence band edge is composed of Bi-6s and Cl-3p antibonding states whereas the conduction band edge is composed of Bi-6p, Cl-3p antibonding states together with a small contribution from Cl-3s. However, the energy states of K are low lying; e.g. the K-3p states (not shown in the figure) occur at ∼13 eV below the VBM. This differs from $Cs_2AgBiBr_6$[14] where Ag contributes energy states near the valence band edge.

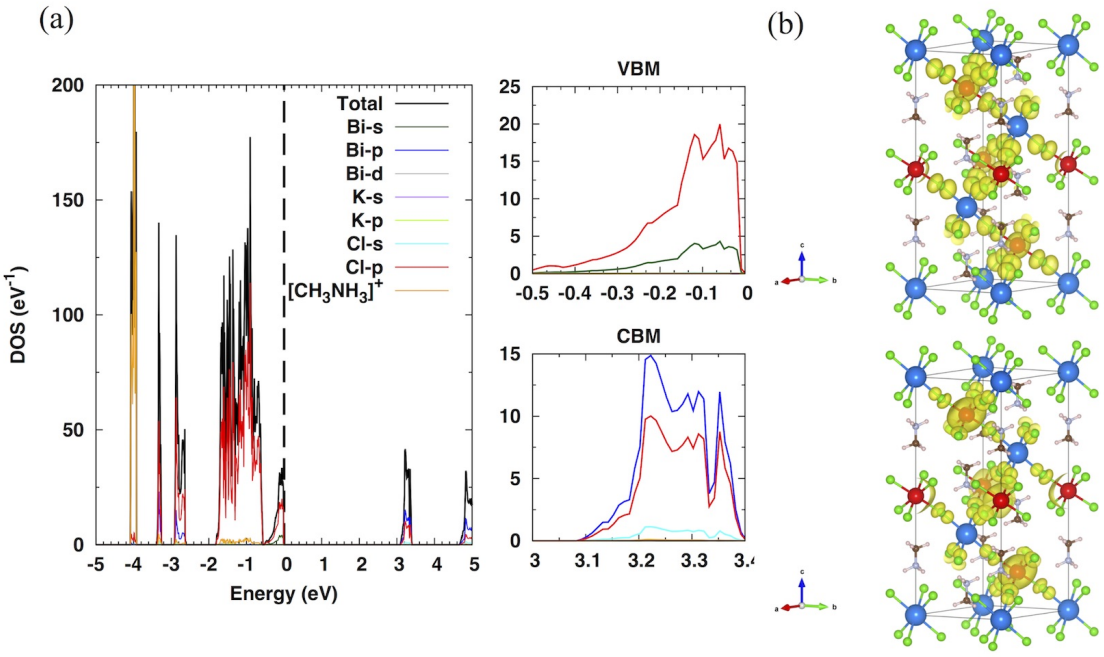

Fig. 4.3 (a) Calculated total and partial density of states of $(MA)_2KBiCl_6$ (b) calculated band decomposed partial charge density (PCD) at the VBM (top) and the CBM (bottom). The electron isosurface level is set at 0.001 eV Å^{-3}. The density clouds are colored yellow and the atoms are: Bi-red, K-blue, Cl-green, C-brown, N-light blue and H-white. Reproduced from Wei et al.[16] with permission from The Royal Society of Chemistry.

4.3.3 Mechanical Properties

Nanoindentation was carried out by Wei and co-workers normal to the (001) plane of the single crystals. The Young's modulus was found to be 10.50 ± 1.18 GPa and the hardness 0.39 ± 0.07 GPa, averaging the results from an indentation depth of 200 nm to 900 nm. In comparison with the experimental mechanical properties of the lead-based perovskites, the Young's modulus of $(MA)_2KBiCl_6$ is comparable with that of $MAPbI_3$ (E≈11 GPa) and lower than that of $MAPbCl_3$ (E≈17–20 GPa)[28]. Since the crystal structures of $MAPbCl_3$ and $(MA)_2KBiCl_6$ adopt the same topology and differ only in terms of the B-site cations, the greater compliance of $(MA)_2KBiCl_6$ can be attributed to the weaker K–Cl bonding in comparison with that of Pb–Cl. Similar mechanical behaviour has been observed in previous work. For example, replacing Zn with alternating Li and B in zeolitic imidazolate frameworks (ZIFs) reduces the elastic modulus from 8–9 GPa for $Zn(Im)_2$ to ∼3 GPa for $LiB(Im)_4$[247].

Single crystal stiffness constants (C_{ij}) were calculated from the stress–strain relationship by applying 2 types of strain: e_1 and $e_3 + e_4$ to the cell (each strain with 0.5% and 1%

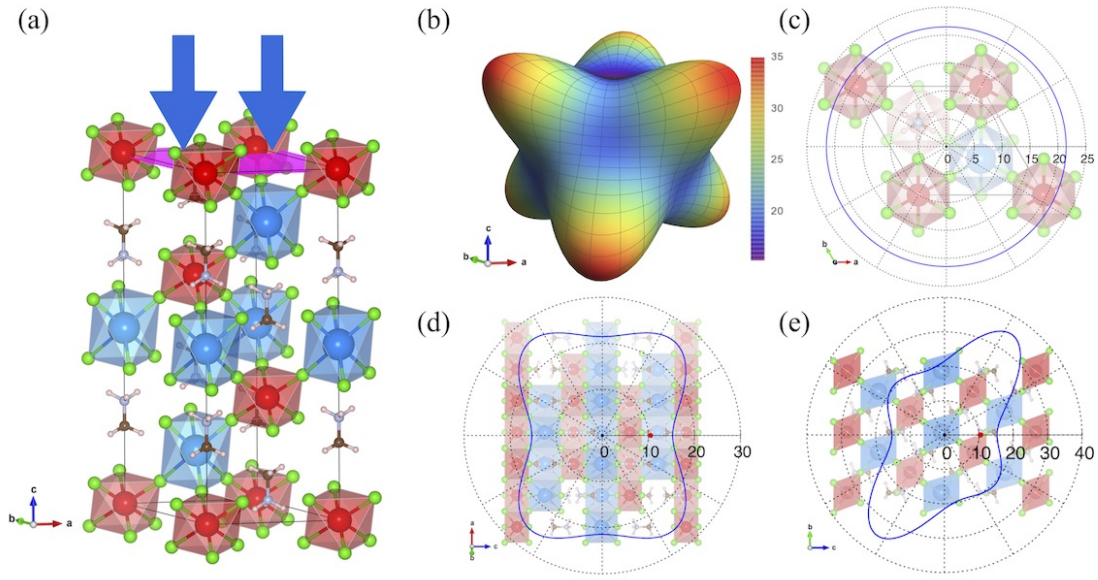

Fig. 4.4 (a) Nanoindentation plane (purple) and direction (blue arrow) (b) Calculated 3D directional Young's modulus of $(MA)_2KBiCl_6$ and its contour plot on (c) (001) plane (d) (010) plane and (e) the plane perpendicular to [100]. Nano-indentation Young's modulus is shown as a red dot in (d) and (e) along c-axis compared with DFT results (blue curve). Units shown are in GPa. Reproduced from Wei et al.[16] with permission from The Royal Society of Chemistry.

deformation) and relaxing the internal degrees of freedom[248]. A tensorial analysis[249] of the stiffness constants reveals the whole elastic anisotropy of $(MA)_2KBiCl_6$ (Table A.11). In order to better understand the mechanical properties of $(MA)_2KBiCl_6$, the directional Young's modulus in 3D was calculated and is shown in Fig. 4.4 together with contour sections on three different planes. It is easy to see that the directions along Bi–Cl–K bonds have the largest value of the Young's modulus, which is very similar to $MAPbX_3$ (X = Cl, Br and I)[176]. The calculations predict a Young's modulus of 15.28 GPa normal to the (001) facet, which is in reasonable agreement with the experimental nanoindentation results.

4.4 DFT Chemical Screening of $(MA)_2B^IB^{III}X_6$

Motivated by our discovery of $(MA)_2KBiCl_6$, we then performed an in-depth computational screening study on lead-free hybrid double perovskites as potential photovoltaic absorbers. In particular, we applied density function theory (DFT) calculations to study the series of hybrid double perovskites $(MA)_2B^IB^{III}X_6$ with B^I = K, Tl, Ag, Cu and B^{III} = Bi, X = Cl, Br

and I (Fig. 4.1). Based on the calculations, we found another new hybrid double perovskite, $(MA)_2TlBiBr_6$, with a much narrower band-gap than $(MA)_2KBiCl_6$.

4.4.1 Structural Properties

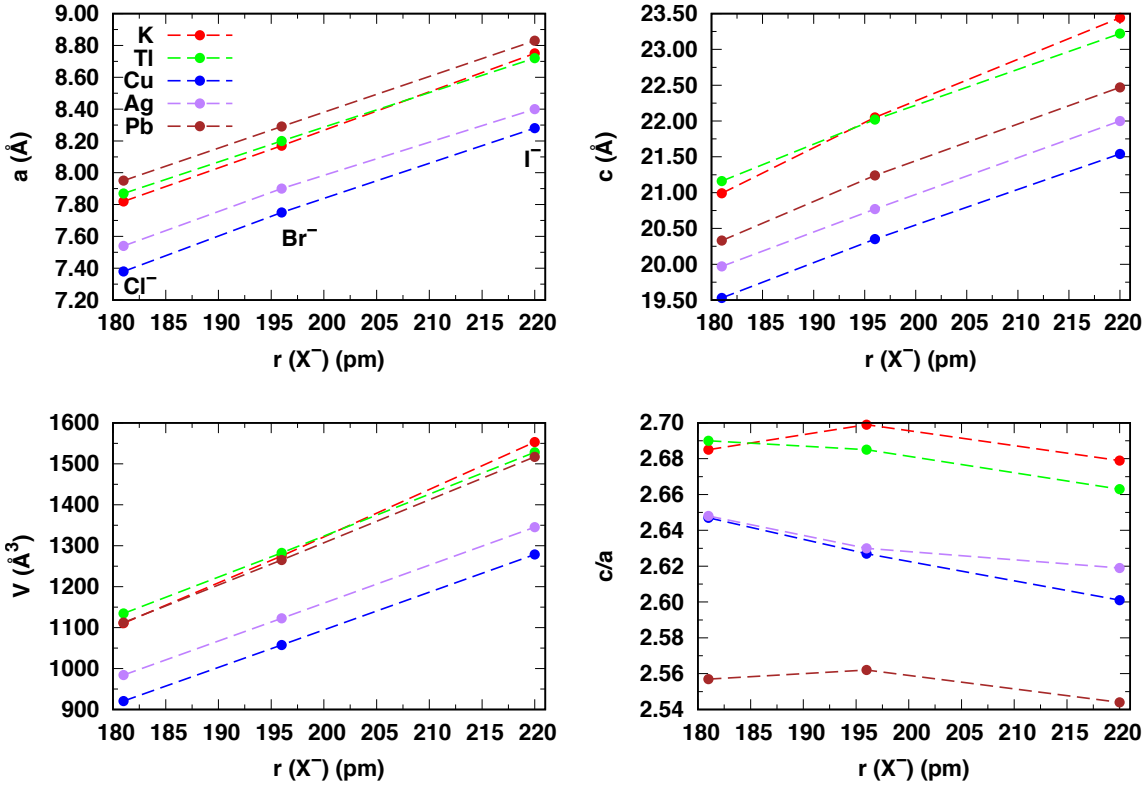

Fig. 4.5 Computed lattice constants a (a), c (b), equilibrium volume (c) and c/a ratio (d) of $(MA)_2B^IB^{III}X_6$ as a function of X anion radius, including the $MAPbX_3$ reference structures. Reproduced from Deng et al.[26] with permission from The Royal Society of Chemistry.

The computed lattice constants (referred to hexagonal axes), equilibrium volumes and c/a ratios of the 15 structures as a function of the X anion radii are given in Table A.4 and displayed in Fig. 4.5. It is seen that the first two quantities increase with increasing anion radius as expected (r_{Cl} = 180 pm, r_{Br} = 196 pm and r_I = 220 pm)[38]. The almost constant variation in c/a ratio indicates that the lattice expansion is approximately isotropic. The various interatomic bond distances (e.g. B^I-X, N$\cdots$X and C$\cdots$X) as a function of the X radii are given in Table A.5 and Fig. A.1 and again show an increasing trend with anion radius. Furthermore as the effective radius of the B^I cation increases, the bond distances also generally increase for each halide (r_{Cu} = 77 pm, r_{Ag} = 115 pm, r_K = 138 pm and r_{Tl} = 150

pm)[38]. Each of these results is consistent with expectations based on the relative sizes of the ions. Hydrogen bonding contributes to the stability of each structure and it can be seen from Fig. A.1 that X···H bond distances, for example, increase as the X anion becomes less electronegative, indicating a weakening of the H-bonds. The various bond angles (e.g. B^I-X-B^{III}, X-B^{III}-X and C-H···X) as a function of the X radii are given in Table A.6 and Fig. A.2 and do not show a strong variation with anion radius. In addition the angles do not deviate much from those expected for the ideal geometry, e.g. 180° for B^I-X-B^{III}, indicating that tilting of the B^IX_6 and $B^{III}X_6$ octahedra is relatively small. For example, ∠Pb-I-Pb is 177.5° in $MAPbI_3$ whereas in orthorhombic $MAPbI_3$, which known to exhibit significant tilting, the equivalent computed angle is 145°[129].

4.4.2 Electronic Properties

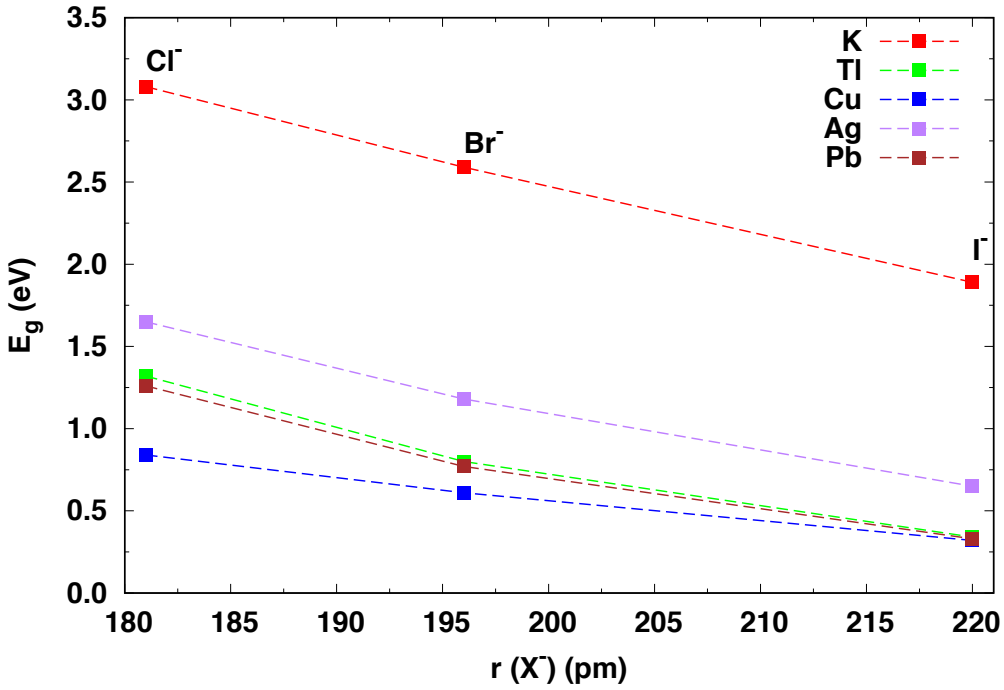

Fig. 4.6 Computed band gaps of $(MA)_2B^IB^{III}X_6$ as a function of X anion radius, including the $MAPbX_3$ reference structures. Reproduced from Deng et al.[26] with permission from The Royal Society of Chemistry.

Fig. 4.6 and Table A.7 give the calculated band gaps of the 15 structures as a function of the X anion radii where it is seen that the gap decreases by up to 1 eV as the radii increase. Furthermore the B^I cation can significantly lower the band gap for a given halide. In all

cases the largest gap is found when B^I = K (3.02 eV for $(MA)_2KBiCl_6$) and the smallest gap when B^I = Cu (0.28 eV for $(MA)_2CuBiI_6$). The calculated gaps for the $MAPbX_3$ reference structures are close to previous calculations on their cubic counterparts[166].

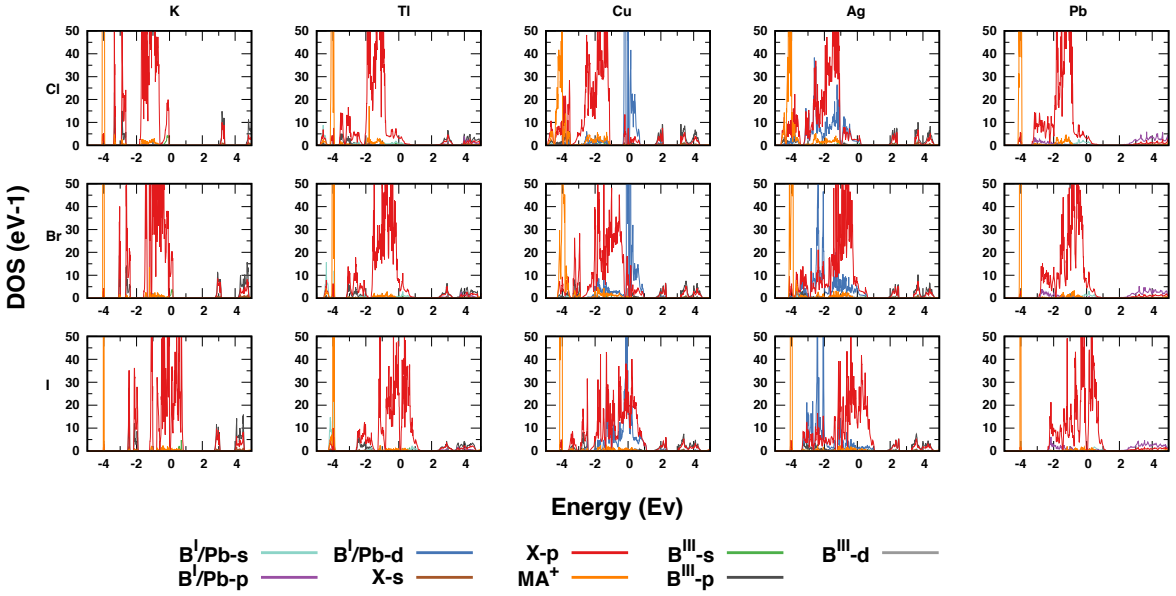

Fig. 4.7 PDOS of hybrid double perovskites $(MA)_2B^IB^{III}X_6$ (B^I=K, Tl, Cu and Ag from the first to the forth column; B^{III}=Bi; X=Cl, Br and I from the first to the last row; $MAPbX_3$ in the last column are shown as comparison). PDOS were aligned with MA^+ states to -4 eV. Adapted from Deng et al.[26] with permission from The Royal Society of Chemistry.

To understand the origin of these effects, the projected density of states (PDOS) are calculated and shown in Fig. 4.7 where attention is paid to the band edges. First, it is seen that the MA cation does not contribute to states at the band edges, in agreement with previous studies on $MAPbI_3$[250]. It is interesting to note that if the MA cation is replaced with Cs in the double perovskites $Cs_2AgBiCl_6$ and $Cs_2AgBiBr_6$, the Cs cation also does not contribute to states near the band edges[14]. Second, X-p states make a large contribution at both the valence band maximum (VBM) and the conduction band minimum (CBM), which indicates that choosing the appropriate halogen, like iodine, is important for obtaining a small band gap semiconducting material. Similarly, appropriate choice of B^I cation is essential because using K, for example, which is strongly ionic, leads to an undesirably large band gap. This is because only X-p, Bi-6s and Bi-6p orbitals contribute to the band edge states (Fig. 4.7). However, using Tl, Tl-6s and Tl-6p orbitals also make a contribution, which reduces the band gap (Fig. 4.7). This is similar to the situation in $MAPbX_3$ where Pb-6s and Pb-6p orbitals are present near the band edges (Fig. 4.7). Incorporating Cu onto the B^I site further reduces the band gap due the presence of Cu-3d orbitals near the VBM (Fig. 4.7).

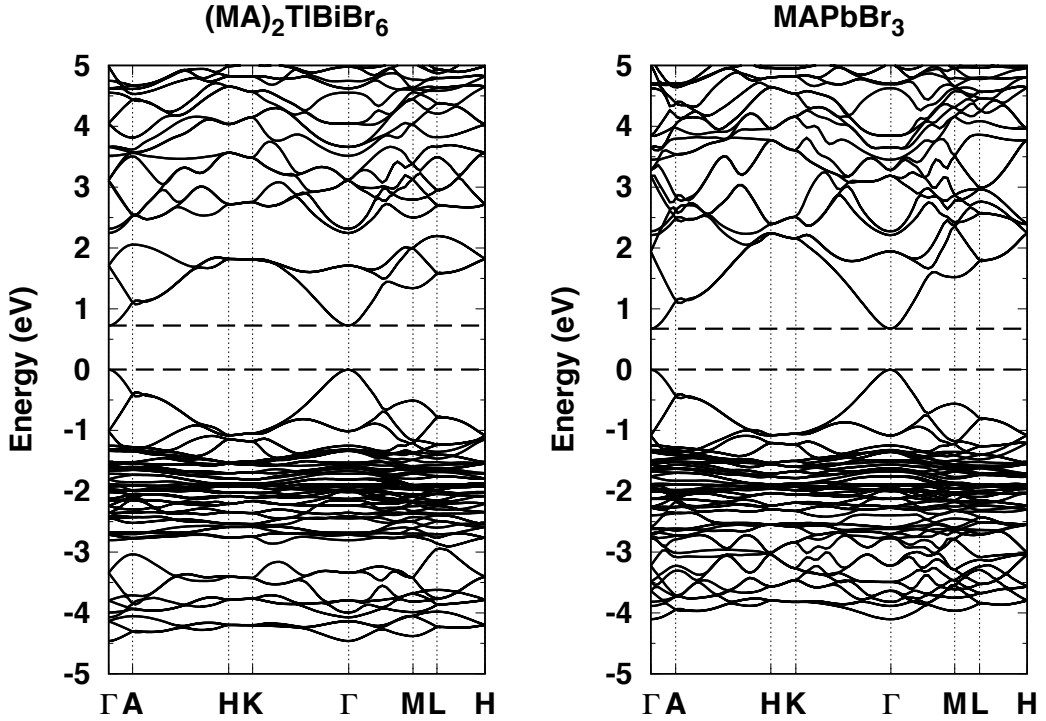

Fig. 4.8 Computed electronic band structures of $(MA)_2TlBiBr_6$ and $MAPbBr_3$. Reproduced from Deng et al.[26] with permission from The Royal Society of Chemistry.

The electronic band structures of the 15 perovskites are collected in Fig. A.3. The band shapes near the band edges, which determine the carrier effective masses, fluctuate more with respect to the X anion than with respect to the B^I cation. B^I = K produces the flattest bands while B^I = Tl or Pb gives the most curved bands. Although all the structures contain the MA cation, their band gaps and carrier effective masses differ widely. The location of the VBM and CBM within the Brillouin Zone depend mostly on the B^I cation, except for K, and are largely independent of the X anion, as shown in Table A.8. When B^I = Tl the band gap is direct but when B^I = Cu or Ag it is indirect which is due to the large density 3d states near the VBM of the latter. It is seen that the band structures of $(MA)_2CuBiX_6$ and $(MA)_2AgBiX_6$ are quite similar due to their similar electronic configurations. Furthermore, because $(MA)_2TlBiX_6$ and $MAPbX_3$ are isoelectronic, their band structures are also very similar as illustrated in Fig. 4.8 above for X = Br.

4.4.3 Mechanical Properties

The mechanical stability of the hybrid double perovskites considered here is important if they are to be used for real world device applications. Tables A.10 and A.11 give the calculated

single crystal stiffness constants C_{ij} of the 15 structures and the corresponding polycrystalline values of Young's modulus (E), bulk modulus (B), shear modulus (G) and Poisson's ratio (ν). $(MA)_2AgBiCl_6$, $(MA)_2AgBiBr_6$, $(MA)_2CuBiCl_6$ and $(MA)_2CuBiBr_6$ are found to be unstable when 1% strain is applied due a rotation of the MA cation making the stress-strain relationship nonlinear. Therefore, the stiffness constants were obtained using only 0.5% strains but even then negative eigenvalues of the stiffness matrix indicate that $(MA)_2CuBiCl_6$ and $(MA)_2CuBiBr_6$ remain unstable[251].

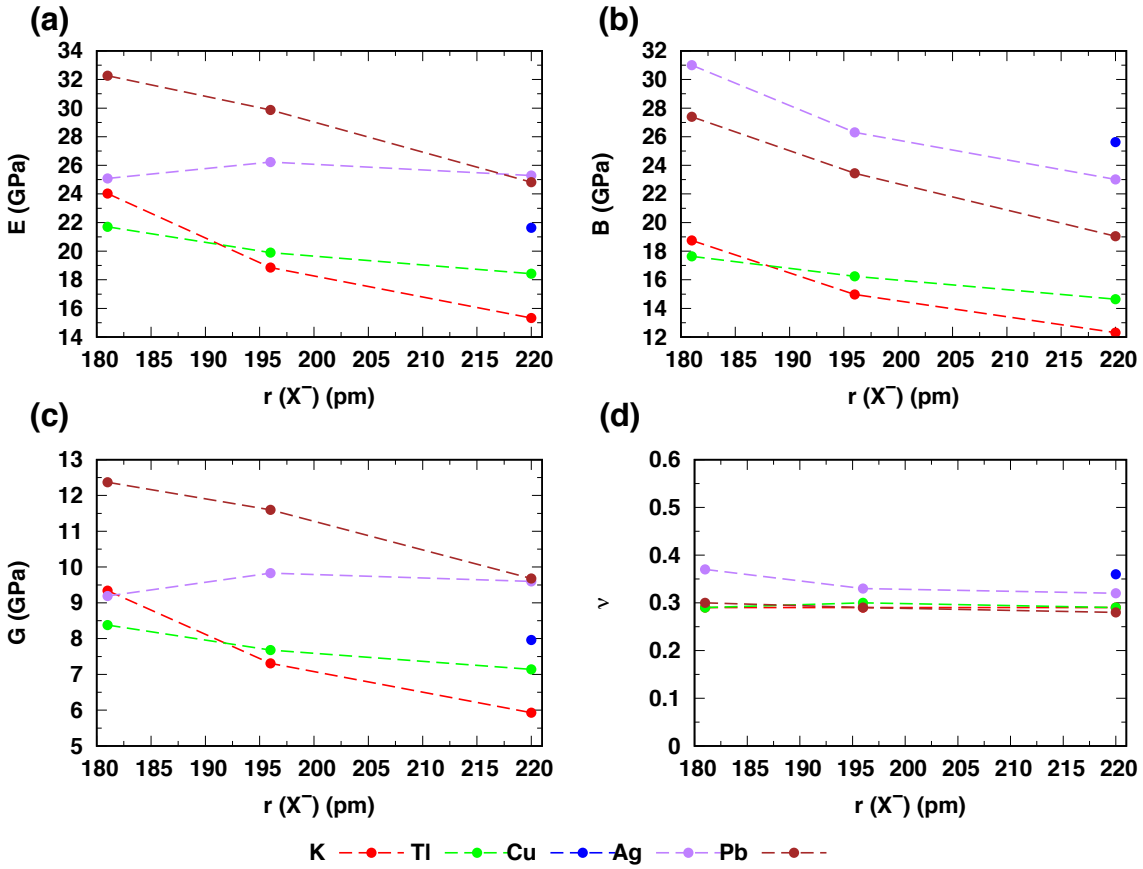

Fig. 4.9 Polycrystalline values of (a) Young's modulus E, (b) bulk modulus B, (c) shear modulus G and (d) Poisson's ratio ν of $(MA)_2B^IB^{III}X_6$ as a function of the X anion radius. Reproduced from Deng et al.[26] with permission from The Royal Society of Chemistry.

Fig. 4.9 show the polycrystalline elastic constants as a function of X anion radius which show that E, B and G decrease with increasing anion radius in agreement with the trend observed from nano-indentation experiments on tetragonal $MAPbX_3$[28]. This can be explained by a decrease in the strength of the X$\cdots$H and B-X bonds as the anion radius increases. However, it is found the Young's moduli of the rhombohedral form of $MAPbX_3$

considered here are larger than the experimental results probably because of the imposed symmetry constraints. The Poisson's ratio is largely independent of X anion radius.

The directional dependence of the single crystal Young's modulus of $(MA)_2KBiX_6$, $(MA)_2TlBiX_6$, $(MA)_2AgBiX_6$ and $MAPbX_3$ is shown in Fig. A.4-A.7. For the first two structures and $MAPbX_3$, the maximum and minimum values lie along B-X bond directions and the diagonal of the B-X cage respectively. However, for $(MA)_2AgBiX_6$ (and $(MA)_2CuBiI_6$ not shown) these maxima and minima reverse directions. This can be explained in terms of the incompressibility of the MA cation and the Goldschmidt tolerance factor (see Table A.9)[132]. Previous experimental studies on $MAPbCl_3$ showed that the most rigid component of the structure is the MA cation rather than the $PbCl_6$ octahedra[246]. Also as Fig. A.1 shows, when incorporating different X and B^I ions, most bond lengths change by around 0.3∼0.4 Å whereas the change in C-N bond length is much smaller, less than 0.01 Å. The tolerance factor for $(MA)_2AgBiX_6$ is relatively large, implying that the B^IXB^{III} framework is too small for the MA cation. Therefore, because MA is incompressible and the framework is too small, when applying strains, the intramolecular interactions between MA and the framework either make MA rotate, or compress the C-N, C-H or N-H bonds inducing a large change in stress. The MA rotations result in the nonlinear stress-strain relationship found in the calculations for those structures with large tolerance factors, and the bond compressions make the Young's modulus along C-N, C-H or N-H directions exhibit a maximum. A comparison between $MAPbX_3$ and $(MA)_2TlBiX_6$ shows that the isoelectronic substitution of Pb to Bi+Tl makes the structure less stiff, which is similar to previous studies on ZIFs[247]. This can be explained by comparing the bond strength of Pb-X in $MAPbX_3$ with Bi-X and Tl-X in $(MA)_2TlBiX_6$. Assuming that bond strength and bond distance (d) are directly correlated, Fig. A.1 shows that $d_{Tl-X} > d_{Pb-X} > d_{Bi-X}$, which indicates that Bi-X is stronger than Pb-X and Tl-X. When applying strains, the weaker Tl-X bond results in a more flexible $(MA)_2TlBiX_6$ structure compared with $MAPbX_3$.

4.4.4 Experiments – Discovery of $(MA)_2TlBiBr_6$

Based on the DFT calculations, attempts were made by Wei and co-workers to synthesize all the predicted structures. Despite the success of the previously reported $(MA)_2KBiCl_6$, only one other hybrid double perovskite, $(MA)_2TlBiBr_6$ was obtained ($(MA)_2AgBiBr_6$ was discovered later, see Section 4.5). For the other compositions, although the appropriate starting stoichiometry was applied, the products are either $(MA)_3BiX_6$ (X = Cl) or $(MA)_3Bi_2X_9$

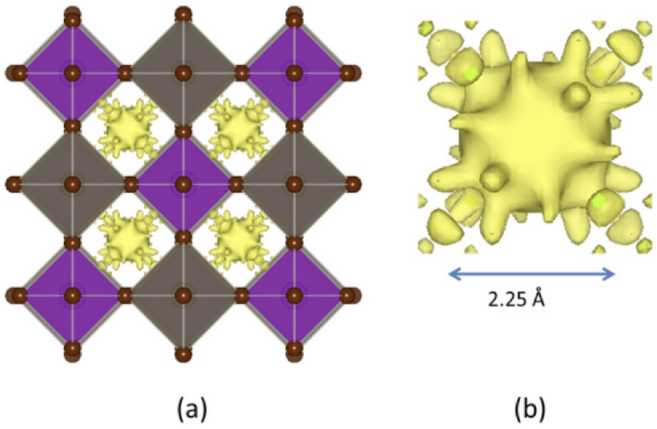

Fig. 4.10 (a) Crystal structure of $(MA)_2TlBiBr_6$ obtained from single crystal X-ray diffraction. $TlBr_6$ and $BiBr_6$ octahedra are grey and purple respectively. The disordered MA cation is shown as yellow electron density in the cavities. (b) MA cation shown as electron density. Both viewed along the c axis. Reproduced from Deng et al.[26] with permission from The Royal Society of Chemistry.

(X= Br, I), which could be because there is either an issue with kinetics during synthesis or maybe $(MA)_3Bi_2X_9$ is the thermodynamically favored phase.

X-ray measurements by Wei and co-workers found that $(MA)_2TlBiBr_6$, crystallizes in the space group $Fm\bar{3}m$ (a = 11.762(2) Å), where Tl and Bi, isoelectronic with Pb, occupy alternating octahedral sites. The MA cations are disordered as shown by the electron density in the cavities in Fig. 4.10, and the size of the electron cluster core (without the branching) is ∼2.25 Å, similar to the size of MA (2.17 Å). Based on the size and the relatively isotropic electron density core, a rotational rather than translational motion of organic cations in the cavity is expected. Structural refinement without MA gives $R_{obs} = 6.31$, with positive and negative residue electron density of -2.65 and 2.29, respectively. The bond length of Bi-Br is 2.778(4) Å and Tl-Br is 3.103(4) Å, which are comparable with the calculated bond lengths of 2.854 Å and 3.145 Å, respectively. And from previously reported cubic $MAPbBr_3$, the Pb-Br bond length is 2.965 Å[107].

Differential scanning calorimetry (DSC) measurements by Wei and coworkers show two possible phase transitions, at approximately −10 °C and −25 °C (Fig. 4.11). Based on the results on the $(MA)_2KBiCl_6$[16], it can reasonably be predicted that one of the low temperature phases would have rhombohedral symmetry. Low temperature single crystal X-ray diffraction, even at −20 °C, indicate heavy twinning, making it very difficult to determine

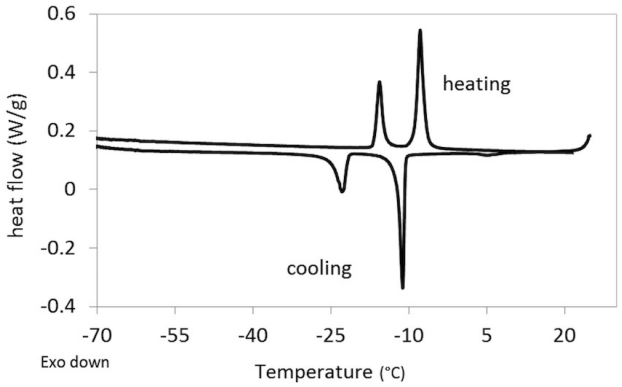

Fig. 4.11 DSC curve for $(MA)_2TlBiBr_6$. Reproduced from Deng et al.[26] with permission from The Royal Society of Chemistry.

the structure. Further studies on the phase transition could be carried out in the future using resonant ultrasound spectroscopy and variable temperature powder X-ray diffraction.

The experimental band gap was measured by Wei and co-workers using optical absorption. By assuming a direct band gap as suggested in the DFT calculation, a Tauc plot was constructed which estimates the optical band gap to be $\sim$2.16eV. This is comparable with that of $MAPbBr_3$ (2.2eV-2.35 eV)[107, 252] and is further consistent with the DFT calculations where the band structures of $(MA)_2TlBiX_6$ shows strong similarities with the corresponding Pb ones. Based on the structural and electronic analysis, $(MA)_2TlBiX_6$ provides an excellent alternative for lead-free perovskites. The DFT calculations, which include SOC, underestimate the band gap (0.72 eV) for this composition, similar to that previously reported for $MAPbI_3$, with 0.60 eV from DFT+SOC compared to 1.55 eV from experiments[19]. However, the toxicity of Tl precludes $(MA)_2TlBiBr_6$ from being a practical alternative to the Pb analogue. Therefore as described in the next section, the nontoxic double perovskite $(MA)_2AgBiBr_6$ was synthesized to solve this problem.

4.5 Discovery of $(MA)_2AgBiBr_6$

The discovery of lead-free hybrid double perovskites provides a viable approach in the search for stable and environmentally benign photovoltaic materials as alternatives to lead-containing systems such as $MAPbX_3$ (X = Cl, Br, or I). Following the work on $(MA)_2KBiCl_6$ and $(MA)_2TlBiBr_6$, a hybrid double perovskite, $(MA)_2AgBiBr_6$, was synthesized by Wei and co-workers and found to have a low band gap of 2.02 eV and is relatively stable and

nontoxic. Its electronic structure, mechanical and optical properties were investigated with a combination of experimental studies and density functional theory calculations.

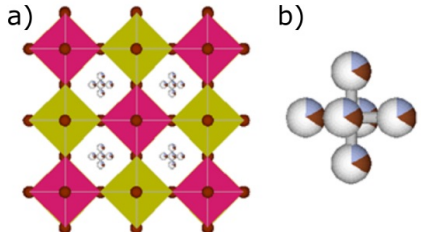

Fig. 4.12 (a) Crystal structure of $(MA)_2AgBiBr_6$, obtained from single-crystal X-ray diffraction. Purple and yellow octahedra represent $BiBr_6$ and $AgBr_6$, respectively. (b) The methylammonium cation was rotated by 5°clockwise around the c axis for better illustration. Partial occupancy is shown as different colors for one sphere. Reprinted with permission from Wei et al.[27]. Copyright (2017) American Chemical Society.

4.5.1 Crystal Structure

Single-crystal X-ray diffraction studies by Wei and co-workers showed that $(MA)_2AgBiBr_6$ crystallizes in the cubic space group $Fm\bar{3}m$ with a lattice parameter a = 11.6370(1) Å. Alternating $AgBr_6$ and $BiBr_6$ octahedra form a 3D framework, resulting in a doubled cell compared to the normal hybrid perovskite (Fig. 4.12). The Ag–Br bond [2.952(2) Å] is slightly longer than the Bi–Br bond [2.868(2) Å]. The orientation of the methylammonium cation, which is disordered in $Fm\bar{3}m$, was determined according to the shape of the electron density. In the final model, the C–N bonds align along the <100> directions, with six possible orientations, each with a probability of 1/6, thus resulting in an apparent octahedron on average.

4.5.2 Chemical Analysis

Chemical analysis was performed by Wei and co-workers on single crystals of $(MA)_2AgBiBr_6$ using energy dispersive spectroscopy (EDS) in a scanning electron microscope (Nova NanoSEM 450) (Fig. A.9 and Table A.12). The spectra were recorded on an inner facet that was carefully cleaved from a large crystal. An average Ag:Bi:Br atomic ratio of 1:1.05:5.3 was obtained, in reasonable agreement with the compound stoichiometry, and no obvious Pb peaks were present. However, the presence of Pb was observed from surfaces of uncleaved crystals that were directly collected from the autoclave without being washed.

4.5.3 Optical and Transport Properties

The optical band gap was estimated by Wei and co-workers from both absorption and diffuse reflectance spectra using UV–visible spectrometry. An absorption cutoff wavelength of ~620 nm was observed (Fig. 4.13a), and the Tauc plot from the reflectance spectrum (Fig. 4.13b), obtained by assuming an indirect band gap, as indicated by our DFT calculations (below), resulted in an E_g of ~2.02 eV. This value is smaller than that of $MAPbBr_3$, which was reported to be 2.2–2.3 eV[107], but is comparable with that of its inorganic analogue, $Cs_2AgBiBr_6$ (1.95–2.19 eV)[14, 13]. This band gap is considered to be narrow enough to exhibit semiconducting properties, but only ionic conductivity [$4.8 \times 10^8 \Omega \cdot cm$] was observed by single-crystal conductivity measurements[253, 254]. This means that its electronic conductivity is probably far lower than the ionic conductivity due to the small number of carriers and/or the low mobility.

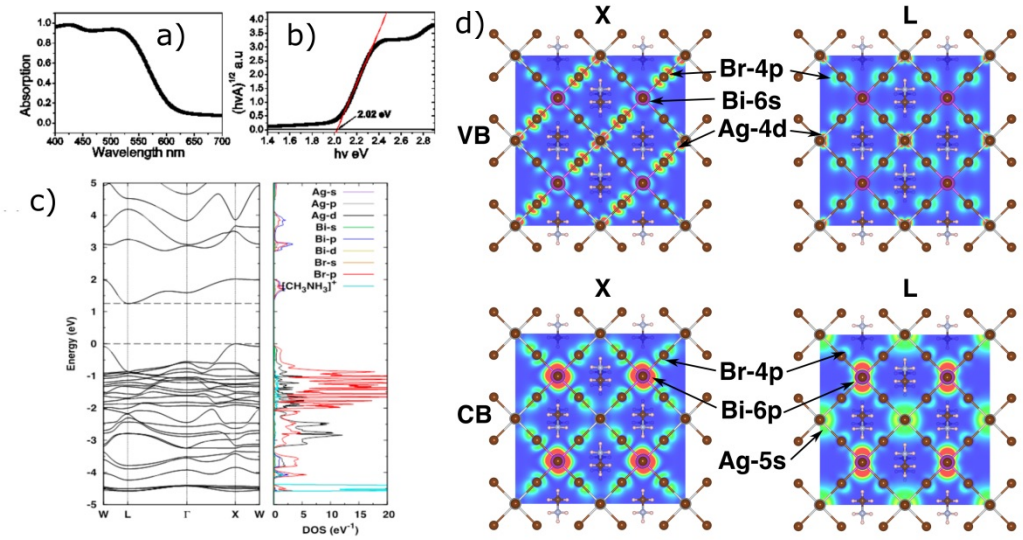

Fig. 4.13 (a) Absorption spectrum and (b) Tauc plot of $(MA)_2AgBiBr_6$. (c) DFT calculated band structure and its projected density of states (PDOS), including the effect of spin-orbit coupling. (d) Partial charge densities visualized in the CB and the VB at points X and L. The following high-symmetry k-points were used for the band structure calculation: Γ (0,0,0), X (0.5,0,0.5), W (0.5,0.25,0.75), and L (0.5,0.5,0.5). Within the inorganic framework, the Ag, Bi, and Br atoms are colored silver, purple, and brown, respectively. The charge density levels vary between 0 (blue) and 0.005 $e/bohr^3$ (red). Reprinted with permission from Wei et al.[27]. Copyright (2017) American Chemical Society.

4.5.4 DFT Calculations

Fig. 4.13c shows the electronic band structure with the projected density of states (PDOS) of $(MA)_2AgBiBr_6$. The atomic structure used for the calculations is described in the Appendix 1 and is based on the X-ray diffraction data. The band structure shows an indirect band gap ($X \rightarrow L$) of 1.25 eV and is similar to our previous DFT results for which we used a rhombohedral structural model (1.11 eV)[26]. However, we acknowledge that in both cases DFT (with spin-orbit coupling) will underestimate the band gap significantly compared with experimental results. As shown by the PDOS, the valence band maximum (VBM) has contributions from Ag 4d, Bi 6s, and Br 4p states, whereas the conduction band minimum (CBM) contains mostly Ag 5s, Bi 6p, and Br 4p states. The charge densities of the VBM (X in VB) and the CBM (L in CB) are visualized in Fig. 4.13d. In comparison with the corresponding lead compound, $MAPbBr_3$, the Ag 4d states lead to an indirect band gap at the band edges for $(MA)_2AgBiBr_6$. As shown in Fig. 4.13d, the X point in the VB is dominated by Bi 6s–Br 4p and Ag 4d–Br 4p antibonding states, whereas the L point in the VB consists mostly of Ag 4d–Br 4p antibonding states with a small contribution from Bi 6p–Br 4p bonding states. For the CB, the X point consists of Bi 6p–Br 4p antibonding states and Ag 4p–Br 4s bonding states, while the L point has contributions from Bi 6p–Br 4p antibonding states. These specific orbital interactions result in the X and L points having the highest and lowest energies in the VB and CB, respectively, thus forming the indirect band gap. Similar orbital interactions were found in our previous computational study of Pb-free hybrid double perovskites and used to explain and compare the nature of the band gap in $(MA)_2AgBiI_6$ and $(MA)_2TlBiI_6$[26].

The effect of the MA cations on the band edge is not significant (Fig. 4.14 compares the band structure with that of the $[AgBiBr_6]^{2-}$ inorganic framework in which the MA cations are replaced by background charges), because they do not contribute to the energy states at the band edges. However, substituting MA^+ with Cs^+ lowers the band gap by $\sim$0.25 eV. This is to be expected as computationally the inorganic framework is held fixed and the ionic radius of the Cs ion is smaller than that of the MA ion[255]. Experimentally, it is not clear whether Cs^+ lowers the band gap because, as noted earlier, values of 1.95 eV[13] and 2.19 eV[14] have been measured for $Cs_2AgBiBr_6$ and these fall on either side of the value determined in this work for $(MA)_2AgBiBr_6$ (2.02 eV). The small difference in the computed band gaps of $Cs_2AgBiBr_6$ and $(MA)_2AgBiBr_6$ has little effect on the band dispersions near the band edges, and as a consequence, the effective masses of the two perovskites are very similar (Fig. 4.14 and Table 4.1). Although some values near X and L are small, implying high

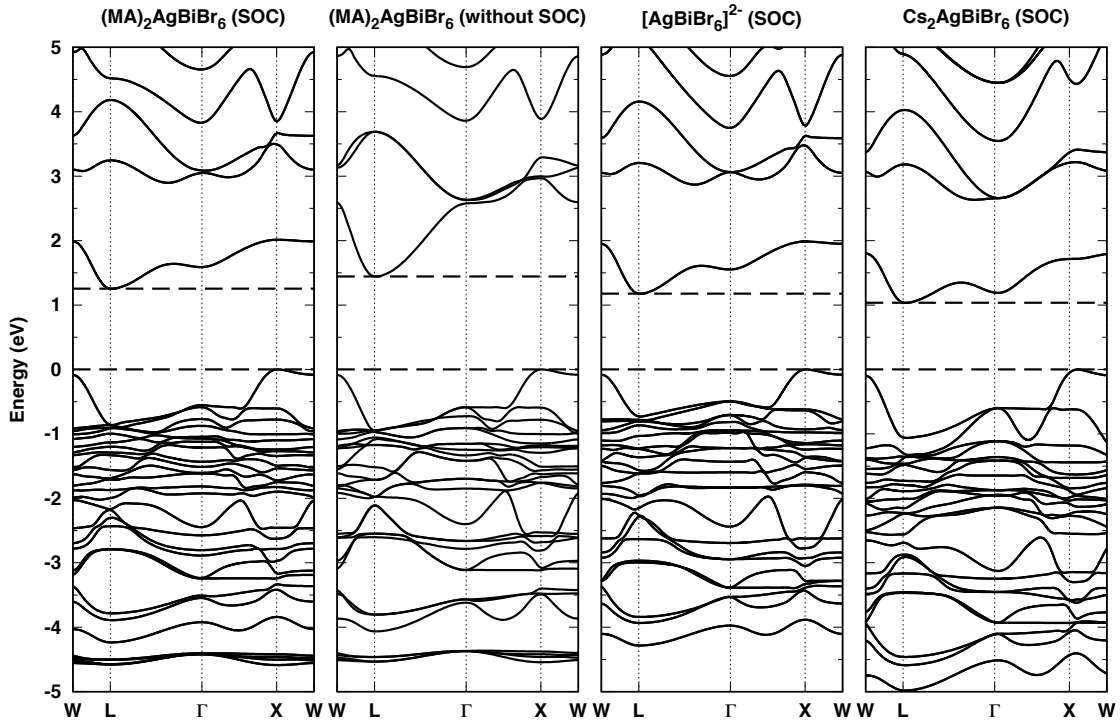

Fig. 4.14 The comparison of DFT calculated electronic band structure of $(MA)_2AgBiBr_6$, $(MA)_2AgBiBr_6$ not including SOC, the $[AgBiBr_6]^{2-}$and $Cs_2AgBiBr_6$. The framework was obtained by replacing the MA^+ inorganic framework of $(MA)_2AgBiBr_6$ cations with background charges and all the calculations used the following high symmetry k-points: Γ (0,0,0), X (0.5,0,0.5), W (0.5,0.25,0.75) and L (0.5,0.5,0.5). Reprinted with permission from Wei et al.[27]. Copyright (2017) American Chemical Society.

Table 4.1 DFT calculated effective masses of $(MA)_2AgBiBr_6$ and $Cs_2AgBiBr_6$ at the band edges. The following high symmetry k-points (in the primitive basis) were used: Γ(0,0,0), X(0.5,0,0.5), W(0.5,0.25,0.75), L(0.5,0.5,0.5), K(0.375,0.375,0.75), U(0.625,0.25,0.625). Reprinted with permission from Wei et al.[27]. Copyright (2017) American Chemical Society.

k-point (path)	$(MA)_2AgBiBr_6$		$Cs_2AgBiBr_6$	
	m_e^*/m_0	m_h^*/m_0	m_e^*/m_0	m_h^*/m_0
X(X-Γ)	-	0.24	-	0.18
X(X-W)	-	0.96	-	0.71
X(X-U)	-	1.37	-	1.37
L(L-W)	0.15	-	0.15	-
L(L-Γ)	0.86	-	0.91	-
L(L-X)	0.21	-	0.21	-
L(L-U)	0.16	-	0.15	-
L(L-K)	0.15	-	0.15	-

carrier mobility, the observed insulating nature of $(MA)_2AgBiBr_6$ probably indicates that the single crystal is an intrinsic semiconductor and can be conductive with optical excitation.

Previous studies have shown that spin–orbit coupling (SOC) is crucial for obtaining the correct band dispersion, and therefore, we have compared the band structure of $(MA)_2AgBiBr_6$ with SOC to that without (Fig. 4.14)[255–257]. It is seen that the reduction in band gap due to SOC is quite small (∼0.18 eV) and significantly smaller than that found in $MAPbI_3$ (1.06 eV)[19]. This is because the atomic number (Z) of Ag is much smaller than that of Pb and the SOC effect is strongly dependent on Z. In the double perovskite $(MA)_2KBiCl_6$, studied previously, the energy states near the band gap belong mostly to Bi and Cl, and unlike the Ag states in $(MA)_2AgBiBr_6$, the K states are located deep in the VB. The effect of this is that a large reduction in the band gap due to SOC is seen in this material, as well[26]. Despite the apparently weak influence of SOC in $(MA)_2AgBiBr_6$,Fig. 4.14 shows that it does change the shape of the conduction bands and therefore remains essential for determining the correct band structure of the material.

4.5.5 Thermal Stability and Phase Transition

Thermogravimetric analysis (TGA) performed by Wei and co-workers showed the compound was stable until a temperature of ∼550 K was reached, using a heating rate of 10 K/min, where decomposition began (Fig. 4.15a). The thermal stability of $(MA)_2AgBiBr_6$ is better than that of $MAPbBr_3$,which decomposes at ∼490 K at a heating rate of 20 K/min, but

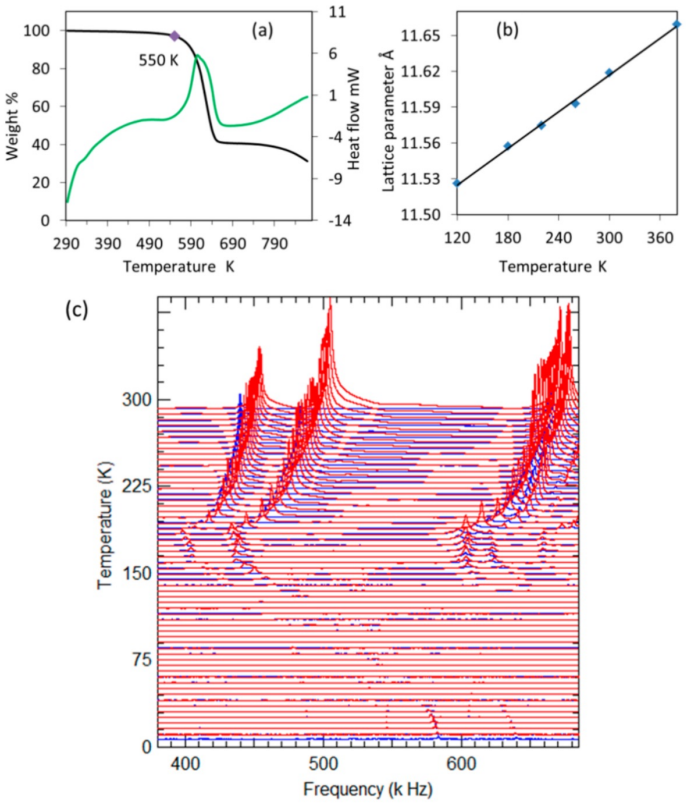

Fig. 4.15 (a) SDT (simultaneous DSC and TGA) measurements with TGA colored black and DSC colored green. (b) Lattice thermal expansion from 120 to 360 K obtained from single-crystal X-ray diffraction. (c) RUS spectra during cooling (blue) and heating (red). The y axis is the amplitude in volts from the detecting transducer; however, the spectra are stacked in proportion to the temperature at which they were recorded, and the axis is labeled as temperature. Reprinted with permission from Wei et al.[27]. Copyright (2017) American Chemical Society.

$(MA)_2AgBiBr_6$ is less thermally stable than $Cs_2AgBiBr_6$ (∼700 K)[13]. No obvious phase transition was detected from the corresponding differential scanning calorimetry (DSC) curve upon heating. Low-temperature DSC was also conducted, and again no obvious phase transitions were detected (Fig. A.10). An approximately linear lattice expansion with a thermal expansion coefficient of $\sim 4.4 \times 10^{-5}$/K was obtained from 120 to 360 K from variable-temperature single-crystal X-ray diffraction (Fig. 4.15b). The crystal color actually changes from red to yellowish brown upon cooling (Fig. A.8).

Although both DSC and XRD indicate that there are no phase transitions upon cooling rom 300 to 120 K, resonant ultrasound spectroscopy (RUS) performed by Wei and co-workers suggests otherwise (Fig. 4.15c). RUS is extremely sensitive to phase transitions through the

influences of strain coupling on the elastic constants[258]. Fig. 4.15c shows segments of the spectra stacked in proportion to the temperature at which they were recorded. Changes in peak shape and disappearance were observed at 185 and 158 K, respectively. The elastic constants scale with the square of the frequencies, f, of individual mechanical resonances of the sample, and the inverse mechanical quality factor, Q^{-1}, obtained from the resonance peak widths, is a measure of acoustic loss. f^2 decreases (i.e., elastic softening) from 300 to 185 K, followed by a slight increase when the temperature is decreased to 158 K, and then an abrupt elastic hardening continued until the temperature reached 7 K. The first discrete feature, at 185 K, is a change in gradient of f^2, and a small peak in Q^{-1} can be seen in Fig. A.11. The second, at 158 K, is another change in gradient and a steep increase in attenuation of the peaks. Sharp resonance peaks, i.e., with low attenuation, reappear below ∼35 K. This evidence of one or two phase transitions contrasts with the DSC results that do not appear to show obvious anomalies in heat capacity, suggesting perhaps that the changes in structure are only short-range. Although the room-temperature structure can be refined in a cubic cell with an a dimension of ∼11.637 Å, weak indications of doubling along all three axes (a' ∼23.3 Å) can be observed throughout the temperature range upon cooling. Therefore, the temperature-dependent behavior is not fully understood at this point, and further crystallographic studies of this system are recommended.

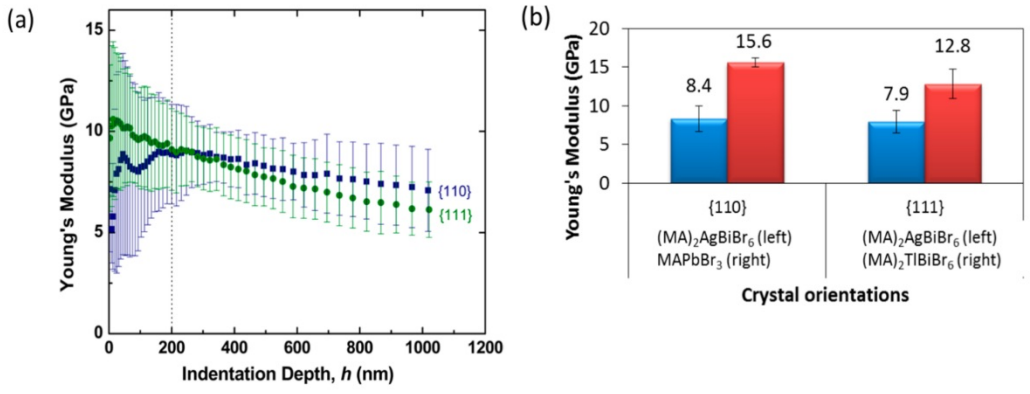

Fig. 4.16 (a) Young's modulus of $(MA)_2AgBiBr_6$ as a function of indentation depth. (b) Comparison of Young's moduli of $(MA)_2AgBiBr_6$ with $MAPbBr_3$[28] (left) and $(MA)_2TlBiBr_6$[26] (right). Reprinted with permission from Wei et al.[27]. Copyright (2017) American Chemical Society.

4.5.6 Mechanical Properties

Fig. 4.16 shows the elastic properties of $(MA)_2AgBiBr_6$ measured by Wei and co-workers using nanoindenation along the normals of the (110) and (111) facets in the cubic space group. The following Young's moduli (E) and hardnesses (H) (see Fig. A.12) were found: $E_{(110)}$ = 8.4 ± 1.7 GPa, and $H_{(110)}$ = 0.47 ± 0.09 GPa; $E_{(111)}$ = 7.9 ± 1.4 GPa, and $H_{(111)}$ = 0.55 ± 0.11 GPa (Fig. 4.16b). The anisotropy observed here is attributed to the different orientations of the inorganic Ag–Br–Bi linkages with respect to indentation directions. It is noticed that the changes in E and H are not significant for different directions. Via comparison of the mechanical properties of $(MA)_2AgBiBr_6$ with those of the analogous lead containing phase, $MAPbBr_3$[28], the nanoindentation results on the 110 facets show that $(MA)_2AgBiBr_6$ is far more compliant than $MAPbBr_3$; this is consistent with the expectation of Bennett et al.[259] that the replacement of two divalent metal cations (Pb in this case) with a monovalent one (Ag) and a trivalent one (Bi) should lead to a decrease in the stiffness of the material. In addition, via comparison of $(MA)_2AgBiBr_6$ with $(MA)_2TlBiBr_6$, the Ag phase shows a Young's modulus lower than that of the Tl-containing double perovskite along the same crystallographic orientation, probably because of the greater packing density in the thallium phase (Fig. 4.16b and Table A.13)[26].

4.6 Discovery of $(MA)_2KYCl_6$ and $(MA)_2KGdCl_6$

Compared with single perovskites, double perovskites have a broader chemical diversity since both the M^I and M^{III} site can be modified. Although there have been many reports of inorganic rare-earth halide double perovskites (e.g. Cs_2LiYCl_6, $Cs_2NaGdCl_6$, Cs_2NaYF_6[145, 260–262]), including several recent bismuth and indium-containing structures such as $Cs_2AgBiCl_6$, $Cs_2AgBiBr_6$, and $Cs_2AgInCl_6$[13–15, 147], only four hybrids halide double perovskites have been reported to date: $(MA)_2KBiCl_6$, $(MA)_2TlBiBr_6$, $(MA)_2AgBiBr_6$ and $(MA)_2AgSbI_6$[16, 26, 27, 103]. Studies on the first three are reported in this thesis. Combining the complex interactions between amine and cavity introduced by polar organic cations such as MA^+ (methylammonium, $CH_3NH_3^+$) with rare-earth or transition element metals is a promising route to multiferroic hybrid halide double perovskites (HHDPs)[263]. In this section we describe the synthesis and characterization of two novel HHDPs, $(MA)_2KGdCl_6$ and $(MA)_2KYCl_6$. Although low-dimensional rare-earth hybrid perovskites have been reported previously[8], we believe that these are the first examples of 3D HHDPs with rare-earth elements. Their structures were characterized using variable temperature single crystal X-ray

diffraction (SCXRD), and density functional theory (DFT) calculations have been used to predict the electronic and mechanical properties of these phases.

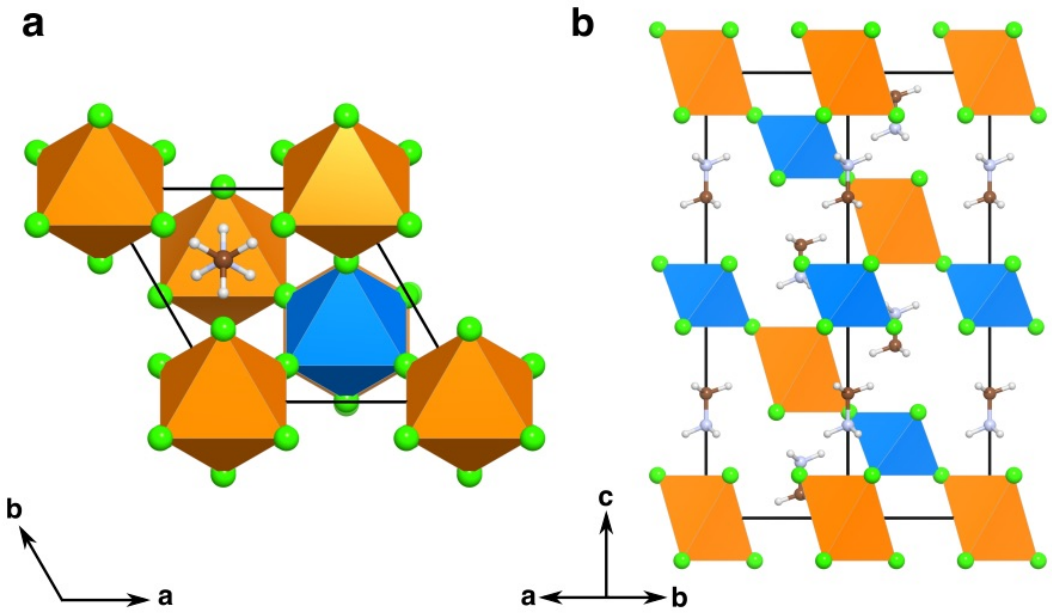

Fig. 4.17 Conventional unit cells of rhomobohedral $(MA)_2KMCl_6$ (M = Gd and Y) at room temperature, viewed (a) along the c axis, and (b) parallel to the a-b plane. KCl_6 and MCl_6 octahedra are shown in orange and blue, respectively. Green: Cl, brown: C, light blue: N, silver: H. Reprinted with permission from Deng et al.[29]. Copyright (2017) American Chemical Society.

4.6.1 Crystal Structures

$(MA)_2KGdCl_6$ and $(MA)_2KYCl_6$, both of which are colourless and transparent, have rhombohedral ($R\bar{3}m$) symmetry at room temperature, as found previously[16] for $(MA)_2KBiCl_6$, with lattice parameters of a = 7.7704(5) Å, c = 20.945(2) Å for $(MA)_2KGdCl_6$ and a = 7.6212(12) Å, c = 20.742(4) Å for $(MA)_2KYCl_6$. As in the previous work on the bismuth compound, the inorganic framework of each HHDP was found to be a network of alternating, corner sharing KCl_6 and MCl_6 octahedra (Figure 4.17a and b), with the MA^+ cations positioned inside the inorganic cage. The orientation of the C-N bond alternates along the c-axis. Bond lengths indicate that the Cl atoms are closer to Gd/Y than K (Table 4.2). Due to the relative size of the M^{III} cations (Gd^{3+}: 93.8 pm and Y^{3+}: 90 pm[38]), $(MA)_2KGdCl_6$ (V = 1095.21(18) $Å^3$) has a slightly larger unit cell volume than $(MA)_2KYCl_6$ (V = 1043.4(4)

Table 4.2 The experimental (300 K) and DFT-calculated (optB86b+vdW) structural properties of rhombohedral $(MA)_2KMCl_6$. Reprinted with permission from Deng et al.[29]. Copyright (2017) American Chemical Society.

Structural Properties	$(MA)_2KGdCl_6$		$(MA)_2KYCl_6$	
	Exp	DFT	Exp	DFT
a (Å)	7.7704(5)	7.7098	7.6212(12)	7.6844
c (Å)	20.945(2)	20.9789	20.742(4)	20.9074
c/a	2.7	2.72	2.72	2.72
V (Å^3)	1095.21(18)	1079.94	1043.4(4)	1069.18
$d_{K\text{-}Cl}$ (Å)	3.0572(14)	3.026	3.0305(17)	3.031
$d_{M\text{-}Cl}$ (Å)	2.6374(12)	2.646	2.5764(15)	2.621
$d_{C\text{-}N}$ (Å)	1.36(2)	1.491	1.40(3)	1.491
$d_{N\cdots Cl}$ (Å)	3.397(10)	3.272	3.341(11)	3.27
$d_{C\cdots Cl}$ (Å)	3.812(13)	3.826	3.727(16)	3.803
K-Cl-M (°)	173.09(10)	172.72	172.74(11)	173.05

Å^3). The tolerance factors[133] of $(MA)_2KYCl_6$ and $(MA)_2KGdCl_6$ are 0.954 and 0.948, respectively, indicating that $(MA)_2KYCl_6$ is slightly more close-packed, and that both are more close-packed than $(MA)_2KBiCl_6$ (0.933). Table 4.2 shows that the lattice parameters predicted by DFT using the optB86b+vdW functional agree well with the experimental observations for both structures and it is seen that optB86b+vdW gives the best equilibrium volume and c/a ratio when compared to the crystallographic results for $(MA)_2KYCl_6$ (Table 4.3). Within the $[KMCl_6]^{2-}$ inorganic framework, the $d_{K\text{-}Cl}$, $d_{M\text{-}Cl}$ bond distances and K-Cl-M bond angles also match well with the SCXRD structure. The main discrepancy between the experiments and the calculations concerns the apparent overestimation of $d_{C\text{-}N}$, as the crystallographic C-N distances represent the time-averaged positions of the electron densities and are shortened by the librations of the MA^+ cation about the c-axis (Fig. 4.18a).

Table 4.3 The lattice parameters of rhombohedral $(MA)_2KYCl_6$ calculated using different exchange correlation functionals compared to experiment. Reprinted with permission from Deng et al.[29]. Copyright (2017) American Chemical Society.

	PBE	PBEsol	PBE+D2	PBE+D3	PBE+TS	optB86b+vdW	Exp
a (Å)	7.9923	7.8032	7.7473	7.7898	7.7798	7.6844	7.6212
c (Å)	20.9998	20.6567	21.0372	20.8178	20.5605	20.9074	20.742
c/a	2.628	2.647	2.715	2.672	2.643	2.721	2.722
V (Å^3)	1161.69	1087.65	1093.5	1094.01	1077.72	1069.20	1043.80

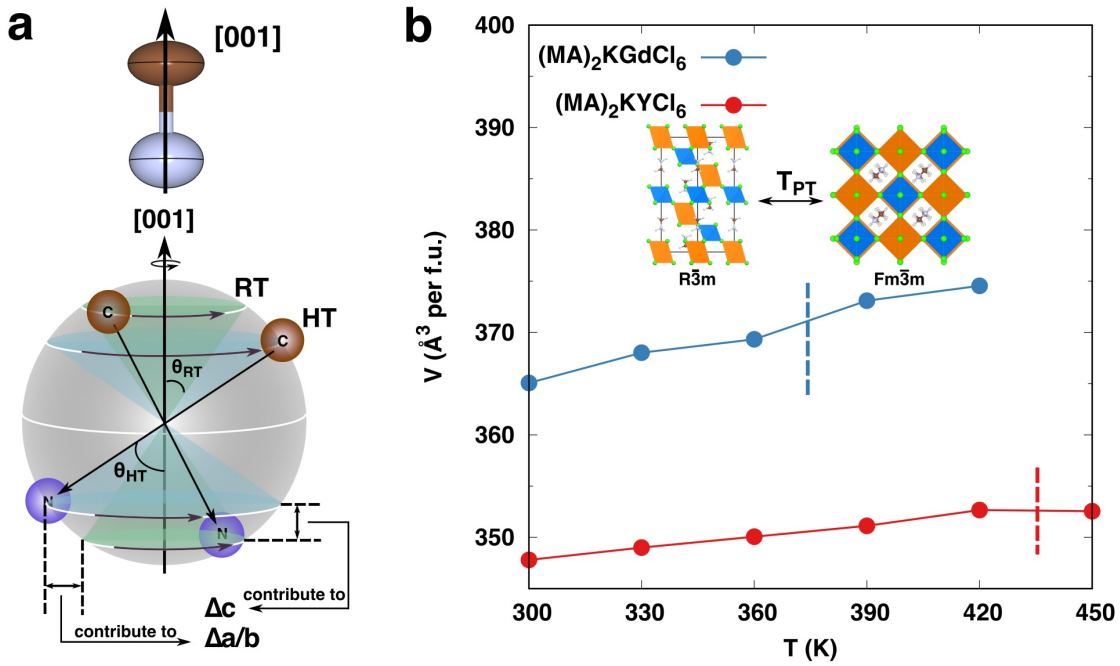

Fig. 4.18 (a) Upper: the experimental disk-shaped thermal ellipsoid of the C-N bond. Lower: illustration of how the libration of the MA^+ cation about the c-axis contributes to the lattice parameters at room temperature (RT) and high temperatures (HT). The libration angles at HT and LT are labelled as ϑ_{HT} and ϑ_{LT} (b) Volumes per formula unit (f.u.) of $(MA)_2KGdCl_6$ and $(MA)_2KYCl_6$ upon heating measured by VT-SCXRD. The approximate rhombohedral-cubic phase transition temperatures T_{PT} are marked by vertical dashed lines. Reprinted with permission from Deng et al.[29]. Copyright (2017) American Chemical Society.

4.6.2 Phase Stability

Synthesis and characterization of the HHDPs was found to be challenging since both materials are deliquescent, similar to the inorganic rare-earth HDPs[144]. In powder form the crystals dissolve quickly (minutes) when exposed to normal laboratory atmosphere. Because of this, the samples were not pure and contained some starting materials, which leads to difficulties for powder characterization. The synthesis temperature was found to be important since too low a temperature (< 70 °C) during evaporation results in the formation of rare-earth chloride hexahydrates in the product. Too high a temperature (> 100 °C) produced twinned crystals. To understand better the relative stabilities of the two rare-earth HHDPs, their decomposition and formation enthalpies (ΔH_d and ΔH_f) were calculated, as defined in Section 4.2, and are given in Table 4.4. Positive values of ΔH_d and negative values of ΔH_f suggest that they are energetically favourable. It is seen that $(MA)_2KYCl_6$ is more stable than both $(MA)_2KGdCl_6$ and the previously synthesized $(MA)_2KBiCl_6$.[16] The latter result

is interesting since experimentally we found $(MA)_2KBiCl_6$ to be much easier to synthesize than its rare-earth counterparts. This is probably because of the synthesis environment and kinetics, which are ignored in DFT calculations. It is well known that rare-earth halides ($M^{III}X_3$) are extremely hydroscopic and can readily form hydrates because M-X bonds, which are also present the HHDPs, are easily attacked by water.[144]

Table 4.4 DFT-calculated (optB86b+vdW) decomposition enthalpies (ΔH_d) and formation enthalpies (ΔH_f) of rhombohedral $(MA)_2KGdCl_6$, $(MA)_2KYCl_6$ and $(MA)_2KBiCl_6$. Units are meV/atom. Reprinted with permission from [29]. Copyright (2017) American Chemical Society.

	$(MA)_2KGdCl_6$	$(MA)_2KYCl_6$	$(MA)_2KBiCl_6$
ΔH_d	6.56	23.52	18.76
ΔH_f	-634.81	-949.48	-719.69

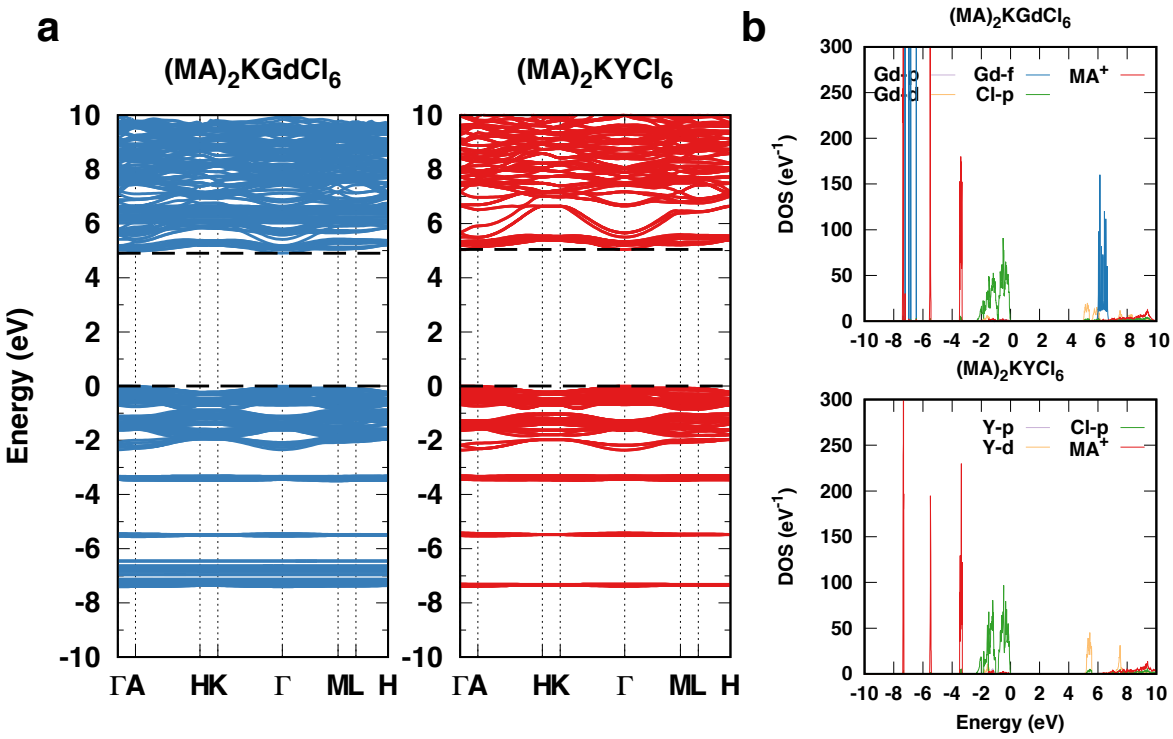

Fig. 4.19 DFT-calculated (a) electronic band structures and (b) projected densities of states (PDOS) for $(MA)_2KGdCl_6$ and $(MA)_2KYCl_6$. Valence band maximum (VBM) are set as zero. Reprinted with permission from Deng et al.[29]. Copyright (2017) American Chemical Society.

4.6.3 Phase Transition

The variable temperature single crystal X-ray diffraction results are shown in Table A.14 and A.15. Like $(MA)_2KBiCl_6$, the $(MA)_2KGdCl_6$ and $(MA)_2KYCl_6$ perovskites transform from a rhombohedral structure ($R\bar{3}m$) to a face centered cubic structure ($Fm\bar{3}m$) on heating above room temperature. The phase transition temperature, T_{PT}, for $(MA)_2KGdCl_6$ is between 360 and 390 K, whereas for $(MA)_2KYCl_6$ it is between 420 and 450 K. The higher T_{PT} for $(MA)_2KYCl_6$ may partly originate from its stronger hydrogen bonding. As discussed in the previous work[16] on $(MA)_2KBiCl_6$, the N$\cdots$Cl distance can be used as an indicator of hydrogen bond strength: the shorter this distance, the closer the amine group is to the Cl anions and the stronger the Cl-H bonding. In Table 4.2 we show that $d_{N\cdots Cl}$ is 3.397(10) Å and 3.341(11) Å for $(MA)_2KGdCl_6$ and $(MA)_2KYCl_6$, respectively, implying that the latter has stronger hydrogen bonds. The different thermal expansion coefficients of the two rare-earth double perovskites can also be rationalized by the different stiffnesses,[264] as discussed further below. Upon heating, both $(MA)_2KMCl_6$ perovskites increase in volume, as shown in Fig. 4.18b and Table A.14 and A.15. However, although the a (and b) lattice parameters increase, the c lattice parameter decreases with temperature (Table A.14 and A.15). This results in a negative thermal expansion coefficient along c (Table 4.5) and a decrease in the c/a ratio for both materials. The effect is larger for $(MA)_2KGdCl_6$ than for $(MA)_2KYCl_6$, and is also observed in $(MA)_2KBiCl_6$. The interatomic bond distances mostly increase upon heating, except for $d_{C\text{-}N}$, which is correlated to the negative thermal expansion along the c-axis. Since the positions of the C and N atoms are refined at the 6c site due to the constraint of symmetry, $d_{C\text{-}N}$ reflects the projection of the average C-N positions onto the c-axis. The anisotropic displacement ellipsoids of C and N deduced from SCXRD are disk-shaped and aligned normal to [001] (Fig. 4.18a top), which indicates that the MA^+ cations are librating off the c-axis. The libration angle increases with temperature, making the projected $d_{C\text{-}N}$ smaller. This libration, which is transmitted through the interaction between amine and cavity to the $[KMCl_6]^{2-}$ framework, combined with the vibrations of the M-Cl octahedra, is responsible for the observed decrease in c and increase in a (and b) upon heating (Fig. 4.18a bottom).

4.6.4 Electronic Structures

The DFT-calculated (optB86b-vdW+SOC) electronic band structures together with the projected density of states (PDOS) for both rare-earth HHDPs in their rhombohedral structure are shown in Fig. 4.19a and b and look very similar. Both perovskites possess large direct

Table 4.5 Linear and volume thermal expansion coefficients (α) for rhombohedral $(MA)_2KMCl_6$ fitted from VT-SCXRD data. The linear coefficients are fitted using data from 300 K to 360 K (420 K) for $(MA)_2KGdCl_6$ ($(MA)_2KYCl_6$) whereas the volume coefficients are fitted using all data points. Units are 10^{-4}/K. Reprinted with permission from Deng et al.[29]. Copyright (2017) American Chemical Society.

	α_a	α_c	α_V
$(MA)_2KGdCl_6$	47.75	-36.76	65.81
$(MA)_2KYCl_6$	29.79	-25.21	29.42

band gaps at the Γ point, with 4.91 eV for $(MA)_2KGdCl_6$ and 5.04 eV for $(MA)_2KYCl_6$. The large band gaps are due to the strongly ionic nature of the K^+ cation and the presence of Cl^-, which has a higher electronegativity and smaller ionic radius than bromine or iodine.[26] Focusing on the orbitals which contribute to the band edge states, Fig. 4.19b shows that the valence band maximum (VBM) of both HHDPs is dominated by Cl $3p$ non-bonding states, whereas the conduction band minimum (CBM) for $(MA)_2KGdCl_6$ and $(MA)_2KYCl_6$ is characterized by Gd $5d$-Cl $3p$ and Y $4d$-Cl $3p$ bonding states, respectively. The energy states of the MA^+ and K^+ cations are localized and energetically inactive, as found previously[16] for $(MA)_2KBiCl_6$. One difference between the two HHDPs is the presence of Gd $4f$ electrons in $(MA)_2KGdCl_6$, but these are deep and localized at around -7 eV, forming 7 extremely flat bands. The direct nature of the band gaps in both materials is related to the Cl $3p$ non-bonding states which dominate the VBM. This is different from other hybrid halide perovskites, such as $(MA)PbBr_3$ and $(MA)_2TlBiBr_6$, where the direct band gaps are strongly related to the Pb and Tl $6s$ lone pairs[26]. Direct band gaps are important in optoelectronic applications because optical absorption and emission processes become much easier. Although the band gaps in the present rare-earth HHDPs are too large to be used in solar cells, other applications such as solid-state lighting may be possible by doping the materials with further rare-earth elements (e.g. Ce^{3+}, Tb^{3+} or Eu^{3+}), as demonstrated previously in oxide garnet systems.[265]

4.6.5 Magnetic Properties

The presence of Gd in $(MA)_2KGdCl_6$ suggests that this HHDP could exhibit magnetic ordering due to unpaired $4f$ electrons. To examine this possibility, spin-polarized DFT calculations were performed on supercells of the primitive cell (i.e. containing two and four Gd atoms respectively). After optimization of the atomic, electronic and magnetic structures, it was found that the difference in energy between the ferromagnetic (FM), antiferromagnetic (AFM) and paramagnetic (PM) states was very small (0.1 - 0.2 meV/f.u.), with the AFM

structure being slightly more stable. In each case the magnetic moment (S_z) of each Gd atom was 6.88 μ_B. The small difference in energy between the states suggests that $(MA)_2KGdCl_6$ may be paramagnetic down to very low temperatures. This situation appears to be similar to that found experimentally[146] for $Cs_2NaGdCl_6$, which is thought to be paramagnetic above ca. 35 mK and ferromagnetic below. As shown in Fig. 4.19b, the $4f$ electrons in the valence band are energetically deep and localized, suggesting a weak magnetic exchange effect and an extremely low Curie temperature. Although $(MA)_2KGdCl_6$ is cation ordered and centrosymmetric at room temperature, the presence of the polar MA^+ cation may cause it to change symmetry on cooling and become ferroelectric. Consequently, there is a potential for $(MA)_2KGdCl_6$ to be multiferroic at low temperatures. The small energy difference between the magnetic states may also mean that it could be used as a magnetocaloric coolant.

Table 4.6 DFT-calculated (optB86b+vdW) polycrystalline[37] Young's modulus (E), bulk modulus (B), shear modulus (G) and Poisson's ratio (ν) for rhombohedral $(MA)_2KGdCl_6$, $(MA)_2KYCl_6$ and $(MA)_2KBiCl_6$[16] and their single crystal maximum values. All units are GPa except ν, which is dimensionless. Reprinted with permission from Deng et al.[29]. Copyright (2017) American Chemical Society.

	E	B	G	ν	E_{max}	E_{min}	G_{max}	G_{min}	ν_{min}	ν_{max}
$(MA)_2KGdCl_6$	26.03	19.63	10.18	0.28	37.1	19.93	15.25	6.56	0.59	0.19
$(MA)_2KYCl_6$	27.38	19.7	10.79	0.27	36.78	22.02	15.28	7.76	0.51	0.14
$(MA)_2KBiCl_6$	24.03	18.75	9.34	0.29	35.17	15.29	14.78	6.28	0.50	0.10

4.6.6 Mechanical Properties

Optoelectronic devices usually contain interfaces between mechanically different materials and thus it is important to understand the elastic properties of HHDPs. The DFT-calculated elastic constants of the two rare-earth HHDPs are shown in Table A.16 and the polycrystalline elastic moduli are given in Table 4.6. Both perovskites are mechanically stable because all the elements in the eigenvectors of their elastic constant matrices are positive. Like other halide perovskites,[16, 26–28, 31] they exhibit relatively low elastic moduli, with $(MA)_2KYCl_6$ being slightly stiffer than $(MA)_2KGdCl_6$, with DFT calculated Young's moduli along <100> of 22.34 GPa and 19.73 GPa, respectively. The flexible hybrid double perovskite structure suggests a flatter energy surface for phase transformations and also explains why $(MA)_2KGdCl_6$ has larger thermal expansion coefficients and $(MA)_2KYCl_6$ has a higher T_{PT}. The stiffness of the HHDPs is mainly related to the strength of the bonds in the inorganic framework.[26] Assuming a direct correlation between bond length and bond

strength, it is seen (Table 4.2) that $d_{K\text{-}X}$ and $d_{M\text{-}X}$ are shorter in $(MA)_2KYCl_6$ compared to $(MA)_2KGdCl_6$, which is consistent with the lower calculated Young's modulus in the latter material (Table 4.6). The calculated single crystal directional Young's moduli of $(MA)_2KYCl_6$ are shown in Fig. 4.20a, b and c projected onto different crystallographic planes. Similar contour maps are found for $(MA)_2KGdCl_6$. The directional Young's modulus is seen to be highly anisotropic, especially on the (010) plane and the plane normal to [100] (Fig. 4.20 b and c), with the largest values along the M-X-K direction and the smallest values along the diagonal of the M-X-K pseudo cubic cage, which is similar to other HHDPs[26].

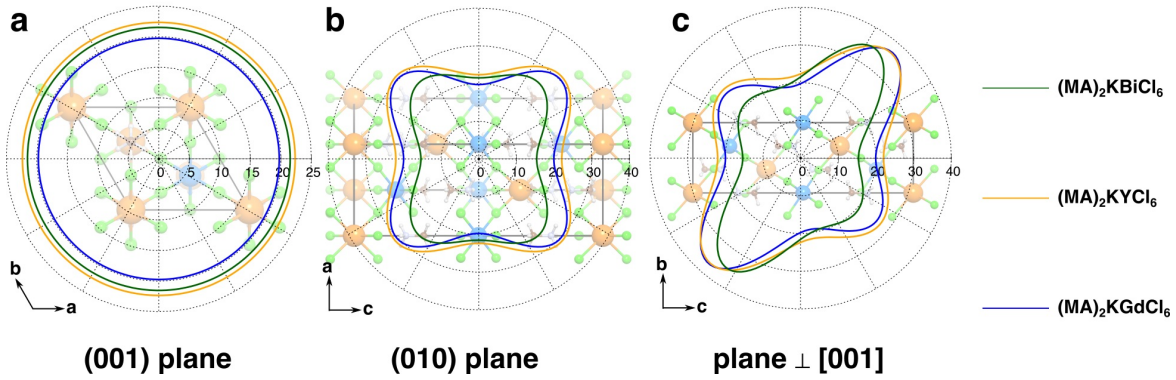

Fig. 4.20 DFT-calculated polar plots of the directional Young's modulus of $(MA)_2KMCl_6$ (M = Y: orange and Gd: blue) as well as previously reported $(MA)_2KBiCl_6$ (green) projected on (a) the (001) plane (b) the (010) plane and (c) the plane perpendicular to [100]. Radii indicate the value of directional Young's modulus and units are GPa. Structure of $(MA)_2KYCl_6$ is shown under the plots. Reprinted with permission from Deng et al.[29]. Copyright (2017) American Chemical Society.

4.7 Conclusions

From this chapter[1] a number of conclusions can be drawn. First in collaboration with Wei and co-workers a new lead-free, hybrid double perovskite, $(MA)_2KBiCl_6$ has been discovered, which shows strong similarities to the widely-studied lead halide perovskites $MAPbX_3$. The system has a wide band gap of 3.04 eV, which is similar to that of the compound $MAPbCl_3$ ($\sim$3.0 eV)[266].

Then we explored trends in the structural, electronic and mechanical properties of hybrid double perovskites using DFT chemical screening. As for electronic properties, using less ionic elements like Br or I for the X-site anion and Tl, Cu and Ag for the B-site cation is

[1]The results described in this chapter have been published in 4 papers, which are Ref. [16, 26, 27, 29].

crucial for achieving a narrow band gap and small effective mass for solar cell applications. The trend in mechanical properties shows that moving from X = Cl to Br to I, the structures are becoming more compliant, which is closely related to the strength of the $B^{I}-X-B^{III}$ framework and the rotation of MA cation inside. In addition, choosing the proper size for the framework and A site cation is also crucial since too large a tolerance factor can make the structure mechanically unstable. WA new hybrid double perovskite–$(MA)_2TlBiBr_6$, which is isoelectronic to $MAPbBr_3$ was also discovered and found to have a much smaller direct band gap than $(MA)_2KBiCl_6$.

Next, we discovered a nontoxic, hybrid double perovskite, $(MA)_2AgBiBr_6$,which has an indirect band gap of $\sim$2 eV. The characteristic of the band gap is explained using DFT calculations, and the presence of Ag is shown to weaken the effect of spin-orbit coupling. The material is stable to air and moisture and exhibits a decomposition temperature higher than and a Young's modulus smaller than that of $MAPbBr_3$. The discovery of $(MA)_2AgBiBr_6$ further demonstrates the importance of the double perovskite approach in the search for lead-free photovoltaic materials that exhibit good stability.

Finally, two new rare-earth hybrid double perovskites, $(MA)_2KGdCl_6$ and $(MA)_2KYCl_6$, have been prepared using a solution evaporation method and their structures characterized using variable temperature single crystal X-ray diffraction. At room temperature both perovskites have rhombohedral symmetry, but on heating above 360 K they transform to cubic symmetry. This behavior is similar to that found previously for $(MA)_2KBiCl_6$. DFT calculations on the rhombohedral phase indicate that the new perovskites have large direct band gaps ($\sim$ 5 eV), are mechanically stable, and could exhibit magnetic ordering at low temperature in the case of $(MA)_2KGdCl_6$. The discovery of these materials expands the scope of hybrid perovskites to rare-earth containing materials, enabling the possibility of future applications in solid-state lighting and magnetism.

Unfortunately, iodide double perovskites could not be synthesized. There are a few reports of such materials in the recent literature, e.g. $(MA)_2AgSbI_6$[267], $(MA)_2AgBiI_6$[268] and Cs_2NaBiI_6[269], but these have not been confirmed and their characterisation does not appear to be definitive.

Chapter 5

Variable Temperature, Pressure and Transport Properties of Halide Perovskites

This chapter summarizes my recently published papers on the variable temperature and pressure properties of halide perovskites[30, 31] and another accepted paper[34] linking the mechanical properties of halide perovskites to their transport properties.

5.1 Introduction

When trying to understand the relationship between a material's structure and its properties, the structural response to an external stimulus such as pressure or temperature provides significant information. In the first study described in this chapter, the variable temperature (100 to 450 K) and high-pressure (p = 0 to 0.74 GPa) crystal chemistry of the black perovskite, formamidinium lead iodide, $FAPbI_3$ (FA = $[(NH_2)_2CH]$), obtained using single crystal X-ray diffraction, are presented. For both stimuli, a phase transition to a tetragonal phase was found. The experimental results were combined with first principles calculations, providing information about the electronic properties of $FAPbI_3$ as well as the most probable orientations of the FA^+ cations.

In the next study, the mechanical properties of formamidinium lead halide perovskites ($FAPbX_3$, X = Br or I) grown by inverse-temperature crystallization and measured by nanoindentation are described. The measured Young's moduli (9.7-12.3 GPa) and hardnesses (0.36-0.45 GPa) indicate good mechanical flexibility and ductility. The effects of hydrogen

bonding are evaluated by performing ab initio molecular dynamics on both formamidinium and methylammonium perovskites and calculating radial distribution functions. The structural and chemical factors influencing these properties are discussed by comparison with corresponding values in the literature for other hybrid perovskites, including double perovskites. It is shown that bonding in the inorganic framework and hydrogen bonding play important roles in determining elastic stiffness. The influence of the organic cation becomes more important for structures at the limit of their perovskite stability, indicated by high tolerance factors.

In the final study described here, a comprehensive set of density functional theory (DFT) calculations is presented which demonstrates that when a methylammonium (MA) cation is substituted into the structure the combined effects of stericity (conformation) and hydrogen-framework interactions improve the material's resistance to deformation. For example, the orientationally-averaged Young's modulus of orthorhombic $MAPbI_3$ increases by about 19% compared to the equivalent inorganic series of structures. It is also shown that, within the carrier-acoustic phonon scattering regime, the electron and hole carrier mobilities of hybrid halide perovskites are lowered by the hydrogen-bonding-induced tilting of the inorganic octahedra. Taken together, these results can help guide the optimization of the mechanical and transport properties of perovskite-based solar cell materials.

5.2 Methods

The first two studies are accompanied by experimental synthesis and characterizations mostly carried out by Dr. Shijing Sun. I performed DFT calculations connected to all the studies including the final work, where Dr. Jung-Hoon Lee and I made equal contributions. Therefore, most of the experimental methodologies are not described here. Later on in this chapter where the results are described, credit is given to Dr. Sun and co-workers when appropriate.

For the first study, the ab initio molecular dynamics (AIMD) simulations were performed using the VASP code[242, 243]. Projected augmented wave (PAW)[270] potentials were used for Pb ($5d^{10}6s^26p^2$) and I ($5s^25p^5$), and the PBE functional[190] with van der Waals correction[110] was used to model the exchange-correlation. A 400 eV planewave kinetic energy cutoff and a Γ point only k-point mesh were used. Relativistic spin-orbit coupling (SOC) was not considered for the ab initio MD since it does not affect structural properties significantly[130]. The simulations were only performed on the 200 K $FAPbI_3$ structure with its unit cell doubled ($2 \times 2 \times 2$, 16 formula units). The experimental lattice parameters and positions of the inorganic elements (Pb and I) were all kept fixed during the simulations which

were first performed for 10 ps to equilibrate the structure and then these data were discarded. Following this a further simulation of 50 ps was performed to collect data for analysis. The trajectories were sampled every 10 fs to determine the preferred orientations of the FA^+ ion. As for the ground state electronic structure calculation, a planewave kinetic energy cutoff of 500 eV was employed. For the density of states (DOS) calculations a $10 \times 10 \times 12$ k-point mesh was used. SOC was considered for both the band structure and DOS calculations[166]. Because the electronic structure of $FAPbI_3$ near the band gap depends mostly on the inorganic elements, i.e. Pb and I, the experimental lattice parameters and ionic positions of Pb and I at different temperatures were fixed throughout the calculations, and FA^+ cation was replaced by a positive background charge. The background charge avoids considering the orientational disorder of the cation.

For the second study, AIMD calculations were performed using the same potentials and the same code, with the following electrons treated explicitly: H ($1s^1$), C ($2s^2 2p^2$), N ($2s^2 2p^3$), Pb ($5d^{10} 6s^2 6p^2$) and Br ($4s^2 4p^5$). The same functional, energy cutoff, k-point and van der Waals corrections as the first study were used also without considering the SOC for the same reason. An NVT ensemble was used and the experimental lattice parameters were applied and kept fixed ($2 \times 2 \times 2$ supercell). The temperature was set at 300 K. The data from the first 10 ps was discarded for equilibration and then the calculations were run for 100 ps for data collection. The radial distribution function (RDF) was analysed using VMD[271] with a bin size of 0.05 Å. The effects of strain were studied using the same parameters used above while applying ±1% strain along the a-axis of the cell.

Table 5.1 A comparison of computed effective radii of all ions obtained from our DFT calculations with those obtained from Shannon's work[38]. Reproduced from Lee and Deng et al.[34] with permission from The Royal Society of Chemistry.

A-site	Radius (Å)		B-site	Radius (Å)		X-site	Radius (Å)	
	This work	Shannon's radii		This work	Shannon's radii		This work	Shannon's radii
K^+	1.31	1.55	Sn^{2+}	1.39	-	Cl^-	2.04	1.78
Rb^+	1.51	1.63	Pb^{2+}	1.41	1.19	Br^-	2.22	1.96
Cs^+	1.76	1.78				I^-	2.47	2.2
Fr^+	1.87	1.8						
MA^+	2.07							

The final study used the same potentials and code as described above. However, the van der Waals functional (optB86b-vdW) was used in the relaxation process and calculation of the elastic moduli. This functional reproduces the experimental lattice parameters[108] of the orthorhombic(o-) $MAPbI_3$ structure better than other functionals like PBEsol, vdW-DF2, PBE+TS and SCAN (Table B.6). The electronic properties, including effective masses

and deformation potentials, were calculated with the PBE functional along with SOC. The following parameters were adopted: a $5 \times 4 \times 5$ Monkhorst-Pack k-point mesh centered at Γ and a 1000 eV plane-wave kinetic energy cutoff, leading to a stress tensor converged to 0.1 kbar. The number of valence electrons treated explicitly were as follows: 14 for Pb ($5d^{10}6s^26p^2$), 14 for Sn ($4d^{10}5s^25p^2$), 7 for I ($5s^25p^5$), 7 for Br ($4s^24p^5$), 7 for Cl ($3s^23p^5$), 9 for K ($3s^23p^64s^1$), 9 for Rb ($4s^24p^65s^1$), 9 for Cs ($5s^25p^66s^1$), 9 for Fr ($6s^26p^67s^1$), 4 for C ($2s^22p^2$), 5 for N ($2s^22p^3$), and 1 for H ($1s^1$). The ions were relaxed until the forces on them were less than 0.01 eV Å^{-1}. The computed lattice parameters of all ground state structures are given in Table B.7. In order to be self-consistent, the tolerance factor was determined directly from the DFT electron density, defining the ionic radii by the volume of a sphere which contains 95% of the electron density, following previous DFT studies[18, 272]. The ionic radii are shown in Table 5.1. The hydrogen-bonding index (H-index), can be used to represent the H bond strength and for the case of hydrogen atoms attached to the nitrogen atom of the MA molecule and it can be evaluated as follows[273]:

$$H-index = \frac{f_{\text{MAPbI}_3}(N-H) - f_{\text{MA}}(N-H)}{f_{\text{MA}}(N-H)} \tag{5.1}$$

where $f_{\text{MA}}(N-H)$ denotes the $N-H$ stretching vibration frequency of a MA molecule in isolation (e.g. contained in a large empty supercell) and $f_{\text{MAPbI}_3}(N-H)$, refers to the corresponding frequency of a MA molecule experiencing hydrogen bonding interactions with its neighboring I ions (N–H$\cdots$I) in the PbI_3 framework of an orthorhombic (o-) $MAPbI_3$ unit cell. The equivalent equation could be written for the hydrogen atoms attached to the carbon atom of the MA molecule but previous studies[129] on o-$MAPbI_3$ have indicated that hydrogen-bond interactions mainly originate from H atoms on nitrogen. Thus, we can use Eq. 5.1 as an overall indicator of the H bond strength in a given hybrid halide perovskite by simply focusing on nitrogen and taking the mean of the three H-indices corresponding to the three hydrogens attached to this atom. The charge carrier mobility μ_{ij} is calculated using the theory of deformation potentials[274] which considers carrier-phonon coupling in the acoustic regime as the dominant charge carrier scattering mechanism:

$$\mu_{ij} = \frac{(8\pi)^{\frac{1}{2}}\hbar^4 e C_{ij}}{3m_{ij}^{*\frac{5}{2}}(k_B T)^{\frac{3}{2}} D_{ij}^2} \tag{5.2}$$

where e is the charge and C_{ij}, m_{ij}^*, and D_{ij} are the stiffness tensor, the effective mass tensor and the deformation potential tensor respectively. m_{ij}^* is calculated from a numerical second order derivative of the band dispersion $\partial^2 E(k)/\partial k^2$. In order to obtain this, we use five

eigenvalues near the valence (conduction) band maxima (minima) located at the Γ-point [0, 0, 0], from Γ to X = [0.5, 0, 0], Γ to Y = [0, 0.5, 0] and Γ to Z = [0, 0, 0.5] in the first Brillouin zone. The number of k-points between two k-points is forty. The effect of spin-orbit coupling is considered. Using a linear relationship between eigenvalue and strain, D_{ij} can be obtained. We apply the ε_1, ε_2, and ε_3 strains to the optimized orthorhombic unit cell and fix all internal coordinates. For each strain, five deformations are used: 0%, ±0.5% and ±1%. By doing so, we can get D_{ij} values for each of the perovskites considered. All eigenvalues are aligned with the 1s core levels of the halogens (X = I, Br, Cl).

5.3 Variable Temperature and Pressure Studies on $FAPbBr_3$

5.3.1 Variable Temperature Study of $FAPbBr_3$

There have been several X-ray diffraction (XRD) and spectroscopy studies in which applying hydrostatic pressure to $MAPbX_3$ (X = I, Br) results in symmetry lowering and changes in electronic properties[275, 122, 276, 119, 277, 278]. $FAPbI_3$ was recently studied at high pressures; however, the authors report the absence of any phase transition, despite the occurrence of an abrupt change of lattice parameters as a function of pressure[279]. In another recent high-pressure study using powder XRD, a transition to an orthorhombic structure in *Imm*2 was reported at 0.34 GPa. The single crystal results do not support their finding[280]. Likewise, temperature-induced phase transitions are also commonly observed; for example, Seshadri et al. applied powder XRD, finding that $FAPbI_3$ undergoes two phase transitions on cooling[281]. Interestingly, the room temperature structure of $FAPbI_3$ has only been revisited quite recently, highlighting the challenges that crystallographers encounter. Using neutron powder diffraction, Weller et al. found a cubic structure with the space-group $Pm\bar{3}m$[157]. Our work follows on from the important findings by Seshadri and Weller, focusing on the orientation of FA^+ using single crystal X-ray diffraction (SCXRD). Furthermore, the SCXRD was used to investigate the crystal chemistry of $FAPbI_3$ under hydrostatic pressure.

Firstly, the crystal structure of $FAPbI_3$ as a function of temperature was considered. Like oxide perovskites, lead iodide perovskites show an increase of symmetry with increasing temperature[119, 151, 107, 108]. In the cubic room temperature structure of $FAPbI_3$, FA^+ cations are disordered due to symmetry requirements[157]. Notably, the perovskite polymorph of $FAPbI_3$ is only metastable at room temperature. Under ambient conditions, the black perovskite polymorph slowly transforms to a low dimensional structure over time. For the variable temperature study, single crystals (edges >0.3 mm) of black $FAPbI_3$ were pre-

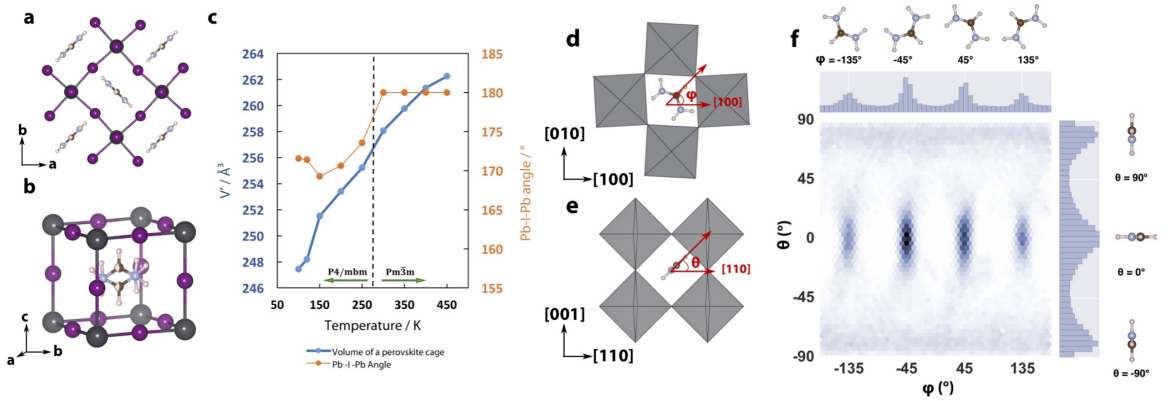

Fig. 5.1 (a)$FAPbI_3$ unit cell in $P4/mbm$ showing disordered FA^+ cations as observed by SCXRD. View is along the c-axis where tilting of the octahedra is seen and the N-N axis lies along <110> in the ab-plane. (b) Illustration of two disordered FA^+ cations superimposed inside a pseudocubic cage. (c) Volume of the pseudocubic perovskite cell, V', for $FAPbI_3$ (blue points), and the Pb-I-Pb angle (orange points) as a function of temperature. Statistical sampling of the FA^+ orientation in the low temperature tetragonal phase is modelled by ab initio MD. The orientation is defined by (d) ϕ (the angle between the C-H vector and the a-axis) and (e) θ (the angle between the C-H vector and ab-plane). The statistical distributions of θ and ϕ are shown in (f). Reproduced from Sun et al.[30] with permission from The Royal Society of Chemistry.

pared by Dr. Sun and co-workers using a previously reported synthetic route[282]. Starting at T = 300 K, untwinned single crystals of $FAPbI_3$ were heated to T = 450 K, then SCXRD data were collected by Dr. Sun and co-workers during stepwise cooling to 100 K. $FAPbI_3$ crystallises in the expected perovskite structure, with $[PbI_3]^-$ forming a ReO_3-type cavity and FA^+ found in the open void for charge balance. At T = 300 K, a cubic phase with a = 6.3566(2) Å and space group $Pm\bar{3}m$ (R_1 = 3.27%) was obtained, which is consistent with the recent observations by Weller et al.[157] (Fig. B.1). It is noticed that in this $Pm\bar{3}m$ phase the Pb-I-Pb angles are 180°, which enables good mixing of Pb 6s orbitals and I 5p orbitals[272]. It should be noted, however, that the thermal motion of the iodide ions is strong perpendicular to the Pb-Pb direction, as observed previously (Fig. B.1)[107]. On cooling $FAPbI_3$ from 450 K, a phase transition is observed between 300 K and 250 K (Table B.1). After carefully examining the systematic absences in the precession images, the low temperature phase in tetragonal symmetry was solved with space group $P4/mbm$ (Fig. 5.1a and b). It should be noted that although un-twinned single crystals were selected for X-ray diffraction, structure solution was complicated by crystal twinning which took place upon cooling during the cubic to tetragonal phase transition. At T = 250 K, structure solution in $P4/mbm$ (R_1 = 4.45%) leads to a tetragonal unit cell with a = 8.9710(7) Å and c = 6.3427(8) Å (see Table B.2).

With respect to the ambient temperature cubic cell, the tetragonal cell is 45° tilted within the ab-plane, leading to the square root relationship of the lattice parameters a and b. Importantly, the phase transition is related to a change of the octahedral tilting system from $a^0a^0a^0$ for $Pm\bar{3}m$ (zero-tilt system) to $a^0a^0c^+$ (one-tilt system) for $P4/mbm$. The octahedral tilt about the c-direction is associated with a reduction of the Pb-I-Pb angles within the ab-plane to 173.6° (Fig. 5.1c).

Interestingly, differential scanning calorimetry performed by Dr. Sun and coworkers does not show clear evidence for a phase transition. However, by measuring SCXRD on a different crystal and applying a smaller temperature interval, the phase transition temperature could be narrowed down to 260-280 K, which is in good agreement with the results of Seshadri et al.[281] Reducing the temperature to T = 200 K further decreases the lattice parameters and Pb-I-Pb angle to a = 8.9491(6) Å, c = 6.3283(6) Å and 170.6(1)° (R_1 = 6.29%). The SCXRD datasets collected by Dr. Sun and coworkers at T = 250, 200, and 150 K were satisfactorily solved in $P4/mbm$ (see Table B.2 and Fig. B.2). Importantly, the SCXRD data allowed them to specify the orientations of the FA^+ cations, which have hitherto been unresolved. In detail, they found the N-N axis of FA^+ lying on the ab-plane (Fig. 5.1a and b). Two possible carbon positions were observed in this dataset at 250 K with C-H bonds aligned parallel to the c-axis, which have been modelled using partial occupancies (Fig. 5.1b). The closest N$\cdots$I distances are 3.7966 (4) Å and 3.7017(3) Å, and the C$\cdots$I distance is 3.8512(3) Å at T = 250 K. For $MAPbI_3$, where the cation positions were well defined at 100 K, the N$\cdots$I distances in the orthorhombic phase are 3.611 Å and 3.681 Å, and the closest C$\cdots$I distance is 4.090 Å[108, 129]. The longer N$\cdots$I distances in $FAPbI_3$ indicate weaker hydrogen bonding.

Ab initio molecular dynamics (AIMD) simulations and ground state density functional theory (DFT) calculations were performed to further analyse the dynamics of the FA^+ cation in the low-temperature tetragonal phase. The MD simulations at T = 200 K show that the FA^+ cation rotates around the N-N axis, while the NH_2 groups do not move significantly, consistent with the experimental observations. Hydrogen bonding interactions between the NH_2 groups and the $[PbI_3]^-$ cage presumably control the energy barrier for the motion of FA^+[283, 129]. In other words, the NH_2 groups are locked, leaving the CH group free to rotate (see Fig. 5.2 for MD simulations of the N-N bond, and Fig. 5.3 and Table B.3 for bond distances). The results are also in agreement with the glassy behaviour of $FAPbI_3$ found recently by Fabini et al.[281] The simulations at T = 46-51 K indicate that C-H bonds were locked-in in different orientations, leading to a loss of long range order of the crystal. Statistical analysis of the MD simulations at 200 K reveals that FA^+ has two preferred orientations, see Fig. 5.1d-f. In the first and statistically more probable orientation,

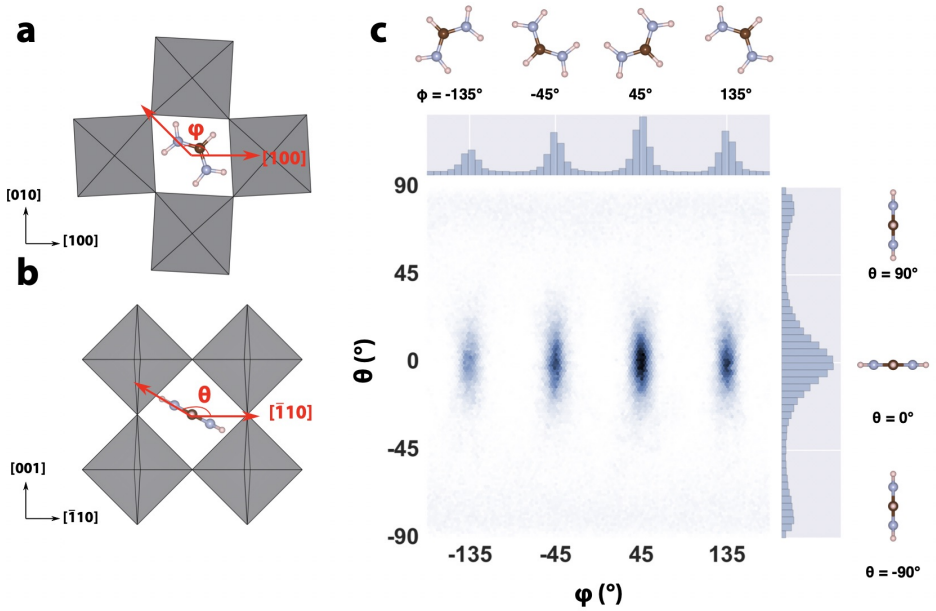

Fig. 5.2 Statistical analysis of the orientation of the FA^+ cation based on its N-N axis. Results determined from ab initio MD simulations. The angles θ and ϕ shown in (a) and (b) define the orientation of the N-N axis with respect to $[100]$ and $[\bar{1}10]$ respectively. The results are equivalent to those shown in Figure 1 of the main text which use the C-H vector to define the orientation of the cation. The statistical distribution of θ and ϕ is shown in (c). Reproduced from Sun et al.[30] with permission from The Royal Society of Chemistry.

the C-H bond of FA^+ lies within the ab plane ($\theta = 0$) and points at the open face of the ReO_3-type cavity formed by lead and iodine. In the second orientation, the C-H bond is parallel to the c-axis ($\theta = 90°$), similarly pointing at an open face. This observation agrees with the tetragonal symmetry where the c-axis depicts the unique axis of the unit cell. The stability of the $FAPbI_3$ structures with FA^+ oriented in the two aforementioned positions is further confirmed by DFT calculations, see Fig. 5.4. The same calculations also give insight into the mechanism of the phase transition: distortions of the cavity due to reduced lattice parameters and bond distances and different octahedral tilting modes can quench the dynamics of FA^+, thereby changing the symmetry of the system[284]. Increased c-axis tilting may be a response to the reduced temperature, and hence the reduced entropy gain from disorder of FA^+, perhaps initiating the phase transition[285].

The experimental SCXRD datasets collected at T = 120 K and T = 100 K were indexed in a primitive tetragonal unit cell for comparative purposes. The volume of the pseudocubic unit cell V' as well as the observed lattice parameters as a function of temperature show clear evidence for a second phase transition below 150 K (Fig. 5.1c and Fig. B.2), which is consistent with low temperature PXRD results[281]. Using SCXRD, it was not possible to

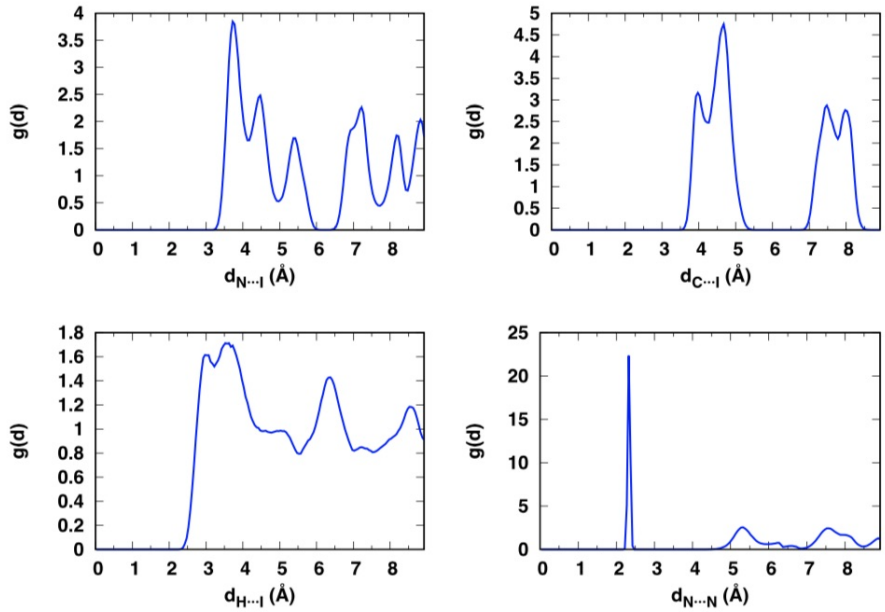

Fig. 5.3 Radial distribution functions (RDF) g(d) of various interatomic distances determined from the ab intio MD simulations. The RDF calculations used a step size of 0.005 Å. Reproduced from Sun et al.[30] with permission from The Royal Society of Chemistry.

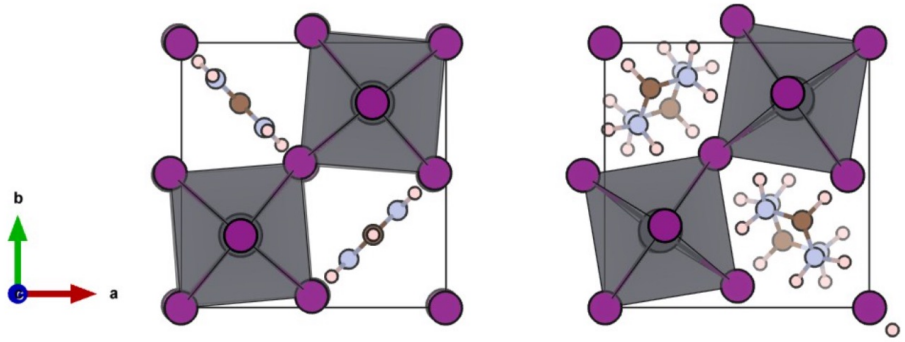

Fig. 5.4 Orientations of the FA^+ cations in relation to the perovskite cage and the octahedral tilting, with (a) tilting in the ab-plane and (b) tilting about the c direction. Reproduced from Sun et al.[30] with permission from The Royal Society of Chemistry.

solve the structure due to additional twinning at T = 120 K, which is further indirect evidence for a phase transition.

Ground state DFT calculations were performed to analyse the impact of the temperature induced phase transition on the electronic properties. For the calculations, a negatively charged $[PbI_3]^-$ framework was used as a structural model in all cases, with lattice parameters obtained from SCXRD. This is a reasonable approach as the band edges in $APbX_3$

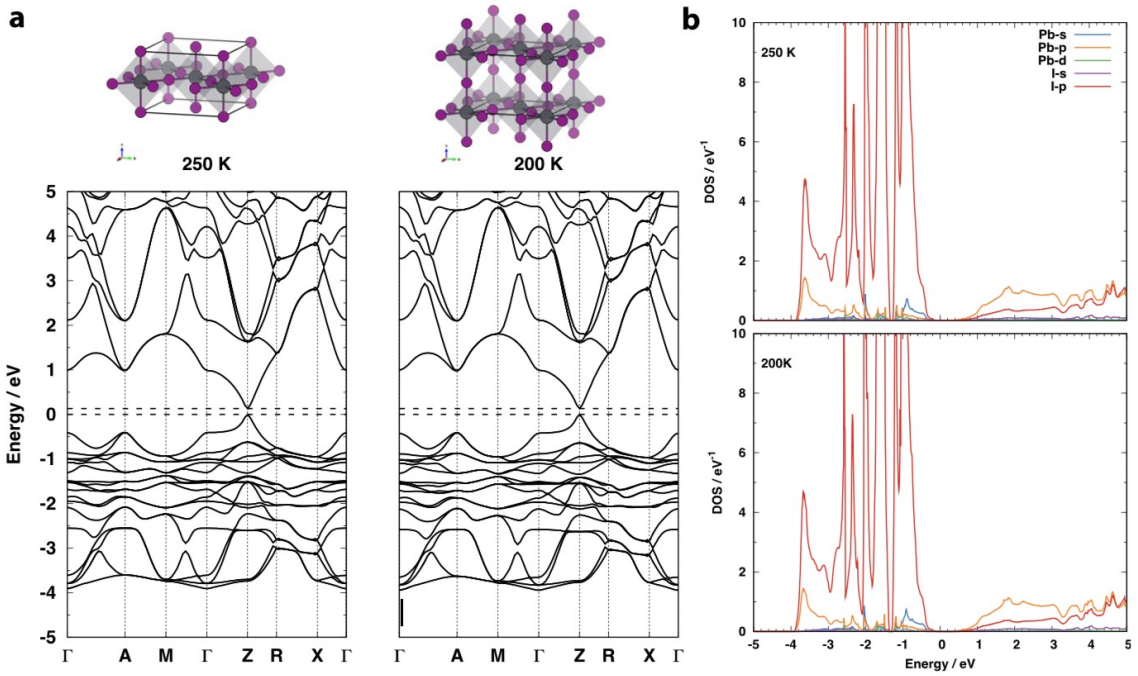

Fig. 5.5 Comparison of the calculated band structure and DOS of $FAPbI_3$ at 250 K and 200 K in which the FA^+ cation has been replaced by a positive background charge. The following high symmetry path for a primitive tetragonal lattice was used for the band structure calculations: Γ(0,0,0), A(0.5,0.5,0.5), M(0.5,0.5,0), Γ(0,0,0), Z(0,0,0.5), R(0,0.5,0.5), X(0,0.5,0) and Γ(0,0,0). Reproduced from Sun et al.[30] with permission from The Royal Society of Chemistry.

materials only exhibit contributions from the inorganic framework[272]. Charge balance was maintained by adding a positive background charge in the calculations. It is noted that DFT calculations that include spin-orbit coupling generally underestimate the band gap; however, as only the relative changes of the band gap were interesting, this is not of further concern. As expected, the calculated band gap decreases by 0.017 eV from T = 300 K (0.148 eV) to T = 250 K (0.131 eV), because of reduced lattice parameters and Pb-I bond lengths. After the phase transition to the tetragonal phase, a Pb-I-Pb angle smaller than 180° is expected to increase the band gap due to a weaker orbital overlap[272] and therefore counteracts the effect of reduced cell dimensions and bond lengths on the band gap. Interestingly, a band gap of E_g = 0.131 eV at T = 200 K was obtained for the tetragonal modification, see Fig. 5.5. As the difference in band gap compared to the other phases is small, the competing effects of reduced cell dimensions and the Pb-I-Pb angle within the ab plane were suggested, which are of similar magnitude and thus cancel each other out.

5.3.2 High Pressure Study of $FAPbBr_3$

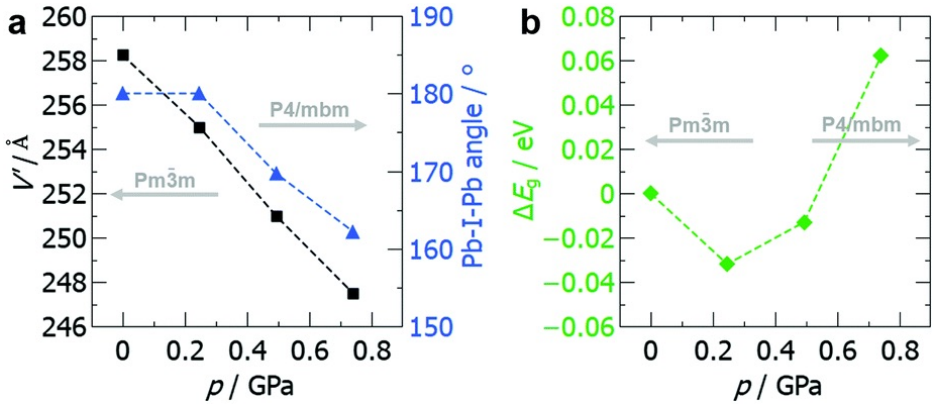

Fig. 5.6 (a) Experimentally measured volume of the pseudocubic cell, V', for $FAPbI_3$ (black points) and the Pb-I-Pb angle (blue points), (b) DFT-computed evolution of the band gap difference, ΔE_g, with respect to the ambient phase as a function of pressure. Reproduced from Sun et al.[30] with permission from The Royal Society of Chemistry.

High-pressure single crystal X-ray diffraction experiments were performed by Dr. Sun and co-workers to further investigate the crystal chemistry of $FAPbI_3$. In agreement with the study of Weller et al.,[157] a cubic lattice was obtained with space-group $Pm\bar{3}m$ and a = 6.36803(16) Å at ambient pressure. Increasing the pressure leads to a reduction of the lattice parameters and Pb-I bond lengths, e.g. a = 6.34132(13) Å at p = 0.25 GPa. A phase transition occurs at p = 0.49 GPa. As in the variable temperature SCXRD study, the indexing routine implemented in CrysAlisPro suggested body-centred cubic as the lattice type. However, close inspection of the (hk0) precession image indicates systematic absences contradicting the assignment of $Im\bar{3}$, see Fig. B.3. Similar to the room temperature study, twinning of the crystal over the phase transition challenges structure solution[286]. Following Glazer tilt notations, and thereby eliminating many space group possibilities, a structure solution in $P4/mbm$ was attempted. The tetragonal solution gives improved refinement values with respect to the cubic solution: R_1 = 6.50% with a = 8.9148(6) Å and c = 6.3138(7) Å. The diffraction intensities that would indicate doubling of the unit cell can then be explained by twinning, similar to that observed in the variable temperature study. Hence, it is believed that $P4/mbm$ is the most likely space group for the high pressure $FAPbI_3$ phase. Analogous to the variable temperature study, the phase transition is signalled by a reduction of the Pb-I-Pb angles within the ab-plane to 169.5° at p = 0.49 GPa. Increasing the pressure to p = 0.74 GPa further reduces the Pb-I-Pb angle to 162.0° and the lattice parameters to a = 8.8430(6) Å and c = 6.27090(6) Å. The volume of the pseudocubic perovskite cell (V') as a function of

pressure is given in Fig. 5.6a. Twinning was explicitly taken into account during structure solution and refinement for datasets with p > 0.25 GPa. Details of the structure solution and refinement statistics are given in Table 5.2. Note that the structure models for p > 0.25 GPa do not include the formamidinium cation, FA^+, which is not well-defined in the high-pressure experiments.

Table 5.2 First order (nearest neighbor) peak positions (Å) obtained from the RDF analysis in Fig. 5.3. Reproduced from Sun et al.[30] with permission from The Royal Society of Chemistry.

$N\cdots I^1$	$C\cdots I^2$	$H\cdots I$	$N\cdots N$
3.73	3.98	3.08	2.33

[1]Bond distances from X-ray diffraction: 3.70(1) Å at T = 250 K and 3.68 (1) Å at T = 200 K.
[2]Bond distances from X-ray diffraction: 3.85(1) Å at T = 250 K and 3.83 (2) Å at T = 200 K.

Ground state DFT calculations have been performed on the negatively charged $[PbI_3]^-$ cage, applying a methodology similar to that described in the previous section. The difference in the computed band gap $\Delta E_g = E_g(p) - E_g(p = ambient)$, as a function of pressure is given in Fig. 5.6b. At p = 0.25 GPa, the reduced lattice parameters and Pb-I bond lengths in the cubic $FAPbI_3$ phase initially leads to a slight reduction of the band gap. This reduction is caused by increased hybridization of the Pb-I antibonding states near the band edges leading to a shift in their energy. As discussed above, the phase transition to the tetragonal phase induces a reduction in the Pb-I-Pb angle within the ab-plane (see Fig. 5.7). At p = 0.49 GPa, the reduction of the Pb-I-Pb angle to about 170° gains in importance, leading to a slight increase of ΔE_g. When the angle decreases to 162.0° at p = 0.74 GPa, the tilting has a pronounced influence on the bonding. This is clear since the band gap difference ΔE_g becomes positive. At this pressure, the Pb-I-Pb angle governs the band gap, which now exceeds the initial band gap at ambient pressure.

5.4 Mechanical Properties of $FAPbX_3$ and Related Hybrid Perovskites

One of the advantages of the HOIPs compared to their inorganic counterparts is that the dynamical and soft nature of the hybrid framework provides further possible applications in

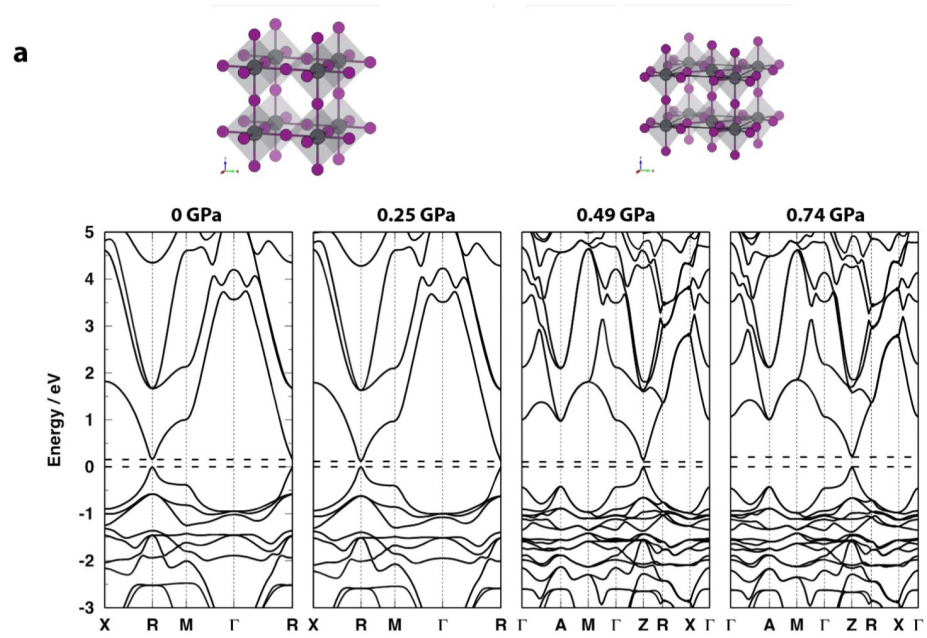

Fig. 5.7 Comparison of the calculated band structure and DOS of $FAPbI_3$ at four different hydrostatic pressures (ambient – 0.74 GPa) in which the FA^+ cation has been replaced by a positive background charge. The following high symmetry path was used for the primitive cubic structures X(0.5,0,0), R(0.5,0.5,0.5), M(0.5,0.5,0) and Γ(0,0,0) while for the primitive tetragonal structures it was Γ(0,0,0), A(0.5,0.5,0.5), M(0.5,0.5,0), Γ(0,0,0), Z(0,0,0.5), R(0,0.5,0.5), X(0,0.5,0) and Γ(0,0,0). Reproduced from Sun et al.[30] with permission from The Royal Society of Chemistry.

flexible and wearable functional devices[287]. As a consequence, the mechanical stability and deformation behavior of hybrid perovskites are attracting increasing attention. A recent computational study on the fracture of $MAPbI_3$ revealed that it is more compressible and ductile than inorganic perovskites, indicating its potential suitability for wearable devices[288]. Following some density functional theory (DFT) calculations on $MABX_3$ (B=Pb, Sn, and X=Br or I)[177], mechanical property measurements were made on similar compositions $MAPbX_3$ (X=Cl, Br or I), revealing Young's moduli in the range 10-20 GPa [176, 178, 180]. However, to the best of my knowledge, there have not been any systematic studies on the elastic properties or deformation behavior of FA-based halide perovskites. These materials are attractive because they have more optimal electronic band gaps and superior thermal stability[289] relative to their MA-based counterparts.

In this section, the anisotropic mechanical properties of $FAPbX_3$ (X=Br or I) obtained by nanoindentation and DFT calculations are described. The results are compared with other hybrid perovskite systems to understand the effects of compositional engineering on their

mechanical response. To better assess the specific effect of hydrogen bonding owing to the presence of the FA and MA cations, ab initio molecular dynamics is used to compare the bonding characteristics of $FAPbBr_3$ and $MAPbBr_3$ at room temperature. By comparing the results with those from previous nanoindentation studies on $MAPbX_3$ (X=I, Br or Cl) single perovskites[176, 178, 180], as well as on $(MA)_2MBiX_6$ (M=K, Tl or Ag, and X=Br or Cl) double perovskites[16, 26, 27], it is possible to assess the mechanical effects of making substitutions on the A, B, and X sites.

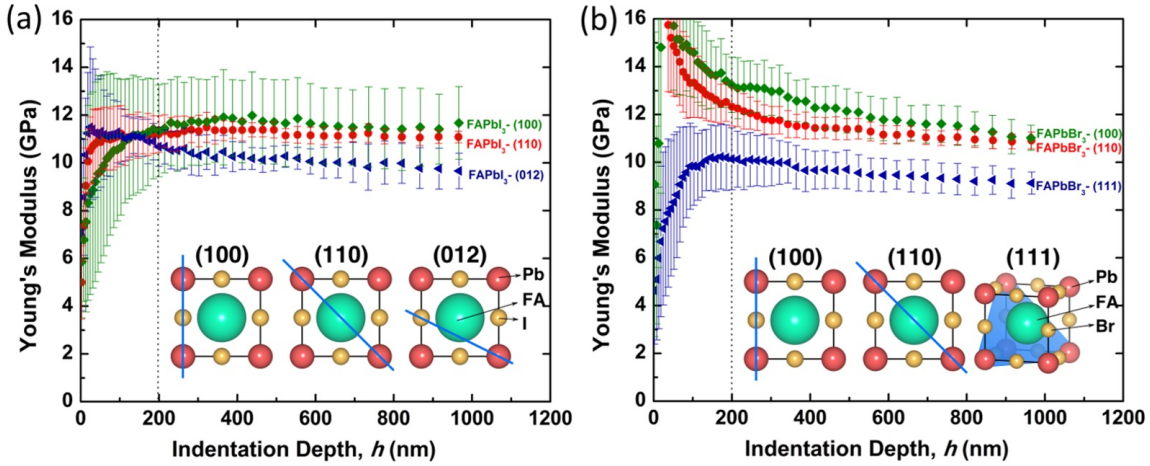

Fig. 5.8 (a) Young's moduli of cubic $FAPbI_3$ as a function of indentation depth. Indentations were conducted on (100), (110) and (012) facets and these planes are highlighted in blue on the unit cells. (b) Young's moduli of cubic $FAPbBr_3$ as a function of indentation depth with indentations conducted on (100), (110) and (111) facets. The Young's modulus obtained at each point is the average of 10 individual indents and the standard deviations are shown with error bars. Reproduced from Sun et al.[31] with permission from John Wiley & Sons.

5.4.1 Comparison between $FAPbBr_3$ and $FAPbI_3$

Both $FAPbI_3$ and $FAPbBr_3$ adopt the cubic ABX_3 perovskite architecture at room temperature with space group $Pm\bar{3}m$. Initially, the crystal structure of $FAPbI_3$ was thought to be trigonal (space group $P3m1$)[10], but this view was recently revised to cubic based on neutron diffraction measurements[157]. The perovskite frameworks consist of corner sharing $[PbX_6]$ octahedra, forming a three-dimensional inorganic network with the organic cation located in the A-site cavities. When the symmetry is cubic, the Pb-X-Pb bond angle is 180°. Nanoindentation experiments were conducted by Dr. Sun and co-workers on the X-ray detectable facets of $FAPbI_3$ and $FAPbBr_3$ single crystals up to an indentation depth of 1000 nm, as shown in Fig. 5.8, and Young's moduli as a function of indentation depths were calculated using

the Oliver-Pharr method[290]. Both $FAPbI_3$ and $FAPbBr_3$ show anisotropy in their stiffness with the overall Young's moduli ranging between 9 and 13 GPa. The perovskite structures are stiffest along the inorganic Pb-X-Pb chains, which are aligned along <100>. Unlike the previous findings with the MA analogues, where $MAPbBr_3$ is significantly stiffer than $MAPbI_3$, the Young's moduli and hardnesses of $FAPbI_3$ and $FAPbBr_3$ are not significantly different (Table 5.3).

Table 5.3 Mechanical properties of $APbX_3$ (A = MA, FA; X = Br, I). Reproduced from Sun et al.[31] with permission from John Wiley & Sons.

This work on $FAPbBr_3$ and $FAPbI_3$			
Crystal	Orientation	Young's Modulus (GPa)	Hardness (GPa)
$FAPbI_3$ Cubic	(100)	11.8 ± 1.9	0.37 ± 0.10
	(110)	11.3 ± 0.7	0.40 ± 0.05
	(012)	10.2 ± 0.5	0.36 ± 0.03
$FAPbBr_3$ Cubic	(100)	12.3 ± 0.8	0.43 ± 0.04
	(110)	11.5 ± 0.4	0.45 ± 0.03
	(111)	9.7 ± 0.8	0.36 ± 0.05
$FAPbI_3$ non-perovskite, hexagonal	(120)	8.2 ± 1.3	0.20 ± 0.02
Reported experimental studies on $MAPbBr_3$ and $MAPbI_3$*			
$MAPbI_3$ Tetragonal[28, 178, 180]	(100)	10.4 - 14.3	0.42 - 0.57
	(112)	10.7 - 14.0	0.46 - 0.55
$MAPbBr_3$ Cubic[28, 178, 180]	(100)	17.7-21.4	0.31-0.36
	(110)	15.6	0.26

*Data were taken from reported nanoindentation measurements to allow comparison with the present results.

Interestingly, the load-displacement curves for $FAPbI_3$ and $FAPbBr_3$ show discontinuities, as illustrated in Fig. 5.9. Similar discontinuities (pop-ins) have been observed previously in organic-inorganic formate perovskites and were attributed to the breaking of hydrogen bonds[32, 291, 292]. Recently, Reyes-Martinez et al. reported the time- and rate-dependent creep behavior of MA- and Cs-based perovskites[180]. They credited the first pop-in positions to the onset of dislocation-led plastic deformation during the indentation. The observed plastic deformation indicates good ductility in these hybrid perovskite systems. Crystallizing in the cubic space group $Pm\bar{3}m$, both $FAPbBr_3$ and $FAPbI_3$ are expected to slip most easily on the {110} <111> slip system. This is consistent with the observation that the

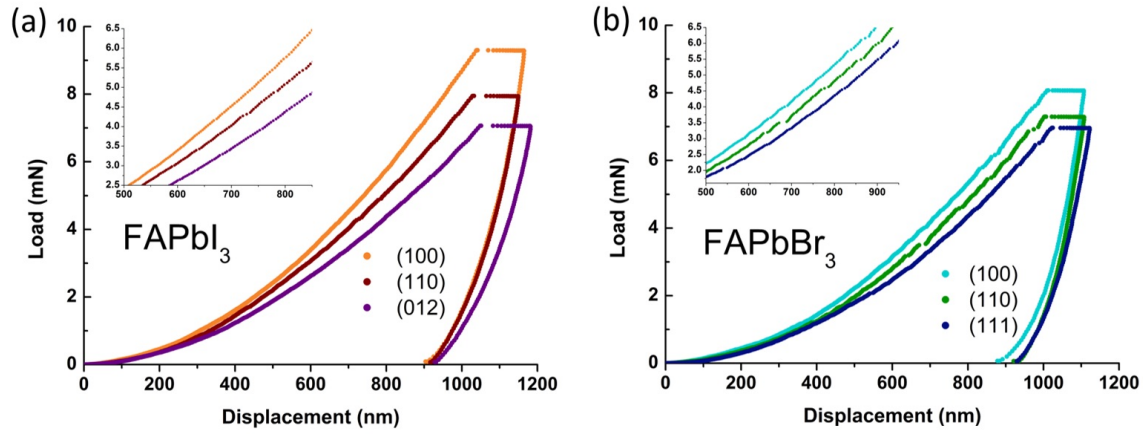

Fig. 5.9 Typical load-displacement curves for (a) cubic $FAPbI_3$ and (b) cubic $FAPbBr_3$. Sections of the loading curves are enlarged and presented in the insets. Indentations were conducted in the dynamic displacement controlled continuous stiffness measurement (CSM) mode[32], until reaching 1000 nm, where the tip was held for 30s with constant loading before unloading. Pop-in events, shown as discontinuities in the loading curves (between 500 nm and 950 nm), are observed in both perovskites, suggesting a series of dislocation nucleation events and associated hydrogen bond breaking. Pop-in events are more pronounced in the bromide perovskite than in the iodide. Reproduced from Sun et al.[31] with permission from John Wiley & Sons.

most frequent and strongest pop-in events are seen on the (110) plane (see Fig. 5.9, insets). On the other hand, the results of the hardness show a less clear trend as the differences between the facets are within the standard deviations (see Fig. B.5). It is seen in Fig. 5.9 that the more pronounced pop-in events occur in $FAPbBr_3$ suggesting that it takes more energy to break the hydrogen bonds in the bromide rather than the iodide owing to the higher electronegativity of the bromine ion.

One significant feature observed in cubic $FAPbI_3$ is a change in properties as it undergoes a phase transition from a perovskite to a non-perovskite structure. The black cubic phase of $FAPbI_3$ is metastable at room temperature and transforms to a yellow hexagonal one-dimensional chain structure within a few days[10]. This hexagonal phase adopts space group $P6_3/mc$ and forms chains of face sharing octahedra along [001] with the FA cations located between the inorganic chains. Leaving the perovskite crystals at ambient conditions for two weeks yielded the hexagonal polymorph with poor crystal quality (see Fig. B.4). The elastic response measured from the freshly synthesized hexagonal phase showed that the interchain stiffness is lower than the three-dimensional framework, with a Young's modulus of 8.2 GPa normal to (120) (Table 5.3 and Fig. B.6). It was not possible to make measurements along the chain direction.

Table 5.4 Physical properties of $APbX_3$ (A = MA, FA, X = Br, I) at room temperature. Reproduced from Sun et al.[31] with permission from John Wiley & Sons.

Crystals	Space group	Tolerance Factor[133]	Pb-X distance (Å)
$FAPbBr_3$	$Pm\bar{3}m$	1.008	2.998
$MAPbBr_3$	$Pm\bar{3}m$	0.927	2.966[119]
$MAPbI_3$	$I4/mcm$ ($I4cm$,$Fmmm$)	0.912	3.146-3.199[119]
$FAPbI_3$	$Pm\bar{3}m$	0.987	3.178[30]

Now the effect of the FA cation on the mechanical properties was considered. In the literature, the influence of the A-site cation is still a topic of discussion with previous reports suggesting that the organic molecule in a hybrid perovskite simply acts to balance the charge and fill the space inside the 12-fold cavity and contributes little to the mechanical behaviour[180]. It is important to mention that the mechanical properties of $FAPbI_3$ are not readily compared to those of $MAPbI_3$ owing to their different crystallographic symmetries at room temperature. The unit cell of cubic $FAPbI_3$ is larger than that of tetragonal $MAPbI_3$ at room temperature, but the Pb-I bond lengths are very similar in both structures (see Table 5.4). From consideration of the Pb-I-Pb bond angles, the octahedral tilting in $MAPbI_3$ is expected to affect the mechanical properties as the deviation of these angles from 180° in $MAPbI_3$ should reduce its stiffness along <100>; however, such tilting also indicates that the tetragonal structure at room temperature is more closely packed than its tolerance factor reveals.

5.4.2 Comparison between $FAPbBr_3$ and $MAPbBr_3$

As $FAPbBr_3$ and $MAPbBr_3$ both crystalize in the same cubic space group, a direct comparison can be made between them. Interestingly, the Young's moduli of $FAPbBr_3$ are substantially lower than those of $MAPbBr_3$ along all indentation directions (Table 5.3). Replacing the MA cation with the larger FA cation increases the Pb-Br bond length by about 1%[293] and weakens the inorganic framework. The lower Young's modulus of $FAPbBr_3$ is evidence that the Pb-Br bond strength is an important factor determining the elastic response of single Pb-based hybrid perovskites. Another aspect of the difference between FA- and MA-based perovskites is their hydrogen-bonding characteristics. One reasonable indicator of the hydrogen-bonding strength in hydrogen-bonded systems is the d_{Y-X} interatomic distance[273, 294], where, in this case, Y = N (or C) and X = Br. However, such distances are difficult to measure using X-ray diffraction in the present system because of the difference

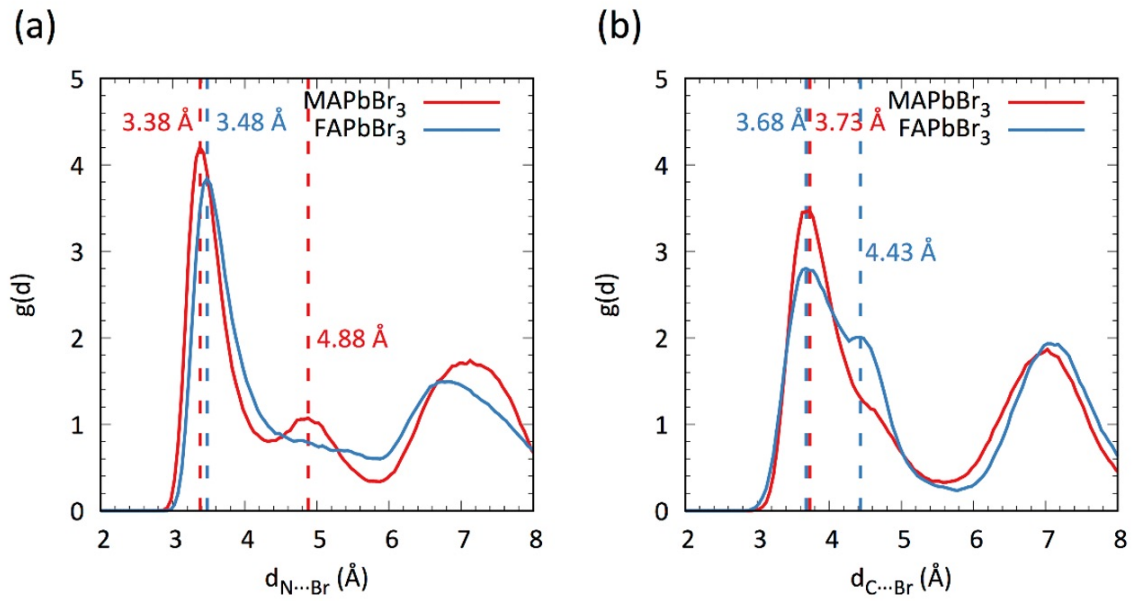

Fig. 5.10 Computed radial distribution functions (g(d)) of $MAPbBr_3$ and $FAPbBr_3$ for (a) N···Br and (b) C···Br interatomic distances. Reproduced from Sun et al.[31] with permission from John Wiley & Sons.

in atomic number between Br and N (or C) and the presence of FA cation disorder at room temperature. Recent X-ray studies on $MAPbBr_3$ and $FAPbBr_3$ have simply focused on the Pb-Br bond lengths and other distortions of the inorganic framework using X-ray pair distribution functions (PDFs)[295, 152, 33]. Therefore, to further understand the effects of hydrogen bonding on the stiffness of $MAPbBr_3$ and $FAPbBr_3$, ab initio molecular dynamics (AIMD) calculations were performed at 300 K. The results, presented in terms of pairwise radial distribution functions (RDFs), are shown in Fig. 5.10, which shows the statistics of interatomic distances throughout the calculations.

Fig. 5.10a shows that the 1st peaks corresponding to the closest N···Br interatomic distances are at around 3.38 and 3.48 Å for $MAPbBr_3$ and $FAPbBr_3$, respectively. However, the closest C···Br distances are longer (3.73 and 3.68 Å) in $MAPbBr_3$ (∼0.05 Å) than in $FAPbBr_3$, as shown in Fig. 5.10b. Hydrogen bonding depends mainly on the electronegativity of the hydrogen bond donor (C and N here) and the electronegativity of N (3.0) is much larger than C (2.5)[296], hence, the strength of the hydrogen-bonding interaction in N-H···Br is much greater than in C-H···Br. The N···Br distance is a good indicator of the strength of hydrogen bonding and there is a significant difference (∼0.1 Å) in N···Br between $MAPbBr_3$ and $FAPbBr_3$, suggesting that hydrogen bonding in the former is stronger. Previous calculations on $MAPbI_3$ indicated that the MA cation is not located at the center of

the cubic unit cell and molecular translation is very important for stabilizing the structure due to the N-H$\cdots$I hydrogen-bonding interaction[297]. One explanation for the different RDFs could be the different hydrogen-bonding characteristics in $MAPbBr_3$ and $FAPbBr_3$ originating from the symmetry of the organic cation, whereby MA can deviate from the center of the 12-fold inorganic cage more than FA, as FA has a mirror plane containing the C-H bond direction. In addition, the cationic charge is distributed over its entire structure through the π system for $FAPbBr_3$. The same effect was seen experimentally in the low-temperature iodide perovskites, in which the N$\cdots$I distance is longer and the C$\cdots$I distance is shorter in $FAPbI_3$ compared to $MAPbI_3$[30]. The weaker hydrogen bonding in $FAPbBr_3$ contributes to its low stiffness. Applying $\pm 1\%$ strain along the a-axis of the unit cell it was found that the hydrogen bonds were neither compressed nor stretched (see Fig. 5.11), indicating the superior adaptability of the inorganic frameworks to applied load and the mechanical flexibility of $MAPbBr_3$ and $FAPbBr_3$.

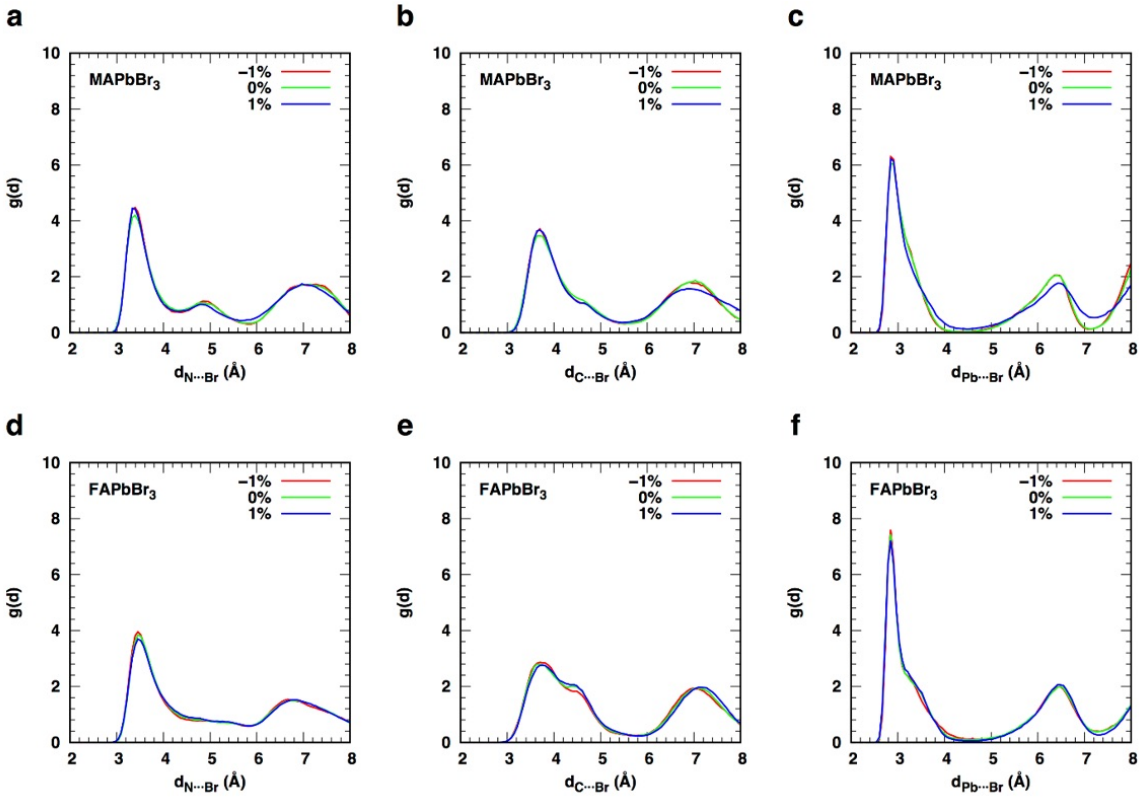

Fig. 5.11 The effect of strain (1%) on the RDF of cubic $MAPbBr_3$ and $FAPbBr_3$ for $N\cdots Br$, $C\cdots Br$ and $Pb\cdots Br$ distances obtained from the AIMD calculations. Reproduced from Sun et al.[31] with permission from John Wiley & Sons.

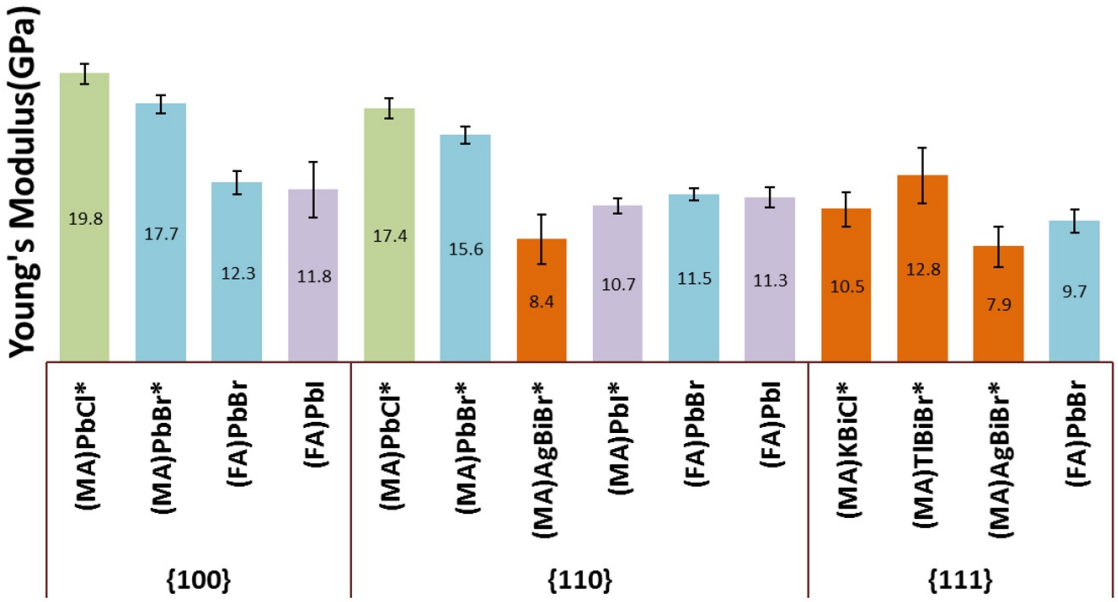

Fig. 5.12 Young's moduli of single and double hybrid halide perovskites normal to the {100}, {110} and {111} planes, respectively. Comparisons of elastic properties of $APbX_3$ with A_2MBiX_6 (A = MA or FA, M = K, Tl or Ag and X = I, Br or I) are shown. For the tetragonal ($MAPbI_3$) and rhombohedral (MA_2KBiCl_6) systems, the equivalent cubic planes are used. All values were determined by nanoindentation using the Oliver-Pharr method at room temperature. *Young's moduli were taken from Ref [28] for $MAPbX_3$ and Refs ([16, 26, 27]) for the double perovskites. Perovskite compositions were labelled with the atom names, instead of the full chemical formulae for presentation purpose. The Cl-, Br- and I-based single perovskites are marked in green, blue and purple respectively. All the double perovskites are marked in orange. Reproduced from Sun et al.[31] with permission from John Wiley & Sons.

5.4.3 Summary of the Mechanical Properties of Halide Perovskite

To further explore the structure-property relationships underlying the observed mechanical behavior, the results were compared with other systems in the broader halide HOIP family. Fig. 5.12 summarizes the reported mechanical properties of single- and double-hybrid halide perovskites to date. When looking at double perovskites with the general formula A_2MBiX_6 (A=MA, M=a monovalent cation), it is found that replacing the B-site ion, Pb^{2+}, with a monovalent cation and a trivalent cation, in this case Bi, reduces the overall stiffness. This trend likely originates in the weaker bonds between the monovalent ion and the halide, which allow for elastic deformation to occur at relatively low stress. A similar phenomenon has been observed in metal-organic frameworks, such as $Zn(Im)_2$ (Im=imidazole), where the stiffness is three times higher than its lithium boron analogue, $LiB(Im)_4$[259].

Considering the effect of the halide, the general trend for the single perovskites is that the stiffness decreases as the electronegativity of the halogen decreases, that is, from Cl to Br to I (green, blue, and purple histograms, respectively, in Fig. 5.12). The smaller electronegativity causes a reduction in Pb-X bond strengths. Concerning the anisotropy of the stiffness, <100> directions in the cubic perovskites are the strongest as they lie along the direction of the lead halide bonds. Fig. 5.13a shows that across the family of lead-based single halide perovskites, longer Pb-X bond distances lead to lower mechanical stiffness. The approximately linear dependence of Young's modulus on bond distance is not observed in double perovskites, as seen in Fig. 5.13b, c. Clearly, the presence of both monovalent and trivalent metal cations in the structure disturbs the uniformity of the bonding and the elastic response of the double perovskite cannot be represented by a single-bond distance.

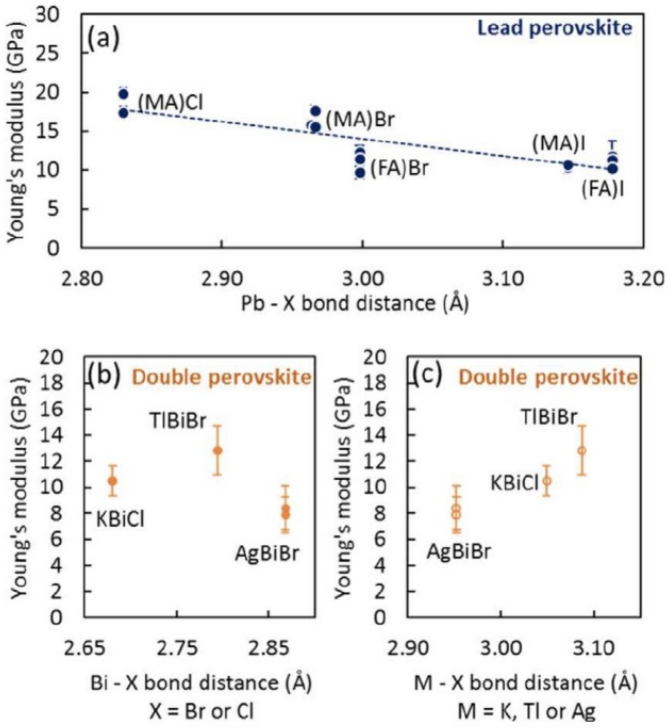

Fig. 5.13 Young's moduli of hybrid halide perovskites as a function of metal-halogen bond distance at room temperature for lead-based single MA and FA perovskites shown in (a)[33], and lead-free double MA perovskites in (b) and (c)[16, 26, 27]. Different data points on the same materials refer to Young's moduli along different crystallographic directions. For $MAPbI_3$, which is tetragonal,, the shortest Pb-I distance was used[33]. Perovskites with different compositions were labelled with the atom names instead of the full chemical formulae. The dotted line is to guide the eye. Reproduced from Sun et al.[31] with permission from John Wiley & Sons.

Interestingly, from Fig. 5.13a, the Young's modulus of $FAPbBr_3$ is lower than expected from its bond strength compared to $MAPbBr_3$. The tolerance factor of $FAPbBr_3$ is high (1.01)[132], indicating that the structure is on the edge of the stability range for a three-dimensional perovskite. Recently, $FAPbBr_3$ and $MAPbBr_3$ were reported to undergo a phase transition to a body-centered cubic structure (space group $Im\bar{3}$) at 0.53 and 0.9 GPa, respectively, using high-pressure X-ray diffraction[119]. The lower phase transition pressure for $FAPbBr_3$ further indicates that it is less mechanically stable than its MA counterpart under external load. One factor is likely to be the weakness of the hydrogen bonding in $FAPbBr_3$, as discussed above. Another factor is that for perovskites with high tolerance factors, the accommodation of large cations increases the possibility of local octahedral tilting, which reduces their mechanical stability while attempting to maintain the overall cubic structure (See Fig. B.7). It should be noted that a hard sphere model was used in the tolerance factor approach, assuming the cations are fully disordered at room temperature. The effect of the asymmetric cation shape on the lattice distortions, however, is not captured in the tolerance-factor calculations. Considering ionic size effects in double perovskites, the mechanical properties of a range of existing and hypothetical hybrid double perovskites were calculated using DFT in space group $R\bar{3}m$[26] as shown in Chapter 4. The results revealed that although most double perovskites are most stiff along the inorganic bond direction, for compositions with high tolerance factors, directions parallel to the C-N bonds of the MA cation become the stiffest, highlighting the role of cationic steric effects and hydrogen bonding.

5.5 Relationship Between Mechanical Properties and Transport Properties

The tunable electronic and optical properties of perovskites described in Chapter 2 are strongly related to key structural distortions within the perovskite unit cell (e.g., tilting of the inorganic octahedra). Previous experimental[298] and theoretical[165, 18, 272] studies have shown that the band gaps of halide perovskites can be tuned by adjusting the degree of octahedral tilting. In particular, the optical band gap increases as the degree of octahedral tilting increases. Furthermore, the previous work has predicted that octahedral tilting increases the effective electron mass, an important quantity affecting electrical conductivity[272]. In this section we present a DFT study linking mechanical property with electron transport. In hybrid halide perovskites containing the methylammonium cation (MA, CH_3NH_3), this octa-

hedral tilting is amplified by hydrogen-bonding interactions between the amine cation and the inorganic framework[272, 129, 299]. These results indicate that hydrogen-bonding can dramatically change the atomic structure within the unit cell, which in turn has a significant effect on the fundamental photovoltaic properties of these materials.

Recently, Motta et al.[164] showed that the band gap of cubic $MAPbI_3$ becomes indirect when the MA cation orients along the [011] direction. This indirect band gap is caused by Rashba splitting, a direct result of hydrogen-bonding-induced inversion symmetry breaking[300, 257]. In addition, hydrogen-bonding plays a key role in the photostriction mechanism. According to a previous experimental study,[301] the photons induce charge transfer from the valence band maximum, which is composed of Pb 6s-I 5p hybridized orbitals, to the conduction band minimum, composed of Pb 6p orbitals. This transition weakens the hydrogen-bonding interactions between the three H ions bonded to N in the MA cation and three neighboring I ions due to an electron density reduction on the I sites, and then makes the Pb-I interatomic length longer.

Interestingly, the MA cation itself can also affect the electrical transport properties of hybrid halide perovskites without any lattice distortion. In particular, Ma and Wang have proposed that the carrier mobility of the tetragonal $MAPbI_3$ phase is influenced by the randomly oriented MA cation, causing a fluctuation of the electrostatic potential[302]. It is also worth noting that hydrogen-bonding and the structural distortion caused by the MA cation are closely related to the material's elastic properties, although the details have yet to be investigated thoroughly. Previous studies[291, 303, 264] have shown that molecular cations dramatically enhance the elastic response of hybrid framework materials, particularly those with the perovskite architecture. Furthermore, this elastic enhancement can affect the electrical transport properties of the material within the acoustic-phonon scattering regime[304–307]. Hence, it is of fundamental importance to clearly elucidate the effect of the MA cation on both the elastic and transport properties of hybrid perovskites. Despite extensive previous studies[304–313, 274, 314, 180, 315, 28, 178, 177, 316–318], on understanding of the role of the MA cation on these properties is still lacking.

In this section, van der Waals (vdW) corrected DFT calculations were used to (i) identify how the MA cation influences the octahedral distortion of the structure and (ii) compute and understand the effect of this cation on the material's mechanical and transport properties, namely the elastic moduli and carrier mobilities. Here the orthorhombic structural model for all halide perovskites considered was adopted since the MA cations are ordered in the orthorhombic phase[108]. The systems studied are ABX_3 and $MABX_3$, where A = K, Rb, Cs and Fr, and B = Sn and Pb. The X-site halogens are Cl, Br and I. Choosing the orthorhombic

model consistently across the series allows us to accurately predict the contribution of the MA cation to the fundamental properties of these perovskites. It is acknowledged that some of these materials might not exist experimentally or do not normally adopt the orthorhombic perovskite structure, but the aim is to explore trends in behavior. Although the MA cations are disordered in the higher temperature tetragonal and cubic phases, the results are relevant to the these phases, too, because the MA-induced lattice distortion can dynamically appear in them as well[319, 320]. In summary, the main purpose of this part of the chapter is to clarify the above mentioned issues using vdW-corrected DFT calculations. It is shown that the combined effects of steric and hydrogen-bonding interactions of the MA cations enhance the elastic properties of the hybrid perovskites relative to their inorganic counterparts. Moreover, MA-induced octahedral tilting increases the effective carrier masses which results in a reduction in carrier mobility.

5.5.1 Octahedral Tilting

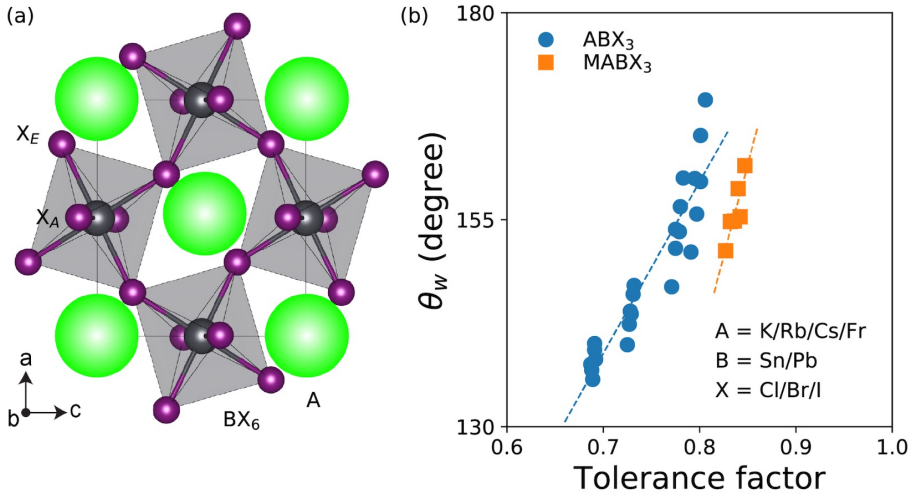

Fig. 5.14 (a) The orthorhombic *Pnma* perovskite structure consisting of BX_6 octahedra (grey) and A site cations (green). (b) Computed weighted average bond angles (θ_w) between $B-X_A-B$ and $B-X_E-B$ as a function of the tolerance factor. Blue and orange symbols correspond to the o-ABX_3 inorganic and o-$MABX_3$ hybrid halide perovskites, respectively. Reproduced from Lee and Deng et al.[34] with permission from The Royal Society of Chemistry.

Fig. 5.14a depicts the orthorhombic perovskite structure (space group *Pnma*) composed of BX_6 octahedra and A-site cations. It is characterized by the octahedral tilt pattern ($a^-b^+a^-$)[134]. As shown in the figure, there exist two different types of X-site ion associated

with the BX_6 octahedra: (i) an apical X-site ion along the b-axis in the *Pnma* setting (labeled X_A) and (ii) an equatorial X-site ion located on the BX_6 octahedral plane (labeled X_E). This results in two different bond angles between the B sites and the X sites: $B-X_A-B$ and $B-X_E-B$. In order to capture the effect of octahedral tilting through these bond angles, weighted average bond angles were calculated defined by $\theta_w = [4\theta(B-X_A-B)+8\theta(B-X_E-B)]/12$. The weighting accounts for the relative multiplicities of the X_A and X_E sites. Fig. 5.14b shows θ_w as a function of the tolerance factor for all compositions. It is seen that octahedral tilting as defined by θ_w increases as the tolerance factor becomes smaller ($\theta_w = 180°$ refers to an untilted structure). This means that steric effects dominate octahedral tilting in halide perovskites. More importantly, Fig. 5.14b and Fig. 5.15 demonstrate that hybrid halide perovskites have octahedra that are more tilted compared to inorganic halide perovskites with the same tolerance factor. This is because hydrogen-bonding amplifies octahedral tilting in hybrid halide perovskites[272, 129]. Sn-based and Pb-based halide perovskites exhibit similar behavior. Thus, one can conclude that the hydrogen-bonding-induced octahedral tilting is a common feature of hybrid halide perovskites. This is consistent with the previous work[272].

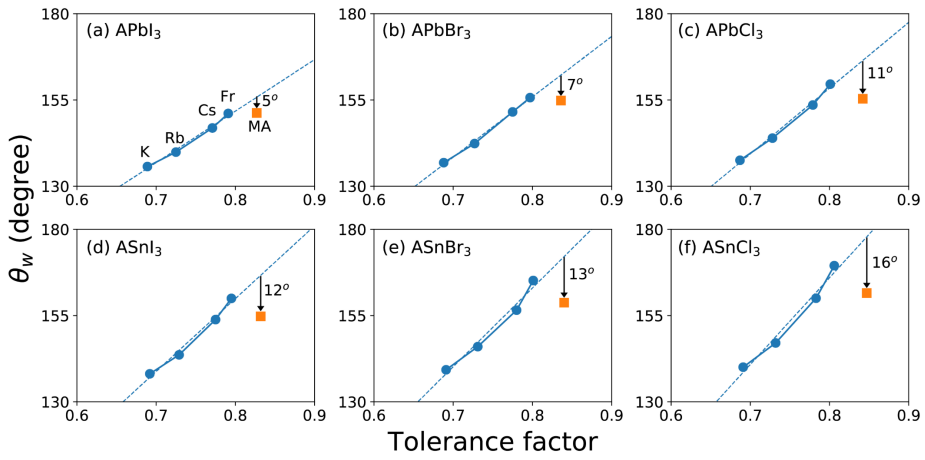

Fig. 5.15 Computed average bond angles (θ_w) as a function of the tolerance factor for (a) o-$APbI_3$, (b) o-$APbBr_3$, (c) o-$APbCl_3$, (d) o-$ASnI_3$, (e) o-$ASnBr_3$, and (f) o-$ASnCl_3$. Blue circles and orange squares show the inorganic and hybrid series respectively. Variations from the inorganic trend lines are denoted by black arrows with their magnitudes.

Fig. 5.15 shows that the angular deviation from the trend line increases across the halogen series (I-Br-Cl) due to the increasing electronegativity of the X-site halogen anion. The electronegativity increases in the sequence I-Br-Cl, and this increase enhances the hydrogen-bonding interaction and hence the tilting. The octahedra in the inorganic Pb

phases are slightly more tilted than in the Sn phases, but the results for the MA phases indicate that the hydrogen bonding effect is nevertheless greater for Sn compared to Pb, as judged by the distances below the dotted lines for the MA systems in Fig. 5.15. The electronegativity of Sn is less than that of Pb[321] and so the X-site halogen anion bonded to Sn tends to have more electron density compared to that bonded to Pb. Hence the Sn-based hybrid halide perovskites have slightly stronger hydrogen-bonds than the Pb-based hybrid halide perovskites. These trends agree well with the computed bond angle θ_w, H-index, and non-covalent interaction calculations (see Fig. 5.15, B.8, and B.9). This hydrogen-bonding-induced lattice distortion and hydrogen-bonding itself may affect structural properties and electronic structure. Therefore, it is very important to quantitatively understand the effect of the MA cation on the elastic and transport properties of hybrid halide perovskites.

5.5.2 Elastic Properties

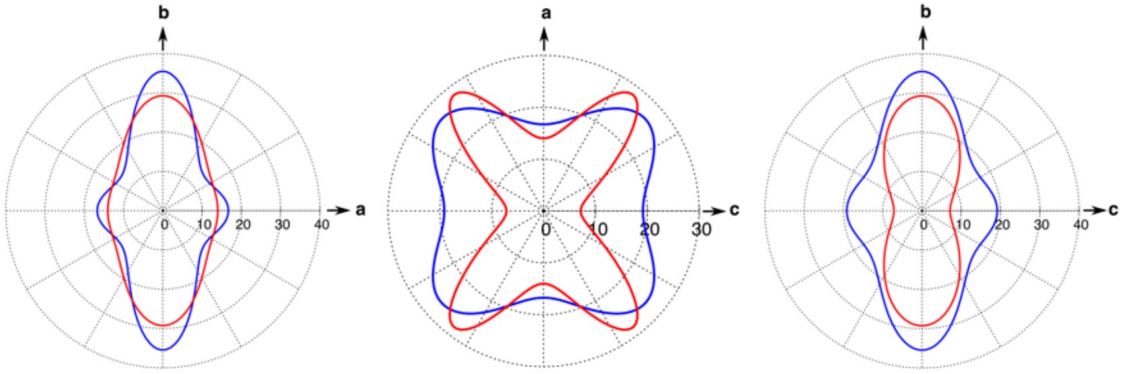

Fig. 5.16 Directionally-dependent Young's modulus E of o-$MAPbI_3$ (blue) and o-$CsPbI_3$ (red) in the ba-, ac-, and bc-planes of the orthorhombic structure. Circles indicate the magnitude of E (GPa). Reproduced from Lee and Deng et al.[34] with permission from The Royal Society of Chemistry.

Having demonstrated how the MA cation influences the lattice distortion of the perovskite structure, now the elastic moduli of both the inorganic o-ABX_3 and hybrid o-$MABX_3$ series were examined. By way of illustration, Fig. 5.16 compares the directionally dependent Young's modulus E of o-$MAPbI_3$ and o-$CsPbI_3$. It is seen that both perovskites exhibit highly anisotropic moduli but that the shapes of the curves are very similar, particularly in terms of the directions of the maxima and minima. Any differences are due to hydrogen bonding or

steric effects, as discussed below. However, the overall similarity of the curves shows that the PbI_3 inorganic framework is mainly responsible for the stiffness of o-$MAPbI_3$.

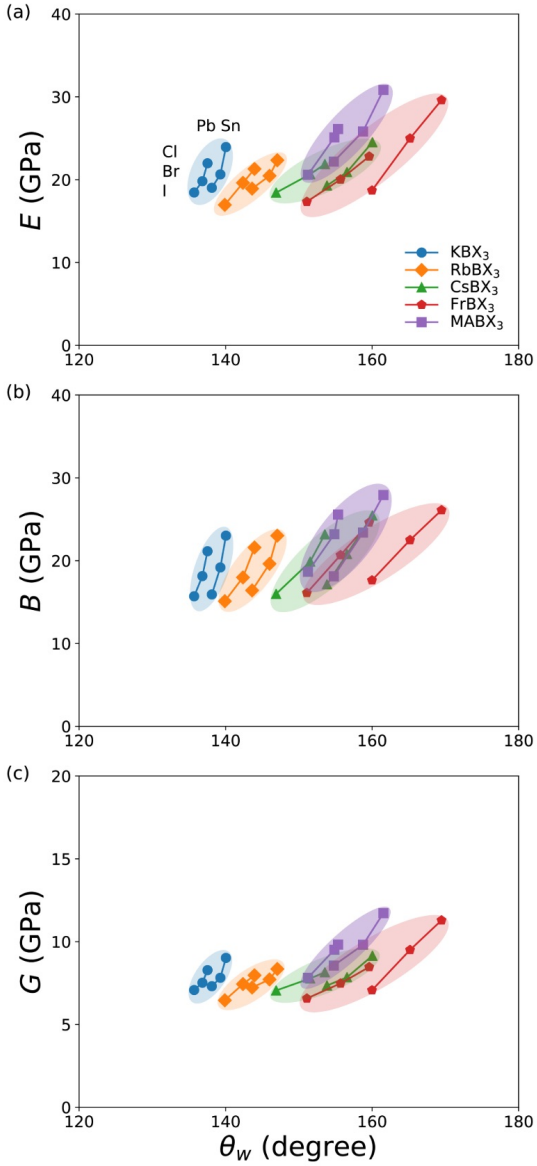

Fig. 5.17 (a) Young's modulus E, (b) bulk modulus B, and (c) shear modulus G as a function of θ_w for the o-ABX_3 inorganic and o-$MABX_3$ hybrid series. Different colors refer to different A-site cations. Reproduced from Lee and Deng et al.[34] with permission from The Royal Society of Chemistry.

Based on this, the effect of chemical substitution on the elastic properties of the halide perovskites is addressed. Fig. 5.17 shows the computed polycrystalline (orientationally-averaged) Young's modulus E, bulk modulus B, and shear modulus G as a function of θ_w.

The numerical values are given in Table B.7. In Fig. 5.17, it can be clearly seen that the elastic moduli generally increase as the X anion is substituted in the sequence I-Br-Cl[28]. In addition, Sn-based halide perovskites have larger moduli than Pb-based halide perovskites. This is because the B-X bond strength increases as the ionic radii of the X-site ions decreases. However, the A-site cations do not contribute as much to the elastic moduli as the B and X-site cations. Interestingly, for o-$FrSnBr_3$ and o-$FrSnCl_3$, all the polycrystalline moduli are larger than those of other Sn-based halide perovskites. This is because Fr ions fit well into the SnX_3 cages compared to other inorganic halide perovskites, making their structures more close-packed. The large tolerance factors of o-$FrSnBr_3$ and o-$FrSnCl_3$ (over 0.8) and their average bond angles θ_w (about 170°) also support this. More interestingly, the polycrystalline moduli of the hybrid halide perovskites are generally larger than those of the inorganic halide perovskites, as seen in Fig. 5.17, where purple squares corresponding to the former are slightly above others in the series. This indicates that the MA cation enhances the elastic properties of hybrid halide perovskites, which will be addressed in more detail below.

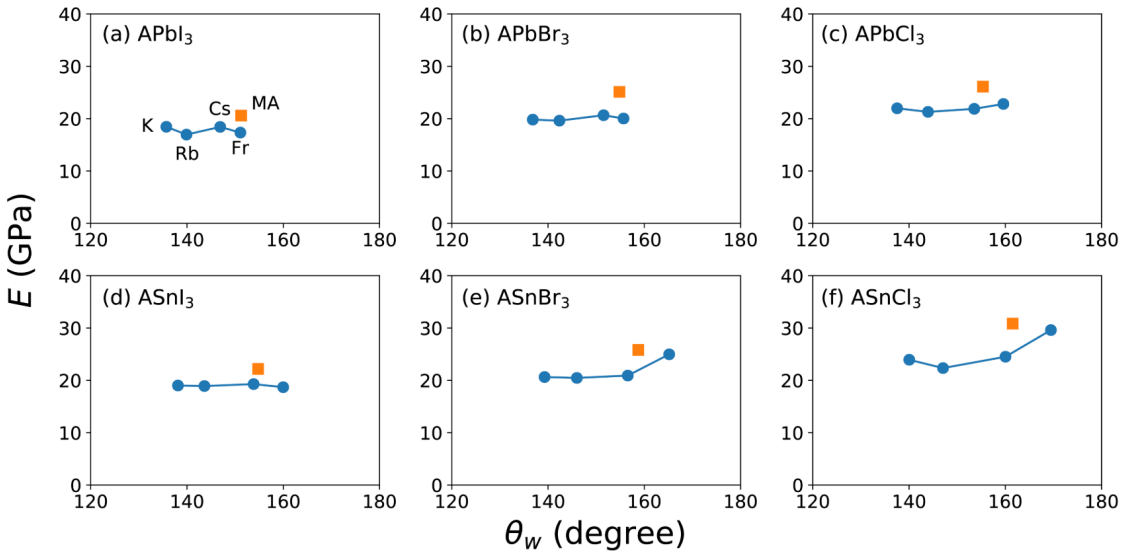

Fig. 5.18 The orientationally-averaged Young's modulus E versus θ_w for (a) o-$APbI_3$, (b) o-$APbBr_3$, (c) o-$APbCl_3$, (d) o-$ASnI_3$, (e) o-$ASnBr_3$, and (f) o-$ASnCl_3$. Blue and orange symbols correspond to the o-ABX_3 inorganic and o-$MABX_3$ hybrid perovskites respectively. Reproduced from Lee and Deng et al.[34] with permission from The Royal Society of Chemistry.

To understand quantitatively how the MA cation influences the elastic properties of hybrid halide perovskites, we consider, for each halide series, how the three main moduli E, B and G vary as a function of θ_w. Fig. 5.18 illustrates the polycrystalline Young's modulus E where

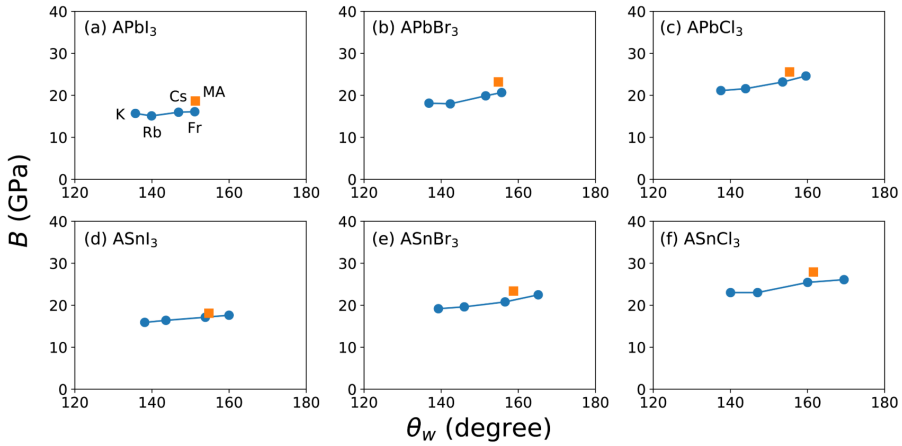

Fig. 5.19 The polycrystalline bulk modulus B versus θ_w for (a) o-$APbI_3$, (b) o-$APbBr_3$, (c) o-$APbCl_3$, (d) o-$ASnI_3$, (e) o-$ASnBr_3$, and (f) o-$ASnCl_3$. Blue and orange symbols correspond to the o-ABX_3 inorganic and o-$MABX_3$ hybrid halide perovskites respectively. Reproduced from Lee and Deng et al.[34] with permission from The Royal Society of Chemistry.

the orange symbols distinguish the hybrid perovskites from the inorganic perovskites shown in blue. The results for the bulk modulus B and shear modulus G are given in Fig. 5.19 and 5.20. Fig. 5.18 shows that the Young's moduli of the hybrid perovskites are always larger than those of inorganic perovskites, indicating their relative stiffness. The same effect is seen for the bulk and shear moduli, showing that hybrid perovskites are also more resistant to hydrostatic pressure and shear deformation. Focusing on the Young's moduli, it can be seen that for o-$MAPbI_3$, for example, E increases by about 19% compared to the inorganic trend line at the same θ_w. In fact, this enhancement is caused by a combination of effects, one due the stericity (conformation) of the MA cation and the other due hydrogen-bonding interactions. Unlike other A-site inorganic cations, the shape of the MA cation is not spherical but approximately cylindrical[272]. In particular, there are six H atoms attached to the C-N bond and these H atoms, which point in different directions, have an important effect on the perovskite's stiffness. Taking o-$MAPbI_3$ as an example, two of the H atoms forming the MA cation are oriented towards the c-axis of the perovskite while the other four are oriented towards the b-axis, as shown in Fig. B.10. Because of this, the stiffness components C_{22} and C_{33} of o-$MAPbI_3$ are larger than those of the inorganic iodide perovskites (see Table B.8), and the same is true within the other halogen groups as well. Thus, the unique conformation of the MA cation makes a significant contribution to the elasticity of hybrid halide perovskites. Furthermore, of course, the H atoms forming the MA cations interact with neighboring halogens via hydrogen bonds. It is suggested that this additional interaction also

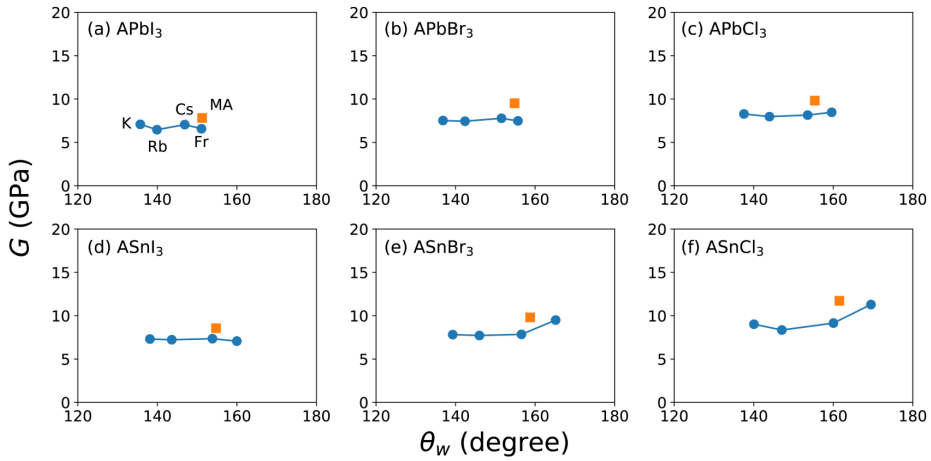

Fig. 5.20 The polycrystalline shear modulus G versus θ_w for (a) o-$APbI_3$, (b) o-$APbBr_3$, (c) o-$APbCl_3$, (d) o-$ASnI_3$, (e) o-$ASnBr_3$, and (f) o-$ASnCl_3$. Blue and orange symbols correspond to the o-ABX_3 inorganic and o-$MABX_3$ hybrid halide perovskites respectively. Reproduced from Lee and Deng et al.[34] with permission from The Royal Society of Chemistry.

enhances the elastic properties, although it is difficult to separate hydrogen-bonding effects from steric effects. Nevertheless, there is clear experimental evidence that the organic cation plays an important role. For instance, the measured Young's modulus of cubic $MAPbBr_3$ (15.6-21.4 GPa) is significantly larger than that of cubic $FAPbBr_3$ (9.7-12.3 GPa) and this can be attributed to the higher symmetry of the FA ($CH(NH_2)_2$) cation and its weaker hydrogen-bonding interaction[31].

Following the above discussion, it might be expected that an increase in the Young's modulus of a hybrid halide perovskite would also increase its charge carrier mobility. This is based on deformation potential theory[322], which relates elastic properties and carrier-phonon interactions to mobility and is represented by Eq. 5.2 above. At the same time, however, hydrogen-bonding-induced octahedral tilting can reduce the carrier mobility since it increases the charge effective mass[272]. Therefore, it is important to understand how the MA cation affects the charge transport properties of hybrid halide perovskites. This is addressed in more detail in the following section.

5.5.3 Electronic Transport Properties

The charge carrier mobilities of all the halide perovskites considered in this study were calculated within the acoustic phonon scattering regime of deformation potential theory[322]. The aim is to predict trends in behavior with respect to chemical changes rather than reproduce experimental values. This is because other scattering mechanisms, such as optical phonons,

defects, impurities or polarons, could also be playing a role. However, we believe that carrier-acoustic phonon scattering is appropriate at low temperatures (∼100K) where, for example, the o-$MAPbI_3$ structure is stable. At room temperature, there is evidence that scattering in tetragonal $MAPbI_3$ is dominated by carrier optical phonon scattering[313]. Nevertheless the topic continues to be discussed both theoretically and experimentally[308, 313, 274]. For example, several studies[304–307, 316] have highlighted the importance of carrier-acoustic phonon coupling, even at room temperature where mobilities in tetragonal $MAPbI_3$ have been observed[304, 323–325] to be proportional to $T^{-1.2} - T^{-1.6}$.

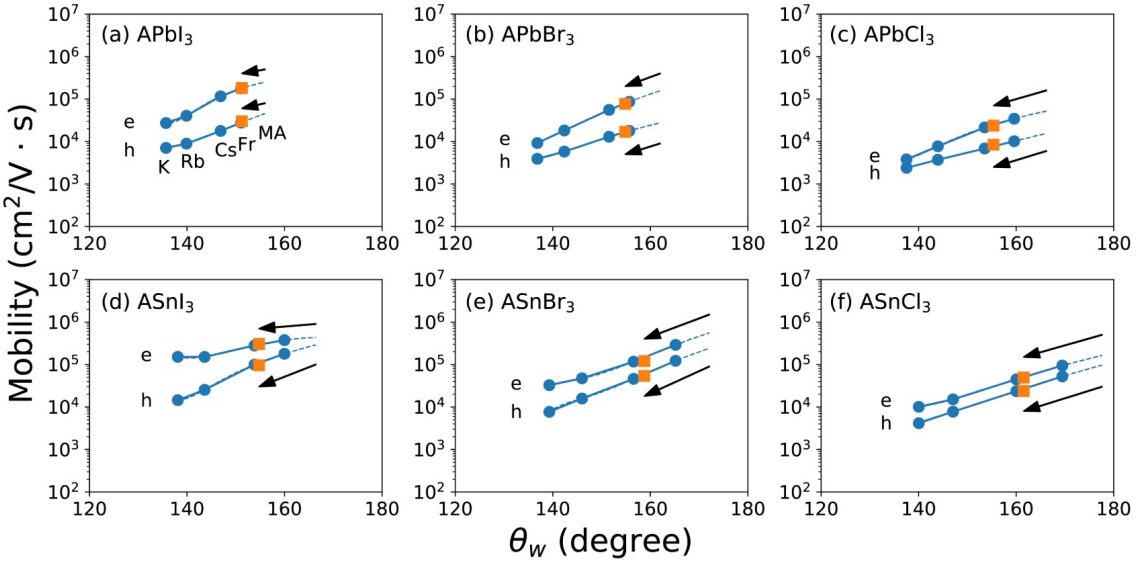

Fig. 5.21 Reduction of mobility due to MA-induced octahedral tilting. Average electron (e) and hole (h) mobilities along the three crystal axes versus θ_w for (a) o-$APbI_3$, (b) o-$APbBr_3$, (c) o-$APbCl_3$, (d) o-$ASnI_3$, (e) o-$ASnBr_3$, and (f) o-$ASnCl_3$. Blue and orange symbols correspond to the o-ABX_3 inorganic and o-$MABX_3$ hybrid halide perovskites, respectively. Arrows indicate the reduction in the e and h mobilities of o-$MABX_3$ with respect to what they would have been for hypothetical o-ABX_3 perovskites having the same size A-site cation. The arrows follow the extrapolated trend lines. The values are calculated at 100 K and shown in Table B.12. The results obtained at 300 K are given in Table B.13 and Fig. B.11. Reproduced from Lee and Deng et al.[34] with permission from The Royal Society of Chemistry.

In order to compute carrier mobilities (both electron and hole) using deformation potential theory, the corresponding deformation potentials and effective carrier masses along each crystal axis need to be determined. The results for the potentials and masses are given in Tables B.10 and B.11, respectively, and are comparable to values computed previously and experimental measurements[306–308, 316]. These values can then be used in Eq. 5.2,

together with the corresponding stiffness tensor components C_{ij}, to obtain the electron and hole mobilities for all the halide perovskites considered (Table B.12). Fig. 5.21 shows the computed mobilities averaged along the three crystal axes as a function of θ_w for each halide series. It is clearly seen that the average carrier mobilities increase with increasing average bond angle, i.e. decreasing octahedral tilt (recall that θ_w= 180° refers to an untilted structure). This is consistent with measurements in other perovskite systems, e.g. doped-$LaCoO_3$, where the carrier mobility is found to increase as θ_w approaches 180°[326]. Fig. 5.21 also shows that the electron mobility is always larger than the hole mobility for all halide perovskites. The calculated mobilities are comparable with previous computational studies[306, 312] on o-$MAPbI_3$ using deformation potential theory, taking into account differences in the temperatures considered. However, as found previously, they are much larger than experimental values, e.g. μ_e ~232 $cm^2/V \cdot s$ for $MASnI_3$, ~536 $cm^2/V \cdot s$ for $CsSnI_3$, ~66, ~25 and ~38 $cm^2/V \cdot s$ for $MAPbI_3$; μ_h ~105 $cm^2/V \cdot s$ for $MAPbI_3$[10, 71, 72]. While this may well be due to the presence of other scattering mechanisms or require methods beyond DFT (single-body theory), e.g. GW (many-body theory), the purpose of the present study is to predict trends in behavior, particularly at low temperatures, as noted above.

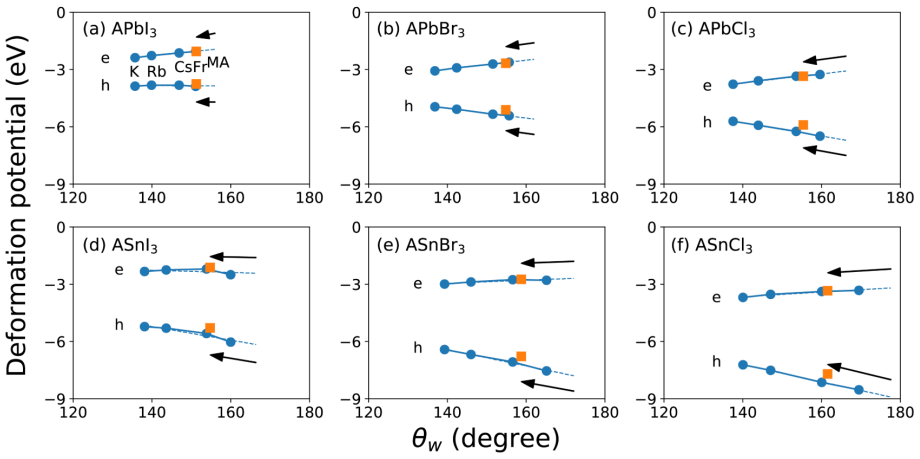

Fig. 5.22 Average deformation potential along the three crystal axes versus θ_w for (a) o-$APbI_3$, (b) o-$APbBr_3$, (c) o-$APbCl_3$, (d) o-$ASnI_3$, (e) o-$ASnBr_3$, and (f) o-$ASnCl_3$. Blue and orange symbols correspond to the o-ABX_3 inorganic and o-$MABX_3$ hybrid halide perovskites respectively. Arrows represent variations of electron (e) and hole (h) deformation potentials caused by hydrogen-bonding induced octahedral tilting. Reproduced from Lee and Deng et al.[34] with permission from The Royal Society of Chemistry.

An important feature of Fig. 5.21 is the reduction in charge carrier mobilities for hybrid halide perovskites. This is illustrated by the black arrows which indicate how the mobilities

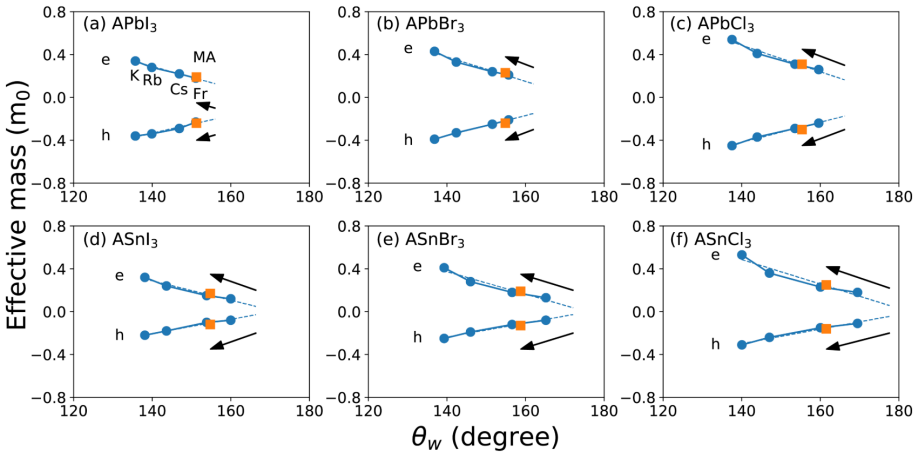

Fig. 5.23 Average effective carrier mass along the three crystal axes versus θ_w for (a) o-$APbI_3$, (b) o-$APbBr_3$, (c) o-$APbCl_3$, (d) o-$ASnI_3$, (e) o-$ASnBr_3$, and (f) o-$ASnCl_3$. Blue and orange symbols correspond to the o-ABX_3 inorganic and o-$MABX_3$ hybrid halide perovskites respectively. Arrows represent variations of electron (e) and hole (h) effective masses caused by hydrogen-bonding induced octahedral tilting. Reproduced from Lee and Deng et al.[34] with permission from The Royal Society of Chemistry.

of o-$MABX_3$ perovskites are reduced relative to what they would have been for hypothetical o-ABX_3 perovskites having the same size A-site cation. For o-$MAPbI_3$, for example, the reduction is nearly a factor of two (note the log scale) and this is caused by hydrogen bonding-induced octahedral tilting. Although the MA cation increases the polycrystalline elastic moduli (except Poisson's ratio) of hybrid halide perovskites, it also increases their average charge effective masses as shown in Fig. B.10. The effect on the average deformation potentials, however, is relatively small, particularly for electrons, and decreases for holes (Fig. 5.22). According to Eq. 5.2, the carrier mobility μ is proportional to m^2 , C and D^{-2} at a given temperature. Since the overall effect of the MA cation is to reduce the mobility, it is therefore apparent that the increase in charge effective mass is having a controlling influence. Thus, the octahedral tilting induced by the MA cation and its hydrogen-bonding interactions is directly affecting the masses of the charge carriers, as suggested in the earlier work[272]. It is clear, therefore, that to maximize the carrier mobility of a hybrid halide perovskite, the organic A-cation has to be chosen carefully so as to minimize the hydrogen-bonding interaction and the resulting rotation of the inorganic octahedra.

5.6 Summary

This chapter[1] has presented three studies concerning the temperature, pressure and transport properties of halide perovskites. In the first study, the variable temperature (100-450 K) and high-pressure (p = ambient - 0.74 GPa) crystal chemistry of the black perovskite formamidinium lead iodide, $FAPbI_3$, were investigated in collaboration with Dr. Sun and coworkers, using single crystal X-ray diffraction. In both cases a phase transition to a tetragonal phase was found. The experimental results were combined with first principles calculations, providing information about the electronic properties of $FAPbI_3$ as well as the most probable orientation of the FA^+ cations.

In the second study, the mechanical response of hybrid perovskites was systematically studied by investigating the behavior of systems containing the formamidinium (FA) cation. Despite the hypothesis that larger cations will lead to tighter packing and stiffer perovskites, it is found that $FAPbBr_3$ is more compliant than expected. There appears to be two main factors contributing to the observed mechanical behavior. First, the effect of hydrogen bonding is evident, as more pronounced pop-in events were observed in the bromide than the iodide perovskite. The calculations indicate that $FAPbBr_3$ exhibits weaker hydrogen bonding than $MAPbBr_3$, as the former shows longer $N\cdots Br$ distances at room temperature. Second, the longer Pb-Br bond length in $FAPbBr_3$ leads to a smaller Young's modulus compared to the values for $MAPbBr_3$. Comparing previous studies on the mechanical properties of hybrid organic-inorganic perovskites with the current work, it is found that although the bond strength of the inorganic framework is a main factor determining stiffness, the size of the organic cations becomes more important when the perovskites are at their limits of structural stability. This steric effect can be qualitatively captured by the tolerance factor. In addition, as the organic cations become ordered at lower temperatures, the importance of hydrogen bonding on mechanical stability is expected to increase. This effect will be interesting to explore in the future.

In the third study, the elastic moduli and charge carrier mobilities of a series of halide perovskites were systematically calculated in an effort to understand the effect of the MA organic cation on the mechanical and transport properties of hybrid perovskites. It was found that the elastic response of halide perovskites is mainly determined by the BX_3 inorganic frameworks. In addition, the unique steric and hydrogen-bonding effects introduced by the MA cation further increase the resistance of hybrid perovskites to elastic deformation. The results show that the conformation of the A-site organic cation and the strength of

[1] The results described in this chapter have been published in 2 papers, which are Ref. [30, 31] and another submitted work.

its hydrogen-bonding interactions with neighboring inorganic polyhedra play an important role in choosing suitable hybrid perovskites for devices with improved mechanical stability. However, this improved mechanical stability does not result in improved carrier mobility. Using deformation potential theory within the carrier-acoustic phonon scattering regime, it is shown that the carrier mobilities of hybrid halide perovskites are in fact reduced relative to what they would have been for an inorganic perovskite having the same size A-site cation, and that this is caused primarily by octahedral tilting and a concomitant increase in charge effective mass. Nevertheless, hybrid perovskites still have mobilities comparable with inorganic perovskites and their superior mechanical stability renders them competitive in the continuing search for the optimal perovskite-based solar cell material.

Chapter 6

Phase Stability and Electronic Structure of Low-Dimensional, Perovskite-Related Iodoplumbates

This chapter contains a work[35] on low dimensional guanidinium lead iodide. I contributed to this work equally with Dr. Shijing Sun.

6.1 Introduction

As discussed in Chapters 1 and 2, despite the excellent potential of hybrid lead perovskites, their susceptibility to thermal degradation and moisture absorption limits their use in practical devices[327]. As a consequence, perovskite-like structures which have reduced octahedral connectivity have attracted increasing attention due to their improved chemical stability[328, 77]. Most current research focuses on hybrid lead iodide perovskites with 3D octahedral connectivity since they exhibit the highest conversion efficiencies in photovoltaics[329]. Considering the size of the A-site cavity in an $APbI_3$ crystal, medium-sized organic cations, such as methylammonium (CNH_6, denoted MA) and formamidinium (CN_2H_5, denoted FA), crystallise in 3D perovskite forms. Smaller and larger cations, such as ammonium (NH_4) and ethylammonium (C_2NH_7, denoted EA), result in TFs less than 0.8 or greater than 1.0, respectively, and lead to the formation of lower dimensional architectures[330, 331]. Interestingly, some of the amines that have TFs close to the 0.8 and 1.0 boundaries can crystallize in more than one polymorph[66]. For example, formamidinium lead iodide forms both a black 3D perovskite and a yellow trigonal perovskite-like structure with a 1D

octahedral arrangement that is face-sharing[10]. Similarly, $CsPbI_3$ undergoes a reconstructive phase transition from a 1D PbI_6 edge-sharing structure to a 3D corner-sharing perovskite between 560 and 600 K[125, 332]. The study of polymorphisms is further motivated by the resulting changes in optical and electronic properties, and a recent report describes the role of the organic cations in the formation of the resultant polymorphs[333].

As an alternative to polar organic cations such as methylammonium, non-polar guanidinium (CN_3H_6, denoted Gua) forms an interesting range of halides. For instance, Kanatzidis and co-workers determined the structures of $GuaGeI_3$ and $GuaSnI_3$, and found them to be hexagonal with 1D octahedral connectivity that is either face-sharing or a combination of face-sharing and corner-sharing[333, 9]. Two compositions have been reported for guanidinium lead iodide, $GuaPbI_3$ and $(Gua)_2PbI_4$[334, 335, 225]. The triiodide has 1D octahedral connectivity whereas for the tetraiodide it is 2D. The observed low dimensionality of these iodides is consistent with the TF of the 3D perovskite form of $GuaPbI_3$, which is 1.03[132]. Computationally, only the hypothetical 3D structure has been studied[39]. As a way of enhancing carrier mobility and chemical stability further, mixed cation perovskites involving Gua have also been synthesised[336, 337]. For example, although devices employing pure $GuaPbI_3$ and $(Gua)_2PbI_4$ have yielded efficiencies of only 0.45%[338]. Soe et al. recently presented a series of low dimensional perovskites, $(C(NH_2)_3)(CH_3NH_3)_nPb_nI_{3n+1}$ (n = 1, 2 and 3) using guanidinium and formamidinium as interspacers and achieved an efficiency of 7.26%[339]. With growing interest in adding guanidinium cations to lead iodide systems so as to modify their optical properties and film stability[340], a thorough study of the structural characteristics and phase stability of Gua-based iodoplumbates is needed to guide the rational design of hybrid perovskite solar cell materials.

In this chapter, the synthesis, crystal structures and theoretical analysis of three Gua-based iodoplumbates are presented. The experimental results for $GuaPbI_3$ and $(Gua)_2PbI_4$ confirm the previous studies. In particular, $GuaPbI_3$ adopts the 1D NH_4CdCl_3-type connectivity at room temperature with edge-sharing octahedra and is labelled $GuaPbI_3$-e and $GuaPbI_3$-eRT in Fig. 6.1. However, as discussed below, it undergoes a displacive phase transition upon cooling (labelled $GuaPbI_3$-eLT in Fig. 6.1b) as a result of the reduced disorder of the guanidinium cations. $(Gua)_2PbI_4$ has 2D corner-sharing octahedral connectivity as previously reported[335], but a new composition, $(Gua)_3PbI_5$ is also synthesized and has 1D chains of corner-sharing octahedra. To better understand the observations, a number of density functional theory (DFT) calculations have been performed. In particular, the formation enthalpy of $GuaPbI_3$-e with two other hypothetical polymorphs, $GuaPbI_3$-c and $GuaPbI_3$-f, are compared; these exhibit corner-sharing and face-sharing octahedral connectivities,

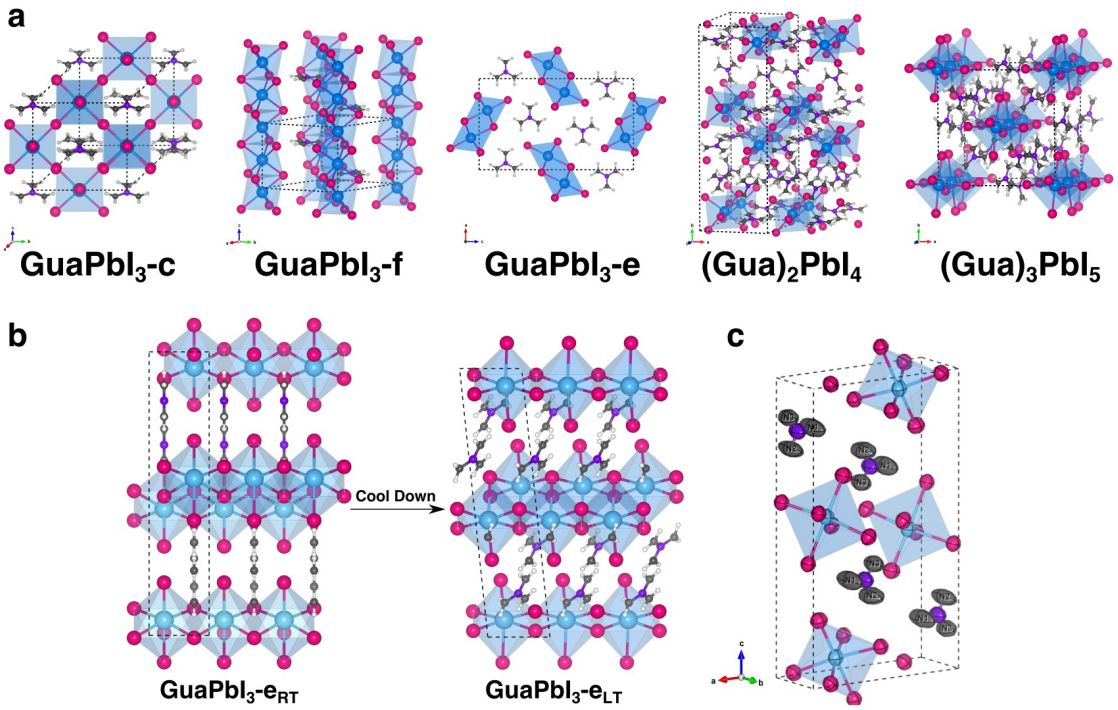

Fig. 6.1 (a) Two hypothetical polymorphs of $GuaPbI_3$ ($GuaPbI_3$-c and $GuaPbI_3$-f) and the observed structures of $GuaPbI_3$ ($GuaPbI_3$-e), $(Gua)_2PbI_4$ and $(Gua)_3PbI_5$. ("c", "f" and "e" denote corner-sharing, face-sharing and edge-sharing inorganic octahedra, respectively), (b) Phase transition of $GuaPbI_3$-e on cooling from room temperature (RT) to 120K (LT), (c) $GuaPbI_3$-eLT showing the observed thermal ellipsoids of guanidinium and the tilting of the inorganic octahedra found from the DFT calculations. Atom colours: Pb: blue, I: pink, N: purple, C: grey and H: silver. Reproduced from Deng et al.[35] with permission from the AIP Publishing.

respectively (see Fig. 6.1a). The structural properties of all three observed iodoplumbates are calculated and the band structures of $(Gua)_2PbI_4$ and $(Gua)_3PbI_5$ are compared to reveal the effects of octahedral connectivity and dimensionality on the electronic characteristics of this family of hybrid perovskites.

6.2 Method

The experimental synthesis and characterizations of the Gua-based iodoplumbate were carried out jointly with Dr. Shijing Sun and I performed all the DFT calculations. One of the precursors, guanidinium iodide (GuaI), was first prepared by adding guanidinium carbonate (8.03 g) to hydriodic acid (HI) (20 g, aqueous solution, 57 wt%) in equal molar amounts. A

white solid was obtained after removing water at 50 °C using a rotational evaporator. The product was stored in an argon glove box. Single crystals of $GuaPbI_3$ and $(Gua)_2PbI_4$ suitable for single-crystal X-ray diffraction were prepared using an adaptation of the Poglitsch and Weber method[151] in which lead iodide (Sigma-Aldrich) is reacted with stoichiometric solid guanidinium iodide in aqueous (57%) HI solution. The crystals could also be produced using lead acetate trihydrate instead of lead iodide. Lead acetate trihydrate (379 mg, 1 mmol) was added to the flask and dissolved in 1mL HI solution upon heating to 120 °C and 1 mmol of solid GuaI was added. The solution was then left to cool to 25 °C and transferred onto a crystallization dish. Yellow precipitates were collected upon evaporation of the solvent. The precipitates were found to contain a mixture of $GuaPbI_3$, $(Gua)_2PbI_4$ and $(Gua)_3PbI_5$ single crystals.

The resulting yellow needle-like, rectangular-shaped and prism-shaped crystals (see Fig. C.1) were characterised by single crystal diffractiometry using an Oxford Diffraction Gemini A Ultra X-ray diffractometer with Mo Kα radiation (λ = 0.7093 Å). CrysAlisPro software (Agilent Technologies) was used for data collection and reduction, unit cell determination and refinement, as well as for applying the face-based analytical absorption correction. The structure of $GuaPbI_3$ was solved by direct methods with SHELX in the Olex2 platform. All non-hydrogen atoms were refined anisotropically and hydrogen atoms were then added to the calculated positions. The crystal data are summarized in Table 6.1.

Optical band gap measurements were performed on a PerkinElmer Lambda 750 UV-Visible spectrometer in reflectance mode with a 2 nm slit width, a 1 nm interval and a wavelength range between 300 and 1200 nm. Bulk samples for UV-Vis measurement were prepared by grinding the $GuaPbI_3$ and $(Gua)_2PbI_4$ single crystals into fine powder. Measurements on $(Gua)_3PbI_5$ were not made because it was phase impure. The band gap was estimated using the Tauc method by converting the reflectance into a Kubelka-Munk function and plotting it against photon energy, $h\nu$ (Fig. 6.2).

The DFT calculations were performed using projector-augmented wave (PAW)[217, 270] pseudopotentials with the valence electrons from Pb ($5d^{10}6s^26p^2$), I ($5s^25p^5$), C ($2s^22p^2$), N ($2s^22p^3$) and H ($1s^2$) treated explicitly. The PBEsol[341] exchange-correlation functional was employed together with spin-orbit coupling (SOC). The complete methodology is implemented in the VASP code[242, 243]. A 500 eV planewave kinetic energy cutoff was used for all calculations and $3\times9\times2, 3\times3\times3, 3\times3\times3, 4\times2\times3$ and $3\times3\times3$ Γ centered k-point meshes were used for $GuaPbI_3$-e, $GuaPbI_3$-c, $GuaPbI_3$-f, $(Gua)_2PbI_4$ and $(Gua)_3PbI_5$ using the Monkhorst-Pack method[211]. Formation enthalpies (H_f) of $GuaPbI_3$-e, $GuaPbI_3$-c, $GuaPbI_3$-f were calculated using $H_f = E(GuaPbI_3) - E(C) - 3E(N) - 6E(H) - E(Pb) -$

Table 6.1 Crystallographic data and refinements of $(Gua)_3PbI_5$, $(Gua)_2PbI_4$ and $GuaPbI_3$ structures. H positions shown in the formula were not considered in the structural solution due to the difficulty of detecting light H in the presence of heavy Pb and I with X-ray diffraction. Reproduced from Deng et al.[35] with permission from the AIP Publishing.

Empirical formula	$C_3I_5N_9H_{18}Pb$	$C_2I_4NH_{12}Pb$	$CI_3N_3H_6Pb$
Formula weight	1021.95	834.97	641.93
Temperature/K	297.5(5)	293(2)	299.7(6)
Crystal system	Monoclinic	Monoclinic	Orthorhombic
Space group	$C2/c$	$P2_1/n$	$Pnma$
a/Å	13.0694(5)	9.2440(3)	11.9866(5)
b/Å	13.1946(5)	26.9511(11)	4.4740(2)
c/Å	12.7212(5)	12.7155(3)	20.8652(10)
α/°	90	90	90
β/°	91.276(4)	91.482(2)	90
γ/°	90	90	90
Volume/Å^3	2193.18(15)	3166.82(17)	1118.96(9)
Z	4	8	4
$\rho_{calc}\ g/cm^3$	3.095	3.503	3.81
mu/mm^{-1}	14.732	18.433	23.293
F(000)	1784	2880	1072
Crystal size/mm^3	0.17×0.09×0.06	0.35×0.11×0.06	0.72×0.08×0.07
2θ range /°	4.388 to 56.64	3.542 to 56.848	3.904 to 46.496
Index ranges	$-17 \le h \le 11$, $-11 \le k \le 17$, $-16 \le l \le 14$	$-9 \le h \le 12$, $-35 \le k \le 15$, $-17 \le l \le 13$	$-13 \le h \le 11$, $-4 \le k \le 4$, $-22 \le l \le 23$
Reflections collected	4425	12954	5700
Independent reflections	2433 [$R_{int} = 0.0284$, $R_{sigma} = 0.0413$]	6990 [$R_{int} = 0.0212$, $R_{sigma} = 0.0342$]	918 [$R_{int} = 0.0403$, $R_{sigma} = 0.0256$]
Data / restraints / parameters	2433/0/103	6990/1/235	918/0/40
Goodness-of-fit on F^2	1.056	1.186	1.018
Final R indexes [I>=2σ (I)]	$R_1 = 0.0367$, w$R_2 = 0.0784$	$R_1 = 0.0301$, w$R_2 = 0.0667$	$R_1 = 0.0216$, w$R_2 = 0.0482$
Final R indexes [all data]	$R_1 = 0.0547$, w$R_2 = 0.0868$	$R_1 = 0.0365$, w$R_2 = 0.0687$	$R_1 = 0.0258$, w$R_2 = 0.0500$
Largest diff. peak/hole / e·Å^{-3}	1.16/-1.06	2.27/-1.88	0.80/-0.81

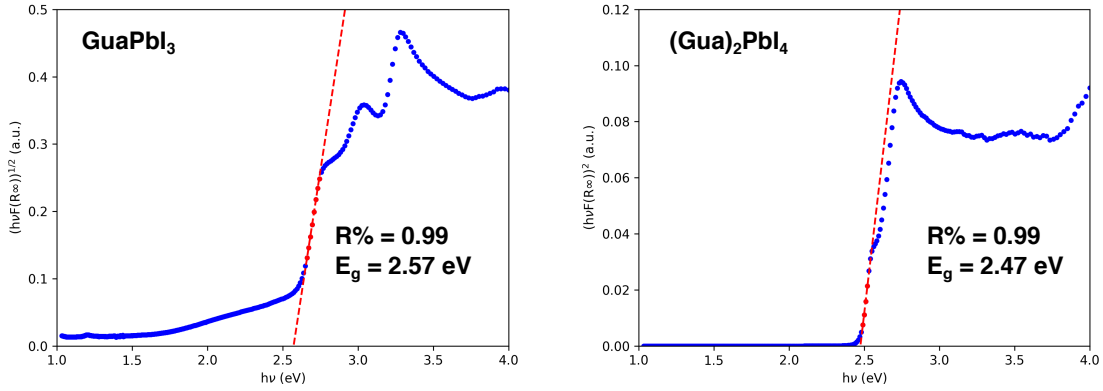

Fig. 6.2 Tauc plots of $GuaPbI_3$ and $(Gua)_2PbI_4$ determined from UV-vis spectroscopy. Reproduced from Deng et al.[35] with permission from the AIP Publishing.

$3E(I)$ where E($GuaPbI_3$) is the total energy per formula unit of $GuaPbI_3$ and E(C), E(N), E(H), E(Pb) and E(I) are the total energies per atom of the elements using standard state structures. Here we used graphite, nitrogen gas, hydrogen gas, fcc lead and orthorhombic iodine and all the gas phases were optimized by placing a dimer in a $15 \times 15 \times 15$ Å^3 box in a Γ k-point calculation. The relative formation enthalpy ΔH_f was determined by setting the lowest H_f to zero.

6.3 Results

6.3.1 Structural Characterization

Single crystals of Gua-based iodoplumbates, $(Gua)_xPbI_{x+2}$ (x = 1, 2 and 3), were examined by single-crystal X-ray diffraction (SCXRD). The crystals were grown under the same experimental conditions as reported previously[339] for FA- and MA-based perovskites and the different stoichiometries were obtained by tuning the ratio of Gua^+ and Pb^{2+} ions in the starting materials. For $GuaPbI_3$ and $(Gua)_2PbI_4$, pure phase crystals were readily obtained. For $(Gua)_3PbI_5$, mixed phase samples containing $(Gua)_3PbI_5$, $(Gua)_2PbI_4$ and $GuaPbI_3$ were harvested. Single crystals of $(Gua)_3PbI_5$ were collected from the mixture for structural characterization. The crystal structures were solved using SCXRD, primarily at room temperature.

$GuaPbI_3$, which is yellow in colour and needle-like at room temperature, crystallises in the orthorhombic space group, *Pnma*, with lattice parameters a = 11.9987(8) Å, b = 4.4693(4) Å and c = 20.874(2) Å, which is consistent with a recent powder X-ray- diffraction

(PXRD) study by Jodlowski et al.[225] The crystal adopts a 1D double chain structure, within which each Pb^{2+} ion is coordinated by six I-ions in a distorted octahedral environment. The PbI_6 octahedra are connected by common edges and arranged into double chains along the b-axis and the guanidinium ions fit in the spaces between the double chains, as shown in Fig. 6.1 ($GuaPbI_3$-e) and Fig. C.2. There are three different kinds of Pb-I bonds with Pb-I distances ranging from 3.07 Å to 3.25 Å (terminal Pb-I_3 = 3.074 Å, two bridging bonds of Pb-I_2 = 3.207 Å, and three bridging bonds of Pb-I_1 = 3.246 Å and Pb-$I_1{}^1$= 3.435 Å). The chain-like structure of $GuaPbI_3$ is of the type found in NH_4CdCl_3 and is isostructural with NH_4PbI_3[330] and the room temperature δ phase of $CsPbI_3$ and $RbPbI_3$[125] grown by the Bridgman technique[239]. Although the PbI_6 octahedra are observed to be distorted, there is no obvious stereo-chemical effect due to Pb lone pairs. The cis I-Pb-I angles vary between 87.0° and 93.6°, and the trans I_2-Pb-I_3 angles are 172.9°. $GuaPbI_3$-e was found to crystallize out quickly from the mother liquor and remain stable in air (HI aqueous solution) between 4°C and 90°C with tuned solution concentrations of the reactants. The SCXRD data collected for $GuaPbI_3$-e at 120K shows that a phase transition takes place on cooling, and the resultant unit cell exhibits monoclinic symmetry with lattice parameters a = 4.5742(4) Å, b = 11.7679(9) Å, c = 19.5361(18)Å and β = 94.2°. The inorganic framework retains the same double edge-sharing connectivity; however, heavy twinning upon cooling inhibited accurate determination on the atomic positions.

Crystals of $(Gua)_2PbI_4$ are orange and rectangular-shaped at room temperature and crystallises in space group $P2_1/n$ with lattice parameters a = 9.2440(3) Å, b = 26.9511(11) Å, c = 12.7155(3) Å and β = 91.482(2)°, which is consistent with previous work[334]. As shown in Fig. 6.1a and Fig. C.3, the structure consists of double layers of corner-sharing octahedra with 2D connectivity. Gua cations fill the cavities between two polyhedra within a layer and between layers. The two adjacent polyhedra in the same layer along the a-axis are heavily tilted in order to accommodate a guanidinium cation, with the most distorted Pb-I-Pb angle being as low as 154.405(19)°. This indicates that the Gua cation is too large to fit in the perovskite cage and is consistent with the theoretical prediction using the Tolerance Factor approach. The concept of extending the Goldschmidt Tolerance Factor to hybrid perovskites and the method used to estimate the size of the organic cations are reliable and thus indicate that lone pair effects, which can produce a distorted 3D perovskite, are not as dominant as the size factor in this case, unlike in the Sn and Ge-based guanidinium perovskites mentioned previously.

$(Gua)_3PbI_5$ is yellow at room temperature and crystallises in the monoclinic space group $C2/c$ with lattice parameters a = 13.0694(5) Å, b = 13.1946(5) Å, c = 12.7212(5) Å and

β = 91.276(4)°. This composition has not been reported previously and the structure is characterised by a PbI_6 network of corner-sharing octahedra forming 1D chains extending along the c-axis, as shown in Fig. 6.1a and Fig. C.4. The octahedra are less distorted than in $GuaPbI_3$-e with Pb-I bond lengths ranging from 3.2123(6) to 3.2505(2) Å and a bridging Pb-I-Pb angle between two adjacent octahedra of 156.13(3)°. The $(Gua)_3PbI_5$ structure has the same inorganic connectivity as that reported for $(FA)_3PbI_5$ with space group $P2_1/c$[342, 343]. In addition, similar corner-sharing chains were observed in $[NH_2C(I)=NH_2]_3PbI_5$ by Mitzi and co-workers in the 90s[344].

The effective radius of Gua^+ (278 pm) is larger than that of either MA^+ (217 pm) or FA^+ (253 pm), which are the only two organic cations which form hybrid $[Am]PbI_3$ phases that adopt the 3D perovskite structure. As noted above, the TF of $GuaPbI_3$ in a 3D perovskite architecture is 1.03(9)[132], which is slightly above the limit for stability[134]. The effective radius of Gua^+ is comparable to EA^+ (274 pm), which forms the $EAPbI_3$ structure containing infinite chains of face-sharing PbI_6 polyhedra[345]. It is therefore interesting that $GuaPbI_3$ adopts an edge-sharing double chain structure instead of forming a face-sharing hexagonal structure like $EAPbI_3$.

Table 6.2 DFT calculated structural properties of $(Gua)_xPbI_{x+2}$ (x=1,2,3) compared experimental measurements and a previous computational study[39]. Reproduced from Deng et al.[35] with permission from the AIP Publishing.

Structural Properties	$GuaPbI_3$-c		$GuaPbI_3$-f	$GuaPbI_3$-e		$(Gua)_2PbI_4$		$(Gua)_3PbI_5$	
	3D corner-sharing		1D face-sharing	1D edge-sharing		2D corner-sharing		1D corner-sharing	
	DFT	DFT[39]	DFT	DFT	Exp	DFT	Exp	DFT	Exp
a (Å)	9.37	9.34	9.44	12.16	11.99	9.23	9.24	13.32	13.07
b (Å)	9.37	9.34	9.44	4.37	4.47	27.05	26.95	12.92	13.19
c (Å)	10.35	10.33	7.81	20.63	20.87	12.65	12.72	12.44	12.72
α (°)	90	89.6	90	90	90	90	90	90	90
β (°)	90	90.4	90	90	90	91.18	91.48	90	91.28
γ (°)	120	119.4	120	90	90	90	90	90	90
V / f.u. ($Å^3$)	261.97	262.03	300.18	274.22	279.81	394.45	395.85	535.22	548.29
ρ (g/cm^3)	4.2	4.11	3.58	3.92	3.85	3.52	3.5	3.17	3.5

6.3.2 DFT Structures and Formation Enthalpies

The DFT-calculated structural properties of edge-sharing $GuaPbI_3$-e, two hypothetical corner-sharing and face-sharing structures $GuaPbI_3$-c and $GuaPbI_3$-f, as well as Gua_2PbI_4 and Gua_3PbI_5, are shown in Table 6.2. The relaxed lattice parameters of $GuaPbI_3$-e, $(Gua)_2PbI_4$ and $(Gua)_3PbI_5$ agree well with the experimental measurements presented here. To understand better the structural stability of $GuaPbI_3$, two hypothetical polymorphs were constructed

Table 6.3 DFT-calculated relative formation enthalpies (ΔH_f) of $GuaPbI_3$. Reproduced from Deng et al.[35] with permission from the AIP Publishing.

Polymorph	ΔH_f (kJ/mol per f.u.)
$GuaPbI_3$-e ($GuaPbI_3$-eRT)	11.41
$GuaPbI_3$-f	0.09
$GuaPbI_3$-c	17.82
$GuaPbI_3$-eLT	0

(Fig. 6.1a): (i) a 3D corner-sharing perovskite structure $GuaPbI_3$-c and (ii) a 1D face-sharing structure, $GuaPbI_3$-f, isostructural with the two polymorphs of $FAPbI_3$ having space groups $P3m1$ and $P6_3mc$, respectively. The numbers of formula units per conventional unit cell of $GuaPbI_3$-c, $GuaPbI_3$-f and $GuaPbI_3$-e are 3, 2 and 4 respectively. The results for $GuaPbI_3$-c are in good agreement with a previous computational study[39] and those for $GuaPbI_3$-e are consistent with the experimental data (Table 6.2). The three $GuaPbI_3$ polymorphs have similar stabilities in terms of enthalpy, as seen from Table 6.3. The difference in formation enthalpy between $GuaPbI_3$-e and $GuaPbI_3$-c shows that $GuaPbI_3$-e is slightly more stable, with a difference of 6.41 kJ/mol per formula unit (f.u.). This value is 2 times larger than thermal energy at 298K (2.48 kJ/mol per f.u.), which suggests that thermodynamically there is only a small difference between the enthalpies of the two structures. The formation enthalpy of $GuaPbI_3$-f is 11.32 kJ/mol per f.u. lower than the experimental structure, $GuaPbI_3$-e. It is therefore surprising that, although $GuaPbI_3$-f is predicted to be the most stable polymorph using DFT, experimentally $GuaPbI_3$-e is found at room temperature. However, by performing DFT relaxation on $GuaPbI_3$-e without applying any symmetry constraints, a lower symmetry structure ($GuaPbI_3$-eLT) with space group $P2_1/c$ was obtained. The guanidinium cations in $GuaPbI_3$-e are aligned perpendicular to the chain direction (b-axis), whereas in $GuaPbI_3$-eLT they are tilted (Fig. 6.1b). Importantly, the experimental stability of this structure using low temperature (120 K) SCXRD was confirmed, i.e. a transformation into the $P2_1/c$ structure was observed on cooling. As indicated by the thermal ellipsoids derived from the SCXRD (Fig. 6.1c), the guanidinium cations are clearly tilted, in agreement with DFT results here. The DFT-calculated formation enthalpy of $GuaPbI_3$-eLT is slightly lower than that of $GuaPbI_3$-f (0.09 kJ/mol per f.u.). However, this enthalpy difference is still much smaller than kT at room temperature (2.48 kJ/mol per f.u.). Therefore, there must be other reasons for the relative stabilities of these structures, such as synthesis environment, entropy and kinetics. On cooling to 120 K, $GuaPbI_3$-eLT forms a greater number of hydrogen bonds to stabilize the structure (see Fig. C.5) and this lowers both its symmetry and enthalpy. As a consequence,

entropy must play a role in stabilizing $GuaPbI_3$-e at room temperature. A previous study on the phase behaviour of metal organic frameworks has attributed the observed polymorphs to entropic differences caused by hydrogen bonding and density[346]. Comparing the calculated densities of the three $GuaPbI_3$ polymorphs (Table 6.2), the following trend is observed: $GuaPbI_3$-f < $GuaPbI_3$-e < $GuaPbI_3$-c. This would suggest the possibility that the lowest density/highest entropy $GuaPbI_3$-f phase might form at higher temperatures.

It is well known that hydrogen bonding and, in particular, H···I bonding, plays an important role in determining the structure and stability of hybrid halide perovskites, where it can affect, for example, the degree of octahedral tilting[129]. Experimentally, the positions of the hydrogen atoms are difficult to determine using XRD with a material containing heavy elements such as Pb and I. However, DFT can be employed to calculate these positions together with various interatomic distances and bond angles, which can be used as indicators of bond strengths. In this work the calculated I···N interatomic distances and N-H···I bond angles were used for this purpose. As shown in Fig. C.5, $d_{I\cdots N}$ and ∠N-H···I distances and angles for every system studied in the present work vary between 3.6-4.0 Å and 100°-170°, respectively. This indicates an intermediate level of hydrogen bonding strength (compared, for example, with $MAPbI_3$, where the distances are ∼3.5-3.6 Å[129]). Interactions in the lower dimensional structures like $(Gua)_2PbI_4$ and $(Gua)_3PbI_5$, which contain multiple Gua cations, are complex, as shown from the $d_{I\cdots N}$ and ∠N-H···I distributions. For each guanidinium cation, there are 6, 12, 6, 10.5 and 9.3 hydrogen bonds associated with the $GuaPbI_3$-e, $GuaPbI_3$-c, $GuaPbI_3$-f, $(Gua)_2PbI_4$ and $(Gua)_3PbI_5$ structures, respectively. Comparing the bond lengths and bond angles of the three polymorphs of $GuaPbI_3$ in Fig. C.5, it is shown that most of the H bonds in $GuaPbI_3$-e are weaker than in $GuaPbI_3$-c and $GuaPbI_3$-f.

6.3.3 DFT Electronic Properties

DFT-calculated electronic band structures, along with their projected densities of states (PDOS), are shown in Fig. 6.3 and include spin-orbit coupling (SOC). The calculated band gaps, with and without SOC, are compared with the measured values in Table 6.4. For the $GuaPbI_3$ series, $GuaPbI_3$-c, $GuaPbI_3$-e and $GuaPbI_3$-f have calculated SOC band gaps of 0.36 eV, 2.27 eV and 2.50 eV, respectively, which compare with a measured value of 2.57 eV for $GuaPbI_3$-e. For $(Gua)_2PbI_4$ and $(Gua)_3PbI_5$, the SOC band gaps are 1.52 eV and 1.94 eV, respectively, while the measure value for $(Gua)_2PbI_4$ is 2.47 eV. In general, the calculated values are smaller than the measured ones, as expected for DFT+SOC. The PDOS indicates that the band edges are dominated by Pb-6s, 6p and I-5p states which originate from the Pb-I

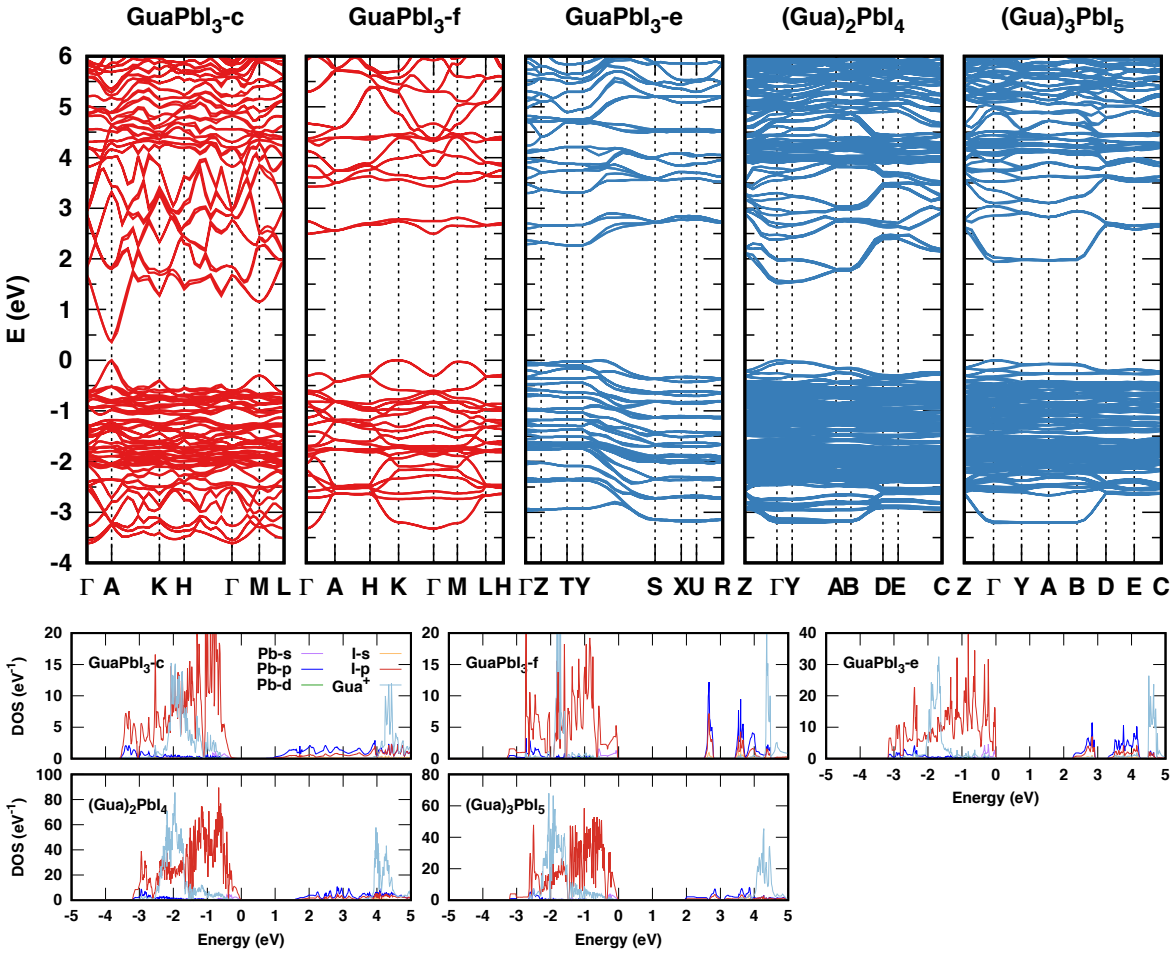

Fig. 6.3 DFT-calculated electronic band structures (red plots are hypothetical structures and blue plots are for those experimentally observed) and their projected densities of states (PDOS) considering spin-orbit coupling (SOC). Following high symmetric paths are used: $GuaPbI_3$-c: Γ(0,0,0) - A(0,0,0.5) - H(-0.3333,0.6667,0.5) - K(-0.3333,0.6667,0) - Γ(0,0,0) - M(0,0.5,0) - L(0,0.5,0.5) - H(-0.3333,0.6667,0.5); $GuaPbI_3$-f: Γ(0,0,0) - A(0,0,0.5) - H(-0.3333,0.6667,0.5) - K(-0.3333,0.6667,0) - Γ(0,0,0) - M(0,0.5,0) - L(0,0.5,0.5) - H(-0.3333,0.6667,0.5); $GuaPbI_3$-e: Γ(0,0,0) - Z(0,0,0.5) - T(-0.5,0,0.5) - Y(-0.5,0,0) - S(-0.5,0.5,0) - X(0,0.5,0) - U(0,0.5,0.5) - R(-0.5,0.5,0.5); Gua_2PbI_4 and Gua_3PbI_5: Z(0,0,0.5) - Γ(0,0,0) - Y(0,0.5,0) - A(-0.5,0.5,0) - B(-0.5,0,0) - D(-0.5,0,0.5) - E(-0.5,0.5,0.5) - C(0,0.5,0.5). Reproduced from Deng et al.[35] with permission from the AIP Publishing.

inorganic framework. The inorganic and organic (Gua) states are well decoupled at the band edges. There are two factors in the present study that can influence the electronic properties significantly: (i) the connectivity and (ii) the dimensionality of the inorganic Pb-I framework. Pb-I connectivity will change the orbital overlaps and hence the average Pb-I-Pb bond angles, as shown in Fig. 6.4. For the three polymorphs of $GuaPbI_3$ it is seen that the band gaps decrease as the connectivity changes from face-sharing to edge-sharing to corner-sharing,

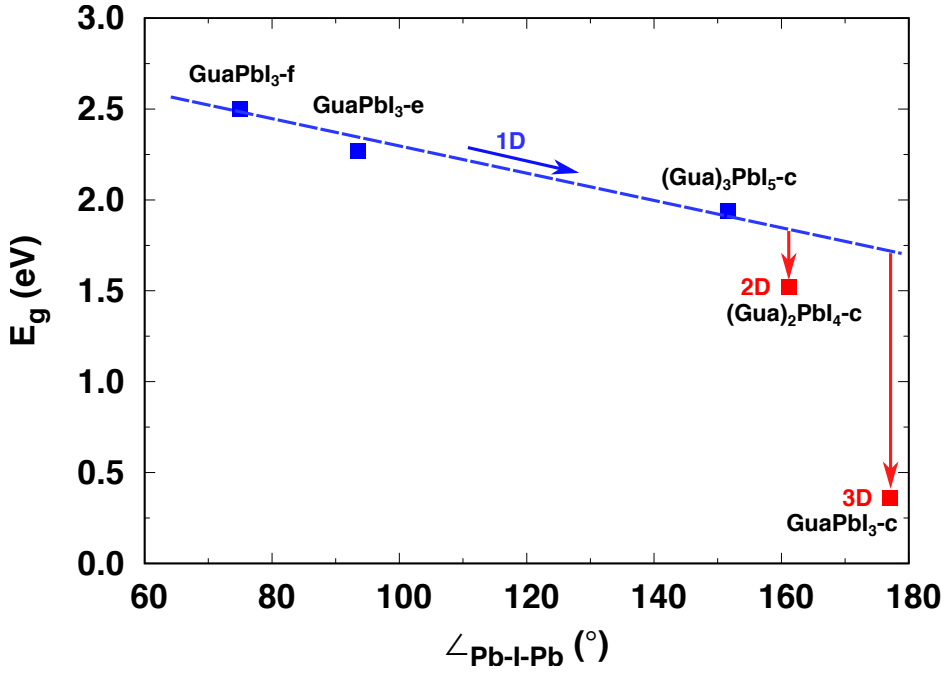

Fig. 6.4 DFT-calculated band gaps (E_g including SOC) as a function of the averaged Pb-I-Pb bond angles in $(Gua)_xPbI_{x+2}$ (x = 1, 2 and 3) using the data in Table C.1. "c", "f" and "e" denote $GuaPbI_3$ structures with corner-sharing, face-sharing and edge-sharing octahedral, respectively. $GuaPbI_3$-f and $GuaPbI_3$-c are hypothetical structures. Structures with 1D octahedral connectivity are shown with blue symbols whereas those with 2D connectivity ($(Gua)_2PbI_4$) and 3D connectivity ($GuaPbI_3$-c) are shown with red symbols. The red arrows show the effect of quantum confinement in 2D (∼0.25 eV) and 3D (∼1.25 eV) compared to 1D structures. Reproduced from Deng et al.[35] with permission from the AIP Publishing.

Table 6.4 DFT calculated electronic band gaps with ($E_{g,SOC}$) and without (E_g) including spin-orbit coupling (SOC), their difference $\Delta E_g = E_g - E_{g,SOC}$, and comparison with experimental measurements ($E_{g,exp}$). Units are in eV. Reproduced from Deng et al.[35] with permission from the AIP Publishing.

	$E_{g,SOC}$	E_g	ΔE_g	$E_{g,exp}$
$GuaPbI_3$-e	2.27	2.92	0.65	2.57
$GuaPbI_3$-f	2.50	2.87	0.38	-
$GuaPbI_3$-c	0.36	1.49	1.13	-
$(Gua)_2PbI_4$	1.52	2.08	0.56	2.47
$(Gua)_3PbI_5$	1.94	2.42	0.48	Colour: Yellow

while at the same time the bond angles increase. Dimensionality affects electronic properties by the confinement of forming Pb-I chains or planes, which usually increases the band gap as the dimensionality decreases. Therefore, it is expected that the band gap to follow the

following trend: face-sharing > edge-sharing > corner-sharing and 1D > 2D > 3D, which is clearly seen in Fig. 6.4. From the band structures shown in Fig. 6.4, directions that are quantum confined (e.g. the direction perpendicular to the $[PbI_3]^-$ chains in $GuaPbI_3$-e), the band dispersion becomes extremely flat (e.g. from Γ-Y-A-B in $GuaPbI_3$-e). A similar trend has also been reported recently in Sn-based low-dimensional perovskites[333]. Connectivity and dimensionality also affect relativistic interactions. Table 6.4 shows that the computed differences in band gap (ΔE_g) for each structure with and without SOC increases as the band gap decreases. However, ΔE_g for $(Gua)_3PbI_5$ is smaller than $GuaPbI_3$-e. This is because $GuaPbI_3$-e has a double-chain instead of a single-chain structure so that the relativistic effect is larger in $GuaPbI_3$-e. This is an excellent illustration of how to tune the band gap of a hybrid perovskite by controlling the connectivity and dimensionality of the inorganic framework.

6.4 Summary

This Chapter has presented a combined experimental and computational analysis of the effects of octahedral connectivity and dimensionality on the stabilities of three guanidinium-based iodoplumbates. The SCXRD experiments show that $GuaPbI_3$ has 1D edge-sharing octahedral connectivity, $(Gua)_2PbI_4$ has 2D corner-sharing octahedral connectivity, and $(Gua)_3PbI_5$ has 1D corner-sharing octahedral connectivity. $(Gua)_3PbI_5$ is a new composition whereas $GuaPbI_3$ and $(Gua)_2PbI_4$ have been synthesised previously. The measured band gap of $(Gua)_2PbI_4$ is smaller than that of $GuaPbI_3$. DFT calculations of the structure of the three iodoplumbates are consistent with the measurements and in particular confirm the stability of the low temperature form of $GuaPbI_3$ with $P2_1/c$ symmetry. Calculations of the formation enthalpies of two other hypothetical polymorphs of $GuaPbI_3$, one with 1D face-sharing connectivity and the other with 3D corner-sharing connectivity, suggest that entropy must play a role in stabilising the observed form of $GuaPbI_3$ with *Pnma* symmetry at room temperature. The calculated band structures of the iodoplumbates confirm that their band gaps increase with reducing dimensionality due to quantum confinement effects. Octahedral connectivity is also shown to affect the band gap, with face-sharing octahedra resulting in the largest band gap. Overall, the results add to the knowledge of the effects of connectivity and dimensionality on the stabilities and electronic properties of hybrid perovskites, particularly those that are guanidinium based, and may motivate further studies on mixed cation perovskites in the rational design of materials for photovoltaic devices.

Chapter 7

Conclusions

Extraordinary progress achieved over the last 7 years has pushed the efficiency of hybrid perovskites to over 22%, making them ideal candidates for next-generation solar cell applications. Their structural and chemical diversity, together with their electronic and optical tunability, continue to encourage scientists in this field to find higher efficiency, more stable and lead-free HOIPs. Although these materials are complex with the presence of dispersion forces, spin-orbit coupling and structural disorder bringing much challenge to theory and experiments, combining DFT calculations with experiments makes a really powerful tool for studying various properties of HOIPs. In Chapter 4, a series of hybrid halide double perovskites having the formula $(MA)_2M^{I}M^{III}X_6$ ($(MA)_2KBiCl_6$, $(MA)_2TlBiBr_6$, $(MA)_2AgBiBr_6$, $(MA)_2KYCl_6$ and $(MA)_2KGdCl_6$), were discovered experimentally with guidance from DFT calculations, with the aim of replacing Pb in the widely studied (MA/FA)PbI_3. In Chapter 5, the properties of hybrid perovskites under pressure, temperature and applied load were studied, including phase stabilities, transitions and mechanical properties of $FAPbX_3$, followed by a computational study linking the elastic properties to electronic transport properties. In Chapter 6, a study of low-dimensional perovskites containing guanidinium $(Gua)_xPbI_{x+3}$ (x = 1, 2 and 3) was presented, focusing on phase stabilities, phase transitions and trends in electronic properties. These studies provide alternative routes for designing novel materials for different purposes using the "perovskite" structure as a template both computationally and experimentally.

Due to the complexity and structural diversity of hybrid perovskites, there are still a huge number of interesting topics worthy of study in the future. Here I just list some of the opportunities that emerged during my Ph.D. study:

Firstly, concerning hybrid double perovskites discussed in Chapter 4, we only studied materials containing methylammonium and a single halide element. Hybrid double per-

ovskites containing other organic cations, e.g. FA, EA and Gua might exist. Also, novel low dimensional hybrid double perovskites are worthy to study as well.

Secondly, mechanical properties are crucial for device applications, but there are not many theoretical (or experimental) studies for HOIPs. As shown in Chapter 5, there are many factors contributing to the mechanical properties of HOIPs, e.g. H-bonding, octahedral tilting, B-X bond strengths, size of the A-site cation, crystal symmetry and the dynamical rotations of A-site cation. DFT could possibly provide a way of designing mechanically stable materials and identifying the most important factors affecting the mechanical properties of HOIPs.

Lastly, it is clear that the tolerance factor is a useful geometrical parameter for designing perovskite materials. However, using cations with similar size to MA^+, e.g. hydrazinium $[NH_2NH_3]^+$ or hydroxylammonium $[NH_3OH]^+$, does not result in a stable 3D perovskite structure. This might be due to the method of synthesis including the kinetics of the reactions or the stability of the A-site cation . DFT calculations or AIMD might possibly explain this.

References

[1] W. Shockley and H. J. Queisser, J. Appl. Phys. **32**, 510 (1961).

[2] http://www.nrel.gov/ncpv/images/efficiency_chart.jpg (2018).

[3] M. A. Green, A. Ho-Baillie, and H. J. Snaith, Nat. Photonics **8**, 506 (2014).

[4] I. Chung, J.-H. Song, J. Im, J. Androulakis, C. D. Malliakas, H. Li, A. J. Freeman, J. T. Kenney, and M. G. Kanatzidis, J. Am. Chem. Soc. **134**, 8579 (2012).

[5] C. J. Howard and H. T. Stokes, Acta Cryst. B **58**, 565 (2002).

[6] C. J. Howard and H. T. Stokes, Acta Cryst. B **54**, 782 (1998).

[7] M. D. Smith, E. J. Crace, A. Jaffe, and H. I. Karunadasa, Annu. Rev. Mater. Res. (2018).

[8] B. Saparov and D. B. Mitzi, Chem. Rev. **116**, 4558 (2016).

[9] C. C. Stoumpos, L. Frazer, D. J. Clark, Y. S. Kim, S. H. Rhim, A. J. Freeman, J. B. Ketterson, J. I. Jang, and M. G. Kanatzidis, J. Am. Chem. Soc. **137**, 6804 (2015).

[10] C. C. Stoumpos, C. D. Malliakas, and M. G. Kanatzidis, Inorg. Chem. **52**, 9019 (2013).

[11] B. Chabot and E. Parthe, Acta Cryst. **B34**, 645 (1978).

[12] A. J. Lehner, D. H. Fabini, H. A. Evans, C.-A. He bert, S. R. Smock, J. Hu, H. Wang, J. W. Zwanziger, M. L. Chabinyc, and R. Seshadri, Chem. Mater. **27**, 7137 (2015).

[13] A. H. Slavney, T. Hu, A. M. Lindenberg, and H. I. Karunadasa, J. Am. Chem. Soc. **138**, 2138 (2016).

[14] E. T. McClure, M. R. Ball, W. Windl, and P. M. Woodward, Chem. Mater. **28**, 1348 (2016).

[15] G. Volonakis, M. R. Filip, A. A. Haghighirad, N. Sakai, B. Wenger, H. J. Snaith, and F. Giustino, J. Phys. Chem. Lett. **7**, 1254 (2016).

[16] F. Wei, Z. Deng, S. Sun, F. Xie, G. Kieslich, D. M. Evans, M. A. Carpenter, P. D. Bristowe, and A. K. Cheetham, Mater. Horiz. **3**, 328 (2016).

[17] C. C. Stoumpos and M. G. Kanatzidis, Adv. Mater. **28**, DOI: 10.1002/adma.201600265 (2016).

[18] M. R. Filip, G. E. Eperon, H. J. Snaith, and F. Giustino, Nat. Commun. **5**, 5757 (2014).

[19] P. Umari, E. Mosconi, and F. De Angelis, Sci. Rep. **4**, 4467 (2014).

[20] J. H. Noh, S. H. Im, J. H. Heo, T. N. Mandal, and S. I. Seok, Nano Lett. **13**, 1764 (2013).

[21] L. Protesescu, S. Yakunin, M. I. Bodnarchuk, F. Krieg, R. Caputo, C. H. Hendon, R. X. Yang, A. Walsh, and M. V. Kovalenko, Nano Lett. **15**, 3692 (2015).

[22] K. Wu, A. Bera, C. Ma, Y. Du, Y. Yang, L. Li, and T. Wu, Phys. Chem. Chem. Phys. **16**, 22476 (2014).

[23] W.-J. Yin, J.-H. Yang, J. Kang, Y. Yan, and S.-H. Wei, J. Mater. Chem. A **3**, 8926 (2015).

[24] J. P. Perdew and K. Schmidt, in *AIP Conf. Proc.*, Vol. 577 (2001) pp. 1–20.

[25] S. J. Clark, M. D. Segall, C. J. Pickard, P. J. Hasnip, M. I. Probert, K. Refson, and M. C. Payne, Z. Kristallogr. **220**, 567 (2005).

[26] Z. Deng, F. Wei, S. Sun, G. Kieslich, A. K. Cheetham, and P. D. Bristowe, J. Mater. Chem. A **4**, 12025 (2016).

[27] F. Wei, Z. Deng, S. Sun, F. Zhang, D. M. Evans, G. Kieslich, S. Tominaka, M. A. Carpenter, J. Zhang, P. D. Bristowe, *et al.*, Chem. Mater. **29**, 1089 (2017).

[28] S. Sun, Y. Fang, G. Kieslich, T. J. White, and A. K. Cheetham, J. Mater. Chem. A **3**, 18450 (2015).

[29] Z. Deng, F. Wei, F. Brivio, Y. Wu, S. Sun, P. D. Bristowe, and A. K. Cheetham, J. Phys. Chem. Lett. **8**, 5015 (2017).

[30] S. Sun, Z. Deng, Y. Wu, F. Wei, F. H. Isikgor, F. Brivio, M. W. Gaultois, J. Ouyang, P. D. Bristowe, A. K. Cheetham, *et al.*, Chem. Commun. **53**, 7537 (2017).

[31] S. Sun, F. H. Isikgor, Z. Deng, F. Wei, G. Kieslich, P. D. Bristowe, J. Ouyang, and A. K. Cheetham, ChemSusChem **10**, 3683 (2017).

[32] W. Li, M. S. R. N. Kiran, J. L. Manson, J. A. Schlueter, A. Thirumurugan, U. Ramamurty, and A. K. Cheetham, Chem. Commun. **49**, 4471 (2013).

[33] G. Laurita, D. H. Fabini, C. C. Stoumpos, M. G. Kanatzidis, and R. Seshadri, Chem. Sci. **8**, 5628 (2017).

[34] J.-H. Lee, Z. Deng, N. C. Bristowe, P. Bristowe, and T. Cheetham, J. Mater. Chem. C , Accepted (2018).

[35] Z. Deng, G. Kisleich, P. D. Bristowe, A. K. Cheetham, and S. Sun, APL Mater. **6**, 114202 (2018).

[36] S. D. Stranks and H. J. Snaith, Nat. Nanotechnol. **10**, 391 (2015).

[37] R. Hill, Proc. Phys. Soc. London, Sect. A **65**, 349 (1952).

[38] R. D. Shannon, Acta Cryst. A **32**, 751 (1976).

[39] G. Giorgi, J.-I. Fujisawa, H. Segawa, and K. Yamashita, J. Phys. Chem. C **119**, 4694 (2015).

[40] D. M. Chapin, C. S. Fuller, and G. L. Pearson, US Patent **Feb 5**, 2,780,765 (1957).

[41] D. E. Carlson and C. R. Wronski, Appl. Phys. Lett. **28**, 671 (1976).

[42] J. Britt and C. Ferekides, Appl. Phys. Lett. **62**, 2851 (1993).

[43] P. Jackson, D. Hariskos, E. Lotter, S. Paetel, R. Wuerz, R. Menner, W. Wischmann, and M. Powalla, Prog. Photovoltaics Res. Appl. **19**, 894 (2011).

[44] B. O'Regan and M. Grätzel, Nature **353**, 737 (1991).

[45] G. Li, R. Zhu, and Y. Yang, Nat. Photonics **6**, 153 (2012).

[46] A. Nozik, Physica E **14**, 115 (2002).

[47] H. J. Snaith, J. Phys. Chem. Lett. **4**, 3623 (2013).

[48] N.-G. Park, J. Phys. Chem. Lett. **4**, 2423 (2013).

[49] A. Kojima, K. Teshima, Y. Shirai, and T. Miyasaka, J. Am. Chem. Soc. **131**, 6050 (2009).

[50] E. Edri, S. Kirmayer, A. Henning, S. Mukhopadhyay, K. Gartsman, Y. Rosenwaks, G. Hodes, and D. Cahen, Nano Lett. **14**, 1000 (2014).

[51] H. Zhou, Q. Chen, G. Li, S. Luo, T.-b. Song, H.-S. Duan, Z. Hong, J. You, Y. Liu, and Y. Yang, Science **345**, 542 (2014).

[52] L. Meng, J. You, T.-F. Guo, and Y. Yang, Acc. Chem. Res. **49**, 155 (2016).

[53] H. J. Snaith, A. Abate, J. M. Ball, G. E. Eperon, T. Leijtens, N. K. Noel, S. D. Stranks, J. T.-W. Wang, K. Wojciechowski, and W. Zhang, J. Phys. Chem. Lett. **5**, 1511 (2014).

[54] E. Unger, E. Hoke, C. Bailie, W. Nguyen, A. Bowring, T. Heumüller, M. Christoforo, and M. McGehee, Energy Environ. Sci. **7**, 3690 (2014).

[55] N. J. Jeon, J. H. Noh, Y. C. Kim, W. S. Yang, S. Ryu, and S. I. Seok, Nat. Mater. **13**, 897 (2014).

[56] W. S. Yang, J. H. Noh, N. J. Jeon, Y. C. Kim, S. Ryu, J. Seo, and S. I. Seok, Science **348**, 1234 (2015).

[57] N. K. Noel, S. D. Stranks, A. Abate, C. Wehrenfennig, S. Guarnera, A.-A. Haghighirad, A. Sadhanala, G. E. Eperon, S. K. Pathak, M. B. Johnston, A. Petrozza, L. M. Herz, and H. J. Snaith, Energy Environ. Sci. **7**, 3061 (2014).

[58] J.-H. Im, C.-R. Lee, J.-W. Lee, S.-W. Park, and N.-G. Park, Nanoscale **3**, 4088 (2011).

[59] Editorial, Nat. Mater. **13**, 837 (2014).

[60] H.-S. Kim, C.-R. Lee, J.-H. Im, K.-B. Lee, T. Moehl, A. Marchioro, S.-J. Moon, R. Humphry-Baker, J.-H. Yum, J. E. Moser, *et al.*, Sci. Rep. **2** (2012).

[61] M. M. Lee, J. Teuscher, T. Miyasaka, T. N. Murakami, and H. J. Snaith, Science **338**, 643 (2012).

[62] J. H. Heo, S. H. Im, J. H. Noh, T. N. Mandal, C.-S. Lim, J. A. Chang, Y. H. Lee, H.-j. Kim, A. Sarkar, M. K. Nazeeruddin, *et al.*, Nat. Photonics **7**, 486 (2013).

[63] J. M. Ball, M. M. Lee, A. Hey, and H. J. Snaith, Energy Environ. Sci. **6**, 1739 (2013).

[64] J. Burschka, N. Pellet, S.-J. Moon, R. Humphry-Baker, P. Gao, M. K. Nazeeruddin, and M. Grätzel, Nature **499**, 316 (2013).

[65] M. Liu, M. B. Johnston, and H. J. Snaith, Nature **501**, 395 (2013).

[66] N. J. Jeon, J. H. Noh, W. S. Yang, Y. C. Kim, S. Ryu, J. Seo, and S. I. Seok, Nature **517**, 476 (2015).

[67] F. Deschler, M. Price, S. Pathak, L. E. Klintberg, D.-D. Jarausch, R. Higler, S. Hu ttner, T. Leijtens, S. D. Stranks, H. J. Snaith, *et al.*, J. Phys. Chem. Lett. **5**, 1421 (2014).

[68] V. D'Innocenzo, G. Grancini, M. J. Alcocer, A. R. S. Kandada, S. D. Stranks, M. M. Lee, G. Lanzani, H. J. Snaith, and A. Petrozza, Nat. Commun. **5**, 3586 (2014).

[69] G. Xing, N. Mathews, S. Sun, S. S. Lim, Y. M. Lam, M. Grätzel, S. Mhaisalkar, and T. C. Sum, Science **342**, 344 (2013).

[70] S. D. Stranks, G. E. Eperon, G. Grancini, C. Menelaou, M. J. P. Alcocer, T. Leijtens, L. M. Herz, A. Petrozza, and H. J. Snaith, Science **342**, 341 (2013).

[71] Q. Dong, Y. Fang, Y. Shao, P. Mulligan, J. Qiu, L. Cao, and J. Huang, Science **347**, 967 (2015).

[72] D. Shi, V. Adinolfi, R. Comin, M. Yuan, E. Alarousu, A. Buin, Y. Chen, S. Hoogland, A. Rothenberger, K. Katsiev, *et al.*, Science **347**, 519 (2015).

[73] W. Nie, H. Tsai, R. Asadpour, J.-C. Blancon, A. J. Neukirch, G. Gupta, J. J. Crochet, M. Chhowalla, S. Tretiak, M. A. Alam, *et al.*, Science **347**, 522 (2015).

[74] A. Miyata, A. Mitioglu, P. Plochocka, O. Portugall, J. T.-W. Wang, S. D. Stranks, H. J. Snaith, and R. J. Nicholas, Nat. Phys. **11**, 582 (2015).

[75] J. M. Frost, K. T. Butler, F. Brivio, C. H. Hendon, M. Van Schilfgaarde, and A. Walsh, Nano Lett. **14**, 2584 (2014).

[76] D. P. McMeekin, G. Sadoughi, W. Rehman, G. E. Eperon, M. Saliba, M. T. Hörantner, A. Haghighirad, N. Sakai, L. Korte, B. Rech, *et al.*, Science **351**, 151 (2016).

[77] D. H. Cao, C. C. Stoumpos, O. K. Farha, J. T. Hupp, and M. G. Kanatzidis, J. Am. Chem. Soc. **137**, 7843 (2015).

[78] L. N. Quan, M. Yuan, R. Comin, O. Voznyy, E. M. Beauregard, S. Hoogland, A. Buin, A. R. Kirmani, K. Zhao, A. Amassian, *et al.*, J. Am. Chem. Soc. **138**, 2649 (2016).

[79] H. Tsai, W. Nie, J.-C. Blancon, C. C. Stoumpos, R. Asadpour, B. Harutyunyan, A. J. Neukirch, R. Verduzco, J. J. Crochet, S. Tretiak, *et al.*, Nature **536**, 312 (2016).

[80] Z. Wang, Q. Lin, F. P. Chmiel, N. Sakai, L. M. Herz, and H. J. Snaith, Nat. Energy **2**, 17135 (2017).

[81] M. Grätzel, Nat. Mater. **13**, 838 (2014).

[82] F. Hao, C. C. Stoumpos, D. H. Cao, R. P. Chang, and M. G. Kanatzidis, Nat. Photonics **8**, 489 (2014).

[83] Y. Takahashi, R. Obara, Z.-Z. Lin, Y. Takahashi, T. Naito, T. Inabe, S. Ishibashi, and K. Terakura, Dalton Trans. **40**, 5563 (2011).

[84] A. Babayigit, D. D. Thanh, A. Ethirajan, J. Manca, M. Muller, H.-G. Boyen, and B. Conings, Sci. Rep. **6**, 18721 (2016).

[85] F. Hao, C. C. Stoumpos, R. P. Chang, and M. G. Kanatzidis, J. Am. Chem. Soc. **136**, 8094 (2014).

[86] Y. Kutes, L. Ye, Y. Zhou, S. Pang, B. D. Huey, and N. P. Padture, J. Phys. Chem. Lett. **5**, 3335 (2014).

[87] Z. Xiao, Y. Yuan, Y. Shao, Q. Wang, Q. Dong, C. Bi, P. Sharma, A. Gruverman, and J. Huang, Nat. Mater. **14**, 193 (2015).

[88] J. H. Heo, H. J. Han, D. Kim, T. K. Ahn, and S. H. Im, Energy Environ. Sci. **8**, 1602 (2015).

[89] P. Hohenberg and W. Kohn, Phys. Rev. **136**, B864 (1964).

[90] W. Kohn and L. J. Sham, Phys. Rev. **140**, A1133 (1965).

[91] W. Kohn, Rev. Mod. Phys. **71**, 1253 (1999).

[92] A. Jain, S. P. Ong, G. Hautier, W. Chen, W. D. Richards, S. Dacek, S. Cholia, D. Gunter, D. Skinner, G. Ceder, *et al.*, APL Mater. **1**, 011002 (2013).

[93] A. R. Oganov and C. W. Glass, J. Chem. Phys. **124**, 244704 (2006).

[94] C. J. Pickard and R. Needs, J. Phys.: Condens. Matter **23**, 053201 (2011).

[95] J. Tauc, Mater. Res. Bull. **3**, 37 (1968).

[96] K.-I. Kobayashi, T. Kimura, H. Sawada, K. Terakura, and Y. Tokura, Nature **395**, 677 (1998).

[97] R. E. Cohen, Nature **358**, 136 (1992).

[98] Y. Maeno, H. Hashimoto, K. Yoshida, S. Nishizaki, T. Fujita, J. Bednorz, and F. Lichtenberg, Nature **372**, 532 (1994).

[99] W. Zhang, Y. Cai, R.-G. Xiong, H. Yoshikawa, and K. Awaga, Angew. Chem. Int. Ed. **122**, 6758 (2010).

[100] A. M. Ganose, C. N. Savory, and D. O. Scanlon, J. Phys. Chem. Lett. **6**, 4594 (2015).

[101] G. Kieslich, S. Kumagai, K. T. Butler, T. Okamura, C. H. Hendon, S. Sun, M. Yamashita, A. Walsh, and A. K. Cheetham, Chem. Commun. **51**, 15538 (2015).

[102] S. Chen, R. Shang, B.-W. Wang, Z.-M. Wang, and S. Gao, Angew. Chem. Int. Ed. **127**, 11245 (2015).

[103] W. Li, Z. Wang, F. Deschler, S. Gao, R. H. Friend, and A. K. Cheetham, Nat. Rev. Mater. **2**, 16099 (2017).

[104] D. Weber, Z. Naturforsch. B **33**, 1443 (1978).

[105] C. K. Møller, Nature **182**, 1436 (1958).

[106] C. C. Stoumpos and M. G. Kanatzidis, Acc. Chem. Res. **48**, 2791 (2015).

[107] T. Baikie, Y. Fang, J. M. Kadro, M. Schreyer, F. Wei, S. G. Mhaisalkar, M. Grätzel, and T. J. White, J. Mater. Chem. A **1**, 5628 (2013).

[108] M. T. Weller, O. J. Weber, P. F. Henry, A. M. Di Pumpo, and T. C. Hansen, Chem. Commun. **51**, 4180 (2015).

[109] S. Grimme, J. Comput. Chem. **25**, 1463 (2004).

[110] S. Grimme, J. Comput. Chem. **27**, 1787 (2006).

[111] S. Grimme, J. Antony, S. Ehrlich, and H. Krieg, J. Chem. Phys. **132**, 154104 (2010).

[112] A. Tkatchenko and M. Scheffler, Phys. Rev. Lett. **102**, 073005 (2009).

[113] M. Dion, H. Rydberg, E. Schröder, D. C. Langreth, and B. I. Lundqvist, Phys. Rev. Lett. **92**, 246401 (2004).

[114] L. D. Whalley, J. M. Frost, Y.-K. Jung, and A. Walsh, J. Chem. Phys. **146**, 220901 (2017).

[115] E. L. Da Silva, J. M. Skelton, S. C. Parker, and A. Walsh, Phys. Rev. B **91**, 144107 (2015).

[116] L. D. Whalley, J. M. Skelton, J. M. Frost, and A. Walsh, Phys. Rev. B **94**, 220301 (2016).

[117] M. Murakami, K. Hirose, K. Kawamura, N. Sata, and Y. Ohishi, Science **304**, 855 (2004).

[118] A. R. Oganov and S. Ono, Nature **430**, 445 (2004).

[119] A. Jaffe, Y. Lin, C. M. Beavers, J. Voss, W. L. Mao, and H. I. Karunadasa, ACS Cent. Sci. **2**, 201 (2016).

[120] F. Capitani, C. Marini, S. Caramazza, P. Postorino, G. Garbarino, M. Hanfland, A. Pisanu, P. Quadrelli, and L. Malavasi, J. Appl. Phys. **119**, 185901 (2016).

[121] S. Jiang, Y. Fang, R. Li, H. Xiao, J. Crowley, C. Wang, T. J. White, W. A. Goddard, Z. Wang, T. Baikie, *et al.*, Angew. Chem. Int. Ed. **55**, 6540 (2016).

[122] Y. Wang, X. Lu, W. Yang, T. Wen, L. Yang, X. Ren, L. Wang, Z. Lin, and Y. Zhao, J. Am. Chem. Soc. **137**, 11144 (2015).

[123] I. Swainson, M. Tucker, D. Wilson, B. Winkler, and V. Milman, Chem. Mater. **19**, 2401 (2007).

[124] B. Magyari-Köpe, L. Vitos, G. Grimvall, B. Johansson, and J. Kollar, Phys. Rev. B **65**, 193107 (2002).

[125] D. Trots and S. Myagkota, J. Phys. Chem. Solids **69**, 2520 (2008).

[126] G. H. Imler, X. Li, B. Xu, G. E. Dobereiner, H.-L. Dai, Y. Rao, and B. B. Wayland, Chem. Commun. **51**, 11290 (2015).

[127] F. Hao, C. C. Stoumpos, Z. Liu, R. P. Chang, and M. G. Kanatzidis, J. Am. Chem. Soc. **136**, 16411 (2014).

[128] L.-y. Huang and W. R. Lambrecht, Phys. Rev. B **90**, 195201 (2014).

[129] J.-H. Lee, N. C. Bristowe, P. D. Bristowe, and A. K. Cheetham, Chem. Commun. **51**, 6434 (2015).

[130] D. A. Egger and L. Kronik, J. Phys. Chem. Lett. **5**, 2728 (2014).

[131] V. M. Goldschmidt, Naturwissenschaften **14**, 477 (1926).

[132] G. Kieslich, S. Sun, and A. K. Cheetham, Chem. Sci. **5**, 4712 (2014).

[133] G. Kieslich, S. Sun, and A. K. Cheetham, Chem. Sci. **6**, 3430 (2015).

[134] A. Glazer, Acta Cryst. B **28**, 3384 (1972).

[135] D. B. Mitzi, J. Chem. Soc., Dalton Trans. , 1 (2001).

[136] P. P. Boix, S. Agarwala, T. M. Koh, N. Mathews, and S. G. Mhaisalkar, J. Phys. Chem. Lett. **6**, 898 (2015).

[137] I. C. Smith, E. T. Hoke, D. Solis-Ibarra, M. D. McGehee, and H. I. Karunadasa, Angew. Chem. Int. Ed. **126**, 11414 (2014).

[138] B. Lee, C. C. Stoumpos, N. Zhou, F. Hao, C. Malliakas, C.-Y. Yeh, T. J. Marks, M. G. Kanatzidis, and R. P. Chang, J. Am. Chem. Soc. **136**, 15379 (2014).

[139] C. C. Stoumpos, D. H. Cao, D. J. Clark, J. Young, J. M. Rondinelli, J. I. Jang, J. T. Hupp, and M. G. Kanatzidis, Chem. Mater. **28**, 2852 (2016).

[140] S. Sun, S. Tominaka, J.-H. Lee, F. Xie, P. D. Bristowe, and A. K. Cheetham, APL Mater. **4**, 031101 (2016).

[141] K. Bagnall, J. Laidler, and M. Stewart, J. Chem. Soc. A , 133 (1968).

[142] L. Morss and J. Fuger, Inorg. Chem. **8**, 1433 (1969).

[143] L. R. Morss, M. Siegal, L. Stenger, and N. Edelstein, Inorg. Chem. **9**, 1771 (1970).

[144] G. Meyer, Prog. Solid State Chem. **14**, 141 (1982).

[145] P. A. Tanner, C. S. Mak, N. M. Edelstein, K. M. Murdoch, G. Liu, J. Huang, L. Seijo, and Z. Barandiarán, J. Am. Chem. Soc. **125**, 13225 (2003).

[146] M. Roser, J. Xu, S. J. White, and L. Corruccini, Phys. Rev. B **45**, 12337 (1992).

[147] G. Volonakis, A. A. Haghighirad, R. L. Milot, W. H. Sio, M. R. Filip, B. Wenger, M. B. Johnston, L. M. Herz, H. J. Snaith, and F. Giustino, J. Phys. Chem. Lett. **8**, 772 (2017).

[148] C. N. Savory, A. Walsh, and D. O. Scanlon, ACS Energy Lett. **1**, 949 (2016).

[149] F. Giustino and H. J. Snaith, ACS Energy Lett. **1**, 1233 (2016).

[150] W. Meng, X. Wang, Z. Xiao, J. Wang, D. B. Mitzi, and Y. Yan, J. Phys. Chem. Lett. **8**, 2999 (2017).

[151] A. Poglitsch and D. Weber, J. Chem. Phys. **87**, 6373 (1987).

[152] J. J. Choi, X. Yang, Z. M. Norman, S. J. Billinge, and J. S. Owen, Nano Lett. **14**, 127 (2013).

[153] A. M. Leguy, J. M. Frost, A. P. McMahon, V. G. Sakai, W. Kockelmann, C. Law, X. Li, F. Foglia, A. Walsh, B. C. O'regan, *et al.*, Nat. Commun. **6**, 7124 (2015).

[154] I. Swainson, C. Stock, S. Parker, L. Van Eijck, M. Russina, and J. Taylor, Phys. Rev. B **92**, 100303 (2015).

[155] D. A. Egger, A. M. Rappe, and L. Kronik, Acc. Chem. Res. **49**, 573 (2016).

[156] J. M. Frost, K. T. Butler, and A. Walsh, APL Mater. **2**, 081506 (2014).

[157] M. T. Weller, O. J. Weber, J. M. Frost, and A. Walsh, J. Phys. Chem. Lett. **6**, 3209 (2015).

[158] A. Dualeh, T. Moehl, N. Tétreault, J. Teuscher, P. Gao, M. K. Nazeeruddin, and M. Grätzel, ACS Nano **8**, 362 (2013).

[159] C. Eames, J. M. Frost, P. R. Barnes, B. C. O'regan, A. Walsh, and M. S. Islam, Nat. Commun. **6**, 7497 (2015).

[160] A. Filippetti and A. Mattoni, Phys. Rev. B **89**, 125203 (2014).

[161] W.-J. Yin, T. Shi, and Y. Yan, Adv. Mater. **26**, 4653 (2014).

[162] W. Geng, L. Zhang, Y.-N. Zhang, W.-M. Lau, and L.-M. Liu, J. Phys. Chem. C **118**, 19565 (2014).

[163] G. Giorgi, J.-I. Fujisawa, H. Segawa, and K. Yamashita, J. Phys. Chem. C **118**, 12176 (2014).

[164] C. Motta, F. El-Mellouhi, S. Kais, N. Tabet, F. Alharbi, and S. Sanvito, Nat. Commun. **6**, 7026 (2015).

[165] A. Amat, E. Mosconi, E. Ronca, C. Quarti, P. Umari, M. K. Nazeeruddin, M. Grätzel, and F. D. Angelis, Nano Lett. **14**, 3608 (2014).

[166] J. Even, L. Pedesseau, J.-M. Jancu, and C. Katan, J. Phys. Chem. Lett. **4**, 2999 (2013).

[167] A. Seidl, A. Görling, P. Vogl, J. Majewski, and M. Levy, Phys. Rev. B **53**, 3764 (1996).

[168] F. Giustino, *Materials modelling using density functional theory: properties and predictions* (Oxford University Press (UK), 2014).

[169] J. Feng and B. Xiao, J. Phys. Chem. Lett. **5**, 1278 (2014).

[170] E. Menéndez-Proupin, P. Palacios, P. Wahnón, and J. Conesa, Phys. Rev. B **90**, 045207 (2014).

[171] M. R. Filip and F. Giustino, Phys. Rev. B **90**, 245145 (2014).

[172] M. A. Green, Y. Jiang, A. M. Soufiani, and A. Ho-Baillie, J. Phys. Chem. Lett. **6**, 4774 (2015).

[173] J. S. Townsend, *A modern approach to quantum mechanics* (University Science Books, 2000).

[174] L. Yu and A. Zunger, Phys. Rev. Lett. **108**, 068701 (2012).

[175] L. Yu, R. S. Kokenyesi, D. A. Keszler, and A. Zunger, Adv. Energy Mater. **3**, 43 (2013).

[176] S. Sun, Y. Fang, G. Kieslich, T. J. White, and A. K. Cheetham, J. Mater. Chem. A **3**, 18450 (2015).

[177] J. Feng, APL Mater. **2**, 081801 (2014).

[178] Y. Rakita, S. R. Cohen, N. K. Kedem, G. Hodes, and D. Cahen, MRS Commun. **5**, 623 (2015).

[179] Y. He and G. Galli, Chem. Mater. **26**, 5394 (2014).

[180] M. A. Reyes-Martinez, A. L. Abdelhady, M. I. Saidaminov, D. Y. Chung, O. M. Bakr, M. G. Kanatzidis, W. O. Soboyejo, and Y.-L. Loo, Adv. Mater. **29** (2017).

[181] M. Born and R. Oppenheimer, Ann. Phys. **389**, 457 (1927).

[182] V. Fock, Z. Phys. **61**, 126 (1930).

[183] M. Head-Gordon, R. J. Rico, M. Oumi, and T. J. Lee, Chem. Phys. Lett. **219**, 21 (1994).

[184] G. D. Purvis III and R. J. Bartlett, J. Chem. Phys. **76**, 1910 (1982).

[185] C. Møller and M. S. Plesset, Phys. Rev. **46**, 618 (1934).

[186] J. Pople, R. Seeger, and R. Krishnan, Int. J. Quantum Chem. **12**, 149 (1977).

[187] R. Krishnan and J. A. Pople, Int. J. Quantum Chem. **14**, 91 (1978).

[188] J. P. Perdew and Y. Wang, Phys. Rev. B **45**, 13244 (1992).

[189] J. P. Perdew, J. Chevary, S. Vosko, K. A. Jackson, M. R. Pederson, D. Singh, and C. Fiolhais, Phys. Rev. B **46**, 6671 (1992).

[190] J. P. Perdew, K. Burke, and M. Ernzerhof, Phys. Rev. Lett. **77**, 3865 (1996).

[191] Y. Zhao and D. G. Truhlar, J. Chem. Phys. **125**, 194101 (2006).

[192] J. Kohanoff, *Electronic structure calculations for solids and molecules: theory and computational methods* (Cambridge University Press, 2006).

[193] J. P. Perdew, M. Ernzerhof, and K. Burke, J. Chem. Phys. **105**, 9982 (1996).

[194] C. Lee, W. Yang, and R. G. Parr, Phys. Rev. B **37**, 785 (1988).

[195] J. Heyd, G. E. Scuseria, and M. Ernzerhof, J. Chem. Phys. **118**, 8207 (2003).

[196] K. Burke, J. Chem. Phys. **136**, 150901 (2012).

[197] L. Hedin, Phys. Rev. **139**, A796 (1965).

[198] F. Aryasetiawan and O. Gunnarsson, Rep. Prog. Phys. **61**, 237 (1998).

[199] G. Onida, L. Reining, and A. Rubio, Rev. Mod. Phys. **74**, 601 (2002).

[200] J. Hubbard, Proc. R. Soc. Lond. A **276**, 238 (1963).

[201] J. Hubbard, Proc. R. Soc. Lond. A **281**, 401 (1964).

[202] J. Hubbard, Proc. R. Soc. Lond. A **277**, 237 (1964).

[203] J. Hubbard, Proc. R. Soc. Lond. A **296**, 82 (1967).

[204] J. Hubbard, Proc. R. Soc. Lond. A **285**, 542 (1965).

[205] J. Hubbard, Proc. R. Soc. Lond. A **296**, 100 (1967).

[206] V. I. Anisimov, F. Aryasetiawan, and A. Lichtenstein, J. Phys.: Condens. Matter **9**, 767 (1997).

[207] J. Klimeš, D. R. Bowler, and A. Michaelides, Phys. Rev. B **83**, 195131 (2011).

[208] J. Klimeš, D. R. Bowler, and A. Michaelides, J. Phys.: Condens. Matter **22**, 022201 (2009).

[209] M. C. Payne, M. P. Teter, D. C. Allan, T. Arias, and J. Joannopoulos, Rev. Mod. Phys. **64**, 1045 (1992).

[210] R. Car and M. Parrinello, Phys. Rev. Lett. **55**, 2471 (1985).

[211] H. J. Monkhorst and J. D. Pack, Phys. Rev. B **13**, 5188 (1976).

[212] G. Kresse and J. Furthmuller, Universität Wien, VASP-Guide (2002).

[213] R. M. Martin, *Electronic structure: basic theory and practical methods* (Cambridge university press, 2004).

[214] D. Hamann, M. Schlüter, and C. Chiang, Phys. Rev. Lett. **43**, 1494 (1979).

[215] D. Vanderbilt, Phys. Rev. B **41**, 7892 (1990).

[216] P. E. Blöchl, Phys. Rev. B **50**, 17953 (1994).

[217] G. Kresse and D. Joubert, Phys. Rev. B **59**, 1758 (1999).

[218] K. Lejaeghere, G. Bihlmayer, T. Björkman, P. Blaha, S. Blügel, V. Blum, D. Caliste, I. E. Castelli, S. J. Clark, A. Dal Corso, *et al.*, Science **351**, aad3000 (2016).

[219] R. P. Feynman, Phys. Rev. **56**, 340 (1939).

[220] M. T. Dove, *Introduction to lattice dynamics*, Vol. 4 (Cambridge university press, 1993).

[221] S. Baroni, S. De Gironcoli, A. Dal Corso, and P. Giannozzi, Rev. Mod. Phys. **73**, 515 (2001).

[222] O. Nielsen and R. M. Martin, Phys. Rev. B **32**, 3792 (1985).

[223] W. Voigt, *Lehrbuch der kristallphysik (mit ausschluss der kristalloptik)* (Springer-Verlag, 2014).

[224] A. Reuss, ZAMM Z. Angew. Math. Mech. **9**, 49 (1929).

[225] A. D. Jodlowski, A. Yépez, R. Luque, L. Camacho, and G. de Miguel, Angew. Chem. Int. Ed. **55**, 14972 (2016).

[226] B. D. Cullity, *Elements of X-ray Diffraction* (Pearson, 2001).

[227] A. K. Cheetham and A. L. Goodwin, Nat. Mater. **13**, 760 (2014).

[228] H. M. Rietveld, J. Appl. Crystallogr. **2**, 65 (1969).

[229] H. M. Rietveld, Acta Cryst. **22**, 151 (1967).

[230] G. Pawley, J. Appl. Crystallogr. **14**, 357 (1981).

[231] J. S. Evans, in *Mater. Sci. Forum*, Vol. 651 (Trans Tech Publ, 2010) pp. 1–9.

[232] G. M. Sheldrick, Acta Cryst. A **64**, 112 (2008).

[233] G. M. Sheldrick, Acta Cryst. C **71**, 3 (2015).

[234] O. V. Dolomanov, L. J. Bourhis, R. J. Gildea, J. A. Howard, and H. Puschmann, J. Appl. Crystallogr. **42**, 339 (2009).

[235] R. Jakubas, J. Zaleski, and L. Sobczyk, Ferroelectrics **108**, 109 (1990).

[236] A. J. Lehner, D. H. Fabini, H. A. Evans, C.-A. Hébert, S. R. Smock, J. Hu, H. Wang, J. W. Zwanziger, M. L. Chabinyc, and R. Seshadri, Chem. Mater. **27**, 7137 (2015).

[237] F. Pelle, B. Blanzat, and B. Chevalier, Solid State Commun. **49**, 1089 (1984).

[238] W. Smit, G. Dirksen, and D. Stufkens, J. Phys. Chem. Solids **51**, 189 (1990).

[239] I. Flerov, M. Gorev, K. Aleksandrov, A. Tressaud, J. Grannec, and M. Couzi, Mater. Sci. Eng. R-Rep. **24**, 81 (1998).

[240] F. Prokert and K. Aleksandrov, Phys. Status Solidi B **124**, 503 (1984).

[241] G. E. Eperon, G. M. Paternò, R. J. Sutton, A. Zampetti, A. A. Haghighirad, F. Cacialli, and H. J. Snaith, J. Mater. Chem. A **3**, 19688 (2015).

[242] G. Kresse and J. Hafner, Phys. Rev. B **47**, 558 (1993).

[243] G. Kresse and J. Furthmüller, Comput. Mater. Sci. **6**, 15 (1996).

[244] K. Momma and F. Izumi, J. Appl. Crystallogr. **44**, 1272 (2011).

[245] S. L. Dudarev, G. A. Botton, S. Y. Savrasov, C. J. Humphreys, and A. P. Sutton, Phys. Rev. B **57**, 1505 (1998).

[246] L. Chi, I. Swainson, L. Cranswick, J.-H. Her, P. Stephens, and O. Knop, J. Solid State Chem. **178**, 1376 (2005).

[247] T. D. Bennett, J.-C. Tan, S. A. Moggach, R. Galvelis, C. Mellot-Draznieks, B. A. Reisner, A. Thirumurugan, D. R. Allan, and A. K. Cheetham, Chem. - Eur. J. **16**, 10684 (2010).

[248] Y. Le Page and P. Saxe, Phys. Rev. B **65**, 104104 (2002).

[249] J. F. Nye, *Physical properties of crystals: their representation by tensors and matrices* (Oxford university press, 1985).

[250] A. Filippetti and A. Mattoni, Phys. Rev. B **89**, 125203 (2014).

[251] F. Mouhat and F. m. c.-X. Coudert, Phys. Rev. B **90**, 224104 (2014).

[252] H. B. Kim, I. Im, Y. Yoon, S. Do Sung, E. Kim, J. Kim, and W. I. Lee, J. Mater. Chem. A **3**, 9264 (2015).

[253] S. Tominaka, S. Henke, and A. K. Cheetham, CrystEngComm **15**, 9400 (2013).

[254] S. Tominaka and A. Cheetham, RSC Adv. **4**, 54382 (2014).

[255] F. Zheng, L. Z. Tan, S. Liu, and A. M. Rappe, Nano Lett. **15**, 7794 (2015).

[256] T. Etienne, E. Mosconi, and F. De Angelis, J. Phys. Chem. Lett. **7**, 1638 (2016).

[257] A. Stroppa, D. Di Sante, P. Barone, M. Bokdam, G. Kresse, C. Franchini, M.-H. Whangbo, and S. Picozzi, Nat. Commun. **5**, 5900 (2014).

[258] M. A. Carpenter, J. Phys.: Condens. Matter **27**, 263201 (2015).

[259] T. D. Bennett, J.-C. Tan, S. A. Moggach, R. Galvelis, C. Mellot-Draznieks, B. A. Reisner, A. Thirumurugan, D. R. Allan, and A. K. Cheetham, Chem.–Eur. J. **16**, 10684 (2010).

[260] C. A. Morrison, R. P. Leavitt, and D. E. Wortman, J. Chem. Phys. **73**, 2580 (1980).

[261] C. Ma, P. A. Tanner, S. Xia, and M. Yin, Opt. Mater. **29**, 1620 (2007).

[262] M. G. Brik and K. Ogasawara, Phys. Rev. B **74**, 045105 (2006).

[263] P. Jain, V. Ramachandran, R. J. Clark, H. D. Zhou, B. H. Toby, N. S. Dalal, H. W. Kroto, and A. K. Cheetham, J. Am. Chem. Soc. **131**, 13625 (2009).

[264] W. Li, A. Thirumurugan, P. T. Barton, Z. Lin, S. Henke, H. H. M. Yeung, M. T. Wharmby, E. G. Bithell, C. J. Howard, and A. K. Cheetham, J. Am. Chem. Soc. **136**, 7801 (2014).

[265] J. L. Wu, G. Gundiah, and A. K. Cheetham, Chem. Phys. Lett. **441**, 250 (2007).

[266] B.-w. Park, B. Philippe, T. r. Gustafsson, K. r. Sveinbjo rnsson, A. Hagfeldt, E. M. Johansson, and G. Boschloo, Chem. Mater. **26**, 4466 (2014).

[267] Y.-J. Li, T. Wu, L. Sun, R.-X. Yang, L. Jiang, P.-F. Cheng, Q.-Q. Hao, T.-J. Wang, R.-F. Lu, and W.-Q. Deng, RSC Adv. **7**, 35175 (2017).

[268] P. Cheng, T. Wu, Y. Li, L. Jiang, W. Deng, and K. Han, New J. Chem. **41**, 9598 (2017).

[269] C. Zhang, L. Gao, S. Teo, Z. Guo, Z. Xu, S. Zhao, and T. Ma, Sustainable Energy & Fuels (2018), 10.1039/c8se00154e.

[270] P. E. Blöchl, Phys. Rev. B **50**, 17953 (1994).

[271] W. Humphrey, A. Dalke, and K. Schulten, J. Mol. Graphics **14**, 33 (1996).

[272] J.-H. Lee, N. C. Bristowe, J. H. Lee, S.-H. Lee, P. D. Bristowe, A. K. Cheetham, and H. M. Jang, Chem. Mater. **28**, 4259 (2016).

[273] X.-Z. Li, B. Walker, and A. Michaelides, PNAS **108**, 6369 (2011).

[274] L. M. Herz, ACS Energy Lett. **2**, 1539 (2017).

[275] I. Swainson, M. Tucker, D. Wilson, B. Winkler, and V. Milman, Chem. Mater. **19**, 2401 (2007).

[276] M. Szafranski and A. Katrusiak, J. Phys. Chem. Lett. **7**, 3458 (2016).

[277] S. Jiang, Y. Fang, R. Li, H. Xiao, J. Crowley, C. Wang, T. J. White, W. A. Goddard III, Z. Wang, T. Baikie, *et al.*, Angew. Chem. Int. Ed. **55**, 6540 (2016).

[278] L. Kong, G. Liu, J. Gong, Q. Hu, R. D. Schaller, P. Dera, D. Zhang, Z. Liu, W. Yang, K. Zhu, *et al.*, PNAS **113**, 8910 (2016).

[279] G. Liu, L. Kong, J. Gong, W. Yang, H.-k. Mao, Q. Hu, Z. Liu, R. D. Schaller, D. Zhang, and T. Xu, Adv. Funct. Mater. **27**, 1604208 (2017).

[280] P. Wang, J. Guan, D. T. Galeschuk, Y. Yao, C. F. He, S. Jiang, S. Zhang, Y. Liu, M. Jin, C. Jin, *et al.*, J. Phys. Chem. Lett. **8**, 2119 (2017).

[281] D. H. Fabini, C. C. Stoumpos, G. Laurita, A. Kaltzoglou, A. G. Kontos, P. Falaras, M. G. Kanatzidis, and R. Seshadri, Angew. Chem. Int. Ed. **55**, 15392 (2016).

[282] M. I. Saidaminov, A. L. Abdelhady, G. Maculan, and O. M. Bakr, Chem. Commun. **51**, 17658 (2015).

[283] K. T. Butler, K. Svane, G. Kieslich, A. K. Cheetham, and A. Walsh, Phys. Rev. B **94**, 180103 (2016).

[284] N. Onoda-Yamamuro, T. Matsuo, and H. Suga, J. Phys. Chem. Solids **51**, 1383 (1990).

[285] K. T. Butler, A. Walsh, A. K. Cheetham, and G. Kieslich, Chem. Sci. **7**, 6316 (2016).

[286] M. Szafranski and A. Katrusiak, J. Phys. Chem. Lett. **8**, 2496 (2017).

[287] B. J. Kim, D. H. Kim, Y.-Y. Lee, H.-W. Shin, G. S. Han, J. S. Hong, K. Mahmood, T. K. Ahn, Y.-C. Joo, K. S. Hong, N.-G. Park, S. Lee, and H. S. Jung, Energy Environ. Sci. **8**, 916 (2015).

[288] J. Yu, M. Wang, and S. Lin, ACS Nano **10**, 11044 (2016).

[289] G. E. Eperon, S. D. Stranks, C. Menelaou, M. B. Johnston, L. M. Herz, and H. J. Snaith, Energy Environ. Sci. **7**, 982 (2014).

[290] W. Oliver and G. Pharr, J. Mater. Res. **19**, 3 (2004).

[291] J. C. Tan and A. K. Cheetham, Chem. Soc. Rev. **40**, 1059 (2011).

[292] J. Tan, C. Merrill, J. Orton, and A. Cheetham, Acta Mater. **57**, 3481 (2009).

[293] A. A. Zhumekenov, M. I. Saidaminov, M. A. Haque, E. Alarousu, S. P. Sarmah, B. Murali, I. Dursun, X.-H. Miao, A. L. Abdelhady, T. Wu, O. F. Mohammed, and O. M. Bakr, ACS Energy Lett. **1**, 32 (2016).

[294] M. L. Huggins, J. Am. Chem. Soc. **75**, 4126 (1953).

[295] R. J. Worhatch, H. Kim, I. P. Swainson, A. L. Yonkeu, and S. J. L. Billinge, Chem. Mater. **20**, 1272 (2008).

[296] L. Pauling, *The Nature of the Chemical Bond* (Cornell University Press, 1960).

[297] J. S. Bechtel, R. Seshadri, and A. V. der Ven, J. Phys. Chem. C **120**, 12403 (2016).

[298] M. R. Linaburg, E. T. McClure, J. D. Majher, and P. M. Woodward, Chem. Mater. **29**, 3507 (2017).

[299] J. H. Lee, J.-H. Lee, E.-H. Kong, and H. M. Jang, Sci. Rep. **6**, 21687 (2016).

[300] F. Brivio, K. T. Butler, A. Walsh, and M. van Schilfgaarde, Phys. Rev. B **89**, 155204 (2014).

[301] Y. Zhou, L. You, S. Wang, Z. Ku, H. Fan, D. Schmidt, A. Rusydi, L. Chang, L. Wang, P. Ren, L. Chen, G. Yuan, L. Chen, and J. Wang, Nat. Commun. **7**, 11193 (2016).

[302] J. Ma and L.-W. Wang, Nano Lett. **17**, 3646 (2017).

[303] J.-C. Tan, P. Jain, and A. K. Cheetham, Dalton Trans. **41**, 3949 (2012).

[304] M. Karakus, S. A. Jensen, F. D'Angelo, D. Turchinovich, M. Bonn, and E. Cánovas, J. Phys. Chem. Lett. **6**, 4991 (2015).

[305] T. M. Brenner, D. A. Egger, A. M. Rappe, L. Kronik, G. Hodes, and D. Cahen, J. Phys. Chem. Lett. **6**, 4754 (2015).

[306] Y. Wang, Y. Zhang, P. Zhang, and W. Zhang, Phys. Chem. Chem. Phys. **17**, 11516 (2015).

[307] P.-A. Mante, C. C. Stoumpos, M. G. Kanatzidis, and A. Yartsev, Nat. Commun. **8**, 14398 (2017).

[308] J. M. Frost, Phys. Rev. B **96**, 195202 (2017).

[309] A. Létoublon, S. Paofai, B. Ruffle, P. Bourges, B. Hehlen, T. Michel, C. Ecolivet, O. Durand, S. Cordier, C. Katan, *et al.*, J. Phys. Chem. Lett. **7**, 3776 (2016).

[310] A. J. Neukirch, W. Nie, J.-C. Blancon, K. Appavoo, H. Tsai, M. Y. Sfeir, C. Katan, L. Pedesseau, J. Even, J. J. Crochet, *et al.*, Nano Lett. **16**, 3809 (2016).

[311] A. M. Lomonosov, X. Yan, C. Sheng, V. E. Gusev, C. Ni, and Z. Shen, Phys. Status Solidi Rapid Res. Lett. **10**, 606 (2016).

[312] T. Zhao, W. Shi, J. Xi, D. Wang, and Z. Shuai, Sci. Rep. **7**, 19968 (2016).

[313] A. D. Wright, C. Verdi, R. L. Milot, G. E. Eperon, M. A. Pérez-Osorio, H. J. Snaith, F. Giustino, M. B. Johnston, and L. M. Herz, Nat. Commun. **7**, 11755 (2016).

[314] A. Filippetti, A. Mattoni, C. Caddeo, M. I. Saba, and P. Delugas, Phys. Chem. Chem. Phys. **18**, 15352 (2016).

[315] X. Deng, X. Wen, C. F. J. Lau, T. Young, J. Yun, M. A. Green, S. Huang, and A. W. Y. Ho-Baillie, J. Mater. Chem. C **4**, 9060 (2016).

[316] Y.-B. Lu, X. Kong, X. Chen, D. G. Cooke, and H. Guo, Sci. Rep. **7**, 41860 (2017).

[317] M. Sendner, P. K. Nayak, D. A. Egger, S. Beck, C. Müller, B. Epding, W. Kowalsky, L. Kronik, H. J. Snaith, A. Pucci, and R. Lovrinčić, Mater. Horiz. **3**, 613 (2016).

[318] A. M. A. Leguy, A. R. Goñi, J. M. Frost, J. Skelton, F. Brivio, X. Rodríguez-Martínez, O. J. Weber, A. Pallipurath, M. I. Alonso, M. Campoy-Quiles, M. T. Weller, J. Nelson, A. Walsh, and P. R. F. Barnes, Phys. Chem. Chem. Phys. **18**, 27051 (2016).

[319] A. N. Beecher, O. E. Semonin, J. M. Skelton, J. M. Frost, M. W. Terban, H. Zhai, A. Alatas, J. S. Owen, A. Walsh, and S. J. L. Billinge, ACS Energy Lett. **1**, 880 (2016).

[320] R. X. Yang, J. M. Skelton, E. L. da Silva, J. M. Frost, and A. Walsh, J. Phys. Chem. Lett. **8**, 4720 (2017).

[321] A. Allred, J. Inorg. Nucl. Chem. **17**, 215 (1961).

[322] J. Bardeen and W. Shockley, Phys. Rev. **80**, 72 (1950).

[323] T. J. Savenije, C. S. Ponseca, L. Kunneman, M. Abdellah, K. Zheng, Y. Tian, Q. Zhu, S. E. Canton, I. G. Scheblykin, T. Pullerits, A. Yartsev, and V. Sundström, J. Phys. Chem. Lett. **5**, 2189 (2014).

[324] H. Oga, A. Saeki, Y. Ogomi, S. Hayase, and S. Seki, J. Am. Chem. Soc. **136**, 13818 (2014).

[325] R. L. Milot, G. E. Eperon, H. J. Snaith, M. B. Johnston, and L. M. Herz, Adv. Funct. Mater. **25**, 6218 (2015).

[326] H. Kozuka, K. Ohbayashi, and K. Koumoto, Sci. Technol. Adv. Mater. **16**, 026001 (2015).

[327] G. Divitini, S. Cacovich, F. Matteocci, L. Cinà, A. D. Carlo, and C. Ducati, Nat. Energy **1**, 15012 (2016).

[328] Q. Jiang, D. Rebollar, J. Gong, E. L. Piacentino, C. Zheng, and T. Xu, Angew. Chem. Int. Ed. **54**, 7617 (2015).

[329] M. A. Green and A. Ho-Baillie, ACS Energy Lett. **2**, 822 (2017).

[330] L.-Q. Fan and J.-H. Wu, Acta Cryst. E **63**, i189 (2007).

[331] M. Safdari, A. Fischer, B. Xu, L. Kloo, and J. M. Gardner, J. Mater. Chem.A **3**, 9201 (2015).

[332] J. Brgoch, A. J. Lehner, M. Chabinyc, and R. Seshadri, J. Phys. Chem. C **118**, 27721 (2014).

[333] C. C. Stoumpos, L. Mao, C. D. Malliakas, and M. G. Kanatzidis, Inorg. Chem. **56**, 56 (2016).

[334] M. Szafrański, Thermochim. Acta **307**, 177 (1997).

[335] M. Szafrański and A. Katrusiak, Phys. Rev. B **61**, 1026 (2000).

[336] L. Dimesso, A. Quintilla, Y.-M. Kim, U. Lemmer, and W. Jaegermann, Mater. Sci. Eng. B **204**, 27 (2016).

[337] N. D. Marco, H. Zhou, Q. Chen, P. Sun, Z. Liu, L. Meng, E.-P. Yao, Y. Liu, A. Schiffer, and Y. Yang, Nano Lett. **16**, 1009 (2016).

[338] S. A. Kulkarni, T. Baikie, S. Muduli, R. Potter, S. Chen, F. Yanan, P. Bishop, S. S. Lim, T. C. Sum, N. Mathews, and T. J. White, Jpn. J. Appl. Phys **56**, 08MC05 (2017).

[339] C. M. M. Soe, C. C. Stoumpos, M. Kepenekian, B. Traoré, H. Tsai, W. Nie, B. Wang, C. Katan, R. Seshadri, A. D. Mohite, J. Even, T. J. Marks, and M. G. Kanatzidis, J. Am. Chem. Soc. **139**, 16297 (2017).

[340] O. Nazarenko, M. R. Kotyrba, S. Yakunin, M. Aebli, G. Rainò, B. M. Benin, M. Wörle, and M. V. Kovalenko, J. Am. Chem. Soc. **140**, 3850 (2018).

[341] J. P. Perdew, A. Ruzsinszky, G. I. Csonka, O. A. Vydrov, G. E. Scuseria, L. A. Constantin, X. Zhou, and K. Burke, Phys. Rev. Lett. **100**, 136406 (2008).

[342] K. Tanaka, R. Ozawa, T. Umebayashi, K. Asai, K. Ema, and T. Kondo, Physica E **25**, 378 (2005).

[343] K. D. Karlin, ed., *Progress in Inorganic Chemistry* (John Wiley & Sons, Inc., 1999).

[344] S. Wang, D. B. Mitzi, C. A. Feild, and A. Guloy, J. Am. Chem. Soc. **117**, 5297 (1995).

[345] J.-H. Im, J. Chung, S.-J. Kim, and N.-G. Park, Nanoscale Res. Lett. **7**, 353 (2012).

[346] A. K. Cheetham, G. Kieslich, and H. H.-M. Yeung, Acc. Chem. Res. **51**, 659 (2018).

[347] G. Maculan, A. D. Sheikh, A. L. Abdelhady, M. I. Saidaminov, M. A. Haque, B. Murali, E. Alarousu, O. F. Mohammed, T. Wu, and O. M. Bakr, J. Phys. Chem. Lett. **6**, 3781 (2015).

[348] J. Klimeš, D. R. Bowler, and A. Michaelides, Phys. Rev. B **83**, 195131 (2011).

[349] K. Lee, É. D. Murray, L. Kong, B. I. Lundqvist, and D. C. Langreth, Phys. Rev. B **82**, 081101 (2010).

[350] J. Sun, A. Ruzsinszky, and J. Perdew, Phys. Rev. Lett. **115**, 036402 (2015).

Appendix A

Supplementary Tables and Figures for Chapter 4

Table A.1 Atomic coordinates for $(MA)_2KBiCl_6$ obtained from single crystal diffraction compared with values from DFT geometry optimization. Reproduced from Wei et al.[16] with permission from The Royal Society of Chemistry.

Atom	Experiments			DFT		
	x	y	z	x	y	z
Bi	0.6667	0.3333	0.3333	0.66667	0.33333	0.33333
K	0.3333	0.6667	0.1667	0.33333	0.66667	0.16667
Cl	0.50292(19)	0.49708(19)	0.26189(13)	0.50064	0.49936	0.26155
C	0.3333	0.6667	0.4456(9)	0.33333	0.66667	0.44560
N	0.3333	0.6667	0.3815(8)	0.33333	0.66667	0.37450
H1	-	-	-	0.25664	0.74336	0.46244
H2	-	-	-	0.40409	0.59591	0.35508

Table A.2 Interatomic distances for $(MA)_2KBiCl_6$ from experiments compared with DFT. Reproduced from Wei et al.[16] with permission from The Royal Society of Chemistry.

Atom 1	Atom 2	D_{Exp} (Å)	D_{DFT} (Å)
Bi	Cl	2.681(2)	2.7061
K	Cl	3.049(2)	3.0162
N	C	1.35(3)	1.4924
C	H1	-	1.0969
N	H2	-	1.0410
H1	Cl	-	3.0317
H2	Cl	-	2.3586
N	Cl	3.406(1)	3.279
C	Cl	3.848(2)	3.856

Table A.3 Bond angles for $(MA)_2KBiCl_6$ from experiments compared with DFT. Reproduced from Wei et al.[16] with permission from The Royal Society of Chemistry.

Bond Angle (°)	Exp	DFT
K-Cl-Bi	173.04(12)	172.51
Cl^1-Bi-Cl^2	91.76(9)	92.00
Cl^1-Bi-Cl^3	88.24(9)	88.00
Cl^5-K-Cl^4	98.33(9)	98.86
Cl^4-K-Cl^6	81.67(9)	81.14
C-H1$\cdots$Cl	-	132.32
N-H2$\cdots$Cl	-	146.70

[1]1-y, x-y, z; [2]1+y, -x, z; [3]4/3-x, 2/3-y, 2/3-z; [4]2/3-x, 4/3-y, 1/3-z; [5]1-y, 1+x-y, z; [6]2/3-y+x, 1/3+x, 1/3-z.

Table A.4 Lattice constants (Å), equilibrium volume (Å^3) and c/a ratio of hybrid double perovskites. Reproduced from Deng et al.[26] with permission from The Royal Society of Chemistry.

A	B^I	B^{III}	X	a	c	V	c/a
MA	K	Bi	Cl	7.82	20.99	1110.64	2.69
MA	K	Bi	Br	8.17	22.05	1274.99	2.70
MA	K	Bi	I	8.75	23.44	1553.34	2.68
MA	Tl	Bi	Cl	7.87	21.16	1134.52	2.69
MA	Tl	Bi	Br	8.20	22.02	1282.42	2.69
MA	Tl	Bi	I	8.72	23.22	1528.19	2.66
MA	Cu	Bi	Cl	7.38	19.53	920.57	2.65
MA	Cu	Bi	Br	7.75	20.35	1057.67	2.63
MA	Cu	Bi	I	8.28	21.54	1278.68	2.60
MA	Ag	Bi	Cl	7.54	19.97	984.27	2.65
MA	Ag	Bi	Br	7.90	20.77	1122.54	2.63
MA	Ag	Bi	I	8.40	22.00	1345.23	2.62
MA	Pb	Pb	Cl	7.95	20.33	1112.42	2.56
MA	Pb	Pb	Br	8.29	21.24	1265.21	2.56
MA	Pb	Pb	I	8.83	22.47	1517.20	2.54

Table A.5 Interatomic distances (Å) of hybrid double perovskites. Reproduced from Deng et al.[26] with permission from The Royal Society of Chemistry.

A	B^I	B^{III}	X	B^{III}-X	B^I-X	X···H1	X···H2	N···X	C···X	C-N	C-H1	N-H2
MA	K	Bi	Cl	2.706	3.016	3.032	2.359	3.279	3.856	1.492	1.097	1.041
MA	K	Bi	Br	2.851	3.141	3.245	2.554	3.466	4.069	1.495	1.097	1.041
MA	K	Bi	I	3.058	3.335	3.585	2.783	3.702	4.406	1.497	1.098	1.042
MA	Tl	Bi	Cl	2.706	3.056	3.125	2.340	3.272	3.936	1.494	1.097	1.041
MA	Tl	Bi	Br	2.854	3.145	3.286	2.518	3.442	4.103	1.495	1.097	1.042
MA	Tl	Bi	I	3.063	3.292	3.511	2.782	3.699	4.337	1.497	1.098	1.042
MA	Cu	Bi	Cl	2.753	2.609	2.567	2.267	3.150	3.441	1.479	1.094	1.038
MA	Cu	Bi	Br	2.899	2.715	2.739	2.436	3.319	3.617	1.484	1.095	1.039
MA	Cu	Bi	I	3.103	2.875	2.990	2.675	3.560	3.872	1.488	1.097	1.041
MA	Ag	Bi	Cl	2.722	2.764	2.708	2.299	3.199	3.565	1.486	1.095	1.039
MA	Ag	Bi	Br	2.871	2.858	2.871	2.467	3.365	3.733	1.489	1.097	1.040
MA	Ag	Bi	I	3.078	3.004	3.109	2.727	3.618	3.976	1.492	1.098	1.041
MA	Pb	Pb	Cl	2.844	2.868	2.878	2.340	3.255	3.748	1.491	1.097	1.041
MA	Pb	Pb	Br	2.969	2.990	3.072	2.512	3.428	3.936	1.494	1.097	1.041
MA	Pb	Pb	I	3.155	3.172	3.353	2.744	3.665	4.212	1.497	1.098	1.042

Table A.6 Bond angles (°) in hybrid double perovskites. Reproduced from Deng et al.[26] with permission from The Royal Society of Chemistry.

A	B^{I}	B^{III}	X	B^{I}-X-B^{III}	X1-B^{III}-X2	X1-B^{III}-X2	X5-B^{I}-X4	X4-B^{I}-X6	C-H1$\cdots$X	N-H2$\cdots$X
MA	K	Bi	Cl	172.51	92.00	88.00	98.86	81.14	132.32	146.70
MA	K	Bi	Br	172.80	91.58	88.42	98.89	81.11	132.68	146.03
MA	K	Bi	I	174.11	90.87	89.13	97.68	82.32	132.93	147.21
MA	Tl	Bi	Cl	173.05	91.58	88.42	98.51	81.49	131.26	148.24
MA	Tl	Bi	Br	174.01	90.87	89.13	97.82	82.18	132.09	147.46
MA	Tl	Bi	I	175.14	90.33	89.67	96.72	85.02	133.27	146.97
MA	Cu	Bi	Cl	176.83	90.81	89.19	95.41	84.59	136.28	141.92
MA	Cu	Bi	Br	178.10	91.42	88.58	94.17	85.84	136.83	142.23
MA	Cu	Bi	I	179.27	91.83	88.17	92.88	87.12	137.60	142.79
MA	Ag	Bi	Cl	175.36	90.30	89.71	96.42	83.58	134.70	144.05
MA	Ag	Bi	Br	176.60	90.35	89.65	95.26	84.74	135.46	144.03
MA	Ag	Bi	I	177.57	90.89	89.11	94.39	85.61	136.40	143.66
MA	Pb	Pb	Cl	174.53	92.21	87.79	95.63	84.37	136.30	146.01
MA	Pb	Pb	Br	175.94	91.15	88.85	94.67	85.33	135.99	146.40
MA	Pb	Pb	I	177.50	90.31	89.69	93.27	86.73	136.00	147.40

Table A.7 Electronic band gaps (eV) of hybrid double perovskites. Reproduced from Deng et al.[26] with permission from The Royal Society of Chemistry.

A	B^{I}	B^{III}	X	E_g (DFT+SOC)	E_g (exp)
MA	K	Bi	Cl	3.02	3.04
MA	K	Bi	Br	2.54	
MA	K	Bi	I	1.84	
MA	Tl	Bi	Cl	1.23	
MA	Tl	Bi	Br	0.72	2.16*
MA	Tl	Bi	I	0.28	
MA	Cu	Bi	Cl	0.79	
MA	Cu	Bi	Br	0.56	
MA	Cu	Bi	I	0.28	
MA	Ag	Bi	Cl	1.57	
MA	Ag	Bi	Br	1.11	
MA	Ag	Bi	I	0.6	
MA	Pb	Pb	Cl	1.15	2.88*[347]
MA	Pb	Pb	Br	0.67	2.20*[20]
MA	Pb	Pb	I	0.27	

*E_g measured in cubic symmetry by experiments.

Table A.8 Positions of valance band maximum (VBM) and conduction band minimum (CBM). Reproduced from Deng et al.[26] with permission from The Royal Society of Chemistry.

A	B^{I}	B^{III}	X	VBM	CBM
MA	K	Bi	Cl	L	A
MA	K	Bi	Br	Near L	A
MA	K	Bi	I	Γ	A
MA	Tl	Bi	Cl	Γ	Γ
MA	Tl	Bi	Br	Γ	Γ
MA	Tl	Bi	I	Γ	Γ
MA	Cu	Bi	Cl	M	L
MA	Cu	Bi	Br	M	L
MA	Cu	Bi	I	M	L
MA	Ag	Bi	Cl	M	L
MA	Ag	Bi	Br	M	L
MA	Ag	Bi	I	M	L
MA	Pb	Pb	Cl	Γ	Γ
MA	Pb	Pb	Br	Γ	Γ
MA	Pb	Pb	I	Γ	Γ

Table A.9 Tolerance factors of double perovskites. Reproduced from Deng et al.[26] with permission from The Royal Society of Chemistry.

	Cl	Br	I
K	0.933	0.923	0.907
Cu	1.038	1.021	0.997
Tl	0.915	0.905	0.892
Ag	0.97	0.957	0.939
Pb	0.938	0.927	0.912

Table A.10 Single crystal elastic stiffness constants (C_{ij}) of hybrid double perovskites. All units are in GPa. Reproduced from Deng et al.[26] with permission from The Royal Society of Chemistry.

A	B^{I}	B^{III}	X	C_{11}	C_{12}	C_{13}	C_{14}	C_{33}	C_{44}	C_{66}
MA	K	Bi	Cl	31.75	11.75	14.38	-3.58	24.79	12.11	10.00
MA	K	Bi	Br	25.03	9.13	11.99	-3.89	18.90	10.68	7.95
MA	K	Bi	I	19.60	7.15	9.97	-3.58	17.40	8.94	6.23
MA	Tl	Bi	Cl	29.79	10.73	14.28	-4.29	21.45	11.86	9.53
MA	Tl	Bi	Br	25.91	9.43	13.36	-4.28	22.08	11.35	8.24
MA	Tl	Bi	I	24.29	8.52	11.72	-4.59	19.42	10.69	7.89
MA	Cu	Bi	Cl	55.40	33.67	21.95	13.81	57.62	5.70	10.86
MA	Cu	Bi	Br	50.49	26.65	20.75	7.96	43.25	4.79	11.92
MA	Cu	Bi	I	44.75	20.24	15.96	5.19	38.27	6.15	12.26
MA	Ag	Bi	Cl	47.23	28.00	24.07	3.44	36.46	10.30	9.61
MA	Ag	Bi	Br	43.93	20.64	18.87	3.04	34.39	9.19	11.65
MA	Ag	Bi	I	38.21	16.99	16.02	1.19	33.22	8.84	10.61
MA	Pb	Pb	Cl	45.67	17.40	22.15	-6.56	33.22	17.91	14.14
MA	Pb	Pb	Br	40.67	13.86	18.48	-6.30	29.26	15.93	13.41
MA	Pb	Pb	I	33.15	10.92	15.08	-5.76	23.82	13.96	11.12

Table A.11 Calculated polycrystalline elastic Young's modulus (E), bulk modulus (B), shear modulus (G), Poisson's ratio (ν) as well as the range of corresponding single crystal elastic modulus. All units are in GPa except ν. $(MA)_2CuCl_6$ and $(MA)_2CuBr_6$ are not mechanically stable therefore properties are not shown here. Reproduced from Deng et al.[26] with permission from The Royal Society of Chemistry.

A	B^{I}	B^{III}	X	E	B	G	ν	E_{max}	E_{min}	G_{max}	G_{min}	ν_{max}	ν_{min}
MA	K	Bi	Cl	24.03	18.75	9.34	0.29	35.17	15.29	14.78	6.28	0.50	0.10
MA	K	Bi	Br	18.85	14.97	7.31	0.29	31.06	10.49	13.44	4.28	0.58	0.05
MA	K	Bi	I	15.33	12.31	5.93	0.29	26.14	9.97	11.41	3.66	0.62	0.06
MA	Tl	Bi	Cl	21.70	17.64	8.38	0.29	35.38	11.38	15.13	4.78	0.56	0.07
MA	Tl	Bi	Br	19.90	16.24	7.68	0.30	33.26	11.98	14.35	4.59	0.60	0.07
MA	Tl	Bi	I	18.42	14.64	7.14	0.29	32.01	11.05	14.09	4.24	0.60	0.06
MA	Cu	Bi	Cl	-	-	-	-	-	-	-	-	-	-
MA	Cu	Bi	Br	-	-	-	-	-	-	-	-	-	-
MA	Cu	Bi	I	21.64	25.62	7.96	0.36	30.43	9.20	15.22	3.18	0.96	0.25
MA	Ag	Bi	Cl	25.08	31.00	9.19	0.37	35.45	21.06	13.41	6.50	0.51	0.19
MA	Ag	Bi	Br	26.23	26.31	9.83	0.33	23.36	19.56	13.70	7.14	0.48	0.29
MA	Ag	Bi	I	25.29	23.01	9.60	0.32	23.92	21.99	11.21	8.24	0.39	0.29
MA	Pb	Pb	Cl	32.26	27.39	12.37	0.30	52.53	17.66	22.63	7.28	0.56	0.07
MA	Pb	Pb	Br	29.87	23.45	11.60	0.29	48.74	16.74	21.09	6.94	0.55	0.08
MA	Pb	Pb	I	24.82	19.05	9.68	0.28	41.96	13.50	18.48	5.56	0.57	0.06

Table A.12 EDS elemental analysis. Areas are indicated in Fig. A.9. Reprinted with permission from Wei et al.[27]. Copyright (2017) American Chemical Society.

Area 23				
Element	wt%	normalized wt%	atom%	Error
Br-L	49.07	56.74	72.56	6.95
Ag-L	11.88	13.74	13.01	1.24
Bi-M	25.53	29.52	14.43	2.78
Total	88.52	100	100	
Area 24				
Element	wt%	normalized wt%	atom%	Error
Br-L	49.36	55.76	71.42	6.99
Ag-L	13.35	15.08	14.31	1.37
Bi-M	25.81	29.16	14.28	2.81
Total	88.52	100	100	

Table A.13 Measured Young's Moduli of $MAPbBr_3$, $(MA)_2TlBiBr_6$ and $(MA)_2AgBiBr_6$. Reprinted with permission from Wei et al.[27]. Copyright (2017) American Chemical Society.

		Young's Modulus (GPa)	Standard Deviation
$MAPbBr_3$	{110}	15.6	0.6
$(MA)_2TlBiBr_6$	{111}	12.8	1.9
$(MA)_2AgBiBr_6$	{110}	8.4	1.7
$(MA)_2AgBiBr_6$	{111}	7.9	1.4

Table A.14 VT-SCXRD measured structural properties of $(MA)_2KGdCl_6$. For the high temperature cubic structures, the H, C and N positions were not refined therefore the C-N bond length and N$\cdots$Cl distance are not shown. Reprinted with permission from Deng et al.[29]. Copyright (2017) American Chemical Society.

	300K	330K	360K	390K	420K
Space Group	$R\bar{3}m$	$R\bar{3}m$	$R\bar{3}m$	$Fm\bar{3}m$	$Fm\bar{3}m$
a (Å)	7.7704(5)	7.8063(6)	7.8445(9)	11.4279(6)	11.4426(6)
c (Å)	20.945(2)	20.945(2)	20.791(4)	11.4279(6)	11.4426(6)
c/a	2.7	2.68	2.65	1.00	1.00
V (Å^3)	1095.21(18)	1104.1(2)	1108.0(3)	1492.4(2)	1498.2(2)
$d_{K\text{-}Cl}$ (Å)	3.0572(14)	3.0631(15)	3.0645(19)	3.060(10)	3.069(11)
$d_{M\text{-}Cl}$ (Å)	2.6374(12)	2.6442(14)	2.6457(17)	2.654(10)	2.652(11)
$d_{C\text{-}N}$ (Å)	1.36(2)	1.35(3)	1.31(3)	-	-
$d_{N\cdots Cl}$ (Å)	3.397(10)	3.407(11)	3.430(14)	-	-
K-Cl-M (°)	173.09(10)	173.56(11)	174.10(12)	180.00	180.00

Table A.15 VT-SCXRD measured structural properties of $(MA)_2KYCl_6$. For the high temperature cubic structures, the H, C and N positions were not refined therefore the C-N bond length and N$\cdots$Cl distance are not shown. Reprinted with permission from Deng et al.[29]. Copyright (2017) American Chemical Society.

	300K	330K	360K	390K	420K	450K
Space Group	$R\bar{3}m$	$R\bar{3}m$	$R\bar{3}m$	$R\bar{3}m$	$R\bar{3}m$	$Fm\bar{3}m$
a (Å)	7.6212(12)	7.6360(10)	7.6531(8)	7.6774(9)	7.7141(10)	11.2141(10)
c (Å)	20.742(4)	20.734(3)	20.705(3)	20.635(3)	20.530(4)	11.2141(10)
c/a	2.72	2.72	2.71	2.69	2.66	1.00
V (Å^3)	1043.4(4)	1047.0(3)	1050.2(3)	1053.4(3)	1058.0(3)	1410.2(4)
$d_{K\text{-}Cl}$ (Å)	3.0305(17)	3.0331(15)	3.0398(15)	3.0396(17)	3.042(3)	3.0188(3)
$d_{M\text{-}Cl}$ (Å)	2.5764(15)	2.5789(14)	2.5764(14)	2.5797(15)	2.582(3)	2.5882(3)
$d_{C\text{-}N}$ (Å)	1.40(3)	1.39(3)	1.39(3)	1.33(3)	1.34(5)	-
$d_{N\cdots Cl}$ (Å)	3.341(11)	3.343(10)	3.365(11)	3.366(13)	3.36(3)	-
K-Cl-M (°)	172.74(11)	173.00(11)	173.17(10)	173.50(11)	174.15(14)	180.00

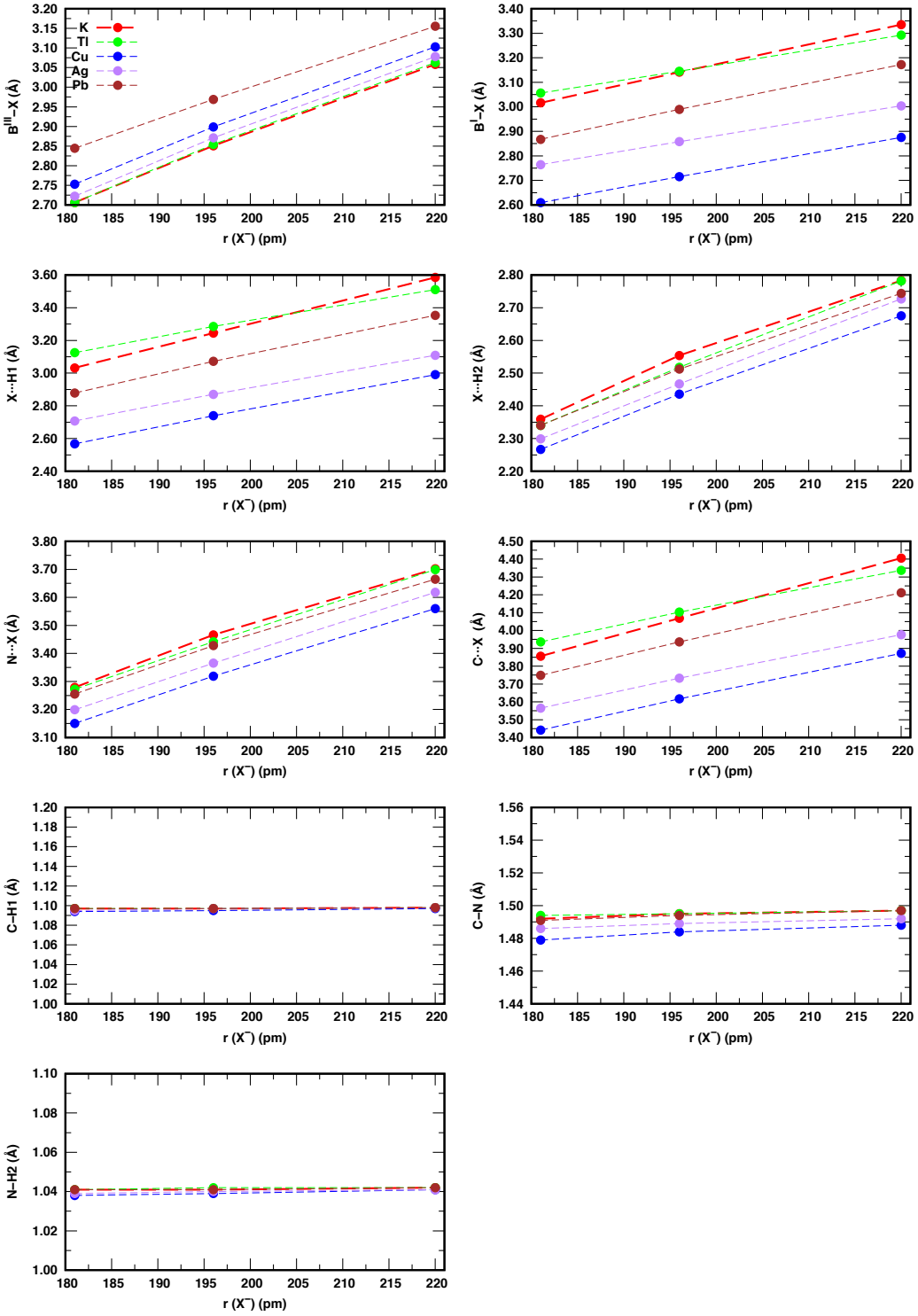

Fig. A.1 Plot of interatomic distances of hybrid double perovskites versus radius of anion X^-. Reproduced from Deng et al.[26] with permission from The Royal Society of Chemistry.

Table A.16 DFT-calculated (optB86b+vdW) elastic constants of rhombohedral $(MA)_2KGdCl_6$, $(MA)_2KYCl_6$ and $(MA)_2KBiCl_6$. Units are GPa. Reprinted with permission from Deng et al.[29]. Copyright (2017) American Chemical Society.

	c_{11}	c_{12}	c_{13}	c_{14}	c_{33}	c_{44}	c_{66}
$(MA)_2KGdCl_6$	29.33	7.80	18.43	-3.05	38.23	13.17	10.76
$(MA)_2KYCl_6$	30.58	9.32	16.29	-2.61	35.32	13.82	10.63
$(MA)_2KBiCl_6$	31.75	11.75	14.38	-3.58	24.79	12.11	10.00

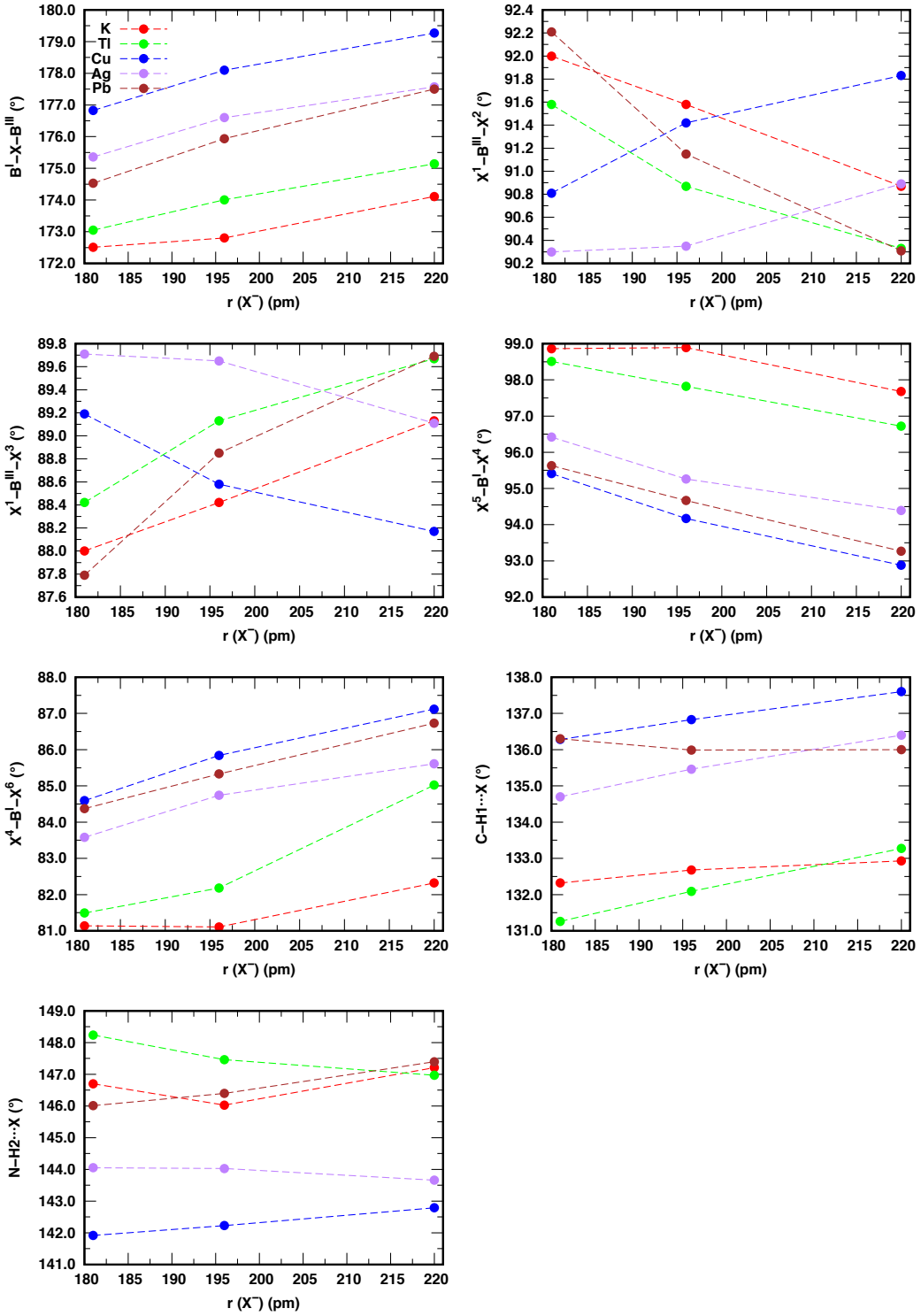

Fig. A.2 Plot of bond angles of hybrid double perovskites versus radius of anion X^-. Reproduced from Deng et al.[26] with permission from The Royal Society of Chemistry.

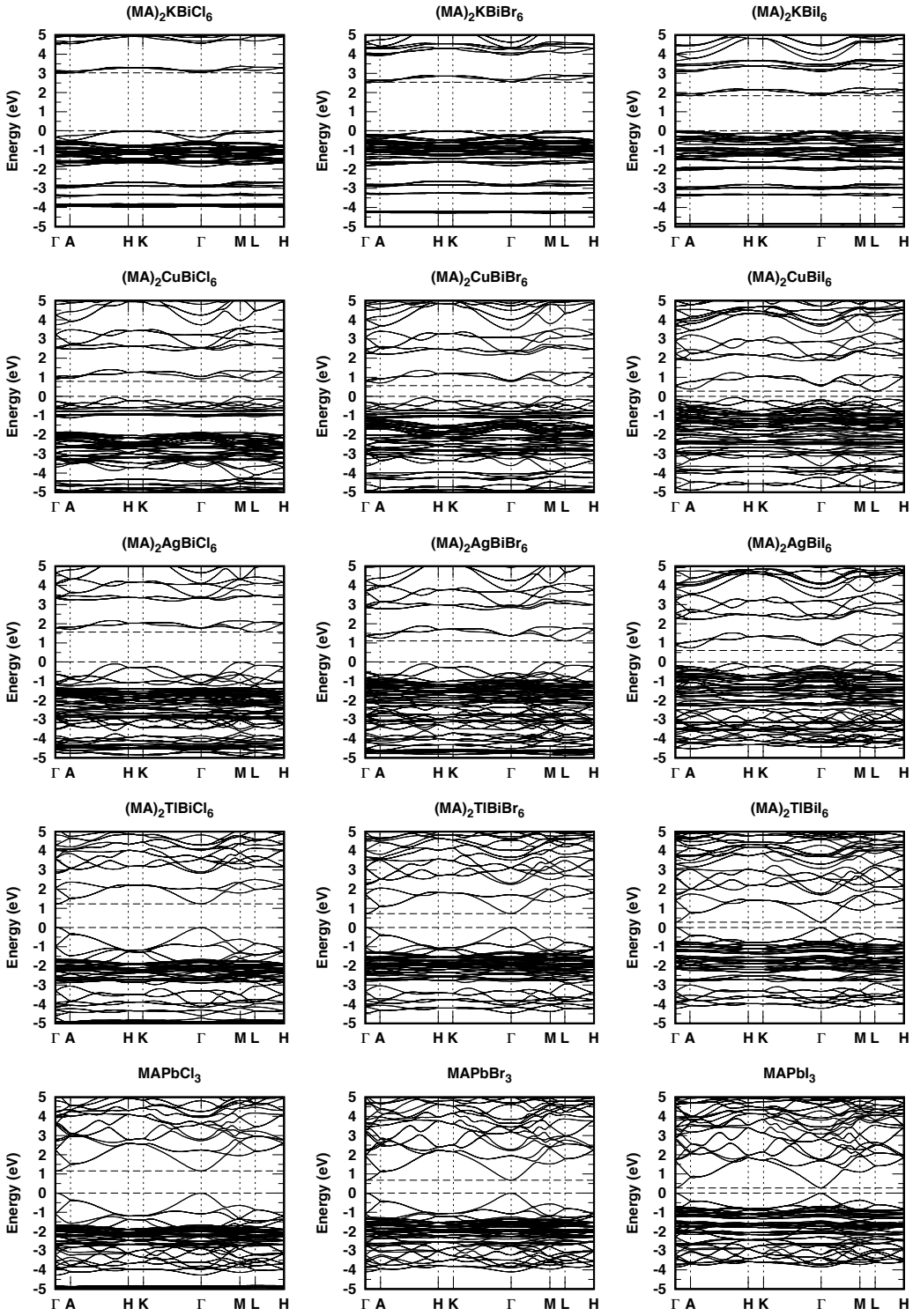

Fig. A.3 Electronic band structures of hybrid double perovskites as well as the reference $MAPbX_3$. The following high symmetry points in the first Brillouin zone were used: Γ(0,0,0), A (0,0,0.5), H (-0.333,0.667,0.5), K (-0.333,0.667,0), M (0,0.5,0) and L (0,0.5,0.5). Reproduced from Deng et al.[26] with permission from The Royal Society of Chemistry.

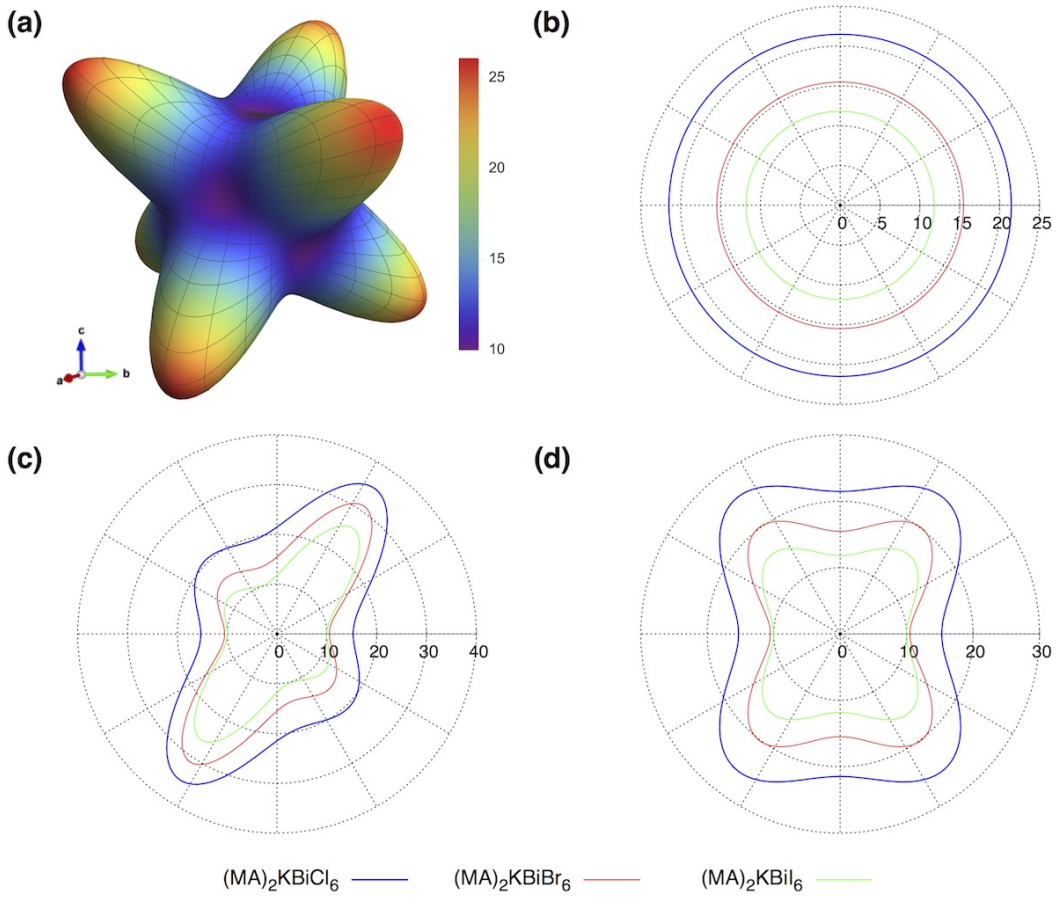

Fig. A.4 (a) Calculated 3D directional Young's modulus of $(MA)_2KBiI_6$ and the contour plots of $(MA)_2KBiX_6$ on (b) (001) plane (c) the plane perpendicular to [100] (d) (010) plane. Units shown are in GPa. Reproduced from Deng et al.[26] with permission from The Royal Society of Chemistry.

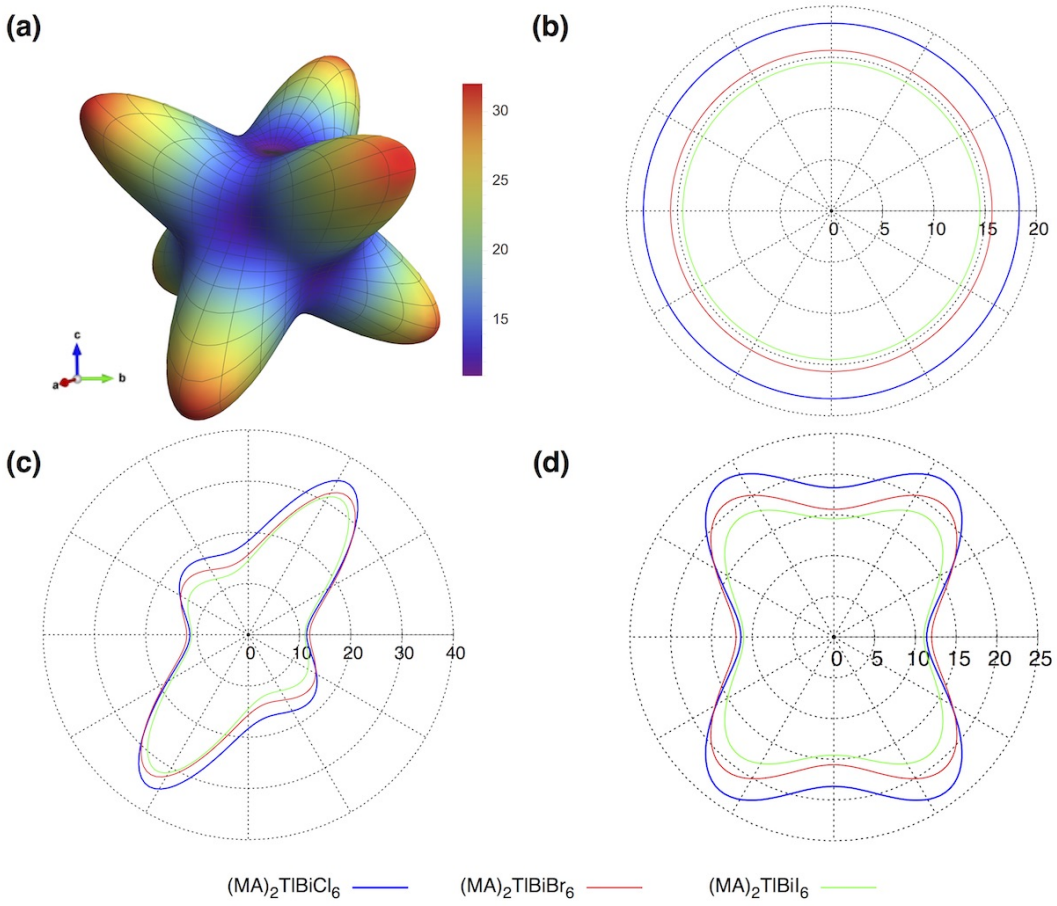

Fig. A.5 (a) Calculated 3D directional Young's modulus of $(MA)_2TlBiI_6$ and the contour plots of $(MA)_2TlBiX_6$ on (b) (001) plane (c) the plane perpendicular to [100] (d) (010) plane. Units shown are in GPa. Reproduced from Deng et al.[26] with permission from The Royal Society of Chemistry.

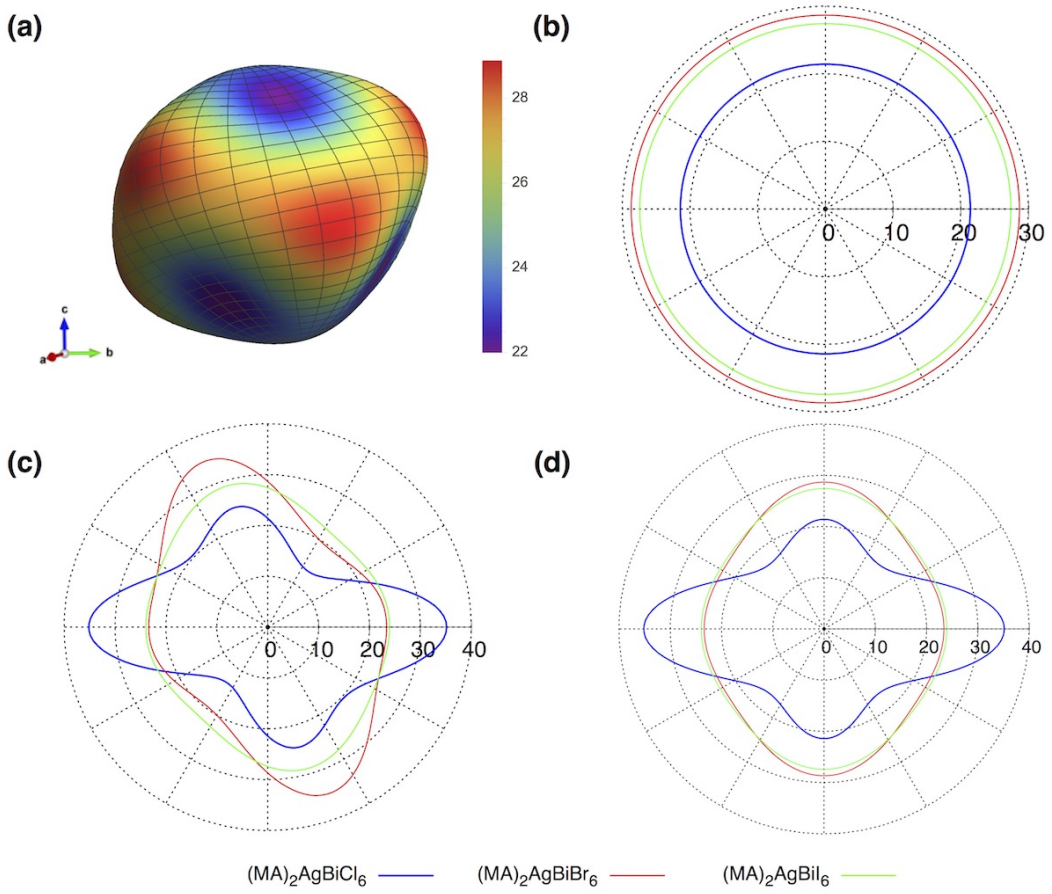

Fig. A.6 (a) Calculated 3D directional Young's modulus of $(MA)_2AgBiI_6$ and the contour plots of $(MA)_2AgBiX_6$ on (b) (001) plane (c) the plane perpendicular to [100] (d) (010) plane. Units shown are in GPa. Reproduced from Deng et al.[26] with permission from The Royal Society of Chemistry.

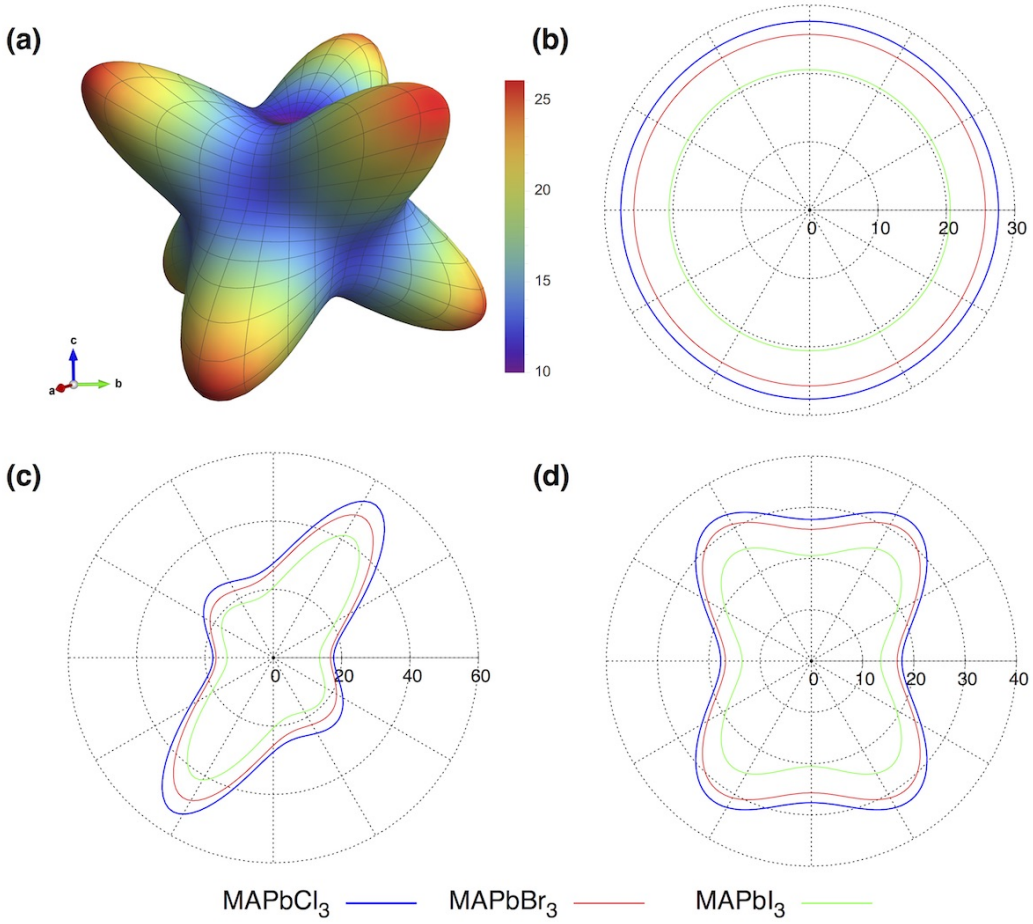

Fig. A.7 (a) Calculated 3D directional Young's modulus of $MAPbI_3$ and the contour plots of $MAPbX_3$ on (b) (001) plane (c) the plane perpendicular to [100] (d) (010) plane. Units shown are in GPa. Reproduced from Deng et al.[26] with permission from The Royal Society of Chemistry.

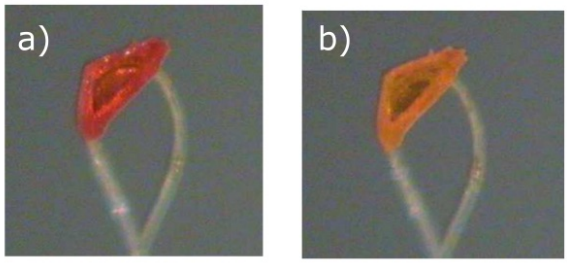

Fig. A.8 Photos of single crystal $(MA)_2AgBiBr_6$ at 300K and 120K. Reprinted with permission from Wei et al.[27]. Copyright (2017) American Chemical Society.

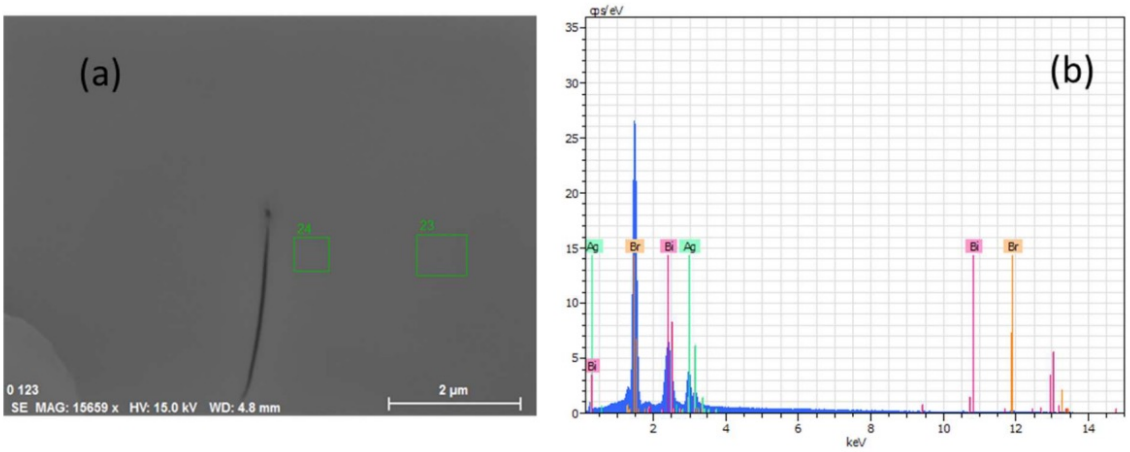

Fig. A.9 SEM image of $(MA)_2AgBiBr_6$ and the corresponding EDS spectrum (area 24). Reprinted with permission from Wei et al.[27]. Copyright (2017) American Chemical Society.

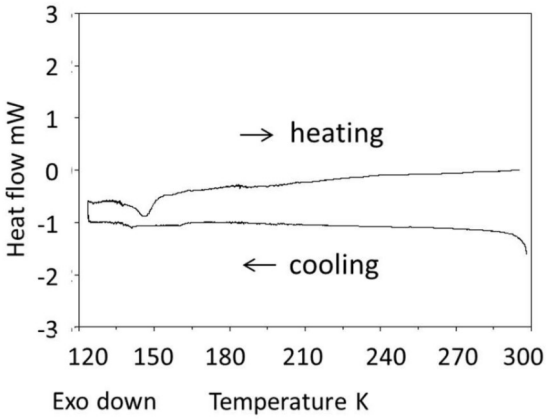

Fig. A.10 DSC curve for $(MA)_2AgBiBr_6$ upon cooling. The peak at 150K is probably due to the liquid nitrogen. Reprinted with permission from Wei et al.[27]. Copyright (2017) American Chemical Society.

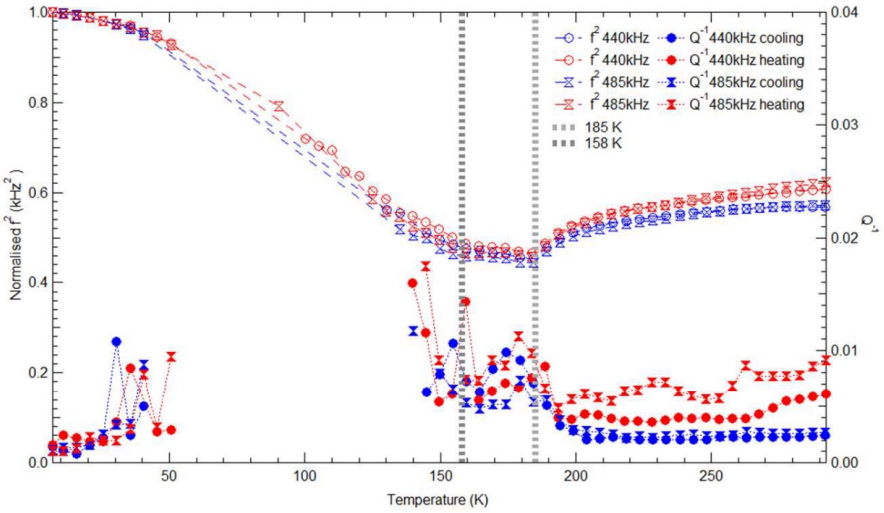

Fig. A.11 Variation of f^2 (proportional to elastic constants) and Q^{-1} (indicative of acoustic attenuation) from selected resonance peaks in RUS spectra collected during cooling (blue) and heating (red). Reprinted with permission from Wei et al.[27]. Copyright (2017) American Chemical Society.

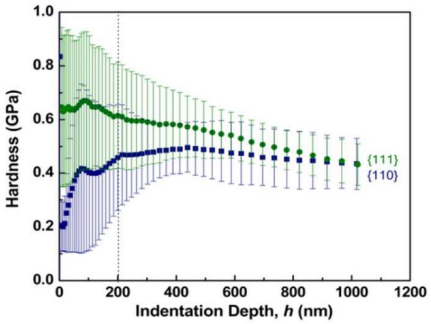

Fig. A.12 Hardness of $(MA)_2AgBiBr_6$ as a function of indentation depth. Reprinted with permission from Wei et al.[27]. Copyright (2017) American Chemical Society.

Appendix B

Supplementary Tables and Figures for Chapter 5

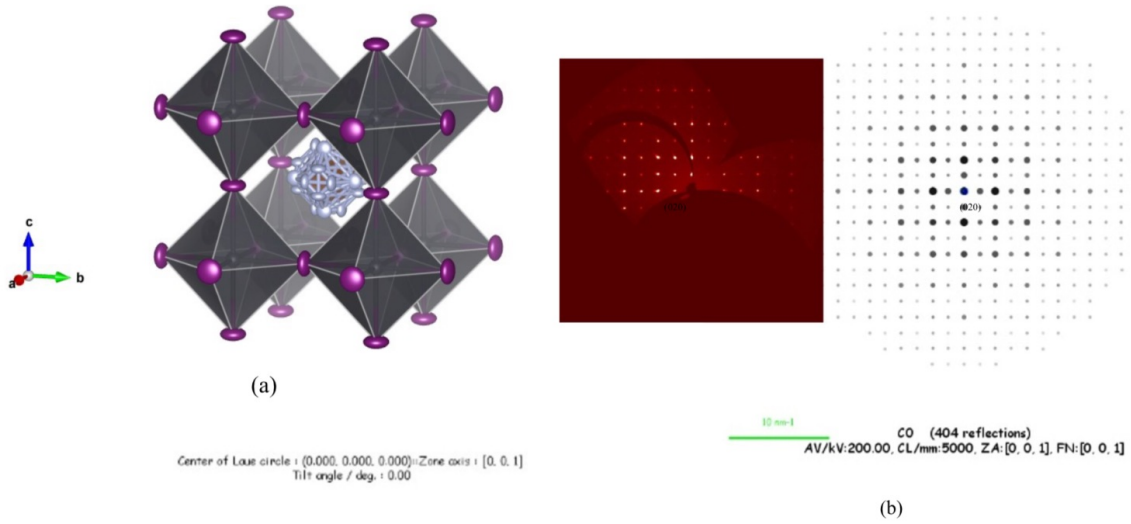

Fig. B.1 (a) Crystal structure of $FAPbI_3$ at 300 K, iodide ions form ellipsoids (shown with 50% probability) that are perpendicular to the Pb-Pb vector in the cubic plane. Grey spheres represent lead,purple represent iodide, carbon (brown) and nitrogen (blue) are modelled with disorder inside the perovskite cage. (b) X-ray diffraction patterns along [001] of $FAPbI_3$ at 300 K. The collected experimental pattern (left) is consistent with the simulated pattern using JEMS image simulation software (right) after structural solutions in the space group of $Pm\bar{3}m$. Reproduced from Sun et al.[30] with permission from The Royal Society of Chemistry.

Table B.1 Details of change in lattice parameters with temperature. Reproduced from Sun et al.[30] with permission from The Royal Society of Chemistry.

	Temperature (K)	a(Å)	c (Å)	Unit Cell Volume (Å^3)
1	300	6.3566(2)		256.84(1)
2	450	6.4009(5)		262.25(4)
3	400	6.3936(4)		261.36(3)
4	350	6.3806(3)		259.77(2)
5	300	6.3667(2)		258.07((2)
6	250	8.9710(7)	6.3427(8)	510.45(9)
7	200	8.9491(6)	6.3283(6)	506.80(7)
8	150	8.9267(6)	6.3126(6)	503.03(7)
9	120	8.8869(3)	6.2854(5)	496.40(5)
10	100	8.8750(20)	6.2820(30)	494.90(3)

Table B.2 Details of the structure solution using variable temperature X-ray diffraction. Reproduced from Sun et al.[30] with permission from The Royal Society of Chemistry.

Empirical formula	CN_2PbI_3[1]			
Formula weight	632.96			
Crystal size/mm^3	$0.24 \times 0.14 \times 0.06$			
Radiation	MoKα (λ = 0.71073)			
Crystal system	Cubic		Tetragonal	
Space group	$Pm\bar{3}m$		$P4/mbm$	
Z	1		2	
F(000)	266		522	
Temperature (K)	299.95(10)	150.00 (14)	200.00 (14)	249.95 (10)
a/Å	6.3667(2)	8.9267(6)	8.9491(6)	8.9710(7)
b/Å	6.3667(2)	8.9267(6)	8.9491(6)	8.9710(7)
c/Å	6.3667(2)	6.3126(6)	6.3283(6)	6.3427(8)
α/°	90	90	90	90
β/°	90	90	90	90
γ/°	90	90	90	90
Volume/Å^3	258.07(2)	503.03(8)	506.81(8)	510.45(10)
Density (calculated)/$g \cdot cm^{-1}$	4.073	4.146	4.115	4.092
μ/mm^{-1}	25.243	25.9	25.706	25.523
2θ range for data collection/°	6.4 to 55.678	6.454 to 56.202	6.438 to 56.048	6.422 to 55.902
Index ranges	$-3 \le h \le 8, -8 \le k \le 1, -3 \le l \le 8$	$-9 \le h \le 10, -3 \le k \le 11, -8 \le l \le 1$	$-11 \le h \le 3, -10 \le k \le 9, -1 \le l \le 8$	$-10 \le h \le 9, -11 \le k \le 3, -8 \le l \le 1$
Reflections collected	584	1051	1064	1089
Independent reflections	90 [$R_{int} = 0.0771, R_{sigma} = 0.0439$]	337 [$R_{int} = 0.0445, R_{sigma} = 0.0423$]	343 [$R_{int} = 0.0445, R_{sigma} = 0.0472$]	346 [$R_{int} = 0.0420, R_{sigma} = 0.0403$]
Data/restraints/parameters	90/0/9	337/14/14	343/3/14	346/3/18
Goodness-of-fit on F^2	1.025	1.128	1.293	1.055
Final R indexes [$l \ge 2\sigma(l)$]	$R_1 = 0.0442, wR_2 = 0.1065$	$R_1 = 0.0648, wR_2 = 0.1579$	$R_1 = 0.0629, wR_2 = 0.1948$	$R_1 = 0.0445, wR_2 = 0.1159$
Final R indexes [all data]	$R_1 = 0.0532, wR_2 = 0.1386$	$R_1 = 0.0781, wR_2 = 0.1677$	$R_1 = 0.0776, wR_2 = 0.2072$	$R_1 = 0.0655, wR_2 = 0.1323$
Largest diff. peak/hole/e^{-3}	0.82/-2.32	4.11/-3.02	3.00/-2.31	2.31/-1.46

[1]H positions were not considered in the structural solution due to the difficulty of detecting light H in the presence of heavy Pb and I in X- ray diffraction.

Table B.3 Fractional Atomic Coordinates and Equivalent Isotropic Displacement Parameters (Å^2) for low temperature phases. U_{eq} is defined as 1/3 of of the trace of the orthogonalized U_{IJ} tensor. Reproduced from Sun et al.[30] with permission from The Royal Society of Chemistry.

		Atom	x	y	z	Occupancy	U	Symmetry
300K	1	Pb	0.5	0.5	0.5	1	0.046	m-3m
	2	I1	0	0.5	0.5	1	0.046	4/mmm
250K	1	Pb	0	0	0.5	1	0.034	4/m
	2	I1	0	0	0	1	0.094	4/m
	3	I2	0.236	0.736	0.5	1	0.087	m2m
	4	N	0.6	0.1	0	1	0.37	m2m
	5	C	0	0.5	0.118	0.5	0.167	m2m
200K	1	Pb	0	0	0.5	1	0.033	4/m
	2	I1	0	0	0	1	0.089	4/m
	3	I2	0.23	0.73	0.5	1	0.098	m2m
	4	N	0.602	0.102	0	1	0.21	m2m
	5	C	0	0.5	0.108	0.5	0.09	2mm
150K	1	Pb	0	0	0.5	1	0.027	4/m
	2	I1	0	0	0	1	0.088	4/m
	3	I2	0.227	0.727	0.5	1	0.095	m2m
	4	N	0.601	0.101	0	1	0.943	m2m
	5	C	0	0.5	0.109	0.5	0.22	m2m

Table B.4 Details of the structure solution for the high-pressure experiments. Note that, as explained in the main text, the phase transition that occurs between p = 0.25 GPa and 0.49 GPa is related to twinning of the crystal, which makes structure solution extremely challenging. Reproduced from Sun et al.[30] with permission from The Royal Society of Chemistry.

Radiation	Synchrotron radiation λ = 0.4859 Å			
Pressure	Ambient	0.25 GPa	0.49 GPa	0.74 GPa
Formula	N_2CPbI_3	N_2CPbI_3	PbI_3	PbI_3
Z	1	1	2	2
Crystal system	Cubic	Cubic	Tetragonal	Tetragonal
Space-group	$Pm\bar{3}m$	$Pm\bar{3}m$	$P4/mbm$	$P4/mbm$
a/Å	6.36803(16)	6.34132(13)	8.9148(6)	8.8430(6)
b/Å	6.36803(16)	6.34132(13)	8.9148(6)	8.8430(6)
c/Å	6.36803(16)	6.34132(13)	6.3138(7)	6.27090(6)
α/°	90	90	90	90
β/°	90	90	90	90
γ/°	90	90	90	90
Volume/Å^3	258.24(2)	255.00(16)	501.78(9)	491.01(8)
μ/mm-1	9.357	9.476	9.621	9.833
F(000)	261	261	482	482
2Θ range for data collection/°	6.186 to 37	4.392 to 44.816	4.414 to 33.51	4.432 to 44.746
Index ranges	$-8 \le h \le 8, -7 \le k \le 7, -9 \le l \le 8$	$-8 \le h \le 8, -9 \le k \le 9, -7 \le l \le 7$	$-10 \le h \le 10, -6 \le k \le 6, -7 \le l \le 7$	$-7 \le h \le 7, -13 \le k \le 13, -8 \le l \le 8$
Reflections collected	1540	1532	1123	2338
Independent reflections	111 [$R_{int} = 0.0379, R_{sigma} = 0.0123$]	110 [$R_{int} = 0.0474, R_{sigma} = 0.0156$]	186 [$R_{int} = 0.0392, R_{sigma} = 0.0138$]	372 [$R_{int} = 0.0568, R_{sigma} = 0.0285$]
Data/restraints/param eters	111/0/9	110/0/9	186/0/9	372/0/9
Goodness-of-fit on F^2	1.145	1.218	1.137	1.317
Final R indexes [I>=2σ (I)]	$R_1 = 0.0223, wR_2 = 0.0586$	$R_1 = 0.0257, wR_2 = 0.0520$	$R_1 = 0.0650, wR_2 = 0.1928$	$R_1 = 0.0679, wR_2 = 0.2398$
Largest diff. peak/hole/e$^-$3	0.63/-0.80	0.83/-0.87	2.31/-1.52	7.36/-6.04

Table B.5 Fractional Atomic Coordinates and Equivalent Isotropic Displacement Parameters ($Å^2$) for low temperature phases. U_{eq} is defined as 1/3 of of the trace of the orthogonalized U_{IJ} tensor. Reproduced from Sun et al.[30] with permission from The Royal Society of Chemistry.

p = ambient				
Atom	x	y	z	U(eq)
Pb1	0	0	0	37.7(3)
I2	0	0	5000	91.5(5)
C1	5000	5000	5000	170(30)
N1	4260(80)	6680(110)	5000	80(20)
Pb-I-Pb angle: 180°				
p = 0.25 GPa				
Atom	x	y	z	U(eq)
Pb1	0	0	0	36.9(2)
I2	0	5000	0	104.0(6)
C1	5000	5000	5000	170(30)
N1	3260(120)	4270(110)	5000	110(30)
Pb-I-Pb angle: 180°				
p = 0.49 GPa				
Atom	x	y	z	U(eq)
Pb1	0	0	0	37.6(10)
I1	5000	5000	5000	102(3)
I2	7271(4)	7729(4)	10000	95.4(14)
Pb-I-Pb angle: 169.53(13)°				
p = 0.74 GPa				
Atom	x	y	z	U(eq)
Pb1	0	0	0	38.1(7)
I1	5000	5000	5000	79(2)
I2	2104(5)	2896(5)	10000	83.0(13)
Pb-I-Pb angle: 162.00(16)°				

Table B.6 Computed lattice parameters and the polycrystalline (orientationally-averaged) Young's moduli E of the orthorhombic (o-)$MAPbI_3$ structure using different exchange-correlation functionals compared to experiment. Reproduced from Lee and Deng et al.[34] with permission from The Royal Society of Chemistry.

Functionals	Lattice Parameters			E(GPa)
	a (Å)	b (Å)	c (Å)	
PBEsol[341]	8.9762	12.6134	8.4362	20.087
optB86b+vdW[208, 348]	8.8576	12.6751	8.561	20.526
vdW-DF2[349]	9.2098	13.1736	8.8246	18.201
TS5[112]	8.9843	12.7192	8.496	22.677
SCAN[350]	8.9474	12.7222	8.6123	
Exp.[108]	8.8657	12.6293	8.5769	-

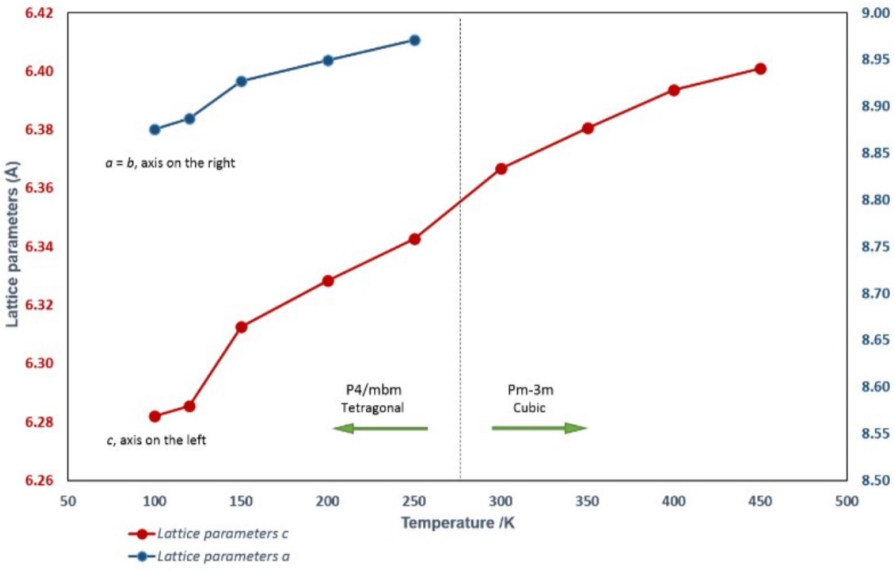

Fig. B.2 Change in lattice parameters as a function of temperature. A cubic to tetragonal phase transition was observed on cooling from 300 K to 250 K and a second phase transition was observed below 150 K. Reproduced from Sun et al.[30] with permission from The Royal Society of Chemistry.

Table B.7 Computed lattice parameters, the polycrystalline Young's modulus E, bulk modulus B, shear modulus G, and Poisson's ratio ν of all halide perovskites. The *Pnma* space group was imposed during optimization of the lattice parameters. Reproduced from Lee and Deng et al.[34] with permission from The Royal Society of Chemistry.

	a (Å)	b (Å)	c (Å)	E (GPa)	B (GPa)	G (GPa)	ν
$KPbI_3$	8.961	11.887	7.911	18.455	15.699	7.076	0.304
$RbPbI_3$	9.074	12.116	8.001	16.964	15.107	6.461	0.313
$CsPbI_3$	9.142	12.489	8.119	18.427	15.977	7.045	0.308
$FrPbI_3$	9.092	12.608	8.302	17.342	16.109	6.566	0.321
$MAPbI_3$	8.858	12.675	8.561	20.526	18.999	7.775	0.317
$KPbBr_3$	8.379	11.139	7.552	19.818	18.143	7.519	0.318
$RbPbBr_3$	8.481	11.449	7.622	19.621	17.98	7.443	0.318
$CsPbBr_3$	8.483	11.77	7.872	20.658	19.894	7.784	0.327
$FrPbBr_3$	8.45	11.882	8	20.028	20.669	7.482	0.339
$MAPbBr_3$	8.543	11.959	7.971	24.798	22.853	9.399	0.319
$KPbCl_3$	7.986	10.674	7.234	21.977	21.144	8.282	0.327
$RbPbCl_3$	8.078	10.943	7.387	21.296	21.592	7.972	0.336
$CsPbCl_3$	8.077	11.282	7.613	21.876	23.184	8.146	0.343
$FrPbCl_3$	7.975	11.346	7.849	22.807	24.609	8.475	0.346
$MAPbCl_3$	8.252	11.442	7.588	26.119	25.575	9.821	0.33
$KSnI_3$	8.851	11.828	7.876	19.022	15.916	7.312	0.301
$RbSnI_3$	8.912	12.058	8.03	18.915	16.409	7.231	0.308
$CsSnI_3$	8.856	12.35	8.359	19.287	17.139	7.348	0.312
$FrSnI_3$	8.753	12.417	8.591	18.704	17.632	7.068	0.323
$MASnI_3$	8.797	12.495	8.499	23.271	19.104	8.971	0.297
$KSnBr_3$	8.292	11.073	7.469	20.645	19.176	7.817	0.321
$RbSnBr_3$	8.345	11.348	7.623	20.473	19.625	7.719	0.326
$CsSnBr_3$	8.289	11.629	7.928	20.92	20.801	7.851	0.332
$FrSnBr_3$	8.182	11.65	8.178	24.978	22.486	9.498	0.315
$MASnBr_3$	8.492	11.753	7.895	25.818	23.387	9.809	0.316
$KSnCl_3$	7.899	10.574	7.172	23.939	23.016	9.022	0.327
$RbSnCl_3$	7.95	10.856	7.333	22.353	23.02	8.352	0.338
$CsSnCl_3$	7.837	11.119	7.701	24.519	25.448	9.153	0.339
$FrSnCl_3$	7.824	11.131	7.86	29.611	26.096	11.294	0.311
$MASnCl_3$	8.281	11.232	7.481	30.836	27.927	11.716	0.316

Table B.8 Computed components of the stiffness tensor C_{ij} (GPa) for all halide perovskites. Reproduced from Lee and Deng et al.[34] with permission from The Royal Society of Chemistry.

	C_{11}	C_{22}	C_{33}	C_{44}	C_{55}	C_{66}	C_{12}	C_{13}	C_{23}
$KPbI_3$	35	27	17	5	12	8	10	15	10
$RbPbI_3$	33	28	15	5	11	8	10	16	9
$CsPbI_3$	31	34	17	6	11	7	9	17	9
$FrPbI_3$	28	36	16	6	12	7	9	16	11
$MAPbI_3$	25	41	31	6	10	5	8	16	13
$KPbBr_3$	41	28	20	5	12	8	13	18	11
$RbPbBr_3$	39	33	18	6	13	9	12	19	12
$CsPbBr_3$	33	40	21	7	14	8	12	20	13
$FrPbBr_3$	31	42	22	6	14	8	12	20	15
$MAPbBr_3$	29	48	35	7	14	6	11	20	16
$KPbCl_3$	48	32	23	6	13	9	15	22	13
$RbPbCl_3$	43	37	22	6	13	9	15	22	15
$CsPbCl_3$	35	46	24	7	16	8	15	23	17
$FrPbCl_3$	35	48	28	7	17	8	13	25	17
$MAPbCl_3$	34	53	40	7	13	7	14	20	20
$KSnI_3$	35	29	17	5	13	8	10	16	9
$RbSnI_3$	33	33	17	5	12	8	9	17	10
$CsSnI_3$	27	36	21	6	12	7	9	16	10
$FrSnI_3$	26	36	21	6	14	7	9	18	12
$MASnI_3$	24	42	33	7	11	6	7	15	13
$KSnBr_3$	41	32	20	5	14	9	13	20	12
$RbSnBr_3$	38	38	20	6	13	9	12	20	13
$CsSnBr_3$	32	43	23	7	15	7	12	21	14
$FrSnBr_3$	34	46	31	7	19	7	10	23	13
$MASnBr_3$	33	48	38	7	13	7	12	19	16
$KSnCl_3$	48	36	26	6	15	10	16	24	15
$RbSnCl_3$	43	43	23	7	15	9	15	25	16
$CsSnCl_3$	35	49	31	8	17	8	14	25	18
$FrSnCl_3$	39	52	41	8	22	7	11	27	14
$MASnCl_3$	42	54	43	9	16	9	16	23	17

Table B.9 Computed components of the stiffness tensor S_{ij} (GPa^{-1}) for all halide perovskites. Reproduced from Lee and Deng et al.[34] with permission from The Royal Society of Chemistry.

	S_{11}	S_{22}	S_{33}	S_{44}	S_{55}	S_{66}	S_{12}	S_{13}	S_{23}
$KPbI_3$	0.05	0.05	0.11	0.2	0.08	0.13	0	-0.04	-0.03
$RbPbI_3$	0.06	0.04	0.15	0.2	0.09	0.13	0	-0.07	-0.03
$CsPbI_3$	0.07	0.03	0.14	0.17	0.09	0.14	0	-0.07	-0.02
$FrPbI_3$	0.08	0.04	0.17	0.17	0.08	0.14	0.01	-0.09	-0.03
$MAPbI_3$	0.06	0.03	0.05	0.17	0.1	0.2	0	-0.03	-0.01
$KPbBr_3$	0.04	0.05	0.09	0.2	0.08	0.13	-0.01	-0.03	-0.02
$RbPbBr_3$	0.05	0.04	0.13	0.17	0.08	0.11	0	-0.06	-0.03
$CsPbBr_3$	0.07	0.03	0.13	0.14	0.07	0.13	0	-0.07	-0.02
$FrPbBr_3$	0.08	0.03	0.13	0.17	0.07	0.13	0	-0.07	-0.03
$MAPbBr_3$	0.06	0.02	0.05	0.14	0.07	0.17	0	-0.03	-0.01
$KPbCl_3$	0.04	0.04	0.09	0.17	0.08	0.11	0	-0.03	-0.02
$RbPbCl_3$	0.05	0.04	0.11	0.17	0.08	0.11	0	-0.05	-0.03
$CsPbCl_3$	0.08	0.03	0.13	0.14	0.06	0.13	0	-0.08	-0.02
$FrPbCl_3$	0.08	0.03	0.11	0.14	0.06	0.13	0	-0.07	-0.02
$MAPbCl_3$	0.04	0.02	0.04	0.14	0.08	0.14	0	-0.02	-0.01
$KSnI_3$	0.05	0.04	0.11	0.2	0.08	0.13	0	-0.05	-0.02
$RbSnI_3$	0.06	0.04	0.14	0.2	0.08	0.13	0	-0.06	-0.02
$CsSnI_3$	0.07	0.03	0.09	0.17	0.08	0.14	0	-0.05	-0.01
$FrSnI_3$	0.1	0.03	0.13	0.17	0.07	0.14	0	-0.08	-0.02
$MASnI_3$	0.06	0.03	0.05	0.14	0.09	0.17	0	-0.03	-0.01
$KSnBr_3$	0.05	0.04	0.11	0.2	0.07	0.11	0	-0.05	-0.02
$RbSnBr_3$	0.06	0.03	0.12	0.17	0.08	0.11	0	-0.06	-0.02
$CsSnBr_3$	0.08	0.03	0.12	0.14	0.07	0.14	0	-0.07	-0.02
$FrSnBr_3$	0.06	0.02	0.07	0.14	0.05	0.14	0	-0.04	-0.01
$MASnBr_3$	0.04	0.02	0.04	0.14	0.08	0.14	0	-0.02	-0.01
$KSnCl_3$	0.04	0.04	0.08	0.17	0.07	0.1	0	-0.03	-0.02
$RbSnCl_3$	0.06	0.03	0.14	0.14	0.07	0.11	0	-0.07	-0.03
$CsSnCl_3$	0.07	0.03	0.09	0.13	0.06	0.13	0	-0.05	-0.02
$FrSnCl_3$	0.05	0.02	0.05	0.13	0.05	0.14	0	-0.03	-0.01
$MASnCl_3$	0.03	0.02	0.03	0.11	0.06	0.11	-0.01	-0.02	-0.01

Table B.10 Computed electron (e) and hole (h) deformation potentials D (eV) along the a[100], b[010], and c[001] axes for all halide perovskites. Reproduced from Lee and Deng et al.[34] with permission from The Royal Society of Chemistry.

	$D_h[100]_a$	$D_e[100]_a$	$D_h[010]_b$	$D_e[010]_b$	$D_h[001]_c$	$D_e[001]_c$
$KPbI_3$	-4.16	-3.61	-3.65	-2.12	-3.8	-1.39
$RbPbI_3$	-4.08	-3.25	-3.84	-2.08	-3.53	-1.49
$CsPbI_3$	-4	-2.62	-4.11	-2.08	-3.33	-1.68
$FrPbI_3$	-4.03	-2.3	-4.15	-2.08	-3.46	-1.77
$MAPbI_3$	-4.11	-1.98	-3.27	-2.14	-3.9	-2.04
$KPbBr_3$	-5.17	-4.16	-4.7	-2.87	-4.98	-2.18
$RbPbBr_3$	-5.27	-3.81	-5.26	-2.77	-4.71	-2.15
$CsPbBr_3$	-5.49	-3.19	-5.69	-2.68	-4.84	-2.27
$FrPbBr_3$	-5.55	-2.89	-5.69	-2.69	-5.01	-2.29
$MAPbBr_3$	-5.76	-2.91	-4.65	-2.69	-4.91	-2.41
$KPbCl_3$	-5.86	-4.79	-5.58	-3.6	-5.68	-2.9
$RbPbCl_3$	-6.08	-4.47	-6.08	-3.44	-5.61	-2.87
$CsPbCl_3$	-6.33	-3.82	-6.6	-3.35	-5.77	-2.88
$FrPbCl_3$	-6.4	-3.32	-6.75	-3.41	-6.31	-3.05
$MAPbCl_3$	-6.71	-3.83	-5.48	-3.3	-5.51	-2.93
$KSnI_3$	-5.58	-4.74	-5.09	-1.48	-5	-0.77
$RbSnI_3$	-5.57	-4.03	-5.47	-1.75	-4.86	-0.97
$CsSnI_3$	-5.72	-2.6	-5.85	-2.59	-5.18	-1.41
$FrSnI_3$	-6.01	-2.4	-6.21	-3.09	-5.86	-2.01
$MASnI_3$	-5.71	-1.61	-4.82	-3.18	-5.34	-1.58
$KSnBr_3$	-6.72	-5.32	-6.25	-2.16	-6.3	-1.49
$RbSnBr_3$	-6.9	-4.57	-6.93	-2.41	-6.22	-1.66
$CsSnBr_3$	-7.18	-3.17	-7.39	-3.09	-6.65	-2.03
$FrSnBr_3$	-7.36	-2.59	-7.78	-3.24	-7.48	-2.53
$MASnBr_3$	-7.55	-2.94	-6.45	-3.24	-6.36	-2.05
$KSnCl_3$	-7.47	-5.97	-7.06	-2.86	-7.13	-2.23
$RbSnCl_3$	-7.7	-5.23	-7.79	-3.03	-7.05	-2.33
$CsSnCl_3$	-8.06	-3.47	-8.44	-3.75	-7.92	-2.9
$FrSnCl_3$	-8.31	-3.06	-8.79	-3.69	-8.51	-3.22
$MASnCl_3$	-8.81	-4.17	-7.45	-3.47	-6.83	-2.37

Table B.11 Computed electron (e) and hole (h) effective carrier masses m* (in units of rest mass m0) along the a[100], b[010], and c[001] axes for all halide perovskites. Reproduced from Lee and Deng et al.[34] with permission from The Royal Society of Chemistry.

	$m_h^*[100]_a$	$m_e^*[100]_a$	$m_h^*[010]_b$	$m_e^*[010]_b$	$m_h^*[001]_c$	$m_e^*[001]_c$
$KPbI_3$	0.41	0.3	0.35	0.37	0.32	0.34
$RbPbI_3$	0.42	0.27	0.28	0.27	0.32	0.31
$CsPbI_3$	0.4	0.24	0.2	0.16	0.28	0.26
$FrPbI_3$	0.3	0.2	0.17	0.14	0.23	0.21
$MAPbI_3$	0.25	0.2	0.22	0.15	0.25	0.22
$KPbBr_3$	0.41	0.36	0.4	0.51	0.36	0.41
$RbPbBr_3$	0.37	0.33	0.29	0.31	0.34	0.36
$CsPbBr_3$	0.27	0.25	0.2	0.2	0.27	0.27
$FrPbBr_3$	0.23	0.22	0.18	0.17	0.23	0.23
$MAPbBr_3$	0.24	0.23	0.23	0.19	0.26	0.26
$KPbCl_3$	0.46	0.46	0.46	0.62	0.43	0.53
$RbPbCl_3$	0.39	0.39	0.34	0.41	0.38	0.44
$CsPbCl_3$	0.3	0.32	0.25	0.26	0.31	0.34
$FrPbCl_3$	0.25	0.27	0.22	0.23	0.25	0.27
$MAPbCl_3$	0.28	0.31	0.29	0.28	0.32	0.35
$KSnI_3$	0.25	0.3	0.2	0.43	0.2	0.22
$RbSnI_3$	0.21	0.26	0.15	0.25	0.17	0.2
$CsSnI_3$	0.12	0.18	0.08	0.11	0.11	0.16
$FrSnI_3$	0.09	0.14	0.06	0.08	0.08	0.13
$MASnI_3$	0.12	0.2	0.1	0.09	0.13	0.21
$KSnBr_3$	0.26	0.34	0.25	0.63	0.23	0.26
$RbSnBr_3$	0.21	0.3	0.16	0.31	0.19	0.23
$CsSnBr_3$	0.13	0.22	0.1	0.14	0.13	0.19
$FrSnBr_3$	0.09	0.14	0.07	0.1	0.08	0.14
$MASnBr_3$	0.13	0.22	0.11	0.15	0.14	0.21
$KSnCl_3$	0.31	0.42	0.32	0.82	0.29	0.34
$RbSnCl_3$	0.25	0.37	0.21	0.41	0.25	0.31
$CsSnCl_3$	0.16	0.26	0.13	0.19	0.15	0.25
$FrSnCl_3$	0.11	0.19	0.1	0.16	0.11	0.19
$MASnCl_3$	0.15	0.27	0.16	0.24	0.18	0.25

Table B.12 Computed electron (e)and hole (h) mobilities $\mu(cm^2/V \cdot s)$ at 300 K along the a[100], b[010], and c[001] axes for halide perovskites. Reproduced from Lee and Deng et al.[34] with permission from The Royal Society of Chemistry.

	$\mu_h[100]_a$	$\mu_e[100]_a$	$\mu_h[010]_b$	$\mu_e[010]_b$	$\mu_h[001]_c$	$\mu_e[001]_c$
$KPbI_3$	1137	3301	1689	4429	1242	7994
$RbPbI_3$	1077	4903	2692	10464	1293	8108
$CsPbI_3$	1157	9758	7157	44701	2271	10951
$FrPbI_3$	2181	17536	10607	74258	3116	15131
$MAPbI_3$	2986	21668	10747	64657	3825	21029
$KPbBr_3$	862	1821	762	1127	637	2412
$RbPbBr_3$	1015	2708	1625	4721	726	2992
$CsPbBr_3$	1737	6255	4187	19861	1504	6528
$FrPbBr_3$	2309	9528	5645	29195	2064	9602
$MAPbBr_3$	1925	8076	5237	24025	2684	10643
$KPbCl_3$	576	871	445	501	365	834
$RbPbCl_3$	748	1372	892	1769	468	1313
$CsPbCl_3$	1061	2587	2140	6995	838	2705
$FrPbCl_3$	1638	5137	2830	9763	1409	4801
$MAPbCl_3$	1082	2695	2388	7477	1345	3790
$KSnI_3$	2278	1973	3677	6664	2343	78177
$RbSnI_3$	3264	3657	8251	20108	3592	66035
$CsSnI_3$	9313	16868	33249	88977	11546	66044
$FrSnI_3$	20031	40155	61048	134985	19829	53838
$MASnI_3$	8231	33449	38204	95096	12068	39757
$KSnBr_3$	1541	1282	1607	1337	1213	16006
$RbSnBr_3$	2446	2280	4497	7331	1975	17409
$CsSnBr_3$	6001	8585	15720	36005	5589	21583
$FrSnBr_3$	17531	39083	35911	75835	17174	41338
$MASnBr_3$	6306	10700	15776	33699	8352	27283
$KSnCl_3$	951	726	780	434	667	4530
$RbSnCl_3$	1412	1146	2102	2587	963	4972
$CsSnCl_3$	3460	5028	6956	12886	3363	7539
$FrSnCl_3$	8238	17285	12194	21463	8502	15883
$MASnCl_3$	3703	3875	5853	9584	4125	14372

Table B.13 Computed electron (e)and hole (h) mobilities $\mu(cm^2/V \cdot s)$ at 100 K along the a[100], b[010], and c[001] axes for halide perovskites. Reproduced from Lee and Deng et al.[34] with permission from The Royal Society of Chemistry.

	$\mu_h[100]_a$	$\mu_e[100]_a$	$\mu_h[010]_b$	$\mu_e[010]_b$	$\mu_h[001]_c$	$\mu_e[001]_c$
$KPbI_3$	5930	17165	8733	22448	6609	42306
$RbPbI_3$	5546	26323	14609	54387	6664	40847
$CsPbI_3$	5981	50044	35703	242819	11641	55487
$FrPbI_3$	11141	93714	55729	360166	16804	80425
$MAPbI_3$	15097	114133	53960	327720	20880	105133
$KPbBr_3$	4491	9626	4044	5896	3221	12166
$RbPbBr_3$	5317	13553	8294	25353	3790	15839
$CsPbBr_3$	9322	33522	22139	99755	7489	34142
$FrPbBr_3$	12553	51667	30289	156021	10889	52270
$MAPbBr_3$	9802	42855	27554	132713	13505	55900
$KPbCl_3$	3072	4588	2272	2585	1865	4239
$RbPbCl_3$	3907	7245	4758	9338	2500	6640
$CsPbCl_3$	5643	13162	10640	37502	4316	13775
$FrPbCl_3$	8659	26517	14712	51644	7177	25367
$MAPbCl_3$	5747	13663	12382	37226	7178	20284
$KSnI_3$	11285	9899	20020	34988	12309	411248
$RbSnI_3$	16686	18641	39857	108325	19624	326311
$CsSnI_3$	52805	92935	185905	427905	60411	321156
$FrSnI_3$	94117	195595	334177	657575	108550	273596
$MASnI_3$	47349	167268	180799	540424	60092	206966
$KSnBr_3$	8308	6786	8340	6943	6441	84314
$RbSnBr_3$	12523	11714	24518	38759	10480	91602
$CsSnBr_3$	31990	44112	79639	196194	26678	110970
$FrSnBr_3$	81224	216451	187772	443736	98322	212853
$MASnBr_3$	29772	52624	91449	166398	40792	143043
$KSnCl_3$	5062	3712	3912	2264	3532	24285
$RbSnCl_3$	7389	6012	11127	13783	4784	25651
$CsSnCl_3$	16700	26746	36054	70623	18021	37377
$FrSnCl_3$	45119	84782	67936	119297	44671	79477
$MASnCl_3$	19877	20437	30360	50788	21167	77164

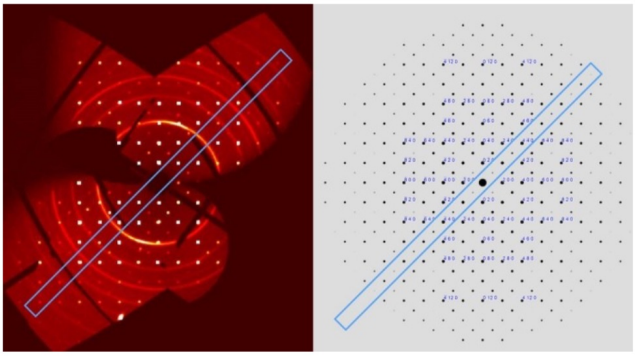

(a) (b)

Fig. B.3 In order to investigate systematic absences in the high-pressure SCXRD datasets, the zero diffraction plane of black $FAPbI_3$ are compared: (a) experimental and (b) simulated after structure solution in $Im\bar{3}$. A R_{wp} value of 9.8% and systematic absences not in agreement with $Im\bar{3}$ (highlighted with the blue boxes) indicate that $Im\bar{3}$ is likely to be a wrong assignment. Reproduced from Sun et al.[30] with permission from The Royal Society of Chemistry.

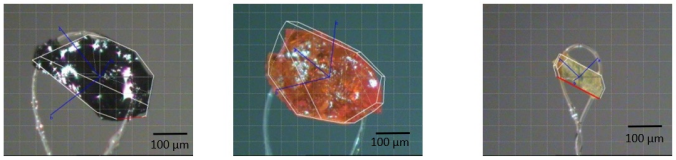

Fig. B.4 Representative photographs (left to right) of cubic $FAPbI_3$, cubic $FAPbBr_3$ and the hexagonal phase of $FAPbI_3$ respectively. The crystals were mounted for single crystal X-ray diffraction. Reproduced from Sun et al.[31] with permission from John Wiley & Sons.

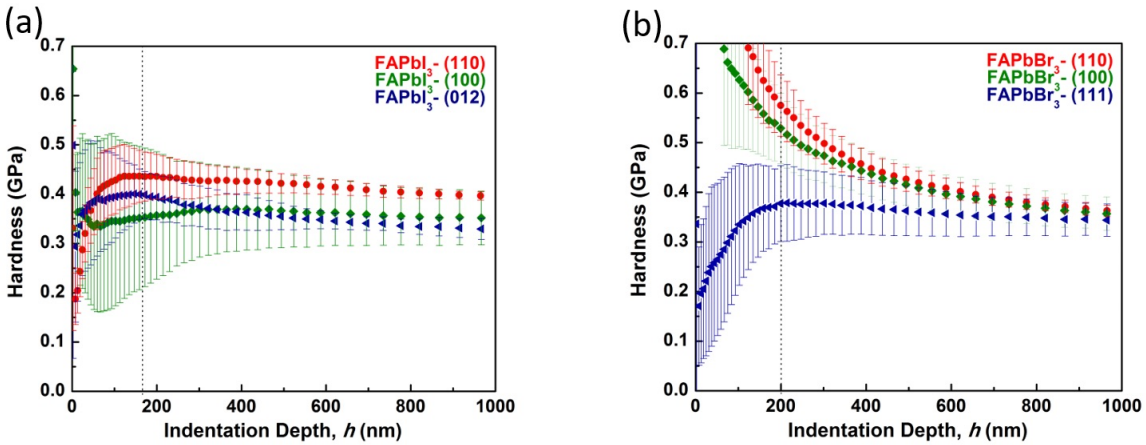

Fig. B.5 Hardness as a function of indentation depth for (a) cubic $FAPbI_3$ and (b) cubic $FAPbBr_3$. Reproduced from Sun et al.[31] with permission from John Wiley & Sons.

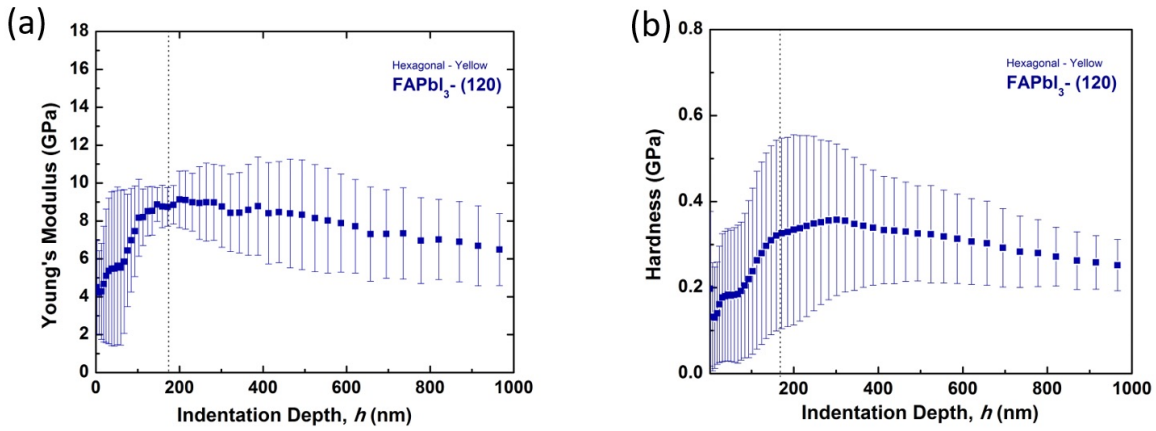

Fig. B.6 Young's modulus and (b) hardness as a function of indentation depth for the hexagonal phase of $FAPbI_3$. Reproduced from Sun et al.[31] with permission from John Wiley & Sons.

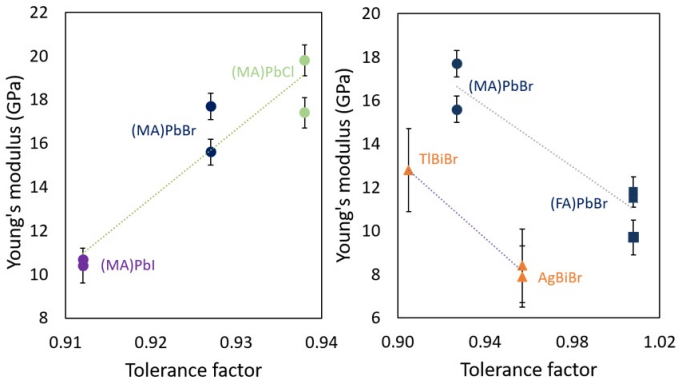

Fig. B.7 (a) Young's modulus (Ref[28]) as a function of tolerance factor for $MAPbX_3$, (X = Cl, Br, I) showing that more closely packed systems have higher stiffness (b) Young's moduli of bromide perovskites showing high tolerance factors. Dotted lines are to guide the eye. Reproduced from Sun et al.[31] with permission from John Wiley & Sons.

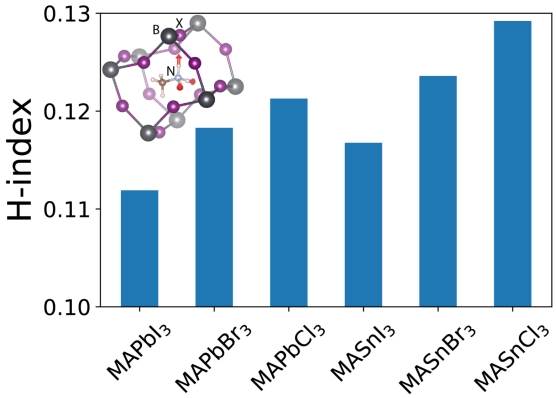

Fig. B.8 Computed average hydrogen-bonding index (H-index) for the three H atoms attached to N on a MA cation for the o-$MABX_3$ hybrid series. Inset represents a schematic view of the three H stretching modes. Reproduced from Lee and Deng et al.[34] with permission from The Royal Society of Chemistry.

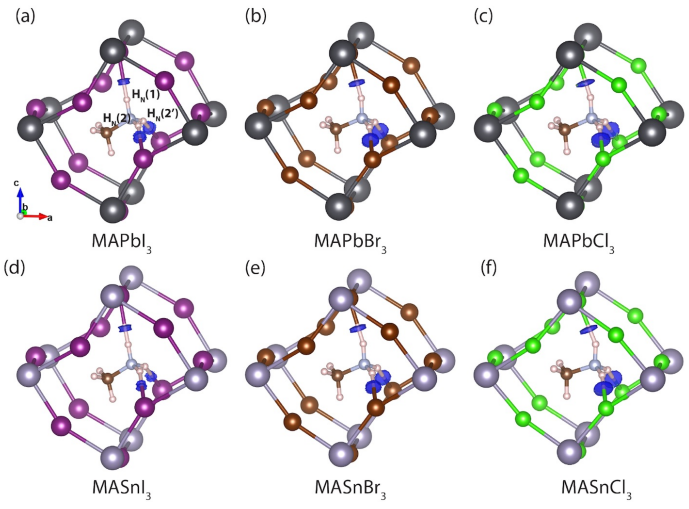

Fig. B.9 Non-covalent interaction density isosurfaces for (a) o-$MAPbI_3$, (b) o-$MAPbBr_3$, (c) o-$MAPbCl_3$, (d) o-$MASnI_3$, (e) o-$MASnBr_3$, and (f) o-$MASnCl_3$. The isosurfaces were generated for s = 0.5 and $-0.04 < \rho < -0.02$ (ρ is the electron density and s is the reduced density gradient). Reproduced from Lee and Deng et al.[34] with permission from The Royal Society of Chemistry.

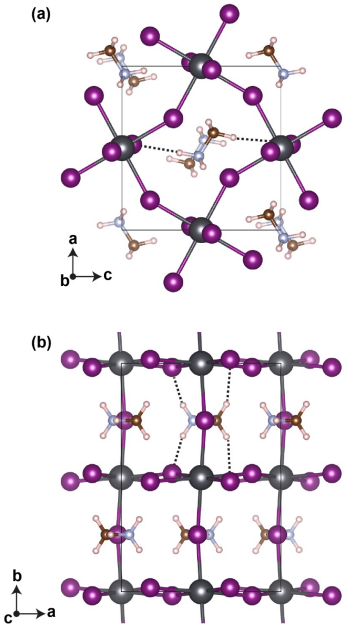

Fig. B.10 (a) ac plane of o-$MAPbI_3$ showing two H atoms on a MA cation oriented along the c-axis. (b) ab plane showing the other four H atoms on the MA cation oriented towards the b-axis. Dotted lines indicate hydrogen-bonding interactions between H and I atoms. Reproduced from Lee and Deng et al.[34] with permission from The Royal Society of Chemistry.

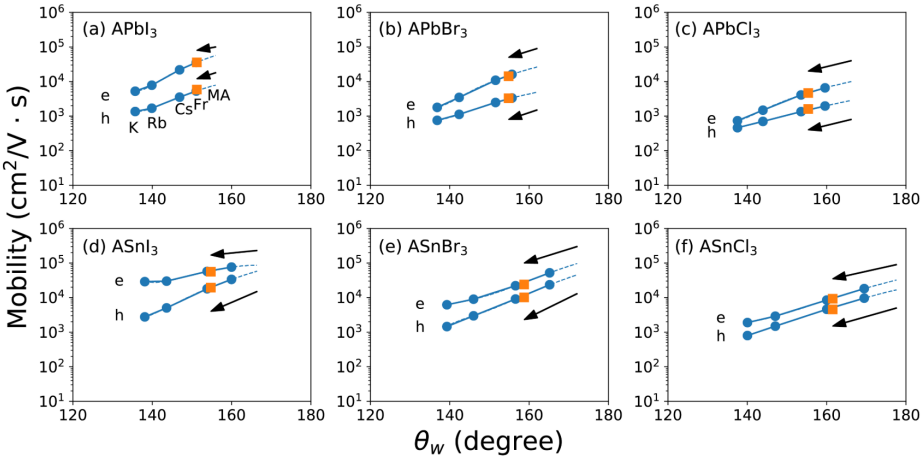

Fig. B.11 Average electron (e) and hole (h) mobilities along the three crystal axes versus θ_w for (a) o-$APbI_3$, (b) o-$APbBr_3$, (c) o-$APbCl_3$, (d) o-$ASnI_3$, (e) o-$ASnBr_3$, and (f) o-$ASnCl_3$. Blue and orange symbols correspond to the o-ABX_3 inorganic and o-$MABX_3$ hybrid halide perovskites respectively. Arrows indicate the reduction in the e and h mobilities of o-$MABX_3$ with respect to what they would have been for hypothetical o-ABX_3 perovskites having the same size A-site cation. The arrows follow the extrapolated trend lines. The values are calculated at 300 K. Reproduced from Lee and Deng et al.[34] with permission from The Royal Society of Chemistry.

Appendix C

Supplementary Tables and Figures for Chapter 6

Fig. C.1 Representative single crystals of (a) $GuaPbI_3$, (b) $(Gua)_2PbI_4$ and (c) $(Gua)_3PbI_5$. Reproduced from Deng et al.[35] with permission from the AIP Publishing.

Table C.1 Details of the structure solution using variable temperature X-ray diffraction. Reproduced from Deng et al.[35] with permission from the AIP Publishing.

	$GuaPbI_3$-e	$GuaPbI_3$-f	$GuaPbI_3$-c	$(Gua)_2PbI_4$	$(Gua)_3PbI_5$
$d_{Pb\text{-}I}$	3.30	3.20	3.21	3.26	3.21
∠Pb-I-Pb	93.49	75.01	177.08	161.21	151.61

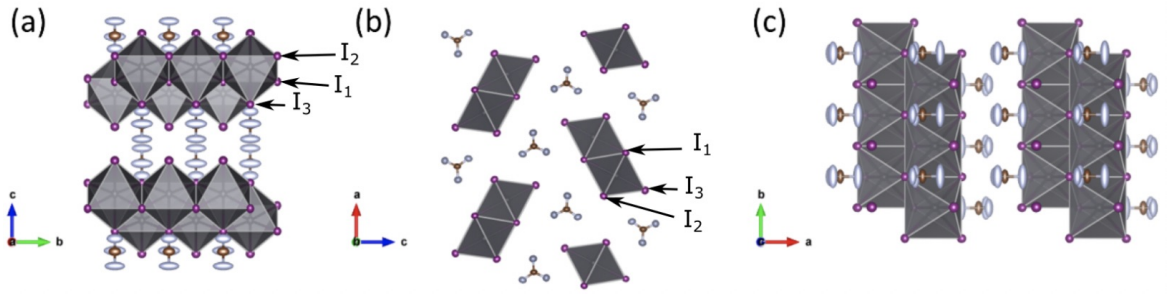

Fig. C.2 Illustration of the crystal structure of $GuaPbI_3$-e along (a) a-axis, (b) b-axis and (c) c-axis, respectively. Key: the grey polyhedra represent the 1D edge-sharing PbI_6 octahedra, purple spheres represent iodide, blue nitrogen and brown carbon. I_1, I_2 and I_3 denote the iodine atoms that define the three different kinds of Pb-I bond. The large ellipsoids of nitrogen show the disorder of the guanidinium cation at room temperature. Hydrogen atoms are not represented. Reproduced from Deng et al.[35] with permission from the AIP Publishing..

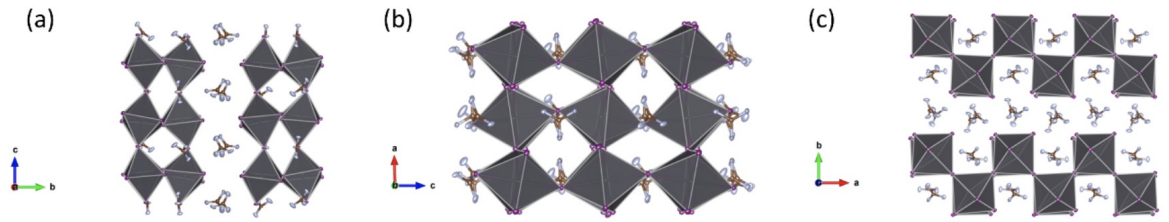

Fig. C.3 Illustration of the crystal structure of $(Gua)_2PbI_4$ along (a) a-axis, (b) b-axis and (c) c-axis, respectively. Key: the grey polyhedra represent the 2D corner-sharing PbI_6 octahedra, purple spheres represent iodide, blue nitrogen and brown carbon. The large ellipsoids of nitrogen represent the disorder of the guanidinum cation at room temperature. Hydrogen atoms are not represented. Reproduced from Deng et al.[35] with permission from the AIP Publishing.

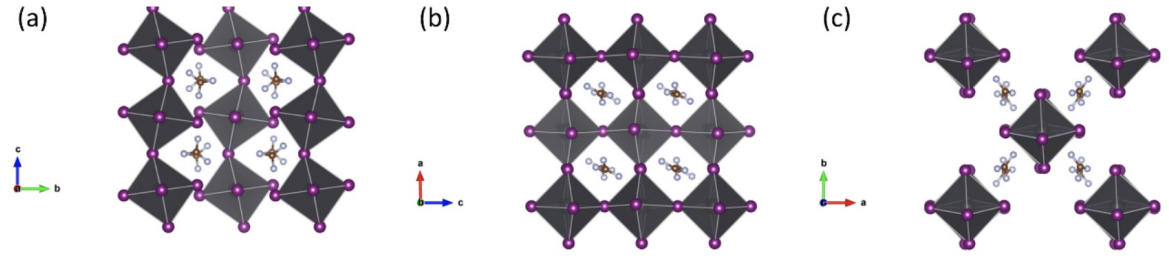

Fig. C.4 Illustration of the crystal structure of $(Gua)_3PbI_5$ along (a) a-axis, (b) b-axis and (c) c-axis, respectively. Key: the grey polyhedra represent the 1D corner-sharing PbI_6 octahedra, purple spheres represent iodide, blue nitrogen and brown carbon. The large ellipsoids of nitrogen represent the disorder of the guanidinum cation at room temperature. Hydrogen atoms are not represented. Reproduced from Deng et al.[35] with permission from the AIP Publishing.

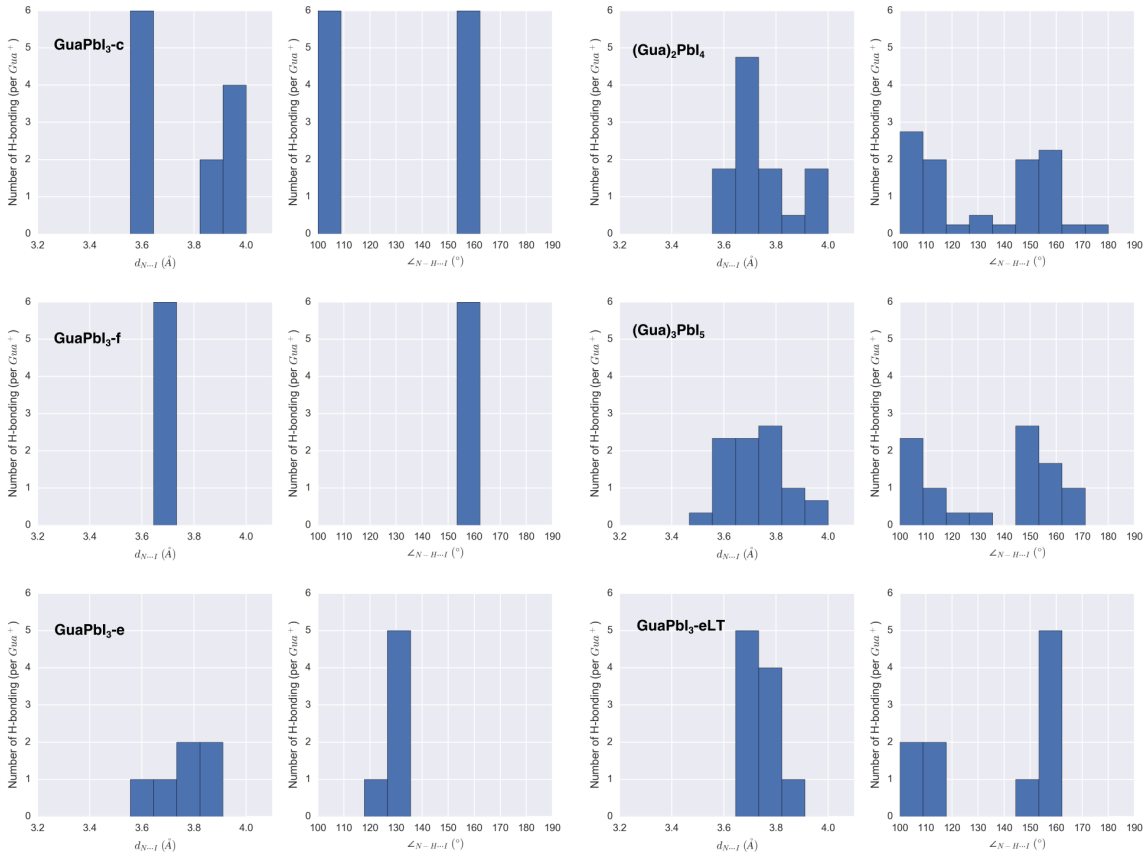

Fig. C.5 Statistical distribution of $d_{N\cdots I}$ bond lengths and ∠N-H···I bond angles determined from the DFT relaxed structures of $(Gua)_xPbI_{x+2}$ (x = 1, 2 and 3). "c", "f" and "e" denote corner-sharing, face-sharing and edge-sharing respectively. "LT" denotes the low temperature (120 K) structure. The criteria for counting H-bonds is: ∠N-H···I > 100° and $d_{N\cdots I} < 4$ Å. Reproduced from Deng et al.[35] with permission from the AIP Publishing.